

Quantum limits on measurement and control of a mechanical oscillator

THÈSE N° 7202 (2016)

PRÉSENTÉE LE 16 SEPTEMBRE 2016
À LA FACULTÉ DES SCIENCES DE BASE
LABORATOIRE DE PHOTONIQUE ET MESURES QUANTIQUES (SB/STI)
PROGRAMME DOCTORAL EN PHOTONIQUE

ÉCOLE POLYTECHNIQUE FÉDÉRALE DE LAUSANNE

POUR L'OBTENTION DU GRADE DE DOCTEUR ÈS SCIENCES

PAR

Vivishek SUDHIR

acceptée sur proposition du jury:

Prof. Y. Bellouard, président du jury
Prof. T. Kippenberg, directeur de thèse
Prof. A. Heidmann, rapporteur
Prof. F. Marquardt, rapporteur
Prof. T. Lasser, rapporteur



ÉCOLE POLYTECHNIQUE
FÉDÉRALE DE LAUSANNE

Suisse
2016

*To my father, who by patiently answering all my questions, became my first science teacher,
And to my mother, who taught me everything else*

To gaze up from the ruins of the oppressive present towards the stars is to recognise the indestructible world of laws, to strengthen faith in reason, to realise the "harmonia mundi" that transfuses all phenomena, and that never has been, nor will be, disturbed.

HERMANN WEYL, Space-Time-Matter

Acknowledgements

It seems to me I am trying to tell you a dream – making a vain attempt, because no relation of a dream can convey the dream-sensation, that commingling of absurdity, surprise, and bewilderment in a tremor of struggling revolt, that notion of being captured by the incredible which is of the very essence of dreams. . .

JOSEPH CONRAD, Heart of Darkness

Experimental physics demands a certain degree of manual dexterity, the patience to tolerate the mundane, and an inexhaustible supply of optimism. Tobias hired me to work on an immensely sophisticated experiment despite any proof of my possessing these qualities; I am indebted to him for the belief he has placed in me. I would also like to acknowledge his dedication to fostering an environment where the pursuit of science is unencumbered by other worldly concerns. Stefan, Ewold and Samuel bore the brunt of a theorist trying to perform delicate experiments; the stern, yet encouraging, stewardship of this trio ensured that I enjoyed the culture shock. Dal Wilson was more than a colleague and a post-doc; his pragmatic approach to physics provided the ideal counter-point in our attempts to forge a deeper understanding of things ranging from vibration isolation to the subtleties of quantum mechanics. Without the patient efforts of Amir, Ryan and Hendrik in designing, fabricating, and testing of devices, none of the results reported here would have been possible. I hope I have been able to bequeath a better vision of the future of our experiment to Sergey. Conversations with Alexey, Daniel and Nathan have enabled me to vicariously learn how to measure microwave “photons”. John Jost once taught me how to decorate a Christmas tree; since then he has imparted some wisdom on frequency metrology, and some on atomic physics. Together with Dal, Victor and Caroline have probably spent the most time with me outside the lab; it was fun to exercise an air of social normalcy with this bunch. Christophe has been an amazing sparring partner on every subject capable of being brought under scientific scrutiny.

The personal space required for the pursuit of science comes through the sacrifice of many people. My family back home in India – parents, sister, grand-parents – have had to patiently wait for the brief interludes when I go home. No words can do justice to this and the very many other pleasures they have surrendered over the years for my sake. Before physics attracted me, I was charmed by someone else; I am lucky to have married her. Long time friends, mentors – Ajith and Subeesh – have played pivotal roles in my being able to engage in physics; I hope to repay this enormous debt, some day.

It was a privilege to have learnt from a few great teachers during my formative years. Their vision of an indelible unity in nature continues to motivate my study of physics.

Abstract

The precision measurement of position has a long-standing tradition in physics. Cavendish's verification of the universal law of gravitation using a torsion pendulum, Perrin's confirmation of the atomic hypothesis via the precise measurement of the Brownian motion, and, the verification of the mechanical effect of electromagnetic radiation, all belong to this classical heritage. Quantum mechanics posits that the measurement of position results in an uncertain momentum; an idea developed to full maturity within the context of interferometric searches for gravity waves. Over the past decade, standing at the confluence of quantum optics and nanomechanics, cavity optomechanics has emerged as a powerful platform to study the quantum limits of position measurements.

The subject of this thesis is the precision measurement of the position of a nano-mechanical oscillator, the fundamental limits of such measurements, and its relevance to measurement-based feedback control. The nano-mechanical oscillator is coupled to light confined in an optical micro-cavity via radiation pressure. The fluctuations in the position of the oscillator are transduced onto the phase of the light, while quantum fluctuations in the amplitude of the light leads to a disturbance in the momentum of the oscillator. We perform an interferometric position measurement with a sensitivity that is 10^5 times below what is required to resolve the zero-point motion of the oscillator, constituting the most precise measurement of thermal motion yet. The resulting disturbance – measurement back-action – is observed to be commensurate with the uncertainty principle, leading to a 10% contribution to the total motion of the oscillator.

The continuous record of the measurement (performed in a 4 K cryogenic environment) furnishes the ability to resolve the zero-point motion of the oscillator within its decoherence rate – the necessary condition for measurement-based feedback control of the state of the oscillator. Using the measurement record as error signal, the oscillator is cooled towards its ground state, resulting in a factor 10^4 suppression of its total (thermal and back-action) motion, to a final occupation of 5 phonons on average.

Measurements generally proceed by establishing correlations between the system being measured and the measuring device. For the class of quantum measurements employed here – continuous linear measurements – these correlations arise due to measurement back-action. These back-action-induced correlations appear as correlations between the degrees of freedom of the measuring device. For interferometric position measurements, quantum correlations are established between the phase and amplitude of the light. In a homodyne measurement, they lead to optical squeezing, while in a heterodyne measurement, they appear as an asymmetry in the sidebands carrying information about the oscillator position. Feedback is used to enhance sideband asymmetry, a first proof-of-principle demonstration of the ability to control quantum correlations using feedback. In the regime where amplified vacuum noise dominates the feedback signal, the disappearance of sideband asymmetry visualises a fundamental limit

ABSTRACT

of linear feedback control. Using a homodyne detector, we also characterise these quantum correlations manifested as optical squeezing at the 1% level.

Keywords: quantum measurement, cavity optomechanics, quantum feedback, quantum correlations

Zusammenfassung

Die präzise Messung von Aufenthaltsorten und Auslenkungen verfügt über eine lange Tradition in der Physik. Hierzu zählen unter anderem Cavendishs Bestätigung des Gravitationsgesetzes mithilfe eines Torsionspendels, Perrins Beleg für die Atomhypothese durch die genaue Vermessung der Brownschen Bewegung, sowie der Nachweis der mechanischen Auswirkungen von elektromagnetischer Strahlung. Die Prinzipien der Quantenmechanik, die im Zusammenhang mit der interferometrischen Detektion von Gravitationswellen weiter vertieft wurden, besagen, dass die Messung des Aufenthaltsortes eines Objekts in einer Unschärfe des Impulses resultiert. Das Feld der Resonator-Optomechanik, welches sich am Schnittpunkt von Quantenoptik und Nanomechanik befindet, hat sich innerhalb des letzten Jahrzehnts zu einem mächtigen Werkzeug zur Untersuchung der Quantengrenze von Positionsmessungen entwickelt.

Diese Arbeit thematisiert die präzise Positionsmessung eines nanomechanischen Oszillators, fundamentale Einschränkungen solcher Messungen, sowie ihre Bedeutung für die messungsbasierte Rückkopplungsregelung. Der nanomechanische Oszillator ist in diesen Experimenten über den Strahlungsdruck an das Licht, welches im Inneren eines Mikroresonators zirkuliert, gekoppelt. Die Fluktuationen in der Auslenkung des Oszillators werden der Phase des Lichts aufgeprägt, wohingegen die Quantenfluktuationen in der Amplitude des Lichts den Impuls des Oszillators stören. Wir führen eine interferometrische Messung der Auslenkung durch, die um einen Faktor von 10^5 unterhalb der Grundzustandsfluktuationen liegt und damit die bis dato präziseste Messung einer thermischen Bewegung darstellt. Unsere Beobachtung der daraus resultierenden Störung durch die Messrückwirkung stimmt mit der Unschärferelation überein und beträgt 10% der gesamten Bewegung des Oszillators.

Die kontinuierliche Messung (durchgeführt in einer Tieftemperatur-Umgebung von 4 K) ermöglicht es, die Grundzustandsfluktuationen innerhalb ihrer Dekohärenzzeit aufzulösen, welches eine notwendige Bedingung für die Rückkopplungskontrolle des Oszillators darstellt. Hierbei wird der Messverlauf als Fehlersignal dazu genutzt, den Oszillator bis dicht an seinen quantenmechanischen Grundzustand zu kühlen. Das Resultat hiervon ist eine um den Faktor 10^4 reduzierte totale Auslenkung (bestehend aus thermischer Bewegung und Messrückwirkung) und einer erreichten durchschnittlichen Besetzungszahl von 5 Phononen.

Generell verläuft eine Messung durch die Erzeugung von Korrelationen zwischen dem gemessenen Objekt und der Messinstanz. In der Art der hier durchgeführten Quantenmessungen, den kontinuierlichen linearen Messungen, entstehen diese Korrelationen durch die Messrückwirkung und erscheinen als Korrelationen zwischen den verschiedenen Freiheitsgraden der Messinstanz. Bei interferometrischen Positionsmessungen werden Quantenkorrelationen zwischen der Phase und der Amplitude des Lichts erzeugt. In der homodynen Detektion resultiert dies in gequetschtem Licht, wohingegen in einem heterodynen Messschema die Korrelationen als eine Asymmetrie in den Seitenbändern, die die Information über die Position des

Oszillatoren enthalten, auftreten. Durch aktive Regelung wird diese Asymmetrie verstärkt und so der erste prinzipielle Nachweis für die Fähigkeit der Kontrolle von Quantenkorrelationen durch Regelung erbracht. In einem System, in dem verstärktes Vakuumrauschen das Regelungssignal beherrscht, demonstriert die ausbleibende Asymmetrie eine fundamentale Beschränkung der Methode der linearen Regelungskontrolle. Des Weiteren quantifizieren wir die Quantenkorrelationen mittels eines Homodyndetektors als optische Quetschung von etwa 1%.

Stichwörter: Quantenmessung, Resonator-Optomechanik, Quantenregelung, Quantenkorrelationen

Résumé

La mesure précise de la position tient une place de choix en physique. La vérification par Cavendish de la loi universelle de la gravitation en utilisant un pendule de torsion ; la confirmation par Perrin de l'hypothèse de l'atome grâce à la mesure précise du mouvement Brownien ; la vérification de l'effet mécanique du rayonnement électromagnétique ; toutes ces expériences capitales appartiennent à un même héritage scientifique. La mécanique quantique postule que la mesure précise de la position cause une incertitude sur la quantité de mouvement ; une idée qui a connu sa maturité dans le contexte de la recherche d'ondes gravitationnelles par interférométrie optique. Au cours de la dernière décennie, résidant à la croisée de l'optique quantique et de la nano-mécanique, l'optomécanique de cavité est devenue une plateforme de choix pour étudier les prédictions des limites imposées par la mécanique quantique sur la précision des mesures de position.

Le sujet de cette thèse étudie la mesure précise de la position d'un oscillateur nano-mécanique, les limites fondamentales d'une telle mesure et sa pertinence sur une boucle de rétroaction basée sur la mesure elle-même. L'oscillateur nano-mécanique est couplé à la lumière confinée dans une micro-cavité optique par l'intermédiaire de la pression de radiation. Les fluctuations de la position de l'oscillateur sont imprimées sur la phase de la lumière, alors que les fluctuations quantiques de l'amplitude entraînent une perturbation de la quantité de mouvement de l'oscillateur. Nous effectuons une mesure de la position par interférométrie avec une sensibilité qui est 10^5 fois meilleure que celle requise pour résoudre le mouvement du point zéro de l'oscillateur. Ceci constitue la mesure la plus précise du mouvement thermique à ce jour. La perturbation résultante observée (la rétro-action de mesure) concorde avec le principe d'incertitude et équivaut à une contribution de 10% du mouvement total de l'oscillateur.

L'enregistrement continu de la mesure (effectuée dans un environnement cryogénique à 4 K) permet de résoudre le mouvement du point zéro de l'oscillateur pendant son délai de décohérence — la condition nécessaire pour contrôler l'état de l'oscillateur par une boucle de rétroaction basée sur la mesure. En utilisant l'enregistrement de la mesure comme signal d'erreur, l'oscillateur est refroidi vers son état fondamental, résultant en une réduction par un facteur 10^4 de son mouvement total (agitation thermique et rétroaction de mesure) et une occupation finale de 5 phonons en moyenne.

En général, les mesures procèdent à l'établissement de corrélations entre le système mesuré et l'appareil de mesure. Pour la classe de mesures quantiques utilisées ici (mesures linéaires continues), ces corrélations surgissent à cause de la rétroaction de mesure. Ces corrélations induites par la rétro-action de mesure apparaissent comme des corrélations entre les degrés de liberté de l'appareil de mesure. Pour des mesures de position par interférométrie, des corrélations quantiques s'établissent entre la phase et l'amplitude de la lumière. Dans une mesure homodyne, elles conduisent à un état optique comprimé tandis que, dans une me-

sure hétérodyne, elles se traduisent par une asymétrie dans les bandes latérales, porteuses de l'information sur la position de l'oscillateur. Une boucle de rétroaction est utilisée pour augmenter l'asymétrie des bandes latérales. Ceci représente la première démonstration de principe de la capacité de contrôler des corrélations quantiques en utilisant une boucle de rétroaction. Dans le régime où le bruit du vide amplifié domine le signal de rétroaction, la disparition de l'asymétrie des bandes latérales établit une limite fondamentale du contrôle par boucle de rétroaction linéaire. Grâce à un détecteur homodyne, nous caractérisons aussi ces corrélations quantiques qui se manifestent sous la forme d'états optiques comprimés par un facteur d'environ 1%.

Mots clés : mesures quantiques, optomécanique de cavité, rétroaction quantique, corrélations quantiques

List of publications

1. D. J. Wilson, **V. Sudhir**, N. Piro, R. Schilling, A. Ghadimi and T. J. Kippenberg, *Measurement-based control of a mechanical oscillator at its thermal decoherence rate*, *Nature* **524**, 325 (2015)
2. **V. Sudhir**, D. J. Wilson, R. Schilling, H. Schütz, S. Fedorov, A. Ghadimi, A. Nunnenkamp and T. J. Kippenberg, *Appearance and disappearance of quantum correlations in measurement-based feedback control of a mechanical oscillator*, arXiv:1602.05942 (2016)
3. **V. Sudhir**, R. Schilling, S. Fedorov, H. Schütz, D. J. Wilson and T. J. Kippenberg, *Quantum correlations of light due to a room temperature mechanical oscillator*, arXiv:1608.00699 (2016)
4. R. Schilling, A. Ghadimi, H. Schütz, **V. Sudhir**, D. J. Wilson and T. J. Kippenberg, *Near-Field Integration of a SiN Nanobeam and a SiO₂ Microcavity for Heisenberg-Limited Displacement Sensing*, *Phys. Rev. Applied* **5**, 054019 (2016)
(featured in a Physics Synopsis: Position Detector Approaches the Heisenberg Limit)
5. H. Okamoto, R. Schilling, H. Schütz, **V. Sudhir**, D. J. Wilson, H. Yamaguchi and T. J. Kippenberg, *A strongly coupled Λ -type micromechanical system*, *Appl. Phys. Lett.* **108**, 153015 (2016)
6. A. Nunnenkamp, **V. Sudhir**, A. K. Feofanov, A. Roulet and T. J. Kippenberg, *Quantum-Limited Amplification and Parametric Instability in the Reversed Dissipation Regime of Cavity Optomechanics* *Phys. Rev. Lett.* **113**, 023604 (2014)
7. T. Ramos, **V. Sudhir**, K. Stannigel, P. Zoller and T. J. Kippenberg, *Nonlinear Quantum Optomechanics via Individual Intrinsic Two-Level Defects*, *Phys. Rev. Lett.* **110**, 193602 (2013)
(Editor's Suggestion, and featured in a Physics Synopsis: Desirable Defects)

Contents

Acknowledgements	vii
Abstract (English/Deutsch/Français)	ix
List of publications	xv
Contents	xvii
1 Prologue	21
1.1 Precise position measurements	23
1.2 Position measurement at the decoherence rate: this thesis	27
2 Foundations	29
2.1 Linear measurements I: formal aspects	30
2.1.1 Tools to characterise fluctuations in continuous measurements	31
2.1.2 System linearly coupled to a thermal environment	34
2.1.3 System linearly coupled to a meter	39
2.2 Phonons and photons	44
2.2.1 Phonons: quantised linear elastodynamics	44
2.2.1.1 Mechanical oscillator in thermal equilibrium	50
2.2.2 Photons: description and detection	54
2.2.2.1 Statistics of optical fluctuations	55
2.2.2.2 Detection of amplitude quadrature: photodetection	58
2.2.2.3 Detection of an arbitrary quadrature: homodyne	61
2.2.2.4 Detection of conjugate quadratures: heterodyne	67
2.2.2.5 Optical cavity coupled to a waveguide	70
2.2.3 Photon-phonon coupling in a cavity	80
2.2.3.1 Effective description: simplified cavity optomechanics	83
2.3 Linear measurements II: cavity-enhanced interferometry	89
2.4 Experimental platform: cryogenic near-field cavity optomechanics	94
2.4.1 Stressed nanostring coupled to an optical microcavity	94
2.4.1.1 Near-field coupling	96
2.4.2 Measurement and calibration of thermomechanical motion	97
2.4.3 Cryogenic operation	102
2.4.3.1 Nature of elastic force: radiation pressure vs. thermoelasticity	106
2.4.4 Experimental schematic	109

3	Measurement-based control	111
3.1	Theoretical and experimental background	112
3.1.1	Theory of feedback cooling of a harmonic oscillator	112
3.1.1.1	Limits due to measurement back-action	115
3.1.1.2	Some remarks on thermodynamics	115
3.1.2	Measurement and feedback using a cavity	116
3.1.2.1	Effect of dynamic back-action	120
3.1.2.2	Measurement back-action	121
3.1.2.3	Modification to measurement imprecision	121
3.1.2.4	Effect of non-ideal feedback phase	122
3.1.2.5	Implementation of feedback	123
3.2	Experimental results	125
3.2.1	Measurement at the thermal decoherence rate	125
3.2.1.1	Imprecision due to thermomechanical noise	128
3.2.1.2	Imprecision due to cavity substrate noise	128
3.2.1.3	Imprecision due to noise in optical fiber	130
3.2.2	Heisenberg-uncertainty-limited measurement	133
3.2.2.1	Back-action due to ohmic heating	135
3.2.3	Feedback cooling to near the ground state	136
3.3	Conclusion	137
4	Quantum correlations in measurement-based control	139
4.1	Origin of sideband asymmetry	140
4.1.1	Relation to ponderomotive squeezing	141
4.1.2	Effect of classical laser noise on sideband asymmetry	142
4.1.2.1	Contribution of excess noise for resonant probing	142
4.1.2.2	Measurement of excess laser noise	145
4.2	Experimental results	148
4.3	Conclusion	155
5	Epilogue	157
5.1	Some future directions	157
5.1.1	Optimal feedback	158
5.1.2	Quantum-enhanced metrology	160
A	Uncertainty inequalities	163
B	Miscellanea on elastodynamics	165
B.1	Principle of least action: equations of motion, boundary conditions	165
B.1.1	Equations of motion	167
B.1.2	Boundary conditions	167
B.2	Transverse and longitudinal elastic waves	168
B.3	Hermiticity of the elastic operator	168
C	Response of an imbalanced interferometer	171
	Bibliography	175

Curriculum Vitae

185

1 Prologue

The history of science shows that even during the phase of her progress in which she devotes herself to improving the accuracy of the numerical measurement of quantities with which she has long been familiar, she is preparing the materials for the subjugation of the new regions, which would have remained unknown if she had been contented with the rough methods of her early pioneers.

JAMES CLERK MAXWELL

ELECTROMAGNETIC radiation holds a unique position in man's interaction with nature. In the form of light, acting as a conduit between far away objects and the human eye, it informs us through vision. In the form of electrostatic forces between atomic-scale bodies, it forms the basis of our tactile sense. Scientific instruments that peer deeper into space and sharper into the atom, interface our feeble senses with that world through electromagnetic signals.

That electromagnetic radiation can be a causative agency took much longer to be realized. The historic anecdote of Archimedes using mirrors to focus the sun's light onto incoming enemy ships to burn them (at the Siege of Syracuse, in 212 BC^{1.1}), illustrates the powerful potential of intense radiation. However, radiation of such intensity was typically limited to astrophysical sources. Indeed, Kepler [1] suggested that the tails of comets point away from the sun because of an outward solar *radiation pressure*. Such a mechanical effect arising from light appears to have found favour with Newton [2] – corpuscles of light, reflecting off a surface, impart a recoil force. In the absence of a quantitative theory of light, these conjectures remained unsubstantiated.

The ensuing 100 years saw a host of experiments attempting to observe the tiny recoil force due to light in a terrestrial setting [3]. Some of these experiments set out to settle the debate between corpuscular and wave theories of light, for it was widely conjectured that if light were a wave, then it would not impart any mechanical force. Bolstered by Cavendish's sensitive measurements of the gravitational force (another exceptionally weak effect) between two spherical bodies [4], the experimentalists converged upon the torsion pendulum as a sufficiently sensitive apparatus to see the pressure due to light. William Crookes pioneered

^{1.1} As reported by Anthemius of Tralles in his *On Burning Glasses*, ca. 700 years after the event.

this experimental technique, using a pair of vanes delicately suspended on a wire, forming a torsion pendulum that would potentially be set in motion when light impinged on one of the vanes. This instrument – Crookes radiometer – did respond to some photo-motive force – however the direction of motion was opposite to that expected if the force were radiation pressure. With the realization that the force at play was due to convection of the surrounding air heated by the absorbed light, a brief experimental hiatus ensued.

In the meantime, several other causative effects of electromagnetic radiation were observed; perhaps most profound among them were Oersted’s observation that a changing electric current causes magnetic effects, and Faraday’s complementary observation that a moving magnet leads to an electric current. A priori, these electric and magnetic effects bore little relation to the mechanical radiation pressure effect that was being ardently pursued. In the same year (1873) that Crookes concluded his unsuccessful experiments to reveal the mechanical effect of light, Maxwell [5] produced his theoretical synthesis of Faraday’s experiments, resulting in a unified description of electrical and magnetic phenomena.

Maxwell, in the second edition of his treatise, and independently Poynting [7] (who incidentally had surveyed the Cavendish experiment [8]), realized that the new electromagnetic theory applied to radiation, and that it provided a quantitative estimate of the pressure exerted by light.

The following decade witnessed the observation of the elusive radiation pressure. Lebedev [9], and independently, Nichols and Hull [6], performed a series of experiments in 1901-1910 that managed to isolate the effect of radiation pressure due to light from a carbon-arc source, and demonstrated that the force was indeed as predicted by Maxwell’s theory. Figure 1.1 depicts the apparatus used in the experiment.

With the triumph of Maxwell’s theory on all fronts (telegraphy, telephony and radio communication being everyday examples), radiation pressure studies on table-top experiments faded into history, partly owing to a lack of intense sources of radiation to amplify its effect. However, its implications for astrophysical phenomena, where such sources are aplenty, continued to be investigated [10, 11] (including its non-negligible effect for artificial satellites and interplanetary missions [12]).

Historically, a circuitous route had to be traversed to return to the question of how one may realize an intense and highly-directional source of light. But this development had its roots in two pillars of physics erected by Maxwell. Maxwell,

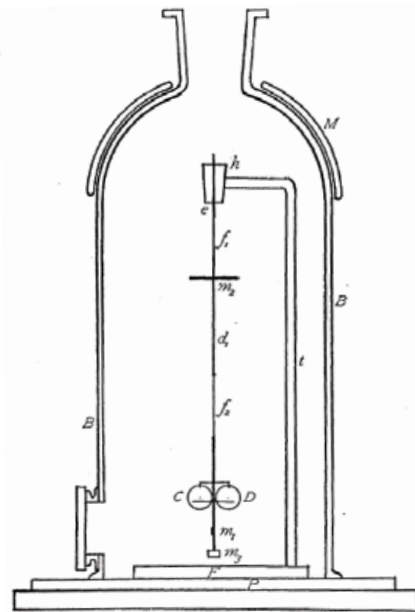


Fig. 1.1 – Nichols’ radiometer. [6] Two silvered mirrors (C and D), hang from a thin quartz wire. An approximately 150 mW light beam impinged upon one of the mirror imparting a force of 10^{-9} N. A much weaker light beam, reflected off the other mirror, formed an optical lever to measure the torque on the pendulum. The observations agreed to within 6% of the theoretical prediction. The glass bell jar was evacuated to eliminate the influence of thermal air currents that plagued Crookes’ experiment [3].

together with Boltzmann and others, had arrived at a microscopic description of particles (for example gaseous atoms in a box) in thermal equilibrium. Suffice it to say that the attempt to apply these ideas to the description of light in thermal equilibrium led to conceptual difficulties. Without going into the details [13], the resolution of these issues warranted a corpuscular description of light! Thus was born the *light quantum*, and with it, the theory of quantum mechanics [14]. Not only did quantum mechanics demand that light waves have a particulate character, but it also implied the reverse, namely, that what had been thought of as being intrinsically particulate (electrons, atoms etc.), have a complementary wave character. Another counter-intuitive prediction is the absence of a state of true rest – an incessant restless residual motion that cannot be quenched. These *vacuum fluctuations*, needless to say, are tiny compared to the typical size of objects – hence very difficult to observe. The qualitative idea of vacuum fluctuations is captured in a basic tenet of quantum theory – Heisenberg’s uncertainty principle – roughly stating that both the position and velocity of objects cannot be simultaneously known. The present thesis studies an incarnation of this prediction, and experimentally observes it.

The weird predictions of quantum mechanics aren’t confined to the realm of pure thought. The laser, invented in the 1960’s, relies crucially on the principles of quantum theory. The invention of the laser, finally made it possible to access intense light fields in the laboratory. Primarily intended as a diagnostic tool to study the absorption and emission characteristics of atoms (i.e. spectroscopy [15, 16]), the laser soon became a tool to actively manipulate and control atomic-scale matter. The work of Ashkin and colleagues in the 1970’s [17, 18] showed that the radiation pressure from a focused laser beam could be used to trap and move small (wavelength-scale) electrically neutral particles^{1,2}. Closely related techniques to cool and eventually stop atoms were proposed [21, 22], and demonstrated [23] in the same decade. Ultimately, spectacular progress along this path led to the use of lasers to trap and control individual atoms [24–27]. These experiments have managed to reveal the vacuum fluctuations of photons [28, 29], individual atoms [30], and collections of ($\approx 10^4 - 10^6$) atoms [31, 32]. In other words, it is now known for a fact that the fantastic predictions of quantum theory are at least valid for atomic-scale objects.

The confluence of two parallel threads of scientific inquiry led to a renewed interest in radiation pressure forces in the mid-1990’s. On the one hand, progress in atomic physics led to the question of whether it is possible to witness quantum mechanical effects on larger assemblies of atoms – macroscopic objects – where the effect of quantum mechanical fluctuations would be even smaller. On the other hand, the question arose as to how measurements precise enough to see the already tiny effects could be devised. In some sense, these two quests are conceptually intertwined – a part of this thesis exposes this connection in an experiment.

1.1 Precise position measurements

Before the question of how a sufficiently precise measurement of the position of an object can be made, it is pertinent to address a more important question of principle. If the object is nominally “at rest”, would a sufficiently precise measurement of its position reveal quantum fluctuations?

^{1,2} On the other hand, electrically charged particles (electrons and ions) were being manipulated using radio-frequency electromagnetic fields, which naturally forces a charged particle [19, 20].

As it turns out there is a purely classical (i.e. non-quantum-mechanical) effect that defies the notion of “at rest” for most objects. Most ubiquitously, objects have a temperature, which means that the atoms that constitute them are in an agitated state – temperature being a measure of this agitation. This random movement of objects, called *thermal motion*, is small for large objects, however, typically much bigger than the quantum vacuum fluctuations. To give a sense of scale, the thermal motion of the mirror hanging off the torsion pendulum used by Nichols (fig. 1.1), weighing a few grams, is of the order of 10^{-9} m, while its vacuum fluctuations are of the order of 10^{-16} m. In comparison, the motion induced by radiation pressure that Nichols and Hull managed to measure was of the order of 10^{-4} m; about 5 orders of magnitude lacking in sensitivity to observe the thermal motion, and 8 orders of magnitude away from observing vacuum fluctuations.

Thermal motion was however observed in the early 1800’s, and played a key role in the development of the atomic hypothesis. Botanist Robert Brown was famously puzzled by the random motion of pollen grains in water which he observed using a microscope^{1.3}. The origin and nature of the apparent spontaneous motion soon became a fountain-head of scientific speculation that continued through the century.

Einstein, in 1905 (his *annus mirabilis*), conjectured that the *Brownian motion* (the thermal motion observed by Brown) was essentially due to the atomic constituents of water randomly hitting the pollen grain – a bold prediction that, if confirmed, could provide proof for Dalton’s theory that all matter is made of atoms. In fact, Maxwell and Boltzmann had used Dalton’s suggestion as a metaphor to construct the kinetic theory of gases, wherein the properties of gases could be derived from simple assumptions regarding a hypothetical atomic constitution. Einstein’s theory was tantamount to the statement that if one placed a large object in the gas, the atoms that made up the gas, would knock the object; in fact, the more frequent the knocks, if the pressure or temperature of the gas were higher. Experimental verification of these predictions was immediate – Jean Perrin not only verified the theory, but also managed to extract the Avogadro number from his measurements [33] – putting the atomic hypothesis on firm experimental foundation. This idea, of measuring what is essentially noise, to discern something useful, continues to be a strong tradition in physics, this thesis being no exception.

Two questions immediately arise: firstly, if the temperature is zero, would there be no Brownian motion? If the object were in contact with no “gas” (i.e. if the pressure were zero), would the motion subside? The answers to these questions bring us back to quantum mechanics. When the temperature is zero, indeed there is no Brownian motion – however, vacuum fluctuations remain. When the object is perfectly isolated, and one tries to verify this fact by performing a measurement, the rules of quantum mechanics dictate that the act of measurement disturbs the object so as to impart an additional motion precisely equal to its vacuum fluctuation, resulting in two units worth of vacuum fluctuations in the observation. Part of this thesis investigates the latter phenomena.

The answers to the above questions also indicate what is necessary in order to observe vacuum fluctuations: a near-zero-temperature environment, a supremely well-isolated system,

^{1.3} Remarkably, the Roman poet-philosopher Titus Lucretius, in his poem *De Rerum Natura* (ca. 60 BC), described the spontaneous motion of dust particles suspended in a sun beam falling across a dark room, and conjectured the presence of an invisible agency responsible for the movement.

and a measuring device that is so exquisite that it is only limited by the laws of quantum mechanics.

In the early 1920's, a decade after Perrin's conclusive measurements of the Brownian motion of microscopic particulate matter suspended in liquids, the first observation of similar thermal motion of a macroscopic object were made. Willem Einthoven, in his Nobel prize (in medicine, for the invention of the electrocardiogram) lecture mentions the curious movement of the extremely light galvanometer needle used in his apparatus, conjecturing it to be the thermal Brownian motion of the needle. In subsequent investigations he found qualitative agreement between the motion and the predictions of the by-then more mature theory of thermal motion [34]. These findings were quickly replicated in a series of experiments by Moll and Burger [35] on a galvanometer suspended on a spring – drastically different from the free movement allowed for the particles in Perrin's experiments and the free needle in Einthoven's galvanometer. The effect of the spring is to render the needle a harmonic oscillator, that responds to a limited range of frequencies with a large amplitude; consequently, these experiments witness the thermal motion of the needle with unprecedented signal-to-noise. The theory of the thermal motion of a harmonic oscillator is quickly furnished by Ising [36] and Ornstein [37]. In fact, Ornstein's work suggests a cause for the thermal motion – the thermal motion of electrons in the galvanometer circuit play the role of gas particles kicking the needle. This pre-empts similar conclusions by Johnson and Nyquist. Throughout the mid-20th century, incarnations of the galvanometer needle were measured with ever increasing precision [38, 39], largely without paying heed to the fundamental limitations of the measuring device(s) being employed.

These early observations (see fig. 1.2) were limited by the large thermal noise inherent in the measuring device itself – mainly in the form of thermal motion of electrons in electronic circuits [40, 41]. All this changes in the 1960's, with the invention of two low-noise sensing platforms – the laser, and the SQUID (superconducting quantum interference device) [42]. In the decades leading up to the 2000's, both these devices, essentially based on interferometric techniques, pushed the frontier of precision displacement measurements.

The ability to fabricate low-mass (hence large vacuum fluctuations) mechanical oscillators of small dimensions, i.e. nano-mechanical oscillators, featuring very high mechanical quality, brought the dream of witnessing the vacuum fluctuations of a macroscopic object ever closer. Integrating such oscillators with sensitive radio-frequency amplifiers, like single-electron transistors [43–45], quantum-point contacts [46, 47], or SQUIDs [48], proved to be fruitful in terms of approaching the sensitivity required to see vacuum fluctuations (i.e. the *standard quantum limit* (SQL)). These efforts were curtailed by the lack of a strong enough coupling between the oscillator and the sensor, or the presence of excess noise in the sensor, or both.

Ultimately, the integration of radio-frequency nano-mechanical oscillators, with high quality optical micro-cavity based interferometer [49], or microwave cavity with a Josephson parametric amplifier [50], proved to be successful in achieving the long-standing goal of measurements of position with the sensitivity at the SQL. The former was demonstrated in the group of Prof. Tobias Kippenberg, few years prior to the commencement of this thesis in the same laboratory.

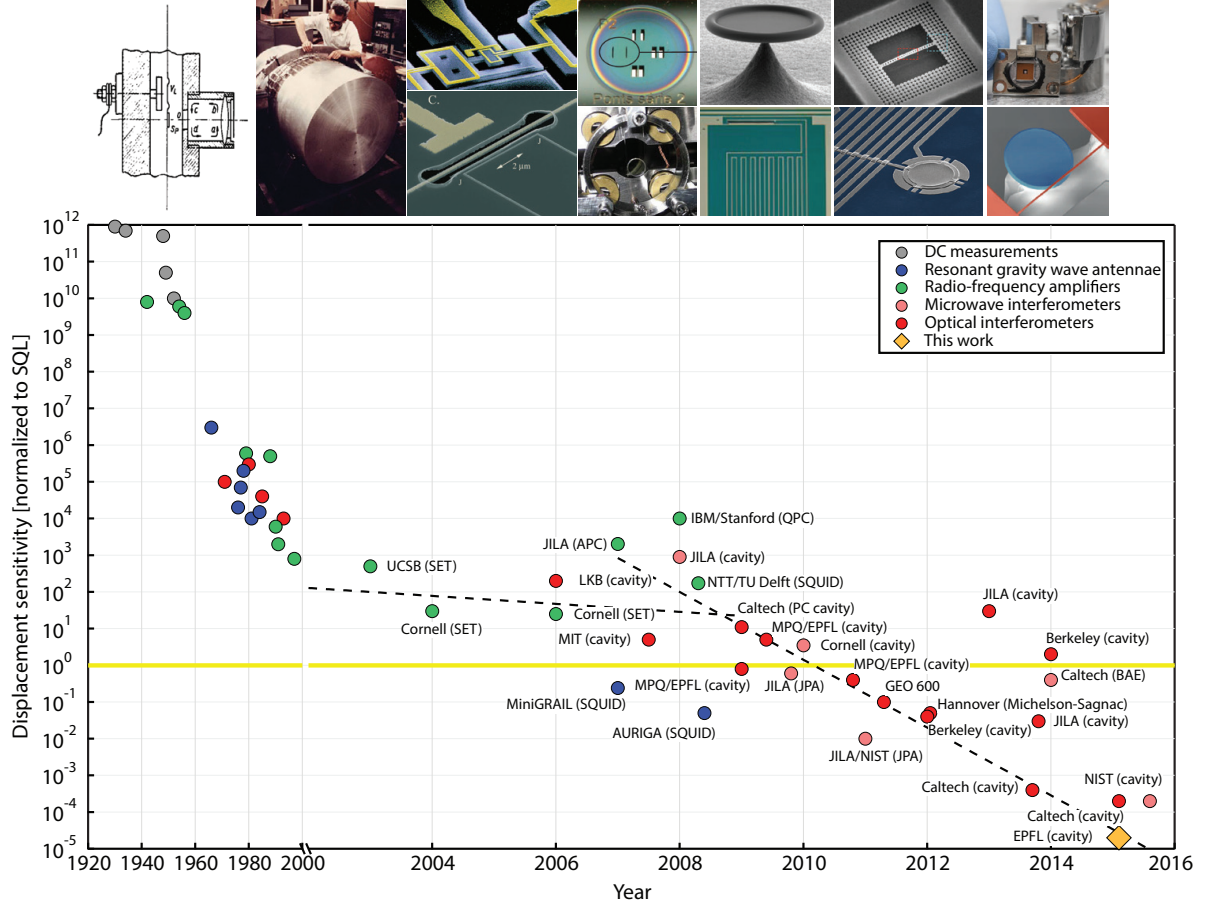


Fig. 1.2 – **Displacement sensitivity over the last century.** Plot shows the improvement over 17 orders of magnitude improvement in the sensitivity in the measurement of position fluctuations over the past 100 years. The past decade has seen spectacular progress owing to the use of low-noise electromagnetic cavities that lead to a build-up of intense fields, interrogating low-mass high-quality-factor nano-mechanical oscillators. Here, the sensitivity is expressed in a natural unit, the sensitivity at the so-called *standard quantum limit* (SQL), which essentially amounts to the sensitivity required to resolve vacuum fluctuations. Work reported in this thesis is the orange diamond on the lower right corner – the most precise measurement of the position of a mechanical oscillator relative to its zero-point motion, at the time of writing.

Both these approaches typify the burgeoning field of *cavity optomechanics* [51], wherein the emphasis has been to tightly integrate high quality mechanical oscillators with a high quality optical (or microwave) cavity. Figure 1.3 shows the principle of cavity optomechanical measurement of the position of mechanical oscillators. In the generic scheme, shown in fig. 1.3a, light is injected into a space formed by two mirrors facing each other. The multiple reflections from either mirror traps the light in the enclosed space, forming an optical cavity. One of the mirrors, mounted on a spring, forms the mechanical oscillator. Its position $x(t)$ is recorded as a phase shift proportional to $\frac{x(t)}{\lambda}$, where λ is the wavelength of light used. The cavity amplifies this tiny phase shift by recycling the light a large number of times, given by the *finesse* \mathcal{F} . Light leaking out of the cavity thus features a phase change given by $\phi(t) \propto \frac{\mathcal{F}}{\lambda} x(t)$. Therefore, a good optical cavity, having a small operating wavelength λ , and a large finesse \mathcal{F} , can transduce the small motion $x(t)$ into a larger phase shift $\phi(t)$. A type of optical cavity (see fig. 1.3b)

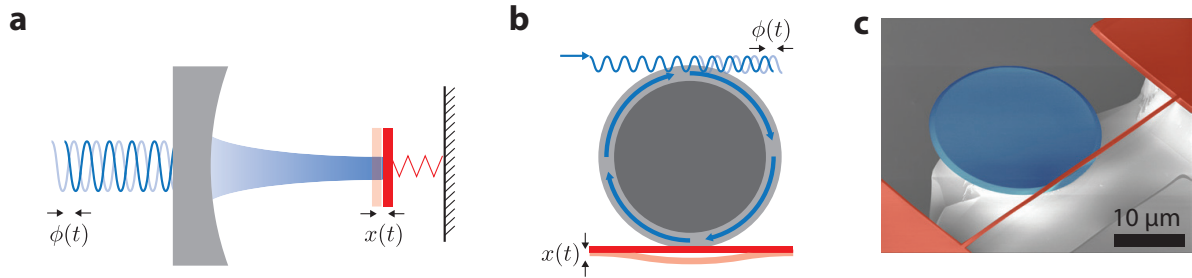


Fig. 1.3 – **Principle of cavity optomechanics.** (a) Generic cavity optomechanical system, consisting of two mirrors facing each other. The mirrors form an optical cavity, trapping light between them (i.e. a Fabry-Perot cavity); one of the mirrors, mounted on a spring, forms the mechanical oscillator. (b) A cavity optomechanical system where the mechanical oscillator is a string, and the optical cavity is formed by continually bending light around a circle (i.e. a whispering gallery mode cavity). (c) False-coloured scanning electron micrograph of the system studied in this thesis; scale bar shows reference for the size of the device.

formed by continually bending light around a curved path – a *whispering-gallery* mode cavity [52] – is used in this thesis. Such cavities, operating at a wavelength of $\lambda \approx 8 \cdot 10^{-7}$ m, can have $\mathcal{F} \approx 10^6$, meaning that a typical vacuum fluctuation amplitude (of the string shown in fig. 3.2c) $x \approx 10^{-15}$ m, would lead to a phase shift of $\phi \approx 0.1$ rad for the light emanating from the cavity. Although small, this phase shift can be measured precisely by comparing the cavity transmission with a reference light beam, in a technique called *homodyne interferometry*.

However, a fundamental impediment presents itself in trying to make this measurement. Since light is itself a quantum mechanical entity, the ability to measure its phase is impeded by the particle nature of photons: the random arrival times of the photons constitute an uncertainty in the timing information in the measurement, essentially scrambling the phase. This uncertainty can be minimized by employing a larger flux of photons, so that (in a naive sense) the inter-arrival intervals of the photon stream is reduced. The price paid for this choice is that the larger photon flux exerts a larger radiation pressure force on the oscillator being measured – in trying to make a precise measurement, the thing being measured gets disturbed – a manifestation of Heisenberg’s uncertainty principle.

1.2 Position measurement at the decoherence rate: this thesis

The disturbance, called *measurement back-action*, plays a prominent role as the precision of the measurement approaches what is required to resolve the vacuum fluctuation of the oscillator – the SQL. The ability to measure position with a sensitivity at the SQL is sufficient to see the vacuum fluctuations of the oscillator if it were free of thermal motion. For typical macroscopic mechanical oscillators, this is never true, unless the environment is maintained at a temperature of 10^{-4} K – an enormous technical challenge. Nevertheless, the preparation and stabilization of the vacuum state of the oscillator is crucial.

In the work reported in this thesis (in Chapter 3), this problem is solved by turning it on its head. Firstly, a measurement of the position fluctuations of an oscillator is made, which is sufficiently sensitive to resolve the vacuum fluctuations of the oscillator before it is overwhelmed by the environment. For the system employed, this corresponds to operating a factor 10^4 below the SQL. The measurement back-action associated with such a measurement

is observed in our experiment. As the next step, this information is used to actively stabilize the vacuum state of the oscillator using feedback [53]. At the time of writing, this remains the sole example of active feedback of a mechanical oscillator to near its ground state.

In a second experiment (in Chapter 4), this capability is employed to study the subtle nature of the act of measurement itself [54]. In particular, measurements of a “system” (the mechanical oscillator in our case), by a “meter” (light), extract information by creating correlations between the meter and the system. These tiny correlations – whose magnitude is comparable to the vacuum fluctuation of the oscillator – are measured using the feedback technique. In doing so, we reveal what it means to make a measurement according to quantum theory. Another subtle aspect that is probed by this experiment is the role of instruments further down the measurement chain that measure the nominal meter that directly “measures” the system under study; this regression is eventually terminated in some *classical* “detector”. In our experiment, the output of such a detector contains traces of the vacuum fluctuations of the meter, which are then fed-back to the system. We show that the effect of these additional fluctuations is to obscure the correlations that are developed between the meter and system.

Chapter 2 develops the necessary theoretical and experimental framework supporting the advances made in subsequent chapters. Details regarding the general construction and operation of the experiment are presented there. Specialized details, relevant to the results reported in subsequent chapters, are to be found in the associated chapters.

2 Foundations

The beginner should not be discouraged if he finds that he does not have the prerequisites to read the prerequisites

PAUL HALMOS

The results reported in this thesis (in chapters 3 and 4) rely on a wide range of theoretical and experimental techniques. The aim of this chapter to provide a review of these preliminaries. The review consists of five, progressively less abstract, sections.

The excursion begins in section 2.1 with a concise (and therefore necessarily abstract) description of linear quantum systems, including continuous linear measurements. The theoretical formalism and vernacular developed therein, forms the conceptual backbone of much of the thesis. Section 2.2 delves into a description of the actors that take part in the experiment – phonons and photons. Following a brief description of low-energy phonons and their quantisation in section 2.2.1, section 2.2.2 gives an account of the electromagnetic field. In particular, section 2.2.2 develops a formalism to describe the fluctuations of the electromagnetic field, and their measurements. A particular class of measurements of the electromagnetic field – interferometric measurements – form the core of the experimental toolbox. Section 2.4 details the concrete realisation in which phonons and photons interact linearly – a near-field cavity optomechanics system deployed in a ^3He cryostat. Section 2.3 applies the abstract formalism developed in section 2.1 to the interferometric measurement of the position of a nano-string oscillator (depicted in fig. 1.3c).

2.1 Linear measurements I: formal aspects

Here are some words which have no place in a formulation with any pretension to physical precision: system, apparatus, environment, microscopic, macroscopic, reversible, irreversible, observable, information, measurement.

JOHN BELL [55]

Despite John Bell's eloquent tirade against the arbitrary division of the universe into a *system* surrounded by an *environment*, the experimental physicist, due to his limited means of enquiry, is forced to subscribe to a well-defined notion of what is considered the *system* under study. In the example relevant to this thesis, it is a macroscopic mechanical oscillator. Everything beyond, is the *environment*. In this sense, the measuring device – the *meter* – is a form of environment, the crucial difference being that the experimenter has the ability to control it. In this thesis, the meter is an electromagnetic field that interacts with the oscillator.

In this section, a self-contained, but somewhat abstract, account of a particular class of measurements – continuous linear measurements – is presented. The purpose of this exposition is, firstly, to establish certain properties of linear measurements which are generally valid, and secondly to provide the conceptual framework for conversing about the experiments. The main results of this development are three fold:

1. observables of quantum systems have a finite minimum noise power even when the system is isolated (the statement of the existence of “vacuum fluctuations”); when linearly coupled to an environment, the minimum is determined by the coupling constant (the quantum mechanical fluctuation-dissipation theorem)
2. when a continuous linear measurement of such an observable is performed, the noise power of the detector output will show at least twice the minimum noise power allowed for the observable (the general statement of the “standard quantum limit”)
3. this minimum is established through a fundamental bound satisfied by the back-action due to the measurement, and the imprecision of the measurement (the statement of the “uncertainty principle”)

These results are not new. The existence of vacuum fluctuations for various simple systems are dealt with in textbooks on quantum mechanics [14, 56]; however the distribution of these fluctuations in time is less commonly described. Various forms of the quantum mechanical fluctuation dissipation theorem, arising from various assumptions made about the system-environment interaction have been derived (to cite a few diverse expositions [57–62]). Statements and proofs of the “standard quantum limit” of continuous linear measurements, and of the associated “uncertainty principle”, have also been given to varying degrees of generality [62–70]. A unified presentation of these ideas, with a few slightly general proofs of certain statements, is provided in the rest of this section.

2.1.1 Tools to characterise fluctuations in continuous measurements

The noise is the signal

ROLF LANDAUER [71]

In quantum mechanics, it is supposed that the *observables* of a system are some set of hermitian operators [14, 72]. Consider for the moment a system, and two generic observables, say \hat{X}_1, \hat{X}_2 . If the system is repeatedly prepared in a definite state $\hat{\rho}$, and one of these observables is measured per preparation, the outcomes will be random real numbers drawn from the eigenspectrum of the observable. Thus, for a given state $\hat{\rho}$, we speak of the “values taken by the observable \hat{X}_i ” to mean the random variable describing the measurement outcomes of said observable; this random variable is drawn according to a probability distribution^{2.1}. The fluctuations of the random variable can be associated with the operator,

$$\delta\hat{X}_i := \hat{X}_i - \langle \hat{X}_i \rangle, \quad \text{where,} \quad \langle \hat{X}_i \rangle = \text{Tr}[\hat{X}_i \hat{\rho}].$$

In a large variety of cases, the dispersion in the random variable may be quantified by the variance of this operator,

$$\text{Var} [\hat{X}_i] := \langle \delta\hat{X}_i^2 \rangle.$$

Note that both the definition of $\delta\hat{X}_i$, and therefore of $\text{Var}[\hat{X}_i]$, rely on a specification of a state; also by definition, $\text{Var} [\hat{X}_i] \geq 0$.

The mathematical structure of quantum mechanics dictates that the variances in the value of the two observables satisfy the constraint (see Appendix A),

$$\text{Var} [\hat{X}_1] \text{Var} [\hat{X}_2] \geq \frac{1}{4} |\langle \{\delta\hat{X}_1, \delta\hat{X}_2\} \rangle|^2 + \frac{1}{4} |\langle [\delta\hat{X}_1, \delta\hat{X}_2] \rangle|^2 \geq \frac{1}{4} |\langle [\delta\hat{X}_1, \delta\hat{X}_2] \rangle|^2, \quad (2.1.1)$$

i.e. that measurement outcomes have a fundamental dispersion determined by the non-commutativity of observables. The first (tighter) inequality above, originally proven by Robertson [74] and Schrödinger [75] for pure states, relies crucially on the positivity of quantum mechanical states, i.e. $\hat{\rho} > 0$ (see Appendix A for general proofs and further discussion)^{2.2}.

The uncertainty inequality in eq. (2.1.1) is essentially kinematic – it does not directly pertain to measurements performed continuously in time. Before describing the latter problem, we prove a useful result.

Lemma 1 (Caves [66]). *For a non-hermitian operator, defined by, $\hat{Z} := \hat{X}_1 + i\hat{X}_2$, where \hat{X}_i are observables, we define the operator corresponding to its fluctuations by $\delta\hat{Z} := \delta\hat{X}_1 + i\delta\hat{X}_2$, and the corresponding variance,*

$$\text{Var} [\hat{Z}] := \left\langle \frac{1}{2} \{ \delta\hat{Z}, \delta\hat{Z}^\dagger \} \right\rangle = \text{Var} [\hat{X}_1] + \text{Var} [\hat{X}_2]. \quad (2.1.2)$$

^{2.1} A peculiarity of quantum mechanics is that although the value taken by each observable, for a fixed state, can be assumed to be drawn from a classical probability distribution (exhibited in Appendix A), there is generally no joint probability distribution for the values of a set of operators [73]

^{2.2} In contrast, the second (looser) inequality, due to Heisenberg [76], Kennard [77], and Weyl [78], by omitting the term characterising the correlations between measurement outcomes, is similar to the classical inequality of Fourier analysis [79].

Then, the following inequality holds,

$$\text{Var}[\hat{Z}] \geq \frac{1}{2} \left| \left\langle \left[\hat{Z}, \hat{Z}^\dagger \right] \right\rangle \right|. \quad (2.1.3)$$

Proof. Note that the definition of the variance eq. (2.1.2) can be related to the left-hand side of the uncertainty inequality in eq. (2.1.1) as follows:

$$\text{Var}[\hat{Z}] = \text{Var}[\hat{X}_1] + \text{Var}[\hat{X}_2] \geq 2\sqrt{\text{Var}[\hat{X}_1] \text{Var}[\hat{X}_2]};$$

here the second relation employs the arithmetic-geometric mean inequality^{2.3}. Using the Heisenberg form of the inequality in eq. (2.1.1), the product of the variances can be bounded, leading to,

$$\text{Var}[\hat{Z}] \geq \left| \left\langle [\delta\hat{X}_1, \delta\hat{X}_2] \right\rangle \right| = \left| \left\langle \frac{1}{2i} [\delta\hat{Z}^\dagger, \delta\hat{Z}] \right\rangle \right|;$$

the second equality simply replaces $\hat{X}_{1,2}$ in terms of \hat{Z}, \hat{Z}^\dagger . □

In order to treat system observables varying in time, the Heisenberg picture is most convenient: the system is in some state $\hat{\rho}_0$ (like the canonical thermal state considered in section 2.1.2), while its observables undergo fluctuations due to the pervasive *environment* that the system is equilibrated with. These fluctuations are reflected in the observables as deviations from their mean values, viz.

$$\delta\hat{X}_i(t) = \hat{X}_i(t) - \text{Tr}[\hat{\rho}_0 \hat{X}_i(t)].$$

The fluctuating part, $\delta\hat{X}_i(t)$, represents a continuous random variable – stochastic process – taking values in the set of observables.

In order to resolve the variance of the process over the different time scales over which the fluctuations happen, we consider the windowed Fourier transform^{2.4},

$$\delta\hat{X}_i^{(T)}[\Omega] := \frac{1}{\sqrt{T}} \int_{-T/2}^{T/2} \delta\hat{X}_i(t) e^{i\Omega t} dt, \quad (2.1.4)$$

^{2.3} For positive real numbers x, y , it is true that $x + y \geq 2\sqrt{xy}$; this follows from the identity, $(\sqrt{x} - \sqrt{y})^2 \geq 0$.

^{2.4} The normalisation warrants clarification: if the integrand were a classical Brownian process, its root-mean-square diverges as the square root of the observation window, i.e. as $T^{1/2}$, which is checked by the normalisation. For a wide class of classical stochastic processes, a theorem due to Donsker [80] guarantees that the integral limits to a Brownian process (a “functional central limit theorem”) – the $T^{-1/2}$ normalisation is necessary. This result from classical probability theory suffices to justify the normalisation.

which is in general non-hermitian. The definition of the variance of a non-hermitian operator in eq. (2.1.2) then implies,

$$\begin{aligned} \text{Var} [\delta\hat{X}_i^{(T)}[\Omega]] &= \left\langle \frac{1}{2} \left\{ \delta\hat{X}_i^{(T)}[\Omega], \delta\hat{X}_i^{(T)}[\Omega]^\dagger \right\} \right\rangle \\ &= \frac{1}{T} \int_{-T/2}^{T/2} \left\langle \frac{1}{2} \left\{ \delta\hat{X}_i(t), \delta\hat{X}_i(t') \right\} \right\rangle e^{i\Omega(t-t')} dt dt' \\ &= \frac{1}{T} \int_{-T/2}^{T/2} \left\langle \frac{1}{2} \left\{ \delta\hat{X}_i(t-t'), \delta\hat{X}_i(0) \right\} \right\rangle e^{i\Omega(t-t')} dt dt' \\ &= \int_{-T/2}^{T/2} \left\langle \frac{1}{2} \left\{ \delta\hat{X}_i(\tau), \delta\hat{X}_i(0) \right\} \right\rangle e^{i\Omega\tau} \left(1 - \frac{|\tau|}{T} \right) d\tau. \end{aligned}$$

Note that here and henceforth we assume processes are weak-stationary, i.e. that their first and second moments are time-translation invariant.

In the limit $T \rightarrow \infty$ (i.e. the limit of infinite resolution in frequency), this variance defines the function,

$$\bar{S}_{X_i X_i}[\Omega] := \lim_{T \rightarrow \infty} \text{Var} [\delta\hat{X}_i^{(T)}[\Omega]] = \int_{-\infty}^{\infty} \left\langle \frac{1}{2} \left\{ \delta\hat{X}_i(t), \delta\hat{X}_i(0) \right\} \right\rangle e^{i\Omega t} dt, \quad (2.1.5)$$

characterising the distribution of the variance of the process about each frequency. The second equality, giving the value of the limit, is the analogue of the Wiener-Khinchine theorem [69, 81]. Firstly, being a variance, $\bar{S}_{X_i X_i}[\Omega] \geq 0$, at all frequencies and for any operator-valued process – reminiscent of a classical power spectral density. Secondly, being a distribution (obtained by applying the Fourier inversion theorem [81] to eq. (2.1.5)),

$$\text{Var} [\delta\hat{X}_i(t)] = \langle \delta\hat{X}_i(0)^2 \rangle = \int_{-\infty}^{\infty} \bar{S}_{X_i X_i}[\Omega] \frac{d\Omega}{2\pi}, \quad (2.1.6)$$

which exhibits the complementary aspect that the integral of the power spectral density is the variance of the process $\delta\hat{X}(t)$. Equations (2.1.5) and (2.1.6) are fundamental properties of the *symmetrised power spectral density* so defined, that render it useful (irrespective of whether it is generically measured in an experiment [69, 82, 83]).

A formal hierarchy that generalises these ideas descends from spectral distributions defined as Fourier transforms of the two-time correlation function of possibly distinct arbitrary (possibly non-hermitian) operators, viz.

$$S_{Z_i Z_j}[\Omega] := \int_{-\infty}^{\infty} \left\langle \delta\hat{Z}_i^\dagger(t) \delta\hat{Z}_j(0) \right\rangle e^{i\Omega t} dt = \int_{-\infty}^{\infty} \left\langle \delta\hat{Z}_i^\dagger[\Omega] \delta\hat{Z}_j[\Omega'] \right\rangle \frac{d\Omega'}{2\pi}, \quad (2.1.7)$$

where the second equality follows from the definition of the continuous Fourier transform,

$$\hat{Z}_i[\Omega] := \int_{-\infty}^{\infty} \hat{Z}_i(t) e^{i\Omega t} dt.$$

Note that we make a subtle notational distinction between, $\hat{Z}_i^\dagger[\Omega]$, the Fourier transform of the operator $\hat{Z}_i^\dagger(t)$, and the hermitian conjugate of the Fourier transform, denoted as $\hat{Z}_i[\Omega]^\dagger$; the

two are related via, $\hat{Z}_i^\dagger[\Omega] = \hat{Z}_i[-\Omega]^\dagger$. The symmetrised spectral distribution corresponding to $S_{Z_i Z_j}$ is defined by,

$$\bar{S}_{Z_i Z_j} := \int_{-\infty}^{\infty} \left\langle \frac{1}{2} \left\{ \delta \hat{Z}_i^\dagger(t), \delta \hat{Z}_j(0) \right\} \right\rangle e^{i\Omega t} dt = \frac{1}{2} \left(S_{Z_i Z_j}[\Omega] + S_{Z_i^\dagger Z_j^\dagger}[-\Omega] \right).$$

Note that when $\hat{Z}_j = \hat{Z}_i$, regardless of whether the operators are hermitian, it is true that the symmetrised spectral density is non-negative, i.e. $\bar{S}_{Z_i Z_i}[\Omega] \geq 0$, so that it may be viewed as a power spectral density.

When the operators are hermitian, denoted \hat{X}_i, \hat{X}_j , similar definitions hold for their unsymmetrised and symmetrised spectral distributions. Further, when $\hat{X}_j = \hat{X}_i$, the symmetrised spectral distribution (equal to the one defined alternatively in eq. (2.1.5)) is related to the unsymmetrised one via.,

$$\bar{S}_{X_i X_i}[\Omega] = \frac{1}{2} (S_{X_i X_i}[\Omega] + S_{X_i X_i}[-\Omega]), \quad (2.1.8)$$

i.e. symmetrisation in ordering is equivalent to symmetrisation in frequency. In particular, the implied frequency symmetry, $\bar{S}_{X_i X_i}[\Omega] = \bar{S}_{X_i X_i}[-\Omega]$, suggests that the single-sided spectrum defined by,

$$\bar{S}_{X_i}[\Omega] := 2 \bar{S}_{X_i X_i}[\Omega], \quad \text{for } \Omega \geq 0,$$

encodes the full information contained in the double-sided symmetrised (double-sided) spectrum $\bar{S}_{X_i X_i}[\Omega]$. In terms of the single-sided spectrum, the variance of the process is,

$$\text{Var} [\delta \hat{X}_i(t)] = \int_0^{\infty} \bar{S}_{X_i}[\Omega] \frac{d\Omega}{2\pi}.$$

2.1.2 System linearly coupled to a thermal environment

We avoid the gravest difficulties when, giving up the attempt to frame hypotheses concerning the constitution of matter, we pursue statistical inquiries as a branch of rational mechanics.

JOSIAH WILLARD GIBBS

Having established the technology to handle the simple statistical properties of operator-valued stochastic processes, we now turn to a physical situation where this can be applied.

Consider a system, with a prescribed average energy, in equilibrium with an environment. The state of the system, described by a single parameter – the temperature T , is the one with the maximal entropy compatible with the average energy. This unique state is the canonical thermal state,

$$\hat{\rho}_\beta = \frac{e^{-\beta \hat{H}_0}}{Z}, \quad (2.1.9)$$

where $\beta = (k_B T)^{-1}$ is the inverse temperature, \hat{H}_0 is the free hamiltonian of the system, and $Z = \text{Tr} e^{-\beta \hat{H}_0}$ is the partition function that ensures the normalisation of the state, i.e. $\text{Tr} \hat{\rho}_\beta = 1$. Note that $\hat{\rho}_{\beta \rightarrow \infty} = |0\rangle\langle 0|$, i.e. the thermal state in the zero temperature limit is the ground state.

The observables of the system, $\{\hat{X}_i\}$, are weak stationary in the thermal state, i.e. their mean values are constant, while their second moments are time translation invariant:

$$\begin{aligned}\langle \hat{X}_i(t) \rangle &= \langle \hat{X}_i(0) \rangle \\ \langle \hat{X}_i(t+t') \hat{X}_j(t') \rangle &= \langle \hat{X}_i(t) \hat{X}_j(0) \rangle.\end{aligned}$$

These equalities follow from the observation that the time evolution operator commutes with the thermal state.

Another interesting property of observables in the thermal state is the Kubo-Martin-Schwinger (KMS) identity^{2.5},

$$\langle \hat{X}_i(t) \hat{X}_j(0) \rangle = \langle \hat{X}_j(0) \hat{X}_i(t + i\hbar\beta) \rangle, \quad (2.1.10)$$

which controls the commutativity of quantum mechanical operators in a thermal state. Naively, the KMS identity may be interpreted to mean that in the high temperature limit, $\beta \rightarrow 0$, all observables commute in the thermal state – reminiscent of classical behaviour. Taking Fourier transforms on both sides, and employing the weak-stationarity of two-time correlators, the KMS identity implies that the unsymmetrised spectra of observables satisfy,

$$S_{X_i X_j}[\Omega] = e^{\beta\hbar\Omega} S_{X_j X_i}[-\Omega].$$

For the case $\hat{X}_j = \hat{X}_i$, this gives the detailed balance relation,

$$S_{X_i X_i}[\Omega] = e^{\beta\hbar\Omega} S_{X_i X_i}[-\Omega]. \quad (2.1.11)$$

Lemma 2 (Kubo). *If the system is presumed to be maintained in the thermal state by a linear coupling to the environment, i.e. by a hamiltonian of the form,*

$$\hat{H}_F(t) = \hat{H}_0 + \sum_i \hat{X}_i \hat{F}_i(t), \quad (2.1.12)$$

where \hat{F}_i is the “generalised force” corresponding to \hat{X}_i , then fluctuations in the observables are given by,

$$\begin{aligned}\delta \hat{X}_j(t) &= \int_{-\infty}^{\infty} \sum_k \chi_{jk}(t-t') \delta \hat{F}_k(t') dt', \\ \Rightarrow \delta \hat{X}_j[\Omega] &= \sum_k \chi_{jk}[\Omega] \delta \hat{F}_k[\Omega],\end{aligned} \quad (2.1.13)$$

^{2.5} The proof follows through a straightforward algebraic manipulation viz., (here $\hat{U}_t = e^{-\frac{i}{\hbar}\hat{H}_0 t}$ is the propagator).

$$\begin{aligned}\langle \hat{X}_i(t) \hat{X}_j(0) \rangle &= \text{Tr} \left[\frac{e^{-\beta\hat{H}_0}}{\mathcal{Z}} \hat{X}_i(t) \hat{X}_j(0) \right] \\ &= \frac{1}{\mathcal{Z}} \text{Tr} \left[e^{-\beta\hat{H}_0} \cdot \hat{U}_t^\dagger \hat{X}_i(0) \hat{U}_t \cdot e^{\beta\hat{H}_0} e^{-\beta\hat{H}_0} \cdot \hat{X}_j(0) \right] \\ &= \frac{1}{\mathcal{Z}} \text{Tr} \left[e^{-\beta\hat{H}_0} \hat{X}_j(0) \cdot (e^{-\beta\hat{H}_0} \hat{U}_t^\dagger) \hat{X}_i(0) (\hat{U}_t e^{\beta\hat{H}_0}) \right] \\ &= \text{Tr} \left[\frac{e^{-\beta\hat{H}_0}}{\mathcal{Z}} \hat{X}_j(0) \cdot \hat{U}_{t+i\hbar\beta}^\dagger \hat{X}_i(0) \hat{U}_{t+i\hbar\beta} \right] \\ &= \langle \hat{X}_j(0) \hat{X}_i(t+i\hbar\beta) \rangle.\end{aligned}$$

where, the “susceptibilities” χ_{jk} are (here $\Theta(t)$ is the Heaviside step function),

$$\chi_{jk}(t) = -\frac{i}{\hbar} \Theta(t) \langle [\hat{X}_j(t), \hat{X}_k(0)] \rangle. \quad (2.1.14)$$

Proof. Standard time-dependent perturbation theory as for example in [84]. \square

The great advantage of the Kubo formalism (and in particular the Kubo formula eq. (2.1.13)) is that by relating the fluctuations in the system’s observables to the fluctuations of a generalised force, it suggests an avenue to probe the system: coherent response measurements, performed by harmonically driving \hat{F}_k and observing the effect in \hat{X}_j , give access to $\chi_{jk}[\Omega]$, which then predict the incoherent behaviour of the system in the absence of an explicit stimulus. Within the regime of its validity, this *linear response* approach is pervasive in physics [85–88].

At a formal level, eq. (2.1.14) gives the response of the system to an external influence, in terms of expectation values of the system operators taken on the equilibrium state of the system. The fluctuations in the system observables are then dictated by the fluctuations of the generalised forces. The formally exact expression for the susceptibility eq. (2.1.14), is useful as a theoretical tool to gain a more precise understanding of the behaviour of the system.

Finally, note that only a subset of observables may be coupled to the environment – the sum in the interaction part of the hamiltonian in eq. (2.1.12) runs over a limited set of observables. For this set of observables that directly couple to the environment, general implications follow from the Kubo formula and the uncertainty inequality eq. (2.1.3).

Proposition 1 (Vacuum fluctuations). *Observables of the system that directly couple to the environment exhibit fluctuations, whose spectral distribution $\bar{S}_{X_i X_i}[\Omega]$ have a minimum positive value,*

$$\bar{S}_{X_i X_i}[\Omega] \geq \hbar |\text{Im } \chi_{ii}[\Omega]|. \quad (2.1.15)$$

Proof. Using the definition of the spectral density eq. (2.1.5), together with the uncertainty relation eq. (2.1.3) gives,

$$\begin{aligned} \bar{S}_{X_i X_i}[\Omega] &= \lim_{T \rightarrow \infty} \text{Var} \left[\delta \hat{X}_i^{(T)}[\Omega] \right] \\ &\geq \lim_{T \rightarrow \infty} \frac{1}{2} \left| \left\langle \left[\delta \hat{X}_i^{(T)}[\Omega], \delta \hat{X}_i^{(T)}[\Omega]^\dagger \right] \right\rangle \right| \\ &= \frac{1}{2} \left| \lim_{T \rightarrow \infty} \frac{1}{T} \int_{-T/2}^{T/2} \langle [\delta \hat{X}_i(t), \delta \hat{X}_i(t')] \rangle e^{i\Omega(t-t')} dt dt' \right|. \end{aligned}$$

The integral can be simplified by using the time-translation invariance of the thermal state two-time correlator, and transforming the integration domain, giving,

$$\begin{aligned} \bar{S}_{X_i X_i}[\Omega] &\geq \left| \frac{1}{2} \int_{-\infty}^{\infty} \langle [\delta \hat{X}_i(\tau), \delta \hat{X}_i(0)] \rangle e^{i\Omega\tau} d\tau \right| \\ &= \hbar \left| \int_{-\infty}^{\infty} \chi_{ii}(\tau) \sin(\Omega\tau) d\tau \right| \\ &= \hbar |\text{Im } \chi_{ii}[\Omega]|. \end{aligned}$$

The second equality follows from recognising that the susceptibility $\chi_{ii}(\tau)$ is causal (i.e. defined only for $\tau \geq 0$), and implementing this constraint by splitting the integral over positive and negative times, and finally using the odd property of the susceptibility (i.e. $\chi_{ii}(-\tau) = -\chi_{ii}(\tau)$). The third equality follows from recognising that the sine-transform is the imaginary part of the Fourier transform. \square

Despite the fact that observables are time-translation invariant in the thermal state, they are not time-reversal invariant. In other words, coupling to the environment can render the system irreversible. The imaginary part of the susceptibility,

$$\text{Im } \chi_{ij}[\Omega] = -\frac{i}{2} \int (\chi_{ij}(t) - \chi_{ij}(-t)) e^{i\Omega t} dt,$$

clearly arises from the lack of invariance to the time-reversal $t \rightarrow -t$, and captures the dissipative behaviour of the system. On the other hand, the coupling to the environment leads to fluctuations in the system's observables, characterised by the spectral density $\bar{S}_{X_i X_i}[\Omega]$. It is therefore natural to enquire whether a precise relation exists between these two quantities that codifies the shared origin of fluctuations and dissipation.

Proposition 2 (Fluctuation-Dissipation). *For a system maintained in a thermal state through its contact with an environment, the fluctuations in the observables that couple to the environment are related to the susceptibility,*

$$\bar{S}_{X_i X_i}[\Omega] = \hbar(2n_\beta(\Omega) + 1) \text{Im } \chi_{ii}[\Omega], \quad (2.1.16)$$

where $n_\beta(\Omega)$ is the Bose occupation at frequency Ω and inverse temperature β ,

$$n_\beta(\Omega) := (e^{\beta\hbar\Omega} - 1)^{-1}. \quad (2.1.17)$$

Proof. First we prove a slightly general result and then specify to the case at hand. Starting from the left-hand side of eq. (2.1.16) in the time domain:

$$\text{Im } \chi_{ij}(t) = -\frac{i}{2} (\chi_{ij}(t) - \chi_{ij}(t)^*) = -\frac{i}{2} (\chi_{ij}(t) - \chi_{ji}(-t)).$$

Using the Kubo formula eq. (2.1.13), and employing time-translation invariance, the susceptibilities can be expressed in terms of correlators,

$$\begin{aligned} \chi_{ij}(t) &= -\frac{i}{\hbar} \Theta(t) \left(S_{X_i X_j}(t) - S_{X_j X_i}(-t) \right) \\ \chi_{ji}(-t) &= -\frac{i}{\hbar} \Theta(-t) \left(S_{X_j X_i}(-t) - S_{X_i X_j}(t) \right), \end{aligned}$$

which gives,

$$\text{Im } \chi_{ij}(t) = \frac{-1}{2\hbar} \left(S_{X_i X_j}(t) - S_{X_j X_i}(-t) \right).$$

Now using the KMS condition (eq. (2.1.10)), the order of observables in the second correlator can be reversed, i.e. $S_{X_j X_i}(-t) = S_{X_i X_j}(t - i\hbar\beta)$. Inserting this back gives,

$$\text{Im } \chi_{ij}(t) = \frac{-1}{2\hbar} \left(S_{X_i X_j}(t) - S_{X_i X_j}(t - i\hbar\beta) \right).$$

Fourier transforming each side and re-arranging results in

$$S_{X_i X_j}[\Omega] = \frac{2\hbar}{1 - e^{-\beta\hbar\Omega}} \text{Im } \chi_{ij}[\Omega], \quad (2.1.18)$$

a general relation between the unsymmetrised cross-spectral distribution with the susceptibility. The required result, we consider the case $\hat{X}_j = \hat{X}_i$, and the symmetrised spectral density,

$$\begin{aligned} \bar{S}_{X_i X_i}[\Omega] &= \frac{1}{2} (S_{X_i X_i}[\Omega] + S_{X_i X_i}[-\Omega]) \\ &= \frac{1}{2} (1 + e^{-\beta\hbar\Omega}) S_{X_i X_i}[\Omega] \\ &= \hbar \left(\frac{e^{\beta\hbar\Omega} + 1}{e^{\beta\hbar\Omega} - 1} \right) \text{Im } \chi_{ii}[\Omega]; \end{aligned}$$

here, the first equality is the symmetric property of the spectral density (eq. (2.1.8)), the second follows from the detailed balance condition eq. (2.1.11), and the third from the relation eq. (2.1.18). Replacing the exponentials in terms of the Bose occupation (eq. (2.1.17)) gives the result. \square

As expressed in eq. (2.1.16), the spectrum of fluctuations of the system observable are related to the susceptibility. Using eq. (2.1.13), the fluctuations may be referred to an effective spectrum of the generalised force. In the case where only one observable, \hat{X} , is coupled to its generalised force \hat{F} , it follows that,

$$\begin{aligned} \bar{S}_{XX}[\Omega] &= \hbar (2n_{\text{BE}}(\Omega) + 1) \text{Im } \chi[\Omega] \\ \Rightarrow \bar{S}_{FF}[\Omega] &= |\chi[\Omega]|^{-2} \bar{S}_{XX}[\Omega] = \hbar (2n_{\beta}(\Omega) + 1) \text{Im } \chi[\Omega]^{-1}, \end{aligned}$$

where $\chi[\Omega]$ is the sole susceptibility involved.

The fluctuation-dissipation theorem eq. (2.1.16) relates the fluctuations in the system to the system-environment coupling and the environment state (determined by the single parameter, temperature). The bound eq. (2.1.15), on the other hand, follows from the non-commutativity of the observable and not on the properties of the environment, and is hence a more general statement. Notably, the zero-temperature limit ($\beta \rightarrow \infty$, for which $n_{\beta}[\Omega] \rightarrow 0$) of eq. (2.1.16) gives eq. (2.1.15), motivating the interpretation that the bound eq. (2.1.15) arises from intrinsic – vacuum – fluctuations in the system.

2.1.3 System linearly coupled to a meter

Sections III and IV brutally seize this formalism and mercilessly beat it to death to extract from it quantum limits on the performance of linear amplifiers.

CARLTON CAVES [66]

Quantum mechanically a *meter* (measuring device) is a reservoir from the perspective of the system; by being coupled to a meter, just like the thermal environment, the system experiences fluctuations from the meter. These fluctuations, arising due to the coupling of a measuring device, is called *measurement back-action*. Unlike a thermal environment, the meter needs to be prepared in some non-equilibrium state. This is because the meter is expected to output a classical record of the observable being measured, which can only be arranged for if the states of the meter corresponding to the various values taken by the system observable it is supposed to measure are macroscopically distinguishable [89].

Ultimately, due to the non-equilibrium nature of the meter state, the fluctuations imparted by the meter – measurement back-action – is not in general determined by the fluctuation-dissipation theorem eq. (2.1.16). However, analogous results can be derived under the minimal assumption of the system-meter coupling being linear and weak.

Very generally (see fig. 2.1), a continuous linear measurement of the observable^{2.6} \hat{X} may be described by an operator \hat{Y} corresponding to the output of a detector. Linearity means that^{2.7} $\hat{Y}(t) \propto \hat{X}(t)$. However, since in general $[\hat{X}(t), \hat{X}(t')] \neq 0$, $\hat{X}(t)$ is not a continuous observable. If \hat{Y} needs to be a continuous observable, it has to necessarily satisfy,

$$[\hat{Y}(t), \hat{Y}(t')] = 0, \quad (2.1.19)$$

rendering it a classical stochastic process [90, 91]. For \hat{Y} to commute with itself, it is necessary that the record is contaminated by some additional process $\hat{X}_n(t)$, arising from the meter^{2.8}, so that,

$$\hat{Y}(t) = \hat{X}(t) + \hat{X}_n(t). \quad (2.1.20)$$

Proposition 3 (Standard Quantum Limit). *When a meter, whose initial state is disentangled with that of the system, provides a continuous linear record $\hat{Y}(t)$, of the observable $\hat{X}(t)$, the noise power in the output satisfies the bound,*

$$\bar{S}_{YY}[\Omega] \geq 2 \cdot \min \bar{S}_{XX}[\Omega] = 2\hbar |\chi[\Omega]|, \quad (2.1.21)$$

i.e. the measurement record contains at least twice the minimum noise in the observable being measured.

^{2.6} In the rest of this section, focus is limited to a single observable, so its index will be dropped.

^{2.7} The most general linear relationship is of the form $\hat{Y}(t) = \int f(t-t')\hat{X}(t-t') dt'$, corresponding to a filtered version of the observable. However, without loss of generality, the filtering may be considered as happening on the classical measurement record, beyond the detector.

^{2.8} On the other hand, if it can be arranged that the observable \hat{X} already satisfies $[\hat{X}(t), \hat{X}(t')] = 0$, then there is no requirement for any additional contamination; \hat{X} is then a *quantum non-demolition* (QND) observable [65, 92].

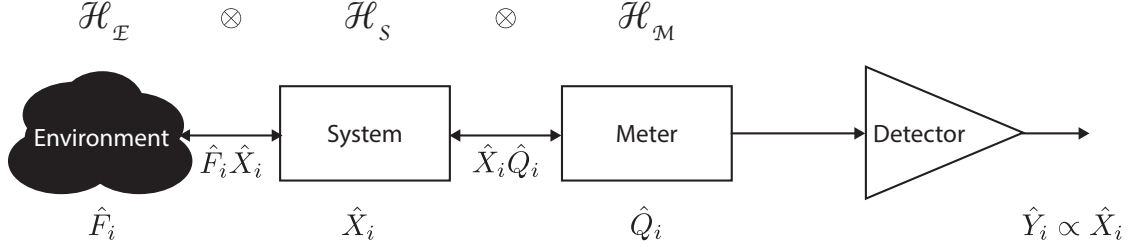


Fig. 2.1 – **Summary of linear response treatment of system-environment-meter coupling.** Schematic of a system \mathcal{S} , in Hilbert space \mathcal{H}_S , with observables $\hat{X}_i \in \mathcal{H}_S$, coupled to its environment \mathcal{E} and a meter \mathcal{M} . The effect of the environment, due to the generalised forces $\hat{F}_i \in \mathcal{H}_E$, is described by the Kubo formula (eq. (2.1.13)). The resulting fluctuations in the observables is given by the fluctuation-dissipation theorem (eq. (2.1.16)). The output of the detector \hat{Y}_i , exhibits fluctuations at least twice the minimum exhibited by \hat{X}_i (eq. (2.1.21)). This fundamental excess arises from quantum fluctuations in the meter variables $\hat{Q}_i \in \mathcal{H}_M$, bounded by the generalised uncertainty principle (eq. (2.1.23)).

Proof. The spectral density of the output eq. (2.1.20) is,

$$\bar{S}_{YY}[\Omega] = \bar{S}_{XX}[\Omega] + \bar{S}_{X_n X_n}[\Omega] + 2\text{Re} \bar{S}_{XX_n}[\Omega].$$

For a meter state initially disentangled with the system, the last term, consisting of the correlations between the system observable \hat{X} and the output noise \hat{X}_n , is zero, i.e.

$$\bar{S}_{YY}[\Omega] = \bar{S}_{XX}[\Omega] + \bar{S}_{X_n X_n}[\Omega].$$

The bound set by vacuum fluctuations (eq. (2.1.15)) implies a least value for \bar{S}_{XX} ; the remaining task is therefore to lower bound $\bar{S}_{X_n X_n}$. Following manipulations similar to the ones in the proof of eq. (2.1.15),

$$\bar{S}_{X_n X_n}[\Omega] \geq \left| \frac{1}{2} \int_{-\infty}^{\infty} \langle [\delta \hat{X}_n(\tau), \delta \hat{X}_n(0)] \rangle e^{i\Omega\tau} d\tau \right|.$$

The commutator of the process \hat{X}_n is fixed by the continuous observability condition eq. (2.1.19): the ansatz eq. (2.1.20) substituted in eq. (2.1.19) gives,

$$[\hat{X}_n(t), \hat{X}_n(t')] = -[\hat{X}(t), \hat{X}(t')].$$

Therefore, the spectral density $\bar{S}_{X_n X_n}$ can be bounded despite any additional knowledge regarding the nature of the contamination, viz.

$$\bar{S}_{X_n X_n}[\Omega] \geq \left| \frac{1}{2} \int_{-\infty}^{\infty} \langle [\delta \hat{X}(\tau), \delta \hat{X}(0)] \rangle e^{i\Omega\tau} d\tau \right| = \hbar |\chi[\Omega]|.$$

Ultimately, this implies,

$$\bar{S}_{YY}[\Omega] = \bar{S}_{XX}[\Omega] + \bar{S}_{X_n X_n}[\Omega] \geq 2 \cdot \hbar |\chi[\Omega]|.$$

□

Conceptually, the standard quantum limit eq. (2.1.21) states that quantum mechanics extorts a penalty twice: once in the form of the vacuum fluctuations of the observable (as in eq. (2.1.15)), and once more, the same price, in the form of unavoidable fluctuations in the linear measurement process. This factor of two may also be understood if the linear measurement process is considered to be an abstract linear amplifier [66, 93]. Note that the statement of the SQL is intimately tied to the system-meter coupling, described by the susceptibility – each possible coupling scheme (for example [94, 95]) has its unique SQL.

In order to understand the origin of the excess noise, it proves useful to consider a slightly less abstract model of the measurement process. Following von Neumann [72], the meter is assumed to be another quantum system with (at least) a pair of canonically conjugate degrees of freedom \hat{Q}_1, \hat{Q}_2 , satisfying,

$$[\hat{Q}_1(t), \hat{Q}_2(t')] = i\hbar \delta(t - t'), \quad (2.1.22)$$

and all other two-time commutators zero. Note that these variables carry the dimensions of the amplitude flux of a travelling wave field. One of these, say \hat{Q}_1 , is linearly coupled to the system observable \hat{X} that needs to be measured; the other, \hat{Q}_2 , is a *pointer* variable linearly coupled to the detector output observable \hat{Y} . Since by definition \hat{Y} commutes with itself at different times, and \hat{Q}_2 does so by being a canonical coordinate of a continuous variable system, one can assume that the detector simply provides a record of the pointer variable, i.e.

$$\hat{Y}(t) \propto \hat{Q}_2(t);$$

the detector simply reads out the pointer variable. Note that the measurement model ensures that there is no back-action on the meter (from the detector) in this final measurement step: the two canonically conjugate meter variables are continuous observables, so that one of them can be read out by the detector without hindrance.

The meter variables, by being quantum mechanical operators, undergo fundamental fluctuations. This property may be codified as the following uncertainty relation.

Proposition 4 (Spectral uncertainty relation [62, 69]). *The canonically conjugate observables $\hat{Q}_{1,2}$ of a quantum mechanical system satisfying the commutation relation (eq. (2.1.22)),*

$$[\hat{Q}_1(t), \hat{Q}_2(t')] = i\hbar \delta(t - t'),$$

satisfy the following inequality for their symmetrised spectra:

$$\bar{S}_{Q_1 Q_1}[\Omega] \bar{S}_{Q_2 Q_2}[\Omega] - \bar{S}_{Q_1 Q_2}^2[\Omega] \geq \frac{\hbar^2}{4}. \quad (2.1.23)$$

Proof. The strategy, similar to the proof of the Robertson-Schrödinger inequality in Appendix A, is to construct an operator \hat{M} such that the identity $\hat{M}^\dagger \hat{M} \geq 0$ induces the required inequality. The choice,

$$\hat{M} := \int \sum_{i=1,2} f_i(\Omega) \delta \hat{Q}_i[\Omega] d\Omega,$$

for some arbitrary complex functions f_i , gives,

$$\begin{aligned}\hat{M}^\dagger \hat{M} &= \int d\Omega d\Omega' \sum_{i,j} f_i^*(\Omega) f_j(\Omega') \delta\hat{Q}_i[\Omega] \delta\hat{Q}_j[\Omega'] \\ &= \int d\Omega d\Omega' \sum_{i,j} f_i^*(\Omega) f_j(\Omega') \left(\frac{1}{2} \{ \delta\hat{Q}_i[\Omega], \delta\hat{Q}_j[\Omega'] \} + \frac{1}{2} [\delta\hat{Q}_i[\Omega], \delta\hat{Q}_j[\Omega']] \right),\end{aligned}$$

where the second equality simply re-expresses the operator product in terms of the (anti-)commutator. Now $\hat{M}^\dagger \hat{M} \geq 0$ implies, after taking expectation values,

$$\int d\Omega d\Omega' \sum_{i,j} f_i^*(\Omega) f_j(\Omega') \left(\bar{S}_{Q_i Q_j}[\Omega] \cdot 2\pi \delta(\Omega + \Omega') + \frac{1}{2} [\delta\hat{Q}_i[\Omega], \delta\hat{Q}_j[\Omega']] \right) \geq 0,$$

where the expectation of the symmetrised anti-commutator has been replaced in terms of the symmetrised spectrum. Since the above inequality is true for any arbitrary functions f_i , and recognising the left-hand side as a quadratic form, it follows that

$$\begin{pmatrix} \bar{S}_{Q_1 Q_1}[\Omega] & \bar{S}_{Q_1 Q_2}[\Omega] + \frac{i\hbar}{2} \\ \bar{S}_{Q_2 Q_1}[\Omega] - \frac{i\hbar}{2} & \bar{S}_{Q_2 Q_2}[\Omega] \end{pmatrix} \geq 0,$$

where the Fourier transformed equivalent of the commutator eq. (2.1.22) has been employed. The sufficient condition for the positivity of this matrix is that its lowest eigenvalue is positive:

$$(\bar{S}_{Q_1 Q_1} + \bar{S}_{Q_2 Q_2}) - \sqrt{(\bar{S}_{Q_1 Q_1} - \bar{S}_{Q_2 Q_2})^2 + 4 \left(\bar{S}_{Q_1 Q_2}^2 + \frac{\hbar^2}{4} \right)} \geq 0,$$

which simplifies to the required result. \square

When the meter is coupled to the system, the bound in eq. (2.1.23) need not be attained – corrections arising from the coupling constants (susceptibilities relating the system and meter variables) give a lower bound larger than $\frac{\hbar^2}{4}$ [62, 69]. In any case, eq. (2.1.23) represents the ultimate bound satisfied by the internal fluctuations of the meter.

The measurement of the system variable \hat{X} , within von Neumann's model, now proceeds as follows: the free meter variables $\hat{Q}_{1,2}^0$ undergo intrinsic fluctuations (assumed to be uncorrelated for simplicity) that satisfy eq. (2.1.23). The fluctuating meter variable \hat{Q}_1 is linearly coupled to the system variable \hat{X} via an interaction of the form $\zeta \hat{X} \hat{Q}_1$; together with the interaction with the thermal environment variable \hat{F} , the system then interacts with its combined environment via the hamiltonian,

$$\hat{H} = \hat{X} (\hat{F} + \zeta \hat{Q}_1). \quad (2.1.24)$$

Here ζ is the (dimensioned) strength of the system-meter coupling.

Within the Kubo formalism, the effect of the coupling is to cause additional motion in all variables participating in the interaction. From the perspective of the system variable, \hat{X} , it is now coupled to an additional force $\zeta \hat{Q}_1$, leading to a perturbation from its intrinsic motion, $\hat{X}^0 = \chi_X \hat{F}$, to,

$$\hat{X}[\Omega] = \chi_X[\Omega] (\hat{F}[\Omega] + \zeta \hat{Q}_1[\Omega]) = \hat{X}^0[\Omega] + \zeta \chi_X[\Omega] \hat{Q}_1[\Omega]. \quad (2.1.25)$$

Here, the second term is the back-action due to the measurement. From the perspective of the meter variable \hat{Q}_1 , it is coupled to a generalised force proportional to \hat{X} , leading to,

$$\hat{Q}_1[\Omega] = \hat{Q}_1^0[\Omega] + \zeta\chi_Q[\Omega]\hat{X}[\Omega] \approx (1 + \zeta^2\chi_Q[\Omega]\chi_X[\Omega])\hat{Q}_1^0[\Omega] + \zeta\chi_Q[\Omega]\hat{X}^0[\Omega] \quad (2.1.26)$$

where \hat{Q}_1^0 is the intrinsic motion of the variable when the meter is free. Here the last term may be interpreted as a transcription of the intrinsic system variable \hat{X}^0 onto the meter, i.e. a *pre-measurement* [72]. In eqs. (2.1.25) and (2.1.26), the susceptibilities χ_X, χ_Q are defined according to the Kubo formula (eq. (2.1.13)) applied with respect to the interaction hamiltonian in eq. (2.1.24). By proper choice of the dimensions of ζ , χ_Q may be rendered dimensionless, this choice is enforced henceforth.

The role of the conjugate meter variable \hat{Q}_2 is to retrieve \hat{Q}_1 , i.e.

$$\hat{Q}_2 = \hat{Q}_1^0 + \hat{Q}_1 = \hat{Q}_2^0 + (1 + \zeta^2\chi_Q\chi_X)\hat{Q}_1^0 + \zeta\chi_Q\hat{X}^0 \approx \hat{Q}_2^0 + \zeta^2\chi_Q\chi_X\hat{Q}_1^0 + \zeta\chi_Q\hat{X}^0,$$

where the second approximation assumes a sufficiently strong measurement interaction. Finally, this pointer variable is coupled to the detector, whose output \hat{Y} is referred to an equivalent system variable \hat{X} , i.e. \hat{Y} is an estimator for \hat{X}^0 based on \hat{Q}_2 ; explicitly,

$$\hat{Y} := \frac{\hat{Q}_2}{\zeta\chi_Q} \approx \hat{X}^0 + \frac{\hat{Q}_2^0}{\zeta\chi_Q} + \zeta\chi_X\hat{Q}_1^0.$$

The total noise power at the detector output, $\bar{S}_{YY}[\Omega]$, is given by,

$$\begin{aligned} \bar{S}_{YY}[\Omega] &= \bar{S}_{XX}^0[\Omega] + \frac{\bar{S}_{Q_2Q_2}^0[\Omega]}{|\zeta\chi_Q[\Omega]|^2} + |\zeta\chi_X[\Omega]|^2 \bar{S}_{Q_1Q_1}^0[\Omega] \\ &\geq \bar{S}_{XX}^0[\Omega] + 2 \left| \frac{\chi_X[\Omega]}{\chi_Q[\Omega]} \right| \sqrt{\bar{S}_{Q_2Q_2}^0[\Omega] \bar{S}_{Q_1Q_1}^0[\Omega]} \\ &\geq \bar{S}_{XX}^0[\Omega] + \hbar \left| \frac{\chi_X[\Omega]}{\chi_Q[\Omega]} \right|. \end{aligned}$$

Here, the second line is obtained by bounding the sum using the arithmetic-geometric mean inequality (see footnote 2.3, on page 32), while the third follows from using the uncertainty principle for the free meter variables (eq. (2.1.23)). Since χ_Q has been chosen dimensionless by proper choice of ζ , it is convenient to interpret $|\chi_Q|$ as a measurement efficiency. In the limit where this efficiency is unity, the detector output takes a minimum value given by,

$$\bar{S}_{YY}[\Omega] \geq \bar{S}_{XX}^0[\Omega] + \hbar |\chi_X[\Omega]| \geq 2 \cdot \hbar |\chi_X[\Omega]|,$$

and equal to the standard quantum limit given in eq. (2.1.21).

In section 2.3, this abstract caricature will be applied to the specific problem where the system is a mechanical oscillator, whose position is being measured using an optical cavity-based interferometer [67, 96]. That example realises von Neumann's ideal, with the quantised electromagnetic field playing the role of the meter.

2.2 Phonons and photons

The career of a young theoretical physicist consists of treating the harmonic oscillator in ever-increasing levels of abstraction.

SIDNEY COLEMAN

The objective of this section is to introduce the dramatis personae of the quantum measurement problem studied in this thesis. Nominally, the *system* is a mechanical oscillator formed by a well-defined mode of a solid-state elastic resonator, excited by its thermal environment in ambient conditions. The *meter* is a mode of an optical cavity excited by a laser source. In section 2.2.1, a formal description of the quantum mechanics of an elastic resonator is given, followed by a brief treatment of a single mode of such a resonator. Section 2.2.2 tackles the analogous development for the electromagnetic field, first describing the travelling wave field that excites the optical cavity, and then the coupling of the cavity to the travelling wave field. True to Sidney Coleman's observation, both the mechanical mode and the optical mode are formally harmonic oscillators. The concrete implementation of either oscillator will be introduced later in section 2.4.

2.2.1 Phonons: quantised linear elastodynamics

Bulk matter, existing in a state where its constituent atoms are bound to each other, maybe assumed to form a continuum. When this system is in mechanical equilibrium, its state at each instant of time maybe specified by the set of positions $\mathbf{r} \in D \subset \mathbb{R}^3$ of the material constituents within the domain D that forms the continuum^{2.9}. This continuum is the elastic body. Changes in the state of the body are described by the transformation,

$$\mathbf{r} \mapsto \mathbf{r} + \mathbf{u}(\mathbf{r}), \quad (2.2.1)$$

wherein the constituents at position \mathbf{r} get displaced to their new position $\mathbf{u}(\mathbf{r})$. \mathbf{u} is called the displacement field, and this map represents the deformation of the continuum. We shall be concerned with elastodynamic phenomena that can be described by the displacement field and its derivatives. We therefore limit the discussion to a sufficiently smooth displacement field^{2.10} $\mathbf{u}(\mathbf{r})$.

Note that eq. (2.2.1) is essentially a geometric transformation of the body; we shall therefore strive to describe and analyse its consequences in suitable language.

The strain tensor, defined by^{2.11}

$$u_{ij}^{(1)}(\mathbf{r}) := \frac{\partial u_i}{\partial r_j}$$

^{2.9}We implicitly assume a non-relativistic setting; in the contrary setting, the specification of the preferred state \mathbf{x} is untenable [97, 98]. However formulations which extend to the relativistic case exist [98–101]; see [102, Chap. 15] for a historical review of these issues.

^{2.10}This excludes phenomena like dislocations and fracture

^{2.11}Note the difference from the standard definition, as considered for example in [103]; we follow [104]

is essential to the description of how distances between points in the body change due to the deformation eq. (2.2.1). In fact, the infinitesimal length element^{2.12} $ds^2 := dr_i dr_i$ changes to [103],

$$\begin{aligned} ds^2 &\rightarrow (dr_i + du_i)(dr_i + du_i) \\ &= \left(dr_i + \frac{\partial u_i}{\partial r_j} dr_j \right) \left(dr_i + \frac{\partial u_i}{\partial r_k} dr_k \right) \\ &\approx dr_i dr_i + \left(u_{ij}^{(1)} + u_{ji}^{(1)} \right) dr_i dr_j \\ &= \left(\delta_{ij} + \left(u_{ij}^{(1)} + u_{ji}^{(1)} \right) \right) dr_i dr_j. \end{aligned}$$

Clearly, the symmetric part of $u^{(1)}$ plays the role of a metric tensor within the body. The tensor $u^{(1)}$ maybe decomposed into three components [104], each describing a possible motion of the body: (a) volume deformation – distances between constituents changing in the same sense throughout the body – characterised by the scalar $\text{Tr } u^{(1)} = \nabla \cdot \mathbf{u}$; (b) shear motion – infinitesimal parallel planes sliding along each other – characterised by the traceless symmetric tensor, $\frac{1}{2}(u_{ij}^{(1)} + u_{ji}^{(1)}) - \frac{\delta_{ij}}{3} \text{Tr } u^{(1)}$; and, (c) rigid rotation characterised by the anti-symmetric tensor, $\frac{1}{2}(u_{ij}^{(1)} - u_{ji}^{(1)})$. The case of rigid translational motion is described by a uniform-in-space displacement field, and therefore has a null strain tensor. Elastodynamics does not concern with rigid motions, henceforth, we may consider $u^{(1)}$ to be symmetric.

In addition to the strain tensor $u^{(1)}$, we consider the object,

$$u_{ijk}^{(2)} := \frac{\partial^2 u_i}{\partial r_j \partial r_k}, \quad (2.2.2)$$

which describes the curvature of lines and surfaces due to the transformation eq. (2.2.1). For example, the (flat) coordinate plane $r_i = 0$ at $t = 0$, is mapped to the (curved) surface $r_i = u_i(\mathbf{r}, t)$ at later times $t > 0$ by the deformation eq. (2.2.1). The curvature of the deformed surface is quantified by the eigenvalues of the matrix (indexed by j, k) $u_{ijk}^{(2)}$.

Fortunately, still higher derivatives of the displacement field need not be considered. For, it is a theorem [105] that all the local geometric properties of surfaces in three-dimensions are captured by combinations of the two tensors $u^{(1)}, u^{(2)}$. This concludes the essential aspects of the kinematics of the displacement field.

In order to derive the dynamics (i.e., equations of motion) of \mathbf{u} , we appeal to the principle of least action [106]. In Hamilton's form, it dictates that the continuous sequence of deformations $t \mapsto \mathbf{u}(\mathbf{r}, t)$, realised at each point in time, is the one that renders the action,

$$\mathcal{S}[\mathbf{u}_i] := \int dt L \left(t, r_i, u_i, \frac{\partial u_i}{\partial t}, \frac{\partial u_i}{\partial r_j}, \frac{\partial^2 u_i}{\partial r_j \partial r_k} \right) \quad (2.2.3)$$

stationary. Here L is the Lagrangian which is in general a function of time, spatial coordinates, displacement field, and its derivatives. Note that the action is a *functional* of the deformation

^{2.12} Note that henceforth, we adopt the summation convention that whenever two indices are repeated, they are implicitly summed over. For instance, $dr_i dr_i = \sum_i dr_i dr_i$ etc.

field \mathbf{u} , associating a real number with a given configuration $\mathbf{u}(\mathbf{r}, t)$ defined over the spatial domain D . Simple principles maybe invoked to fix the form of L , and thence to derive the equations of motion^{2.13}.

In order to clearly identify and delineate the physical symmetry principles involved, and the inference of L therein, we go through them in a sequence of steps:

1. The elastic body is assumed to conform to some loose notion of locality, so that the Lagrangian L is a sum over a Lagrangian density^{2.14} \mathcal{L} defined for each infinitesimal sub-domain of D ; in other words,

$$\mathcal{S}[\mathbf{u}_i] = \int dt \int_D d^3r \mathcal{L} \left(t, r_i, u_i, \frac{\partial u_i}{\partial t}, \frac{\partial u_i}{\partial r_j}, \frac{\partial^2 u_i}{\partial r_j \partial r_k} \right). \quad (2.2.4)$$

2. The assumption of the principle of Galilean relativity [111, 112] – the description of elastic phenomena is assumed independent of translations in time and space, uniform motion, and rotation, i.e. the transformations

$$\begin{aligned} t &\rightarrow t + t_0 \\ r_i &\rightarrow r_i + r_{0i} + v_i t + R_{ij} r_j. \end{aligned} \quad (2.2.5)$$

The principles of invariance under translations in time and uniform motion are Newtonian precepts, which elasticity is expected to obey. Translations in space also fall in this category for systems which evolve freely (i.e. not under the influence of an external force) – here we consider elasticity in this form, where the deformation field evolves under self-consistent forces imposed by deformations in the material. Rotational invariance, on the other hand, requires additional assumptions about the nature of the material forming the body. The description of crystalline material are not invariant to arbitrary rotations, but only to a discrete set which describe its symmetry [113]. We limit ourselves to amorphous material, which is the case relevant to this thesis. For such materials, the various elements of the Galilean transformation eq. (2.2.5) maybe analysed as follows:

- 2.1. Translation invariance in time and space necessitates that the lagrangian be independent of t , r_i and u_i , i.e.,

$$\mathcal{L} = \mathcal{L}(\dot{u}_i, u_{ij}^{(1)}, u_{ijk}^{(2)}). \quad (2.2.6)$$

- 2.2. Invariance under uniform motion only affects rigid translational motion, resulting in the deformation field $u_i(\mathbf{x}, t) = v_i t$. In this case, the only term in \mathcal{L} is the one that depends on \dot{u}_i . This being a vector, rotational invariance further limits possible terms to ones that are functions of the invariant $\dot{u}_i \dot{u}_i$. The simplest non-trivial function provides the first term of the lagrangian, viz.,

$$\mathcal{L}(\dot{u}_i, u_{ij}^{(1)}, u_{ijk}^{(2)}) = \frac{\rho}{2} \dot{u}_i \dot{u}_i + \dots \quad (2.2.7)$$

Here ρ is a positive real number – dimensional analysis shows that it is in fact the mass density of the amorphous material.

^{2.13}See [107, 108] for a lucid articulation of this general idea, and [109, 110] for examples

^{2.14}By abuse of terminology, \mathcal{L} will also be referred to as a Lagrangian

- 2.3. Rotational invariance may now be used to deduce the additional terms that depend on the second and third rank tensor $u^{(1)}$, $u^{(2)}$. These could contribute terms in the Lagrangian so that \mathcal{L} takes the form,

$$\mathcal{L} = \frac{\rho}{2} \dot{u}_i \dot{u}_i - \frac{1}{2} U^{(1)} \llbracket u^{(1)} \rrbracket - \frac{1}{2} U^{(2)} \llbracket u^{(2)} \rrbracket, \quad (2.2.8)$$

where $U^{(i)}$ are functionals of $u^{(i)}$. The factors of $\frac{1}{2}$ are conventional, while the negative sign allows for the loose interpretation that $U^{(1)}$ ($U^{(2)}$) is the potential energy due to elastic stress (local curvature). In order to determine the form of $U^{(i)}$, we seek refuge in the theory of tensor invariants [114].

- 2.4. Firstly we deal with the second rank tensor $u^{(1)}$. Since $U^{(1)}$ a scalar formed from a second rank tensor, we choose the simplest such term,

$$U^{(1)} = \alpha_{ijkl} u_{ij}^{(1)} u_{kl}^{(1)}. \quad (2.2.9)$$

Recognising that $u^{(1)}$ commutes under multiplication gives the basic symmetry $\alpha_{ijkl} = \alpha_{klij}$. The assumed translation invariance in space and time implies that α_{ijkl} is a constant. Finally the choice $u_{ij}^{(1)} = u_{ji}^{(1)}$, implies $\alpha_{ijkl} = \alpha_{jikl} = \alpha_{ijlk}$. Thus,

$$\alpha_{ijkl} = \alpha_{jikl} = \alpha_{ijlk} = \alpha_{klij}. \quad (2.2.10)$$

However α_{ijkl} cannot be any tensor that satisfies this symmetry relation – the term $U^{(1)}$ must be invariant under arbitrary rotations. For second rank tensors in three dimensions, such as $u^{(1)}$, there are three invariants to rotations [114]: $\text{Tr } u^{(1)}$, $\text{Tr } [u^{(1)}]^2$, and $\text{Det } u^{(1)}$. Since $U^{(1)}$ is quadratic in $u^{(1)}$, it must be that $U^{(1)}$ is a linear superposition:

$$\begin{aligned} U^{(1)} &= \mu_1 [\text{Tr } u^{(1)}]^2 + \mu_2 \text{Tr } [u^{(1)}]^2 \\ \text{i.e., } \alpha_{ijkl} u_{ij}^{(1)} u_{kl}^{(1)} &= \mu_1 [u_{ii}^{(1)}]^2 + \mu_2 u_{ij}^{(1)} u_{ji}^{(1)}. \end{aligned} \quad (2.2.11)$$

Together with the symmetry constraints eq. (2.2.10), this fixes the form of α_{ijkl} , viz.,

$$\alpha_{ijkl} = \mu_1 \delta_{ij} \delta_{kl} + \frac{\mu_2}{2} (\delta_{ik} \delta_{jl} + \delta_{jk} \delta_{il}), \quad (2.2.12)$$

in terms of two constants μ_1, μ_2 carrying the dimension of elastic modulus; μ_1 and $\frac{\mu_2}{2}$ are the conventional Lamé constants [103]. Thus, we have an amendment to eq. (2.2.8):

$$\mathcal{L} = \frac{\rho}{2} \dot{u}_i \dot{u}_i - \frac{1}{2} \alpha_{ijkl} u_{ij}^{(1)} u_{kl}^{(1)} + \dots \quad (2.2.13)$$

- 2.5. The case of the third rank tensor $u^{(2)}$ is much more complicated. Invariants of third rank tensors in three dimensions are known [115, 116], and in principle the form of $U^{(2)}$ can be determined in three dimensions. However, owing to the complexity, we restrict attention to the two dimensional case, i.e., to an elastic continuum that may be approximated as a membrane (negligible thickness) or a beam (negligible thickness and width). In the former case, only the single transverse field – displacement of the

membrane surface orthogonal to itself – is relevant, while in the latter case, there are two independent transverse directions. Choosing Cartesian coordinates where the relevant displacement is u_i ($i = 1$ for a membrane, $i = 1, 2$ for a beam), the lowest order invariant composed of the elements, $u_{i11}^{(2)}, u_{i12}^{(2)} = u_{i21}^{(2)}, u_{i22}^{(2)}$ are the invariants of the 2×2 matrix (indexed by j, k for each i) $u_{ijk}^{(2)}$ [117]. In particular, the two invariants are conveniently expressed as $\text{Tr}[u_{ijk}^{(2)}]^2$ and $\det[u_{ijk}^{(2)}]$, so that,

$$U_i^{(2)} \propto (u_{i11}^{(2)} + u_{i22}^{(2)})^2 + (u_{i11}^{(2)}u_{i22}^{(2)} - (u_{i12}^{(2)})^2),$$

for each independent transverse motion u_i . Since $u^{(2)}$ carry dimensions of inverse length (unlike $u^{(1)}$ which is dimensionless), the proportionality factor depends on a length scale set by the dimensions of the continuum. The conventional choice is [117],

$$U_i^{(2)} = K_i M_i \left[(u_{i11}^{(2)})^2 + (u_{i22}^{(2)})^2 - 2(1 - \zeta)(u_{i11}^{(2)}u_{i22}^{(2)} - (u_{i12}^{(2)})^2) \right],$$

where K_i is the elastic modulus, M_i is the moment of inertia about the axis orthogonal to i , and ζ is Poisson's ratio. $U_i^{(2)}$ represents the potential energy due to curvature; for beams and membranes, a significant proportion of energy in higher order elastic modes is due to curvature. Indeed, the equations of motion including this term gives the conventional Euler-Bernoulli theory of beams [117]. However, for the sake of brevity, the ensuing discussion will not address the contribution of $U^{(2)}$.

To recap, the action eq. (2.2.3) is given by,

$$\mathcal{S}[[u_i]] = \int dt \int_D d^3r \mathcal{L}, \quad (2.2.14)$$

where the Lagrangian is (neglecting terms due to local curvature, $u^{(2)}$),

$$\mathcal{L} = \frac{\rho}{2} \dot{u}_i \dot{u}_i - \frac{1}{2} \alpha_{ijkl} (\partial_i u_j) (\partial_k u_l) = \frac{\rho}{2} \dot{u}_i \dot{u}_i - \frac{1}{2} t_{ij} s_{ij}. \quad (2.2.15)$$

In going to the second equality, we have defined the stress tensor,

$$t_{ij} := \alpha_{ijkl} u_{kl}^{(1)}. \quad (2.2.16)$$

This definition is essentially Hooke's law for a linear elastic medium^{2.15}, with the Hooke tensor α_{ijkl} given by (eq. (2.2.10)),

$$\alpha_{ijkl} = \mu_1 \delta_{ij} \delta_{kl} + \mu_2 (\delta_{ik} \delta_{jl} + \delta_{jk} \delta_{il}), \quad (2.2.17)$$

where we have re-defined $\frac{\mu_2}{2} \rightarrow \mu_2$ for notational simplicity, and to conform with the definition of the Lamé constants in vogue [103].

^{2.15} In order to make this identification, it needs to be established that the stress tensor t_{ij} as defined, carries the physical interpretation that its components give the force dF_i (along the x_i direction) on a rectilinear area element dA_j , i.e. that $dF_i = t_{ij} dA_j$. The easiest route is to compare eq. (2.2.15) to that obtained in the conventional development of elastodynamics from Newton's laws [103].

The principle of least action asserts that the motion $\mathbf{u}(\mathbf{r}, t)$ is the one that minimises the action (eq. (2.2.14)), consistent with the appropriate spatial and temporal boundary conditions. Since the three displacement fields u_i are independent, such optimisation maybe performed in a fairly standard manner by setting the functional derivative $\frac{\delta \mathcal{S}}{\delta u_i} = 0$. This gives the equations of motion of elastodynamics [103, 106] (see appendix B.1.1 for details),

$$\begin{aligned} \rho \ddot{u}_i &= \alpha_{ijkl} \partial_j \partial_l u_k = (\mu_1 + \mu_2) \partial_i \partial_j u_j + \mu_2 \partial_j \partial_j u_i \\ \text{or, } \rho \ddot{\mathbf{u}} &= (\mu_1 + 2\mu_2) \nabla (\nabla \cdot \mathbf{u}) - \mu_2 \nabla \times (\nabla \times \mathbf{u}), \end{aligned} \quad (2.2.18)$$

and a set of natural conditions to be satisfied at the boundary ∂D (see appendix B.1.2):

$$\begin{aligned} \text{free boundary: } \quad t_{ij} A_j |_{\partial D} &= 0 \\ \text{fixed-surface: } \quad u_i |_{\partial D} &= 0. \end{aligned} \quad (2.2.19)$$

The vectorial form of the equations of motion (eq. (2.2.18)) suggests the existence of two types of elastic excitations (see appendix B.2): transverse waves (corresponding to $\nabla \cdot \mathbf{u} = 0$) propagating with the velocity $c_T = \sqrt{\mu_2 / \rho}$; and, longitudinal waves (corresponding to $\nabla \times \mathbf{u} = 0$) propagating with the velocity $c_L = \sqrt{(\mu_1 + 2\mu_2) / \rho}$. These waves are the long-wavelength excitations of the underlying microscopic medium, described by the effective theory of elastodynamics.

These excitations maybe quantised on equal footing^{2.16} via the canonical method [14, 56]. An alternate, less formal, route will be pursued here. Firstly, we note that the differential operator,

$$\hat{L}_{ik} := \frac{\alpha_{ijkl}}{\rho} \partial_j \partial_l \quad \text{or,} \quad \hat{\mathbf{L}} = c_L^2 \nabla (\nabla \cdot) - c_T^2 \nabla \times (\nabla \times), \quad (2.2.20)$$

is hermitian with respect to the inner product defined by (here $\text{Vol}(D) = \int_D d^3r$),

$$\langle \mathbf{v}, \mathbf{u} \rangle := \frac{1}{\text{Vol}(D)} \int_D v_i^*(\mathbf{r}) u_i(\mathbf{r}) d^3r,$$

as long as one of the boundary conditions in eq. (2.2.19) is satisfied, and the Hooke tensor satisfies the symmetry constraints in eq. (2.2.10) (see [118], and appendix B.3). Therefore, the eigenvectors $\tilde{\mathbf{u}}_n(\mathbf{x})$ defined by solutions of,

$$\hat{\mathbf{L}} \tilde{\mathbf{u}}_n = \omega_n^2 \tilde{\mathbf{u}}_n,$$

form an orthonormal set [119], i.e.

$$\langle \tilde{\mathbf{u}}_n, \tilde{\mathbf{u}}_{n'} \rangle = \delta_{nn'} \langle \tilde{\mathbf{u}}_n, \tilde{\mathbf{u}}_n \rangle,$$

and is complete [119], i.e.

$$\mathbf{u}(\mathbf{r}, t) = \sum_n \tilde{\mathbf{u}}_n(\mathbf{r}) x_n(t), \quad (2.2.21)$$

^{2.16}Unlike electrodynamics for example, where the transverse excitations are constrained [56]

for any valid displacement field configuration^{2.17} $\mathbf{u}(\mathbf{r}, t)$. Here, the dimensions of w_n are such that x_n carries the dimension of a length. The Lagrangian,

$$L = \int_D d^3r \mathcal{L} = \int_D \left(\frac{\rho}{2} \langle \dot{\mathbf{u}}, \dot{\mathbf{u}} \rangle - \frac{1}{2} \langle \mathbf{u}, \hat{\mathbf{L}} \mathbf{u} \rangle \right) d^3r,$$

expressed in terms of the expansion eq. (2.2.21),

$$L = \sum_n \frac{m_n}{2} \dot{x}_n^2(t) - \frac{k_n}{2} x_n^2(t) =: \sum_n L_n, \quad (2.2.22)$$

simplifies to that of a sum of simple harmonic oscillators, one for each elastic excitation, with generalised coordinates $x_n(t)$. The n^{th} oscillator is characterised by a “mass” m_n [120], and “spring constant” k_n , respectively,

$$m_n = \int_D \rho |\tilde{\mathbf{u}}_n(\mathbf{r})|^2 d^3r, \quad \text{and,} \quad k_n = \int_D w_n^2 |\tilde{\mathbf{u}}_n(\mathbf{r})|^2 d^3r,$$

and it oscillates at the frequency, $\Omega_n = \sqrt{k_n/m_n}$.

The Lagrangian L , in eq. (2.2.22), describes a discrete set of independent harmonic oscillators, each of which can be quantised independently. Following standard procedure [14], the commutation relations between the position operator \hat{x}_n and its conjugate momentum $m_n \dot{\hat{x}}_n$, can be implemented in terms of non-hermitian operators $\hat{b}_n, \hat{b}_n^\dagger$, defined by

$$\hat{b}_n(t) = \frac{1}{2} \left(\frac{\hat{x}_n(t)}{\sqrt{\hbar/2m_n\Omega_n}} + i \frac{m_n \dot{\hat{x}}_n(t)}{\sqrt{\hbar m_n \Omega_n/2}} \right), \quad (2.2.23)$$

satisfying the equal-time commutation relations,

$$[\hat{b}_n(t), \hat{b}_{n'}^\dagger(t)] = \delta_{nn'}.$$

These quantised excitations, due to the above commutator, are bosons - phonons corresponding to the elastic deformation of the medium. The dynamics of each quantised mode is most conveniently described by its hamiltonian [106], $\hat{H}_n = m_n \dot{\hat{x}}_n^2 - \hat{L}_n$, given by,

$$\hat{H}_n = \frac{m_n}{2} \dot{\hat{x}}_n^2 + \frac{m_n \Omega_n^2}{2} \hat{x}_n^2 = \hbar \Omega_n \left(\hat{b}_n^\dagger \hat{b}_n + \frac{1}{2} \right), \quad (2.2.24)$$

where the $\frac{1}{2}$ arises from the intrinsic vacuum fluctuation of the mode. Note that the mass of the oscillator only appears through the definition of \hat{b}_n in eq. (2.2.23).

2.2.1.1 Mechanical oscillator in thermal equilibrium

Focusing on one of the harmonic modes (and therefore dropping the mode index henceforth) with frequency Ω_m , with generalised position $x(t)$, we are interested in its description when it

^{2.17} Since we limit attention to a domain D which is finite, i.e. $\text{Vol}(D) < \infty$, the operator $\hat{\mathbf{L}}$ has a discrete eigenspectrum [119], and so the expansion is necessarily a sum.

is in equilibrium with a thermal environment at temperature T . Using the free hamiltonian \hat{H} is (eq. (2.2.24)),

$$\hat{H} = \hbar\Omega_m \left(\hat{b}^\dagger \hat{b} + \frac{1}{2} \right),$$

the equilibrium is described by the thermal state (see eq. (2.1.9))

$$\hat{\rho}_m = \frac{\exp\left(-\frac{\hat{H}}{k_B T}\right)}{\text{Tr} \exp\left(-\frac{\hat{H}}{k_B T}\right)} = \left(\frac{1}{n_{m,\text{th}} + 1} \right) \left(\frac{n_{m,\text{th}}}{n_{m,\text{th}} + 1} \right)^{\hat{b}^\dagger \hat{b}}. \quad (2.2.25)$$

In the second equality, the state is parametrised in terms of the mean phonon occupation,

$$n_{m,\text{th}} := \text{Tr} \left[\hat{b}^\dagger \hat{b} \hat{\rho}_m \right] = \frac{1}{e^{\hbar\Omega_m/k_B T} - 1} \xrightarrow{k_B T \gg \hbar\Omega_m} \frac{k_B T}{\hbar\Omega_m}.$$

Note that the variance in the oscillator position, due to thermal fluctuations is given by,

$$\text{Var} [\hat{x}] = \text{Tr} [\hat{x}^2 \hat{\rho}_m] = (2n_{m,\text{th}} + 1)x_{\text{zp}}^2, \quad \text{where,} \quad x_{\text{zp}}^2 := \frac{\hbar}{2m\Omega_m}, \quad (2.2.26)$$

exhibiting a contribution from vacuum fluctuations. In fact, the variance in the position when the mean occupation is zero ($n_{m,\text{th}} = 0$), defines the *zero-point motion* x_{zp} .

The development of section 2.1 allows for a finer understanding of the total variance $\text{Var} [\hat{x}]$; in particular, its distribution in frequency. Assuming that the oscillator's position is coupled to a generalised force, $\delta\hat{F}_{\text{th}}(t)$, modelling the fluctuations of the environment degrees of freedom, the equation of motion of the oscillator is [121–124],

$$\frac{d^2\hat{x}}{dt^2} + \Gamma_m \frac{d\hat{x}}{dt} + \Omega_m^2 \hat{x} = \frac{\delta\hat{F}_{\text{th}}}{m}. \quad (2.2.27)$$

The damping rate, Γ_m , introduced here characterises the coupling between the oscillator and its thermal environment. The Fourier transform of the equation,

$$\hat{x}[\Omega] = \chi_x[\Omega] \delta\hat{F}_{\text{th}}[\Omega],$$

$$\text{where,} \quad \chi_x[\Omega] := [m(-\Omega^2 + \Omega_m^2 - i\Omega\Gamma_m)]^{-1},$$

determines the susceptibility, χ_x , that relates the thermal force to the position. The role of the thermal force $\delta\hat{F}_{\text{th}}$, is to maintain the oscillator in the thermal state $\hat{\rho}_m$ ^{2.18} (eq. (2.2.25)). The fluctuation-dissipation theorem (eq. (2.1.16)), essentially codifying this constraint, implies that,

$$\langle \delta\hat{F}_{\text{th}}(t) \delta\hat{F}_{\text{th}}(0) \rangle \approx 2\hbar m \Omega_m \Gamma_m \left(n_{m,\text{th}} + \frac{1}{2} \right) \delta(t)$$

$$\text{and,} \quad \bar{S}_{FF}^{\text{th}}[\Omega] \approx 2\hbar m \Omega_m \Gamma_m \left(n_{m,\text{th}} + \frac{1}{2} \right) \xrightarrow{k_B T \gg \hbar\Omega_m} 2m\Gamma_m k_B T.$$

^{2.18} It is worthwhile to point out that in fact, the equation of motion in eq. (2.2.27), is inconsistent with *any* legitimate quantum state when $k_B T \ll \hbar\Gamma_m$, or, $\hbar\Gamma_m \gtrsim \hbar\Omega_m$ [125–127]. Either regimes are irrelevant to this thesis.

The resulting spectral distribution of the variance in position, characterised by the symmetrised spectral density, takes the form,

$$\bar{S}_{xx}[\Omega] = |\chi_x[\Omega]|^2 \bar{S}_{FF}^{\text{th}}[\Omega] \approx \frac{4x_{\text{zp}}^2}{\Gamma_m} \frac{(\Omega_m \Gamma_m)^2}{(\Omega^2 - \Omega_m^2)^2 + (\Omega \Gamma_m)^2} \left(n_{\text{m,th}} + \frac{1}{2} \right). \quad (2.2.28)$$

It is straightforward to verify that,

$$\int_{-\infty}^{\infty} \bar{S}_{xx}[\Omega] \frac{d\Omega}{2\pi} = \text{Var}[\hat{x}],$$

confirming that the thermal force maintains the oscillator in a thermal equilibrium. Finally note that the spectral density corresponding to zero-point motion of the oscillator,

$$\bar{S}_{xx}^{\text{ZP}}[\Omega] := \bar{S}_{xx}[\Omega] |_{n_{\text{m,th}}=0},$$

achieved at zero temperature, exhibits a non-zero peak,

$$\bar{S}_{xx}^{\text{ZP}}[\Omega_m] = \frac{2x_{\text{zp}}^2}{\Gamma_m}. \quad (2.2.29)$$

An alternate description sheds light on the origin of the vacuum fluctuation component exhibited in the position fluctuation spectrum $\bar{S}_{xx}[\Omega]$. Applying the fluctuation-dissipation relation for the double-sided spectral density, exhibited in eq. (2.1.18), to the mechanical position:

$$\begin{aligned} S_{xx}[\Omega > 0] &= 2\hbar(n_{\text{m,th}} + 1) \text{Im} \chi_x[\Omega] \\ S_{xx}[\Omega < 0] &= 2\hbar n_{\text{m,th}} \text{Im} \chi_x[\Omega], \end{aligned}$$

where the second relation follows from using the detailed balanced condition (eq. (2.1.11)). The behaviour of $S_{xx}[\Omega]$ is determined by the poles of the imaginary part of the mechanical susceptibility $\text{Im} \chi_x$. The four poles,

$$\Omega_* = \pm \Omega_m \left[1 - \frac{\Gamma_m^2}{2\Omega_m^2} \mp i \frac{\Gamma_m}{\Omega_m} \left(1 - \frac{\Gamma_m^2}{4\Omega_m^2} \right)^{1/2} \right]^{1/2}$$

coalesce to the two poles,

$$\Omega_* \approx \pm \Omega_m - \frac{i\Gamma_m}{2},$$

one each on the left/right half planes, in the regime where $\Gamma_m \ll \Omega_m$. This high-Q approximation essentially amounts to assuming that the resonance at positive (negative) frequency is due to processes that are independent of those at the negative (positive) frequency. It must therefore be possible to introduce degrees of freedom that describe these processes, and which, owing to the first-order nature of the pole at either frequency, obeys a first order differential equation.

The creation/annihilation operators \hat{b}, \hat{b}^\dagger are precisely the required degrees of freedom. The equation of motion [128],

$$\frac{d\hat{b}}{dt} = - \left(i\Omega_m + \frac{\Gamma_m}{2} \right) \hat{b} + \sqrt{\Gamma_m} \delta \hat{b}_{\text{in}}(t), \quad (2.2.30)$$

and its hermitian conjugate, model the two poles $\Omega_* \approx \pm\Omega_m - \frac{i\Gamma_m}{2}$. The noise operator $\delta\hat{b}_{\text{in}}$, satisfying

$$\begin{aligned}\langle \delta\hat{b}_{\text{in}}^\dagger(t)\delta\hat{b}_{\text{in}}(0) \rangle &= n_{m,\text{th}}\delta(t) \\ \langle \delta\hat{b}_{\text{in}}(t)\delta\hat{b}_{\text{in}}^\dagger(0) \rangle &= (n_{m,\text{th}} + 1)\delta(t),\end{aligned}\tag{2.2.31}$$

models the thermal force due to the environment. Finally, since the two processes at positive and negative frequencies are independent, the double-sided spectrum of the position fluctuations, $\hat{x} = x_{\text{zp}}(\hat{b} + \hat{b}^\dagger)$, may be expressed as,

$$\begin{aligned}S_{xx}[\Omega] &= x_{\text{zp}}^2 (S_{b^\dagger b^\dagger}[\Omega] + S_{bb}[\Omega]) \\ &= \frac{4x_{\text{zp}}^2}{\Gamma_m} \left(\frac{(n_{m,\text{th}} + 1)(\Gamma_m/2)^2}{(\Omega_m + \Omega)^2 + (\Gamma_m/2)^2} + \frac{n_{m,\text{th}}(\Gamma_m/2)^2}{(\Omega_m - \Omega)^2 + (\Gamma_m/2)^2} \right),\end{aligned}$$

i.e. with no cross-correlations between the terms at positive and negative frequency. The formal definition of the spectra of the (non-hermitian) creation/annihilation operators may be used to interpret the term containing the vacuum contribution (proportional to $(n_{m,\text{th}} + 1)$) as arising from environmental processes that excite the oscillator, followed by a de-excitation, whereas the term devoid of vacuum fluctuation (proportional to $n_{m,\text{th}}$) as arising from processes that happen in reverse. Clearly, the oscillator, being quantized, cannot sustain a process where its vacuum state is annihilated. As a note of caution, note that the unsymmetrised spectrum $S_{xx}[\Omega]$ is not typically measured – the symmetrised spectrum, $\bar{S}_{xx}[\Omega]$, which can be measured, can no longer distinguish between the two processes (see eq. (2.2.28)) – chapter 4 deals with this subtlety.

2.2.2 Photons: description and detection

The experiments reported in this thesis demand a quantum mechanical description of the electromagnetic fields used to perform measurements. The purpose of this subsection is therefore to furnish the necessary formalism.

Quite generally [56], classical electromagnetic fields propagating along a direction, say z -axis, in a homogeneous isotropic linear medium is fully described by the Cartesian components of its transverse vector potential^{2.19}. Disregarding the choice of coordinates in the transverse plane (i.e. polarisation), and assuming a uniform transverse profile, the vector potential field $A(z, t)$ satisfies the property $A(z, t) = A(0, t - z/c)$, c being the velocity of propagation. It is therefore sufficient to consider the field just as a function of time, i.e. $A(t)$. Consequently, the quantised field is described by the operator in the Heisenberg picture [56],

$$\hat{A}(t) = \int_0^\infty \left(\frac{\hbar c}{A\epsilon_0\omega} \right)^{1/2} i \left(\hat{a}[\omega]e^{-i\omega t} - \hat{a}[\omega]^\dagger e^{i\omega t} \right) \frac{d\omega}{2\pi}, \quad (2.2.32)$$

together with the canonical commutation relations,

$$\left[\hat{a}[\omega], \hat{a}[\omega']^\dagger \right] = 2\pi \delta(\omega - \omega'), \quad (2.2.33)$$

with all other commutators vanishing. The electric field corresponding to eq. (2.2.32) is,

$$\hat{E}(t) = \int_0^\infty E_0(\omega) \left(\hat{a}[\omega]e^{-i\omega t} + \hat{a}[\omega]^\dagger e^{i\omega t} \right) \frac{d\omega}{2\pi}, \quad (2.2.34)$$

where $E_0(\omega) := \left(\frac{\hbar\omega}{A\epsilon_0 c} \right)^{1/2}$. Each propagating mode at frequency ω , consisting of a flux of photons at that frequency, is described by the operator $\hat{a}[\omega]$. The commutation relation eq. (2.2.33) implies that the excitations of each mode is a boson.

For a monochromatic field consisting of a carrier at frequency ω_ℓ , it is convenient to choose the ansatz,

$$\hat{a}[\omega] = 2\pi \bar{a} \delta(\omega - \omega_\ell) + \delta\hat{a}[\omega - \omega_\ell], \quad (2.2.35)$$

where $\delta\hat{a}[\omega - \omega_\ell]$ represent fluctuations around the carrier. The fundamental commutation relation eq. (2.2.33) precludes the possibility that $\delta\hat{a}[\omega] = 0$; thus the carrier cannot occur without associated operators to describe fluctuations around it. Considering field fluctuations in a frequency bandwidth 2Λ around ω_ℓ , i.e.

$$\omega \in (\omega_\ell - \Lambda, \omega_\ell + \Lambda),$$

eq. (2.2.34) may be expressed as,

$$\begin{aligned} \hat{E}(t) &= E_0(\omega_\ell) (\bar{a}e^{-i\omega_\ell t} + \bar{a}^*e^{i\omega_\ell t}) + \int_{\omega_\ell - \Lambda}^{\omega_\ell + \Lambda} E_0(\omega) \left(\delta\hat{a}[\omega - \omega_\ell]e^{-i\omega t} + \delta\hat{a}[\omega - \omega_\ell]^\dagger e^{i\omega t} \right) \frac{d\omega}{2\pi} \\ &= E_0(\omega_\ell) (\bar{a}e^{-i\omega_\ell t} + \bar{a}^*e^{i\omega_\ell t}) + \int_{-\Lambda}^{+\Lambda} E_0(\Omega + \omega_\ell) \left(\delta\hat{a}[\Omega]e^{-i(\Omega + \omega_\ell)t} + \delta\hat{a}[\Omega]^\dagger e^{i(\Omega + \omega_\ell)t} \right) \frac{d\Omega}{2\pi}; \end{aligned}$$

^{2.19} The electric and magnetic fields are not independent degrees of freedom of the electromagnetic field – this has to do with the two Gauss laws that constrain them. The scalar and vector potentials, on the other hand, do provide the necessary degrees of freedom. The constraint imposed by Gauss laws are identically satisfied by the vector potential, and fixes the scalar potential. Of the remaining degrees of freedom – the components of the vector potential – choice of gauge leaves two components free. These are the transverse components of the vector potential. See [56] for details.

here $\Omega = \omega - \omega_\ell$ denotes the frequency shift from the carrier. Typical optical signals that are detected are at frequencies $\Omega \ll \omega_\ell$; in this case, firstly $E_0(\Omega + \omega_\ell) = E_0(\omega_\ell)\sqrt{1 + \Omega/\omega_\ell} \approx E_0(\omega_\ell)$, and secondly, the formal limit $\Lambda \rightarrow \infty$ may be taken. In this case,

$$\frac{\hat{E}(t)}{E_0(\omega_\ell)} \approx \left(\bar{a} + \int_{-\infty}^{+\infty} \delta\hat{a}[\Omega] e^{-i\Omega t} \frac{d\Omega}{2\pi} \right) e^{-i\omega_\ell t} + \left(\bar{a}^* + \int_{-\infty}^{+\infty} \delta\hat{a}[\Omega]^\dagger e^{i\Omega t} \frac{d\Omega}{2\pi} \right) e^{i\omega_\ell t},$$

where, the fluctuations about the carrier $\delta\hat{a}[\Omega]$ may be identified as the (double-sided) Fourier transform of a time-domain operator $\delta\hat{a}(t)$ that varies slowly compared to ω_ℓ . The assumptions that lead up to the above expression therefore defines the situation where an elaborate multi-mode description of the electromagnetic field becomes equivalent to a single time-varying mode,

$$\hat{a}(t) = (\bar{a} + \delta\hat{a}(t)) e^{-i\omega_\ell t}, \quad (2.2.36)$$

with fluctuations at frequencies $\Omega \ll \omega_\ell$ around a carrier. The operator $\hat{a}(t)$ describes the amplitude of the photon flux per unit time. The commutation relations eq. (2.2.33) for the field (at optical frequencies) implies that the operator $\delta\hat{a}[\Omega]$ (representing fluctuations at much lower frequencies) satisfies^{2,20},

$$\begin{aligned} [\delta\hat{a}[\Omega], \delta\hat{a}[\Omega']^\dagger] &= 2\pi\delta(\Omega - \Omega') \\ \Rightarrow [\delta\hat{a}(t), \delta\hat{a}(t')^\dagger] &= \delta(t - t'). \end{aligned}$$

In place of these creation/annihilation operators, hermitian quadrature operators may be introduced,

$$\begin{aligned} \delta\hat{q} &:= \frac{1}{\sqrt{2}} (\delta\hat{a}(t) + \delta\hat{a}(t)^\dagger) \\ \delta\hat{p} &:= \frac{1}{i\sqrt{2}} (\delta\hat{a}(t) - \delta\hat{a}(t)^\dagger), \end{aligned} \quad (2.2.37)$$

that satisfy,

$$[\delta\hat{q}(t), \delta\hat{p}(t')] = i\delta(t - t'), \quad (2.2.38)$$

in terms of which, eq. (2.2.36) takes the form,

$$\hat{a}(t) = \left(\bar{a} + \frac{\delta\hat{q}(t)}{\sqrt{2}} + i\frac{\delta\hat{p}(t)}{\sqrt{2}} \right) e^{-i\omega_\ell t} \quad (2.2.39)$$

2.2.2.1 Statistics of optical fluctuations

The behaviour of the optical field in eq. (2.2.34) is specified through the state of the field at each mode at frequency^{2,21} ω . In fact, the ansatz in eq. (2.2.35), describing the separation of

^{2,20} These commutation relations are in fact approximate, with corrections of order Ω/ω_ℓ that come from the equality $\frac{E_0(\Omega+\omega_\ell)}{E_0(\omega_\ell)} = (1 + \Omega/\omega_\ell)^{1/2}$ [129]

^{2,21} Since each mode is independent, as indicated by the commutator eq. (2.2.33), the states of the field live in a Hilbert space that is formed by an infinite continuous tensor product space $\otimes_\omega \mathcal{H}_\omega$, one for each mode. Such objects may be dealt with using the normal rules of Hilbert spaces (i.e. by using the rules applicable to a denumerable tensor product), if there exists a state $|0\rangle$ such that $\int d\omega \hat{a}[\omega]^\dagger \delta\hat{a}[\omega]|0\rangle = 0$ [130]. This state, the *vacuum* state, will henceforth be assumed to exist.

the field into a monochromatic carrier with vacuum fluctuations around it, corresponds to a coherent excitation with complex amplitude \bar{a} at the carrier frequency ω_ℓ ,

$$|\bar{a}\rangle = \exp\left(\bar{a}\hat{a}[\omega_\ell]^\dagger - \bar{a}^*\hat{a}[\omega_\ell]\right)|0\rangle, \quad (2.2.40)$$

the so-called coherent state [131, 132].

However, the description of realistic laboratory fields demands a description of fluctuations in excess of the vacuum at sideband frequencies Ω . In the single-mode approximation leading up to eq. (2.2.36), this means that the operator $\delta\hat{a}(t)$ (or equivalently, $\delta\hat{q}(t), \delta\hat{p}(t)$) may contain classical fluctuations in addition to the intrinsic vacuum, moreover these classical fluctuations could be unequally distributed among the quadratures. In the presence of an accurate knowledge of the source emitting the field, a precise single-mode state may be computed to describe the necessary statistical quantities to describe these fluctuations. However such knowledge is generally cumbersome to obtain^{2.22}; a model is therefore described here that is able to capture the measured fluctuations of sources with the statistical properties of the quadratures.

The detection schemes employed in this thesis (described in section 2.2.2.2) are capable of measuring any desired quadrature of the optical field (eq. (2.2.37)). However, being states with a large coherent amplitude, the two-time correlators of the quadratures contain almost all of the information carried by the state. Thus focus is limited to,

$$\begin{pmatrix} S_{qq}(t) & S_{qp}(t) \\ S_{pq}(t) & S_{pp}(t) \end{pmatrix} := \begin{pmatrix} \langle \delta\hat{q}(t)\delta\hat{q}(0) \rangle & \langle \delta\hat{q}(t)\delta\hat{p}(0) \rangle \\ \langle \delta\hat{p}(t)\delta\hat{q}(0) \rangle & \langle \delta\hat{p}(t)\delta\hat{p}(0) \rangle \end{pmatrix}, \quad (2.2.41)$$

where S_{qq}, S_{pp} are real due to the hermiticity of the quadratures.

It proves useful to separate out from these correlators, contributions that arise purely from a quantum mechanical origin. For example, the commutation relation eq. (2.2.38) implies that,

$$S_{qp}(t) - S_{pq}(t) = i\delta(t).$$

This constraint is identically satisfied by the choice,

$$\begin{aligned} S_{qp}(t) &= \frac{+i}{2}\delta(t) + C_{qp}(t) \\ S_{pq}(t) &= \frac{-i}{2}\delta(t) + C_{qp}(t), \end{aligned}$$

for some function C_{qp} ; computing the symmetrised correlation shows that in fact $C_{qp}(t) = \bar{S}_{qp}(t)$. In a similar vein, the ideal field state – the coherent state eq. (2.2.40) – consisting of vacuum fluctuations at all sideband frequencies has the property $S_{qq}(t) = \frac{1}{2}\delta(t) = S_{pp}(t)$; choosing an ansatz that separates out this vacuum noise power is useful, viz.,

$$\begin{aligned} S_{qq}(t) &= \frac{1}{2}\delta(t) + C_{qq}(t) \\ S_{pp}(t) &= \frac{1}{2}\delta(t) + C_{pp}(t). \end{aligned}$$

^{2.22} For example, even when the source is an ideal laser, the coherent state written above is only an approximation of the emitted state [133, 134].

Thus, eq. (2.2.41) take the form,

$$\begin{pmatrix} \langle \delta \hat{q}(t) \delta \hat{q}(0) \rangle & \langle \delta \hat{q}(t) \delta \hat{p}(0) \rangle \\ \langle \delta \hat{p}(t) \delta \hat{q}(0) \rangle & \langle \delta \hat{p}(t) \delta \hat{p}(0) \rangle \end{pmatrix} = \begin{pmatrix} \frac{1}{2} & \frac{i}{2} \\ \frac{-i}{2} & \frac{1}{2} \end{pmatrix} \delta(t) + \begin{pmatrix} C_{qq}(t) & C_{qp}(t) \\ C_{qp}(t) & C_{pp}(t) \end{pmatrix}, \quad (2.2.42)$$

$$\text{so that, } \bar{S}_{qq}[\Omega] = \frac{1}{2} + C_{qq}[\Omega], \quad \bar{S}_{qp}[\Omega] = C_{qp}[\Omega], \quad \bar{S}_{pp}[\Omega] = \frac{1}{2} + C_{pp}[\Omega].$$

This ansatz need not necessarily be physical, i.e., the two-time correlators need not necessarily arise as expectation values over a quantum state.

Proposition 5. *The necessary condition for the ansatz in eq. (2.2.42) to be physical is that the quadrature spectra, $\bar{S}_{qq}, \bar{S}_{qp}, \bar{S}_{pp}$ satisfy the spectral uncertainty principle eq. (2.1.23), i.e.*

$$\bar{S}_{qq}[\Omega] \bar{S}_{pp}[\Omega] - \bar{S}_{qp}^2[\Omega] \geq \frac{1}{4}, \quad (2.2.43)$$

implying that the classical noise correlators at each frequency satisfy,

$$C_{qp} \leq \left(C_{qq} C_{pp} + (C_{qq} C_{pp})^{1/2} \right)^{1/2} \lesssim \begin{cases} (C_{qq} C_{pp})^{1/2}; & C_{qq} C_{pp} \gg 1 \\ (C_{qq} C_{pp})^{1/4}; & C_{qq} C_{pp} \ll 1 \end{cases} \quad (2.2.44)$$

Proof. Refer [135] for a proof of the fact that eq. (2.2.43) is the necessary condition. Substituting the expressions for \bar{S}_{ij} in terms of C_{ij} ($i, j = q, p$) in eq. (2.2.42) gives,

$$C_{qp}^2 \leq C_{qq} C_{pp} + \frac{1}{2} (C_{qq} + C_{pp}) \leq C_{qq} C_{pp} + \sqrt{C_{qq} C_{pp}},$$

where the second bound is tighter, and follows from the arithmetic-geometric mean inequality, $C_{qq} + C_{pp} \geq 2\sqrt{C_{qq} C_{pp}}$ (see footnote 2.3, on page 32). When $C_{qq} C_{pp} \ll 1$, of the two terms on the right-hand side, one dominates, i.e. $\sqrt{C_{qq} C_{pp}} \gg C_{qq} C_{pp}$; and vice versa. \square

Relation between quadrature fluctuations and amplitude/phase fluctuations

The classical description of a fluctuating electromagnetic field proceeds by identifying two variables that characterise the field at each time: amplitude and phase. The fluctuations in the field are described by elevating the amplitude and phase to classical stochastic processes [136]. Quantum mechanically however, it is not possible to consistently define hermitian operators corresponding to the classical concepts of amplitude and phase^{2.23} [138]. However, small fluctuations in the amplitude and phase of the photon flux amplitude operator $\hat{a}(t)$ may be put in one-to-one correspondence with the quadratures $\delta \hat{q}, \delta \hat{p}$.

For a field with coherent amplitude \bar{a} at frequency ω_ℓ and vacuum fluctuations $\delta \hat{a}_{\text{vac}}$ elsewhere, additional amplitude, $\delta \alpha(t)$ and phase $\delta \phi(t)$ fluctuations may be phenomenologically

^{2.23} Following classical intuition, one expects to be able to perform a polar decomposition of the operator \hat{a} , in the form, $\sqrt{\hat{N}} e^{i\hat{\Phi}}$, with $\sqrt{\hat{N}}, \hat{\Phi}$ hermitian, and thence identify these as respectively the amplitude and phase of the field. Ideally, \hat{N} is also interpreted as the number operator. The essential impediment in achieving this goal is that in infinite dimensional Hilbert spaces, polar decompositions may not be performed consistently [137].

introduced via the ansatz,

$$\begin{aligned}
 \hat{a}(t) &= (|\bar{a}| + \delta\alpha(t) + \delta\hat{a}_{\text{vac}}(t))e^{-i\omega_\ell t + i\delta\phi(t)} \\
 &\approx (|\bar{a}| + \delta\alpha(t) + \delta\hat{a}_{\text{vac}}(t)) (1 + i\delta\phi(t)) e^{-i\omega_\ell t} \\
 &\approx \left((|\bar{a}| + \left(\delta\alpha(t) + \frac{\delta\hat{q}_{\text{vac}}(t)}{\sqrt{2}} \right)) + i \left(|\bar{a}| \delta\phi(t) + \frac{\delta\hat{p}_{\text{vac}}(t)}{\sqrt{2}} \right) \right) e^{-i\omega_\ell t}.
 \end{aligned} \tag{2.2.45}$$

Comparing with eq. (2.2.39),

$$\begin{aligned}
 \delta\hat{q}(t) &= \sqrt{2} \delta\alpha(t) + \delta\hat{q}_{\text{vac}}(t) \\
 \delta\hat{p}(t) &= \sqrt{2 \langle \hat{n} \rangle} \delta\phi(t) + \delta\hat{p}_{\text{vac}}(t).
 \end{aligned}$$

Here, we have used the relation between the mean amplitude \bar{a} the average photon flux, $\langle \hat{n} \rangle := \hat{a}^\dagger \hat{a} \approx |\bar{a}|^2$. These relations suggest the nomenclature, “amplitude” (for $\delta\hat{q}$) and “phase” (for $\delta\hat{p}$) quadratures. In fact, the second equality suggests the definition of a phase operator [69],

$$\delta\hat{\phi} := \frac{\delta\hat{p}}{\sqrt{2 \langle \hat{n} \rangle}}. \tag{2.2.46}$$

that is meaningful for a large class of states. Similarly, the fluctuations in the photon flux, $\delta\hat{n} := \hat{n} - \langle \hat{n} \rangle$, is given by,

$$\delta\hat{n} = \sqrt{2 \langle \hat{n} \rangle} \delta\hat{q}. \tag{2.2.47}$$

The uncertainty relation for the quadratures \hat{q}, \hat{p} in eq. (2.2.43), together with the definition of the number and phase operators eqs. (2.2.46) and (2.2.47), imply the number flux-phase uncertainty relation,

$$\bar{S}_{nn}[\Omega] \bar{S}_{\phi\phi}[\Omega] \geq \frac{1}{4}, \tag{2.2.48}$$

for a propagating electromagnetic field. This uncertainty relation will be seen to play a central role in enforcing the standard quantum limit for interferometric position measurements as discussed in section 2.3.

2.2.2.2 Detection of amplitude quadrature: photodetection

Since this thesis is concerned with electromagnetic fields at optical frequencies ($\omega_\ell \approx 2\pi \cdot 400 \text{ THz}$), the focus of this, and the following two, sections will be the various detection strategies commonly employed for such radiation.

A convenient and common way to detect a propagating optical field, described by the amplitude flux operator $\hat{a}(t)$ (as in eq. (2.2.36)) is to couple it to a detector which absorbs a photon and emits an electron, via the photoelectric effect. The current thus produced – photocurrent – is described by a hermitian operator $\hat{I}(t)$.

Real photodetectors unfortunately do not produce an electron for every photon that is incident. The *quantum efficiency* of the detection process $\eta \leq 1$ may be modelled as transmission through a lossy channel of transmissivity η , followed by an ideal photodetector. A passive lossy

channel that has the appropriate classical limit is offered by a beam-splitter of transmissivity η , whose transmission [139]

$$\hat{a}_\eta(t) = \sqrt{\eta} \hat{a}(t) + i\sqrt{1-\eta} \delta\hat{a}_0(t), \quad (2.2.49)$$

consists of the field to be detected $\hat{a}(t) = (\bar{a} + \delta\hat{a}(t))e^{-i\omega_\ell t}$ as in eq. (2.2.36), and the vacuum fluctuations $\delta\hat{a}_0$ in the other input. On general grounds, without delving into the details of the photoelectric effect [140], it is true that the photocurrent operator is given by^{2.24},

$$\hat{I}(t) = q_e \hat{n}_\eta(t) = \mathcal{R} \hat{P}_\eta(t) \quad (2.2.50)$$

where q_e is the electron charge, the *responsivity* of the detector is,

$$\mathcal{R} = \frac{q_e}{\hbar\omega_\ell} = \frac{q_e\lambda_\ell}{hc} \approx (0.63 \text{ A/W}) \left(\frac{\lambda_\ell}{780 \text{ nm}} \right), \quad (2.2.51)$$

and the operator corresponding to the incident photon flux is,

$$\hat{n}_\eta = \hat{a}_\eta^\dagger(t)\hat{a}_\eta(t) \approx |\bar{a}| \eta \left(|\bar{a}| + \sqrt{2} \delta\hat{q}(t) \right) + |\bar{a}| \sqrt{2\eta(1-\eta)} \delta\hat{p}_0. \quad (2.2.52)$$

Here, $\delta\hat{q}$ ($\delta\hat{p}_0$) is the signal (vacuum) amplitude (phase) quadrature fluctuation. The second approximate equality is obtained by omitting terms second order in fluctuations. In eq. (2.2.50), $\hat{P}_\eta := \hbar\omega_\ell \hat{n}_\eta$, is the operator describing the incident optical power. From eq. (2.2.52), the mean photon flux and the fluctuation in the incident photon flux, are respectively,

$$\begin{aligned} \langle \hat{n}_\eta(t) \rangle &= \eta |\bar{a}|^2 \\ \delta\hat{n}_\eta(t) &:= \hat{n}_\eta(t) - \langle \hat{n}_\eta(t) \rangle = \sqrt{2} |\bar{a}| \left(\eta \delta\hat{q}(t) + \sqrt{\eta(1-\eta)} \delta\hat{p}_0(t) \right). \end{aligned}$$

Since the photocurrent is directly related to the incident photon flux, via eq. (2.2.50),

$$\begin{aligned} \langle \hat{I}(t) \rangle &= \eta q_e |\bar{a}|^2 = \eta \mathcal{R} \hat{P}(t) \\ \delta\hat{I}(t) &= \sqrt{2} q_e |\bar{a}| \left(\eta \delta\hat{q}(t) + \sqrt{\eta(1-\eta)} \delta\hat{p}_0(t) \right), \end{aligned}$$

where $P(t) = \hbar\omega_\ell \langle \hat{a}^\dagger(t)\hat{a}(t) \rangle$ is the power measured without taking into account the losses of the photodetector. Note that the photocurrent is a continuous observable, in the sense of eq. (2.1.19), i.e. $[\delta\hat{I}(t), \delta\hat{I}(t')] = 0$; when illuminated by a large coherent field, photodetectors perform linear measurements on the amplitude quadrature of the incident field.

The (double-sided) spectral density of the photocurrent is therefore,

$$\bar{S}_{II}[\Omega] = 2q_e^2 |\bar{a}|^2 \left(\eta^2 \bar{S}_{qq}[\Omega] + \eta(1-\eta) \bar{S}_{pp}^0[\Omega] \right)$$

^{2.24} An argument due to Glauber [141] goes as follows: the state of the optical field $|\psi\rangle$ that arrives at the detector, undergoes the transformation $|\psi\rangle \rightarrow \hat{a}|\psi\rangle$, corresponding to the absorption of a photon by the detector; the probability that this happens is proportional to the norm $\|\hat{a}|\psi\rangle\| = \langle \psi|\hat{a}^\dagger\hat{a}|\psi\rangle = \langle \hat{n} \rangle$; finally, the photocurrent operator describes the probability of this process, referred to an electron flux. This heuristic argument can be put on rigorous foundation by analysing the state transformation as a quantum jump process [142].

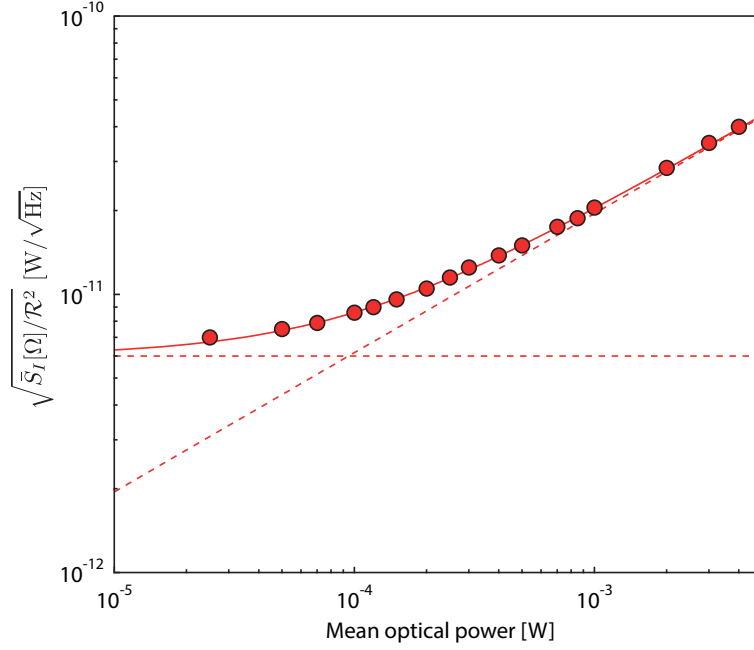


Fig. 2.2 – **Input-referred photocurrent noise.** Measured photocurrent noise at a Fourier frequency $\Omega = 2\pi \cdot 5$ MHz from the optical carrier, referred back to optical power fluctuations. The detector used here is a NewFocus 1801. Below input powers of $\langle P \rangle < 100 \mu\text{W}$, the detector NEP is the dominant source of noise, while above that power, optical shot noise begins to dominate. Solid line shows fit to the model in eq. (2.2.54); dashed lines show detector and shot noise components of the model. Fit enables inference of $\eta \approx 0.78$.

A further approximation may be made at this point. The typical case for photodetection (relevant to this thesis) is where the incident field quadrature carries a signal atop its vacuum fluctuations, viz.

$$\delta\hat{q}(t) = \delta\hat{q}_{\text{vac}}(t) + \delta\hat{q}_{\text{sig}}(t),$$

with the additional assumption that the signal and vacuum are uncorrelated^{2.25}. In this case, $\bar{S}_{qq}[\Omega] = \bar{S}_{qq}^{\text{vac}}[\Omega] + \bar{S}_{qq}^{\text{sig}}[\Omega]$, and further, $\bar{S}_{pp}^0[\Omega] = \frac{1}{2} = \bar{S}_{qq}^{\text{vac}}[\Omega]$; this results in the (single-sided) photocurrent spectrum,

$$\bar{S}_I[\Omega] = 2\eta q_e^2 |\bar{a}|^2 \left(1 + \frac{\eta}{2} \bar{S}_q^{\text{sig}}[\Omega]\right). \quad (2.2.53)$$

The spectral content of the signal rides on a background,

$$\bar{S}_I^{\text{shot}}[\Omega] = 2\eta q_e^2 |\bar{a}|^2 = 2q_e \langle I(t) \rangle = 2q_e \cdot \eta \mathcal{R}P,$$

the amplified vacuum fluctuations of the incident optical field^{2.26}, with the signal-to-noise determined by the overall detection efficiency.

Realistic photodetectors have an additional source of output noise, originating from thermal noise in the electronics, that determines the smallest optical power fluctuation that can be

^{2.25} This assumption fails when the incident field has amplitude squeezing – strong correlations between the signal in the amplitude quadrature and the amplitude vacuum fluctuations, in which case, the photocurrent spectrum in eq. (2.2.53) would contain a term due to the correlation between the signal and vacuum.

^{2.26} The latter expression, in terms of the average photocurrent, may be derived by assuming that the ejected photoelectrons are discrete [143]; this semi-classical interpretation dispenses with the need to attribute any quantum-mechanical character to photodetector shot noise, at least when illuminated by coherent states of the optical field.

detected. This, the noise equivalent power (NEP) of the detector, $\bar{S}_P^{\text{NE}}[\Omega]$, leads to a detector noise contribution in the photocurrent spectrum,

$$\bar{S}_I^{\text{det}}[\Omega] = \mathcal{R}^2 \cdot \bar{S}_P^{\text{NE}}[\Omega],$$

giving the expression for the photocurrent spectrum of a realistic photodetector, viz.,

$$\bar{S}_I[\Omega] = \underbrace{\mathcal{R}^2 \bar{S}_P^{\text{NE}}[\Omega]}_{\bar{S}_I^{\text{det}}} + \underbrace{2\eta \cdot q_e \mathcal{R} \cdot P}_{\bar{S}_I^{\text{shot}}} + \underbrace{\eta^2 q_e \mathcal{R} P \bar{S}_q^{\text{sig}}[\Omega]}_{\bar{S}_I^{\text{sig}}}. \quad (2.2.54)$$

As the expression suggests, once the detector noise is overwhelmed by shot noise, the signal-to-noise has converged to its maximal possible, for given optical power. Figure 2.2 shows a measurement of the detector noise and shot noise contributions for a photodetector (NewFocus 1801) widely employed in this thesis. The fits to the shot noise and detector noise model, eq. (2.2.54), enables extraction of the total quantum efficiency, $\eta \approx 0.78$, consistent with typical quantum efficiencies of $\eta \approx 0.8$ for silicon detectors [144].

2.2.2.3 Detection of an arbitrary quadrature: homodyne

Direct photodetection, having no reference for the phase of the incident field, measures the fluctuations in the amplitude quadrature $\delta\hat{q}$. Other, general quadratures of the form,

$$\delta\hat{q}^\theta(t) := \delta\hat{q}(t) \cos \theta + \delta\hat{p}(t) \sin \theta = \frac{1}{\sqrt{2}} \left(\delta\hat{a}(t) e^{-i\theta} + \delta\hat{a}^\dagger(t) e^{i\theta} \right), \quad (2.2.55)$$

furnish continuous observables of interest. From the commutation relation (implied by eq. (2.2.55) and eq. (2.2.38)),

$$\left[\delta\hat{q}^\theta(t), \delta\hat{q}^{\theta'}(t') \right] = i\delta(t - t') \sin(\theta - \theta'), \quad (2.2.56)$$

it is clear that any quadrature $\delta\hat{q}^\theta(t)$ is a continuous observable (the case $\theta = \theta'$), while pairs of quadratures $\delta\hat{q}^\theta(t), \delta\hat{q}^{\theta+\frac{\pi}{2}}(t)$ are canonically conjugate (the case $\theta = \theta' + \frac{\pi}{2}$). A homodyne detector measures the former; while a heterodyne detector attempts to measure the conjugate observables simultaneously. Both these techniques [145, 146] have been widely employed to characterise quantum states of optical fields [147], and for precision measurements [148].

Figure 2.3a shows a typical balanced homodyne detector. A local oscillator (LO) and signal field impinge on a balanced (i.e. transmissivity $\eta_t = 0.5$ ideally) beam-splitter such that their transverse mode profiles overlap in both output arms. The output fields [139],

$$\begin{pmatrix} \hat{a}_+ \\ \hat{a}_- \end{pmatrix} = \begin{pmatrix} \sqrt{\eta_t} & i\sqrt{1-\eta_t} \\ i\sqrt{1-\eta_t} & \sqrt{\eta_t} \end{pmatrix} \begin{pmatrix} \hat{a}_{\text{sig}} \\ \hat{a}_{\text{LO}} \end{pmatrix}, \quad (2.2.57)$$

are directed onto identical independent photodetectors. The respective photocurrents, $\hat{I}_\pm(t) = q_e \hat{a}_\pm^\dagger(t) \hat{a}_\pm(t)$, are subtracted to obtain the homodyne signal,

$$\begin{aligned} \hat{I}_{\text{hom}}(t) = \hat{I}_+(t) - \hat{I}_-(t) = q_e(1 - 2\eta_t) (\hat{n}_{\text{LO}}(t) - \hat{n}_{\text{sig}}(t)) + \\ 2q_e \sqrt{\eta_t(1 - \eta_t)} i \left(\hat{a}_{\text{sig}}^\dagger(t) \hat{a}_{\text{LO}}(t) - \hat{a}_{\text{LO}}^\dagger(t) \hat{a}_{\text{sig}}(t) \right), \end{aligned} \quad (2.2.58)$$

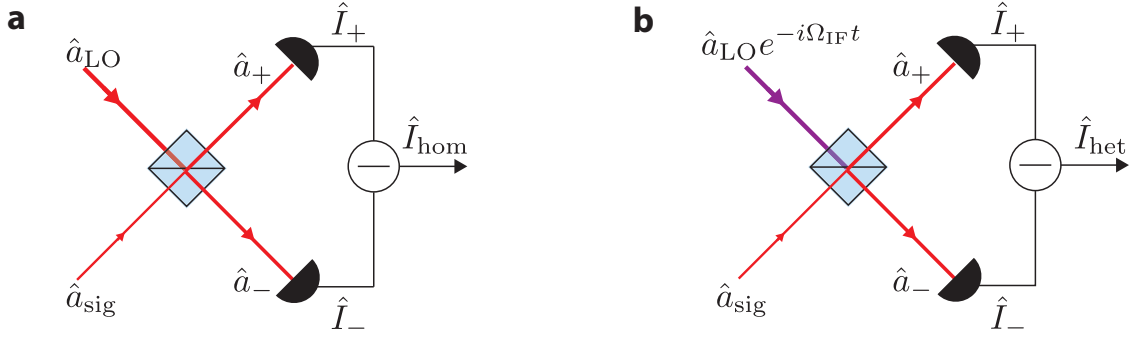


Fig. 2.3 – **Balanced homodyne and heterodyne detectors.** (a) A strong local oscillator field (LO) overlaps with a (weaker) signal beam on a balanced beam-splitter. The resulting output fields are directed onto independent photodetectors. Their difference photocurrent is the homodyne signal. (b) Compared to a homodyne detector, the LO is frequency shifted with respect to the signal by Ω_{IF} .

where $\hat{n}_{LO(sig)}(t) = \hat{a}_{LO(sig)}^\dagger(t)\hat{a}_{LO(sig)}(t)$ is the LO (signal) photon flux. The expression for the homodyne photocurrent may be linearised under the assumption that both the LO and signal are coherent. Their amplitudes are then of the form (see eq. (2.2.36)),

$$\hat{a}_{LO(sig)} = \left(\sqrt{\langle \hat{n}_{LO(sig)} \rangle} + \delta \hat{a}_{LO(sig)}(t) \right) e^{-i(\omega_\ell t + \theta_{LO(sig)})}, \quad (2.2.59)$$

where, the mean amplitude is expressed in terms of the mean photon flux, and $\theta_{LO(sig)}$ are the mean phases of the LO and signal. The mean of the photocurrent eq. (2.2.58) takes the form,

$$\langle \hat{I}_{hom}(t) \rangle \approx q_e(1 - 2\eta_t) (\langle \hat{n}_{LO} \rangle - \langle \hat{n}_{sig} \rangle) - q_e \sqrt{2\eta_t(1 - \eta_t)} \sqrt{4 \langle \hat{n}_{LO} \rangle \langle \hat{n}_{sig} \rangle} \sin \theta_{hom} \quad (2.2.60)$$

while its fluctuation part is given by,

$$\begin{aligned} \delta \hat{I}_{hom}(t) \approx & q_e(1 - 2\eta_t) \left(\sqrt{2 \langle \hat{n}_{LO} \rangle} \delta \hat{q}_{LO}^0 - \sqrt{2 \langle \hat{n}_{sig} \rangle} \delta \hat{q}_{sig}^0 \right) \\ & q_e \sqrt{2\eta_t(1 - \eta_t)} \left(\sqrt{2 \langle \hat{n}_{LO} \rangle} \delta \hat{q}_{sig}^{\theta_{hom} + \pi/2} + \sqrt{2 \langle \hat{n}_{sig} \rangle} \delta \hat{q}_{LO}^{-\theta_{hom} - \pi/2} \right), \end{aligned} \quad (2.2.61)$$

where,

$$\theta_{hom} := \theta_{sig} - \theta_{LO},$$

is the mean phase difference between the signal and LO fields at the combining beam-splitter.

The fluctuating part eq. (2.2.61) suggests that the homodyne detector measures a combination of the LO and signal quadratures at various angles. The signal quadrature $\delta \hat{q}_{sig}^{\theta_{hom} + \pi/2}$ may be singled out by employing a configuration where: (1) the LO is much more powerful than the signal, i.e. $\langle \hat{n}_{LO} \rangle \gg \langle \hat{n}_{sig} \rangle$, and, (2) by balancing the combining beam-splitter, i.e. $\eta_t = \frac{1}{2}$. The latter offers the additional technical advantage that excess classical noise in the strong LO (first term in $\delta \hat{I}_{hom}$ in eq. (2.2.61)) is cancelled [149]. In fact, under these two assumptions, eq. (2.2.60) and eq. (2.2.61) simplify to,

$$\begin{aligned} \langle \hat{I}_{hom}(t) \rangle & \approx -2q_e \sqrt{\langle \hat{n}_{LO} \rangle \langle \hat{n}_{sig} \rangle} \sin \theta_{hom} \\ \delta \hat{I}_{hom}(t) & \approx q_e \sqrt{2 \langle \hat{n}_{LO} \rangle} \cdot \delta \hat{q}_{sig}^{\theta_{hom} + \pi/2}(t), \end{aligned}$$

so that the homodyne photocurrent, by being proportional to the single signal quadrature $\delta\hat{q}_{\text{sig}}^{\theta_{\text{hom}}+\pi/2}$, is a continuous observable providing a linear measurement of the same quadrature.

Following manipulations similar to the ones followed for the analysis of photodetection (leading up to eq. (2.2.54)), the spectrum of the homodyne photocurrent is,

$$\bar{S}_I^{\text{hom}}[\Omega] = \underbrace{\mathcal{R}^2 \bar{S}_P^{\text{NE}}[\Omega]}_{\bar{S}_I^{\text{hom,det}}} + \underbrace{2\eta \cdot q_e \mathcal{R} \cdot P_{\text{LO}}}_{\bar{S}_I^{\text{hom,shot}}} + \underbrace{2\eta^2 q_e \mathcal{R} P_{\text{LO}} \bar{S}_{q_{\theta_{\text{hom}}+\pi/2}}^{\text{sig}}[\Omega]}_{\bar{S}_I^{\text{hom,sig}}}, \quad (2.2.62)$$

where η is the detection efficiency. Note that the homodyne shot noise may be conveniently interpreted as the vacuum fluctuations of the signal field amplified by the coherent LO.

Since direct photodetection samples the amplitude quadrature $\delta\hat{q}$, conventionally, homodyne detectors are employed to sample the phase quadrature $\delta\hat{p}$. In this case (requiring that $\theta_{\text{hom}} = 0$), the relation between the phase quadrature and the phase fluctuation eq. (2.2.46), implies that the homodyne photocurrent spectrum may be expressed as a measurement of the signal phase noise spectrum (omitting the detector noise contribution),

$$\bar{S}_I^{\text{hom}}[\Omega]|_{\theta_{\text{hom}}=0} = 2\eta \cdot q_e \mathcal{R} \cdot P_{\text{LO}} + 4\eta^2 \mathcal{R}^2 P_{\text{LO}} P_{\text{sig}} \bar{S}_{\phi\phi}^{\text{sig}}[\Omega].$$

Note that the role of the strong LO is to amplify the signal vacuum fluctuations above the detector noise – once this is achieved, the signal-to-noise ratio for phase detection is independent of LO power. In this case, the amplified signal vacuum referred as a phase noise spectrum, i.e.

$$\bar{S}_I^{\text{hom}}[\Omega]|_{\theta_{\text{hom}}=0} = 4\eta^2 \mathcal{R}^2 \langle P_{\text{LO}} \rangle \langle P_{\text{sig}} \rangle \left(\bar{S}_{\phi\phi}^{\text{sig}}[\Omega] + \frac{q_e}{2\eta \mathcal{R} \langle P_{\text{sig}} \rangle} \right),$$

gives the imprecision in the homodyne detection of phase fluctuations, viz.

$$\bar{S}_{\phi\phi}^{\text{hom,imp}}[\Omega] = \frac{1}{2\eta} \frac{\hbar\omega_\ell}{\langle P_{\text{sig}} \rangle};$$

hence the colloquialism: “phase shot-noise is inversely proportional to signal power”.

Design and operation of a realistic homodyne detector

Irrespective of the quadrature being measured, the primary experimental challenge of operating a homodyne detector is to maintain a stable and constant phase θ_{hom} , between the signal and LO fields^{2.27}. The strategy employed in this thesis to attain this is detailed subsequently.

^{2.27} Another technical challenge is the ability to realise $\eta = \frac{1}{2}$ perfectly; any deviation leads to imperfect cancellation of LO excess noise (see eq. (2.2.61), and discussion below it). Assuming that $\langle \hat{n}_{\text{LO}} \rangle \gg \langle \hat{n}_{\text{sig}} \rangle$ (typically, $\langle \hat{n}_{\text{LO}} \rangle \gtrsim 100 \cdot \langle \hat{n}_{\text{sig}} \rangle$, in this thesis), eq. (2.2.61) implies that the signal quadrature imprecision from imperfect LO noise cancellation is,

$$\bar{S}_{q_{\theta_{\text{hom}}+\pi/2}}^{\text{sig,imp}}[\Omega] = \frac{(1-2\eta_t)^2}{2\eta_t(1-\eta_t)} \bar{S}_q^{\text{LO}}[\Omega] \approx 8(\eta_t - \frac{1}{2})^2 \bar{S}_q^{\text{LO}}[\Omega].$$

Our design enables $\eta_t = 0.5 \pm 0.05$; combined with the large Fourier frequencies we work at (a few MHz), where the LO can be shot-noise limited up to $\langle P_{\text{LO}} \rangle = 1 - 2 \text{ mW}$, this source of homodyne imprecision is negligible [150].

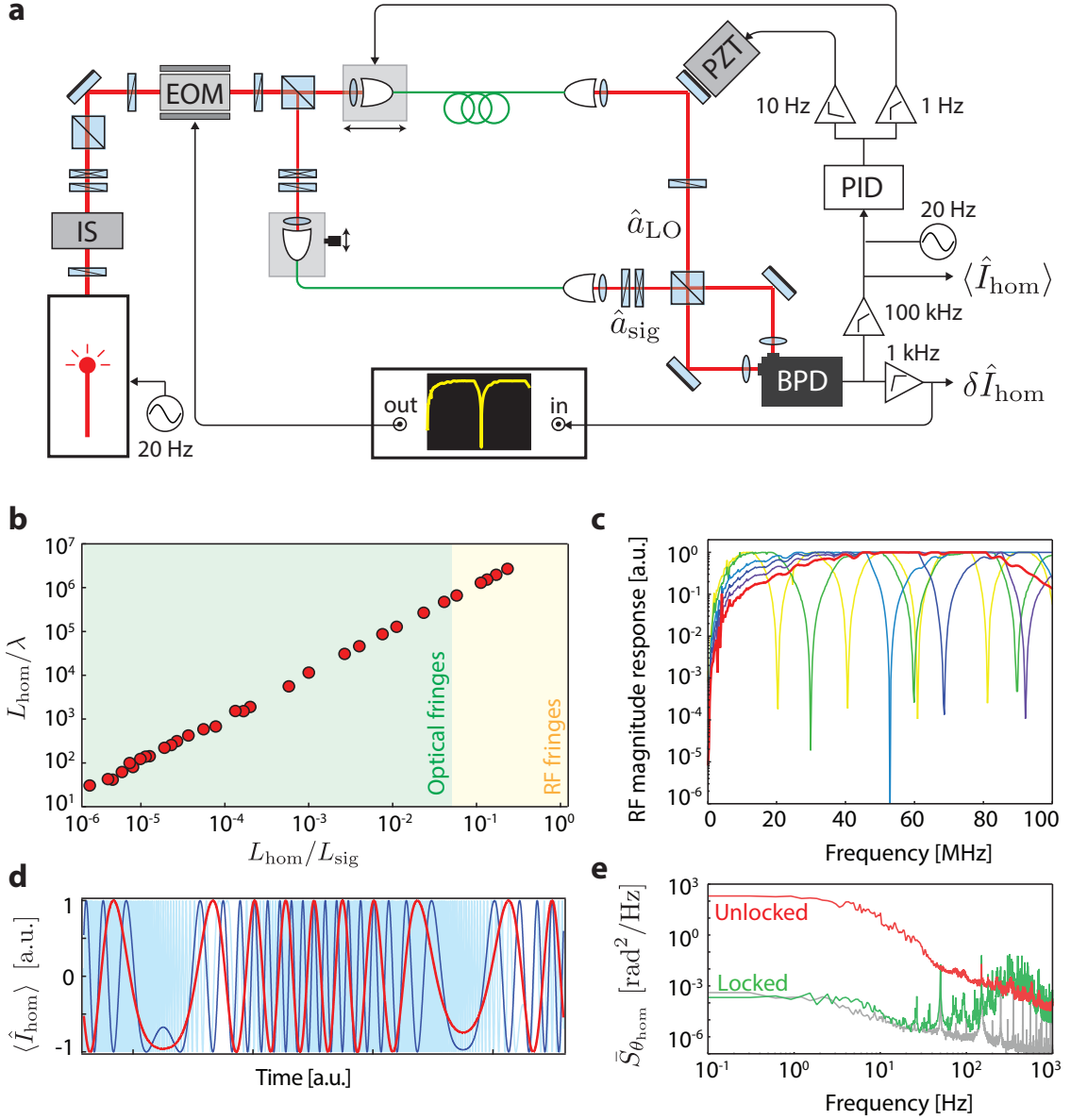


Fig. 2.4 – **Design and operation of homodyne interferometer.** (a) Essential design of the homodyne interferometer, in Mach-Zehnder configuration, that is used in experiment reported in this thesis. Red lines denote free space optical beams, green lines are optical fibres and black lines are radio-frequency electric cables (BNC or SMA). See text for further details. (b) Balancing the interferometer by deterministically changing the physical path length difference L_{hom} . At each stage, counting radio-frequency or optical interference fringes, allows estimation of the imbalance L_{hom}/λ . (c) Magnitude response of the interferometer to an input optical phase modulation injected using the EOM. A radio-frequency network analyser is used to monitor the resulting RF interference. (d) Optical interference fringes in the final stages of balancing. Light and dark blue shows fringe count reduced by micron-scale changes in L_{hom} . Red shows the error signal used to perform active stabilisation of the interferometer. (e) Noise in the homodyne phase θ_{hom} compared for the case where the interferometer is locked (green) vs. free-running (red). Gray trace shows the limit set by electronic noise. (See text for details)

Figure 2.4a depicts the essential layout of the homodyne interferometer employed in this thesis. At its heart is an optical interferometer in Mach-Zehnder configuration. Light from a

laser source (at 780 nm, either an external cavity diode laser – NewFocus Velocity, or a Ti:Sa – Sirah Matisse) is appropriately attenuated, and intensity stabilised (IS, Thorlabs LCC3112/M). Polarisation is then cleaned and aligned, before passing through a broadband electro-optic modulator (EOM, NewFocus 4002, bandwidth DC – 100 MHz). A subsequent half-wave plate divides the light at a polarising beam-splitter to derive the LO and signal fields; the half-wave plate orientation controls their respective powers. The signal field polarisation may be adjusted accordingly thereafter, before being coupled into an optical fiber that is ≈ 10 m long. The LO field is also coupled into a fiber. Both input fiber couplers rest on translation stages, the signal coupler on a manual micrometer stage, while the LO coupler on an electronically controlled one. Both fields subsequently exit into free space. The LO field is reflected off of a mirror mounted on a piezoelectric stack (PZT). The LO and signal are combined at a non-polarising beam-splitter, after their polarisations are aligned. The outputs of the combining beam-splitter are focused onto the two ports of a balanced photodetector (BPD, Femto HCA-S, bandwidth DC – 125 MHz).

In order to enforce a stable homodyne phase θ_{hom} , both the LO and signal are derived from the same laser source. However, the path length difference between the LO and signal arms of the interferometer determines the homodyne phase,

$$\theta_{\text{hom}} = \frac{2\pi}{\lambda} \left(\frac{L_{\text{sig}}}{\nu_{\text{sig}}} - \frac{L_{\text{LO}}}{\nu_{\text{LO}}} \right) \approx \frac{2\pi}{\lambda \nu_{\text{eff}}} (L_{\text{sig}} - L_{\text{LO}}), \quad (2.2.63)$$

where λ is the wavelength of light used, $L_{\text{sig(LO)}}$ is the physical length of the signal (LO) path, $\nu_{\text{sig(LO)}}$ is the refractive index of the signal (LO) path, and $\nu_{\text{eff}} \approx 1.5$ is the approximation assumed for the relevant case where the signal and LO predominantly propagate through an optical fiber. Since we typically need $0 \leq \theta_{\text{hom}} \leq \frac{\pi}{2}$, the fractional path length difference^{2.28},

$$\frac{L_{\text{hom}}}{\lambda} := \frac{L_{\text{sig}} - L_{\text{LO}}}{\lambda}, \quad (2.2.64)$$

needs to be stabilised to order unity for the Mach-Zehnder arms (see fig. 2.4); this is done in three steps.

The first two procedures rely on counting the interference fringes in the photocurrent $\langle \hat{I}_{\text{hom}} \rangle \propto \sin \theta_{\text{hom}}$ (eq. (2.2.60)) to estimate the length imbalance [152]. In the first step, a radio-frequency (RF) response measurement is performed on the optical interferometer. This is done by driving a phase modulator placed at the interferometer input using a network analyser (Agilent, E5061B), and demodulating the response of the interferometer. Figure 2.4c shows a series of such measurements, for varying L_{hom} . The phase modulation $\phi(t)$, effectively a frequency modulation $\omega_{\ell}(t) = \frac{d\phi}{dt}$, leads to a photocurrent,

$$\langle I_{\text{hom}}(t) \rangle \propto \sin \left(\frac{2\pi L_{\text{hom}}}{c\nu_{\text{eff}}} \omega_{\ell}(t) \right) \approx \sin \left(\frac{2\pi L_{\text{hom}}}{c\nu_{\text{eff}}} \omega_{\ell}(0) + 2\pi t \cdot \frac{L_{\text{hom}}}{c\nu_{\text{eff}}} \frac{d\omega_{\ell}}{dt} \right),$$

^{2.28} For the detection of signals at a few MHz from the carrier, such a stringent condition is not necessary. However, the ability to achieve broadband cancellation of excess phase noise injected at the input of the interferometer [145, 151], for example when using semiconductor diode lasers as in experiments reported in chapter 3, demands an interferometer whose arms are length-balanced to within an optical wavelength. Indeed, the contribution of input phase noise in the photocurrent of an imbalanced homodyne interferometer takes the form, $\bar{S}_I^{\text{hom}}[\Omega] \propto \sin^2(\Omega\tau/2) \bar{S}_{\phi}^{\text{in}}[\Omega]$, where τ is the time delay between the two arms (see Appendix C), and $\bar{S}_{\phi}^{\text{in}}$ is the spectrum of excess input phase noise.

exhibiting interference fringes with frequency, $f_{\text{fringe}} = \frac{L_{\text{hom}}}{c v_{\text{eff}}} \frac{d\omega_{\ell}}{dt}$. Thus, the fringe frequency measured, as in fig. 2.4c, provides the length imbalance relative to the laser wavelength, and the RF frequency modulation amplitude. The length imbalance so inferred, is reduced by physically cutting and re-splicing the LO optical fiber. This technique however loses sensitivity once the fringe frequency surpasses the photodetector cutoff; typically this happens at $|L_{\text{hom}}| \approx 10 \text{ cm}$.

In a second step, sensitivity to input frequency changes is increased by working at optical frequencies. The diode laser driving the interferometer is wavelength-modulated^{2.29} $\lambda(t) = \lambda(0) + \delta\lambda(t)$, and the interference fringes in the DC photocurrent (using eq. (2.2.60) and eq. (2.2.63)),

$$\langle \hat{I}_{\text{hom}}(t) \rangle \propto \sin \left(\frac{2\pi L_{\text{hom}}}{v_{\text{eff}} \lambda(t)} \right) \approx \sin \left(\frac{2\pi L_{\text{hom}}}{v_{\text{eff}} \lambda(0)} + 2\pi t \cdot \frac{L_{\text{hom}}}{v_{\text{eff}} \lambda(0)} \cdot \frac{1}{\lambda(0)} \frac{d\lambda}{dt} \right),$$

monitored on an oscilloscope (Tektronix DPO3034). The imbalance, reflected in the frequency of the interference fringes [152] $f_{\text{fringe}} = \frac{L_{\text{hom}}}{v_{\text{eff}} \lambda(0)} \cdot \frac{1}{\lambda(0)} \frac{d\lambda}{dt}$, is reduced by cutting and re-splicing the fiber as before – below $|L_{\text{hom}}| \approx 1 \text{ cm}$, it becomes difficult to precisely cut the fiber. Subsequent adjustment is made by using micro-meter stages carrying the signal and LO input fiber couplers (see fig. 2.4). Interference fringe count gradually reduces, as shown in fig. 2.4d (blue traces), to a point where they become particularly sensitive to slight external disturbances – typically at $L_{\text{hom}} \approx 10\lambda$. Figure 2.4b shows the length imbalance relative to the wavelength inferred from the fringe frequency as the physical length L_{hom} is reduced – the different sensitivities of RF and optical measurements is due to the much smaller wavelength of the latter [152, 153].

Beyond this point, the interferometer has to be actively locked. The error signal is the DC photocurrent $\langle \hat{I}_{\text{hom}} \rangle \propto \sin \theta_{\text{hom}}$, generated by modulating the length $L_{\text{hom}}(t)$. The red trace in fig. 2.4d shows a typical error signal, corresponding to a few cycles of the phase $\theta_{\text{hom}}(t) = \frac{2\pi}{\lambda v_{\text{eff}}} L_{\text{hom}}(t)$ about zero. The length is changed by dithering a mirror placed on a fast piezo-electric stack in the LO free space path (PZT, in fig. 2.4). The error signal is sent through a PID controller with a slow (1 Hz low-pass) and a fast (10 – 300 Hz bandpass) branch^{2.30}. The fast branch actuates the piezo-electric stack, and suppresses high frequency length fluctuations (mostly limited by the onset of piezo-electric resonances at a few kHz). The slow branch actuates a linear motor in the LO path, and is used to counteract slow drifts due to temperature and seismic disturbances. With the optical table floated, the active stabilisation keeps the homodyne interferometer locked indefinitely.

Figure 2.4e shows an in-loop measurement of the apparent fluctuations in θ_{hom} when the interferometer is locked (green trace), compared against the case where it is unlocked (red trace). The data is calibrated by using the fact that the peak-peak DC photocurrent, when the piezo stack is dithered, corresponds to θ_{hom} varying by π . At low frequencies (1 – 100 Hz) the

^{2.29} Formally equivalent to a frequency modulation $\delta\omega_{\ell} = -2\pi \frac{c}{\lambda(0)} \cdot \frac{\delta\lambda}{\lambda(0)}$; however, for an ECDL, by construction, its frequency is modulated via the diode current, providing access to $\delta\omega_{\ell} \approx 2\pi \cdot 100 \text{ GHz}$, whereas the wavelength is modulated by mechanically changing the laser cavity length, leading to $\delta\lambda \approx 10 \text{ nm}$, equivalent to $\delta\omega_{\ell} \approx 2\pi \cdot 5 \text{ THz}$.

^{2.30} The filters are implemented using Stanford Research Systems SR560 pre-amplifiers running off of its internal battery, to reduce sensitivity to 50 Hz fluctuations from power lines. In practice, it is found that appropriate filtering at the PID input is also necessary.

residual apparent fluctuations in θ_{hom} is limited by electronic noise (grey trace) in the detection and feedback loops, whereas at frequencies above 1 kHz, the presence of piezo-mechanical resonances limit the applicable gain. Despite these technical limitations, fig. 2.4e allows an upper-bound of, $\text{Var} [\theta_{\text{hom}}^2]^{1/2} < 100 \text{ mrad}$, for the low frequency stability of the homodyne angle.

2.2.2.4 Detection of conjugate quadratures: heterodyne

Contrary to a homodyne detector where the LO and signal share a common carrier frequency, a heterodyne detector (see fig. 2.3b) employs a frequency detuned LO. For the case where the LO frequency is larger than the signal frequency by Ω_{IF} , the LO and signal fields may be represented by the ansatz (analogous to eq. (2.2.59) for homodyne detection),

$$\hat{a}_{\text{LO}(\text{sig})}(t) = \left(\sqrt{\langle \hat{n}_{\text{LO}(\text{sig})} \rangle} + \delta \hat{a}_{\text{LO}(\text{sig})}(t) \right) e^{-i\omega t} \times \begin{cases} e^{-i(\Omega_{\text{IF}}t + \theta_{\text{LO}})} \\ e^{-i\theta_{\text{sig}}} \end{cases}.$$

For the reasons detailed above for the case of homodyne detection (formally, $\Omega_{\text{IF}} = 0$), it is technically useful to perform balanced detection, i.e. combine the LO and signal on a balanced beam-splitter, using a length-matched interferometer, i.e. the LO and signal arrive at the beam-splitter after propagating for equal times.

Similar to the homodyne case, in the strong LO and length-balanced case, the mean and fluctuating parts of the heterodyne photocurrent (in the strong LO, i.e. $\langle \hat{n}_{\text{LO}} \rangle \gg \langle \hat{n}_{\text{sig}} \rangle$, and balanced, i.e. $\eta_t = \frac{1}{2}$, case),

$$\begin{aligned} \langle \hat{I}_{\text{het}}(t) \rangle &\approx -2q_e \sqrt{\langle \hat{n}_{\text{LO}} \rangle \langle \hat{n}_{\text{sig}} \rangle} \sin(\theta_{\text{het}} + \Omega_{\text{IF}}t) \\ \delta \hat{I}_{\text{het}}(t) &\approx q_e \sqrt{2 \langle \hat{n}_{\text{LO}} \rangle} \delta \hat{q}_{\text{sig}}^{\theta_{\text{het}} + \pi/2 + \Omega_{\text{IF}}t}(t) \end{aligned} \quad (2.2.65)$$

where $\theta_{\text{het}} := \theta_{\text{sig}} - \theta_{\text{LO}}$. Importantly, the photocurrent is not proportional to a unique signal quadrature, but in fact, cycles through each quadrature. Despite this fact, the quadrature commutation relations eq. (2.2.56) conspire to ensure that the heterodyne photocurrent commutes with itself, viz.^{2.31}

$$[\delta \hat{I}_{\text{het}}(t), \delta \hat{I}_{\text{het}}(t')] = 4i q_e^2 \langle \hat{n}_{\text{LO}} \rangle \cdot \delta(t - t') \sin(\Omega_{\text{IF}}(t - t')) = 0,$$

rendering $\delta \hat{I}_{\text{het}}$ a continuous observable.

The spectrum of the heterodyne photocurrent fluctuations is however unlike the homodyne spectrum. In fact, the photocurrent fluctuations (eq. (2.2.65)) expressed in terms of the amplitude operators (using eq. (2.2.55)),

$$\delta \hat{I}_{\text{het}}(t) = q_e \sqrt{\langle \hat{n}_{\text{LO}} \rangle} \left(\delta \hat{a}_{\text{sig}}(t) e^{-i\theta_{\text{het}} - i\Omega_{\text{IF}}t - i\pi/2} + \delta \hat{a}_{\text{sig}}^\dagger(t) e^{i\theta_{\text{het}} + i\Omega_{\text{IF}}t + i\pi/2} \right), \quad (2.2.66)$$

has the two-time correlator (omitting the factor $q_e^2 \langle \hat{n}_{\text{LO}} \rangle$),

$$\begin{aligned} \langle \delta \hat{I}_{\text{het}}(t) \delta \hat{I}_{\text{het}}(t') \rangle &\propto \langle \delta \hat{a}_{\text{sig}}(t) \delta \hat{a}_{\text{sig}}^\dagger(t') \rangle e^{-i\Omega_{\text{IF}}(t-t')} + \langle \delta \hat{a}_{\text{sig}}^\dagger(t) \delta \hat{a}_{\text{sig}}(t') \rangle e^{+i\Omega_{\text{IF}}(t-t')} \\ &\quad - \langle \delta \hat{a}_{\text{sig}}(t) \delta \hat{a}_{\text{sig}}(t') \rangle e^{-2i\theta_{\text{het}}} e^{-i\Omega_{\text{IF}}(t+t')} - \langle \delta \hat{a}_{\text{sig}}^\dagger(t) \delta \hat{a}_{\text{sig}}^\dagger(t') \rangle e^{+2i\theta_{\text{het}}} e^{+i\Omega_{\text{IF}}(t+t')}, \end{aligned}$$

^{2.31} The second equality, by common abuse of notation, holds in the *sense of distribution*; i.e. it holds for any arbitrarily close approximation to $\delta(t)$.

which is not stationary. The last two terms, being a periodic modulation of a stationary term, give rise to what is called *cyclostationary noise* [154, 155]. When the signal field carries excitations in a narrow band centred at frequencies much below the intermediate frequency Ω_{IF} , these non-stationary terms may be omitted^{2.32}. The resulting photocurrent correlator,

$$\begin{aligned} \langle \delta \hat{I}_{\text{het}}(t) \delta \hat{I}_{\text{het}}(0) \rangle &\approx \langle \delta \hat{a}_{\text{sig}}(t) \delta \hat{a}_{\text{sig}}^\dagger(t') \rangle e^{-i\Omega_{\text{IF}}t} + \langle \delta \hat{a}_{\text{sig}}^\dagger(t) \delta \hat{a}_{\text{sig}}(t') \rangle e^{+i\Omega_{\text{IF}}t} \\ &= \langle \delta \hat{q}(t) \delta \hat{q}(0) + \delta \hat{p}(t) \delta \hat{p}(0) \rangle \cos \Omega_{\text{IF}}t \\ &\quad + \langle \delta \hat{p}(t) \delta \hat{q}(0) + \delta \hat{q}(t) \delta \hat{p}(0) \rangle \sin \Omega_{\text{IF}}t, \end{aligned} \quad (2.2.67)$$

is independent of the relative signal-LO phase θ_{het} . Note that due to simultaneous detection of conjugate quadratures, any mutual correlations between the two are reflected in the heterodyne photocurrent. Equation (2.2.67) together with the Wiener-Khinchine theorem (eq. (2.1.5)) gives the (single-sided) spectrum of the heterodyne photocurrent:

$$\bar{S}_I^{\text{het}}[\Omega] = q_e^2 \langle \hat{n}_{\text{LO}} \rangle \left(S_{aa}^{\text{sig}}[\Omega + \Omega_{\text{IF}}] + S_{a^\dagger a^\dagger}^{\text{sig}}[\Omega - \Omega_{\text{IF}}] \right),$$

expressed in terms of the unsymmetrised power spectral density of the (non-hermitian) flux amplitude operators (as defined in eq. (2.1.7)). The left-hand side, being a single-sided spectrum is defined only for $\Omega > 0$; in particular, fluctuations in the optical field originally about the optical carrier are translated to radio-frequencies, $\Omega \approx \Omega_{\text{IF}}$, about the intermediate frequency. For a detector with bandwidth much less than $2\Omega_{\text{IF}}$, the spectrum centred about Ω_{IF} ,

$$\bar{S}_I^{\text{het}}[\Omega - \Omega_{\text{IF}}] \approx q_e^2 \langle \hat{n}_{\text{LO}} \rangle S_{aa}[\Omega]. \quad (2.2.68)$$

consists of only those components slowly varying with respect to Ω_{IF} . In this sense, a heterodyne detector measures the double-sided spectrum of the flux of the optical field, including correlations between its amplitude and phase quadratures.

Explicitly separating out the vacuum fluctuations, from the signal field, i.e. $\delta \hat{a}_{\text{sig}} \rightarrow \delta \hat{a}_{\text{vac}} + \delta \hat{a}_{\text{sig}}$, and introducing the efficiencies for the detection, the spectrum of the heterodyne photocurrent is,

$$\bar{S}_I^{\text{het}}[\Omega - \Omega_{\text{IF}}] = \underbrace{\mathcal{R}^2 \bar{S}_P^{\text{NE}}[\Omega]}_{\bar{S}_I^{\text{het,det}}} + \underbrace{4\eta \cdot q_e \mathcal{R} \cdot \langle P_{\text{LO}} \rangle}_{\bar{S}_I^{\text{het,shot}}} + \underbrace{\eta^2 q_e \mathcal{R} \langle P_{\text{LO}} \rangle}_{\bar{S}_I^{\text{het,sig}}} S_{aa}^{\text{sig}}[\Omega]. \quad (2.2.69)$$

Note that compared to homodyne detection eq. (2.2.62), the shot noise contribution is twice larger, and the signal twice smaller – the former is due to the shot noise from both quadratures being detected, while the latter is due to the signal being spread symmetrically about the intermediate frequency (i.e. double-sidedness). In effect, heterodyne detection is four times less sensitive compared to a homodyne detector. The advantage however is that by detecting both quadratures of the signal field simultaneously, it provides access to correlations between the signal quadratures [162].

^{2.32} In the contrary case, these terms give rise to cyclostationary shot noise [156, 157] – shot noise modulated at Ω_{IF} – in excess of the expectation from a stationary shot noise model. It is generally true that cyclostationary noise may be represented as a sum of correlated stationary noise processes [158] – therefore, it is possible to coherently cancel excess cyclostationary shot noise [156, 159, 160], or use the correlations for benefit [161].

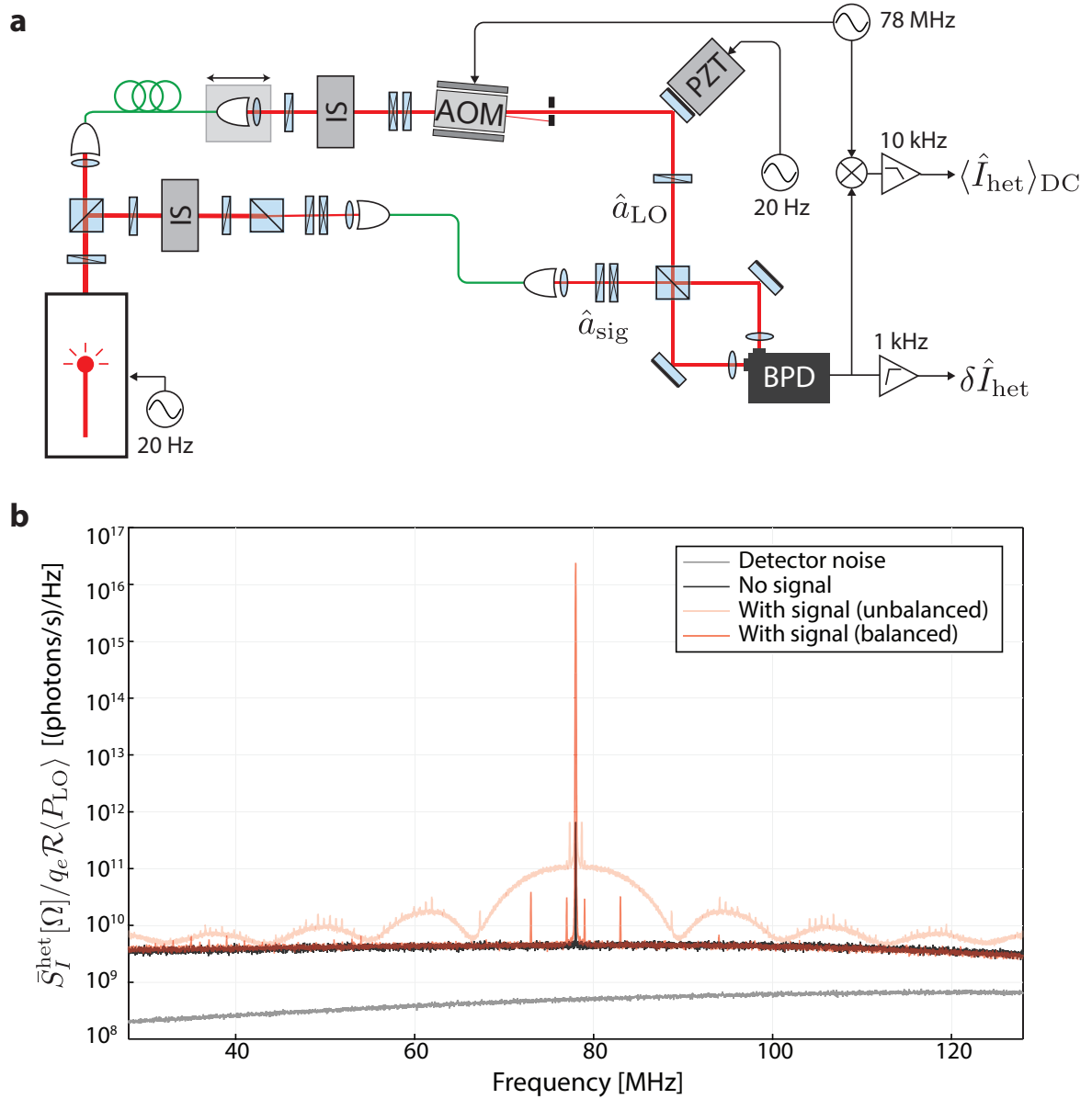


Fig. 2.5 – **Design and operation of heterodyne interferometer.** (a) Essential design of the balanced heterodyne interferometer used in this thesis. An AOM in the LO path produces the desired frequency shift $\Omega_{\text{IF}} = 2\pi \cdot 78$ MHz. (b) Heterodyne photocurrent spectrum for the interferometer unbalanced (light red) and balanced (red). Gray shows the electronic noise of the photodetector, and black the shot noise due to the LO. The spectrum is calibrated using the known DC optical power which is reflected as the variance of the carrier beat signal around the intermediate frequency $\Omega_{\text{IF}} = 2\pi \cdot 78$ MHz.

Design and operation of a realistic heterodyne detector

As illustrated by theoretical considerations, an experimentally practical heterodyne detector inherits all the characteristics of the homodyne detector in fig. 2.4, except for a frequency shifted LO. Figure 2.5a depicts the essential layout of the balanced heterodyne interferometer constructed and employed in this thesis. The substantial difference in the optics is the presence of an acousto-optic modulator (AOM, AA Optoelectronics MT110-B50A1) in the LO arm of the

interferometer. The AOM was operated so as to maximise the diffracted optical power into the first order; at the chosen operation frequency $\Omega_{\text{IF}} = 2\pi \cdot 78 \text{ MHz}$, it was possible to attain a diffraction efficiency > 0.8 .

Similar to the procedure followed to balance the homodyne detector, the input laser wavelength is modulated to induce interference fringes in the photocurrent. However, in the case of the heterodyne, the mean photocurrent eq. (2.2.65), $\langle \hat{I}_{\text{het}}(t) \rangle \propto \sin(\theta_{\text{het}} + \Omega_{\text{IF}}t)$ oscillates at the offset frequency Ω_{IF} . Therefore, to access the fringes resulting from a modulation of the phase θ_{het} , the photocurrent is mixed down using a RF local oscillator at the offset frequency Ω_{IF} (see schematic in fig. 2.5a). The lengths are balanced by nullifying the fringe frequency. Unlike the homodyne, the phase θ_{het} need not be stabilised, since the photocurrent spectrum $\bar{S}_I^{\text{het}}[\Omega]$ (eq. (2.2.65)) is not sensitive to the mean phase.

Figure 2.5b shows the cancellation of input laser noise achieved due to length balance. Shining a LO ($P_{\text{LO}} \approx 1 \text{ mW}$) alone gives rise to a shot noise contribution (black trace) $\bar{S}_I^{\text{het,shot}} \gtrsim 10 \cdot \bar{S}_I^{\text{het,det}}$. For an unbalanced interferometer driven by a (noisy) diode laser, the output photocurrent spectrum gives a direct measure of the laser phase noise transduced by the imbalance of the interferometer (see appendix C). Indeed, the red trace in fig. 2.5b, is consistent with diode laser frequency noise $\bar{S}_\omega[\Omega] = \Omega^2 \bar{S}_\phi[\Omega] \approx 2\pi(35 \text{ Hz}^2/\text{Hz})$, at Fourier frequencies $\Omega \approx 2\pi \cdot 4 \text{ MHz}$ from the carrier.

2.2.2.5 Optical cavity coupled to a waveguide

The typical optical fields we are interested in this thesis, are those that have interacted with an optical cavity. Here we present a schematic of the optical cavity we are interested in, whispering-gallery mode optical microcavities [52, 163], and the coupling of optical fields in and out of such cavities via a waveguide. Several approaches exist to treat this problem (see [164] for a review).

Whispering-gallery mode (WGM) optical cavities, like the one shown in fig. 2.6a, supports optical modes at specific frequencies ω_n roughly commensurate with standing waves resonating around the circumference. For example, for a spherical cavity of radius R and made of a dielectric material of refractive index ν , solutions of Maxwell's equations show that the mode wavelengths λ_n confirm to this intuition, i.e. $\lambda_n \approx 2\pi\nu R/n$ [165].

In general, when the free spectral range of the cavity, $\Delta\omega_{\text{FSR}} := \omega_n - \omega_{n-1}$ is much larger than the energy decay rate κ_n , i.e. $\Delta\omega_{\text{FSR}} \gg \kappa_n$, each mode may be treated independent of the others. Focusing on such a particular mode, described by resonance frequency ω_c , the dynamics of its quantised standing wave amplitude \hat{a} is described by the hamiltonian [164],

$$\hat{H}_c = \hbar\omega_c \hat{a}^\dagger \hat{a} + \hat{H}_{c,0} + \hat{H}_{c,\text{ex}}, \quad (2.2.70)$$

where $\hat{H}_{c,0}$ models coupling to external sources responsible for the intrinsic cavity decay rate κ_0 , and $\hat{H}_{c,\text{ex}}$ models coupling to an external waveguide used to excite the cavity.

In our case, the coupling waveguide is a tapered optical fiber placed in the vicinity of the cavity evanescent field [168, 169]. Care is taken to ensure that the tapered fiber predominantly

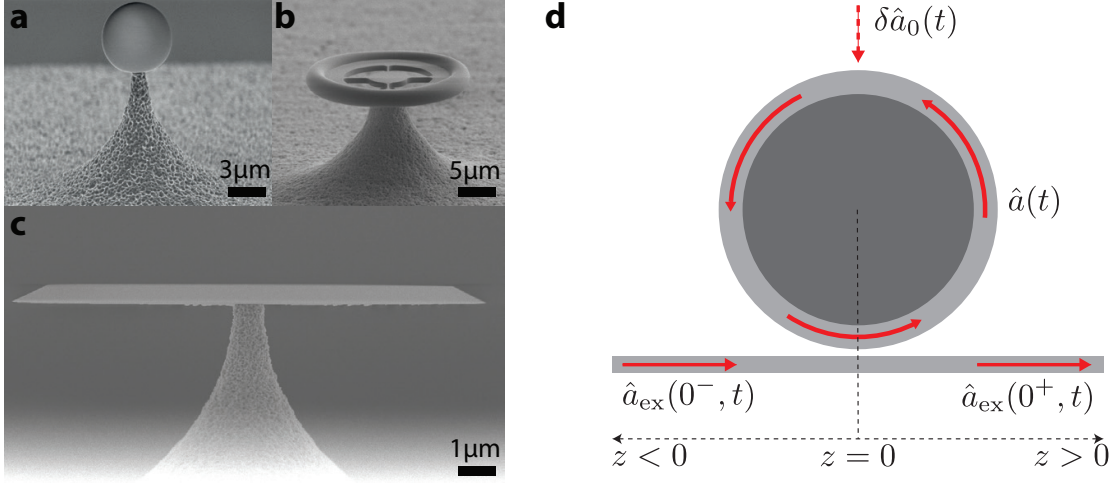


Fig. 2.6 – **Whispering-gallery mode cavities and coupling.** (a-c) A smattering of whispering-gallery mode optical microcavities, where the resonant optical mode circulates along the circumference of the dielectric medium. (a,b) Spherical and toroidal cavities [166] made by CO₂ laser reflow of SiO₂. (c) Disk cavity fabricated by chemical-mechanical polishing [167]. (d) Schematic of waveguide (here, tapered optical fiber) coupling to a whispering gallery mode cavity. The cavity field $\hat{a}(t)$ is excited by the travelling wave field $\hat{a}_{\text{ex}}(z, t)$ of the waveguide through a beam-splitter type interaction at the point $z = 0$. The cavity is also driven by vacuum fluctuations $\delta\hat{a}_0(t)$.

supports a single travelling mode^{2.33} described by an amplitude flux $\hat{a}_{\text{ex}}(z, t)$, along the (longitudinal) z -direction. Note that the travelling mode is normalised to a photon flux, and satisfies the commutation relation (see eq. (2.2.33)),

$$[\hat{a}_{\text{ex}}(z, t), \hat{a}^\dagger(z', t')] = \delta(t - t' - (z - z')/c). \quad (2.2.71)$$

The dynamics of this field is described by the hamiltonian,

$$\hat{H}_{\text{ex}} = \hbar\omega_{\text{ex}}\hat{a}_{\text{ex}}^\dagger(z, t)\hat{a}_{\text{ex}}(z, t) + \hat{H}_{\text{c,ex}} \quad (2.2.72)$$

where ω_{ex} is the frequency of the propagating mode. We model cavity-waveguide coupling as an energy-conserving interaction localised at the point^{2.34} $z = 0$ (see fig. 2.6b) [173], i.e.,

$$\hat{H}_{\text{c,ex}} = i\hbar\sqrt{\kappa_{\text{ex}}} \left(\hat{a}^\dagger(t)\hat{a}_{\text{ex}}(0, t) - \hat{a}(t)\hat{a}_{\text{ex}}^\dagger(0, t) \right). \quad (2.2.73)$$

Inserting eq. (2.2.73) in eq. (2.2.70), and employing the commutation relation $[\hat{a}(t), \hat{a}^\dagger(t)] = 1$, gives the equation of motion for the cavity field,

$$\frac{d\hat{a}}{dt} = -i\omega_c\hat{a} + \sqrt{\kappa_{\text{ex}}}\hat{a}_{\text{ex}}(0, t) + \frac{i}{\hbar}[\hat{a}, \hat{H}_{\text{c,0}}]. \quad (2.2.74)$$

^{2.33} The tapered section, formed by adiabatically stretching a cylindrical optical fiber (780HP, 5 μm mode waist), to a waist of $< 1 \mu\text{m}$, supports degenerate TE, TM₀₀ modes (cutoff at $\approx 730 \text{ nm}$) [170, 171], with an evanescent part guided in free space. The optical fiber itself is excited using free space radiation in TE, TM modes, with a coupling efficiency $\gtrsim 80\%$.

^{2.34} In a more realistic model where the coupling region has a finite extent, κ_{ex} effectively describes the detailed geometry of the coupling [172].

Inserting eq. (2.2.73) in eq. (2.2.72), and employing the commutation relation eq. (2.2.71) gives,

$$\begin{aligned} \frac{d\hat{a}_{\text{ex}}(z, t)}{dt} &= -i\omega_{\text{ex}}\hat{a}_{\text{ex}} + \sqrt{\kappa_{\text{ex}}}\hat{a}(t)\delta(-z/c), \\ \text{or, } -c\frac{d\hat{a}_{\text{ex}}(z, t)}{dz} &= -i\omega_{\text{ex}}\hat{a}_{\text{ex}} + \sqrt{\kappa_{\text{ex}}}\hat{a}(t)\delta(-z/c), \end{aligned} \quad (2.2.75)$$

where the second form is obtained by noting that for a propagating mode, satisfying $\hat{a}_{\text{ex}}(z, t) = \hat{a}_{\text{ex}}(0, t - z/c)$, time and the space derivative along the direction of propagation are related as, $\partial_t \hat{a}_{\text{ex}}(z, t) = -c\partial_z \hat{a}_{\text{ex}}(z, t)$, with c the propagation velocity in the waveguide. Integrating the latter equation within the coupling region, $z \in (0^-, 0^+)$, and employing the properties of the delta function,

$$\hat{a}_{\text{ex}}(0^+, t) = \hat{a}_{\text{ex}}(0^-, t) - \sqrt{\kappa_{\text{ex}}}\hat{a}(t). \quad (2.2.76)$$

Defining the input (output) fields as the propagating field before (after) the coupling region:

$$\hat{a}_{\text{in, out}}(t) := \hat{a}_{\text{ex}}(0^\mp, t), \quad (2.2.77)$$

eq. (2.2.76) takes the form of an input-output relation,

$$\hat{a}_{\text{out}}(t) = \hat{a}_{\text{in}}(t) - \sqrt{\kappa_{\text{ex}}}\hat{a}(t), \quad (2.2.78)$$

between the waveguide and cavity modes in a scattering description of their coupling.

Returning to the equation for the cavity field in eq. (2.2.74), the discontinuity at $z = 0$ may be manipulated as,

$$\hat{a}_{\text{ex}}(0, t) = \frac{1}{2} (\hat{a}_{\text{ex}}(0^-, t) + \hat{a}_{\text{ex}}(0^+, t)) = \hat{a}_{\text{in}} - \frac{\sqrt{\kappa_{\text{ex}}}}{2}\hat{a}(t);$$

here the first equality uses continuity of the field at the coupling point, and the second follows from the input-output relation (eq. (2.2.78)). Inserting this back in the equation of motion for the cavity field, eq. (2.2.74),

$$\frac{d\hat{a}}{dt} = -\left(i\omega_c + \frac{\kappa_{\text{ex}}}{2}\right)\hat{a} + \sqrt{\kappa_{\text{ex}}}\hat{a}_{\text{in}}(t) + \frac{i}{\hbar}[\hat{H}_{c,0}, \hat{a}].$$

Thus, coupling to the external waveguide opens a decay channel for the cavity mode, described by the external decay rate κ_{ex} . The explicit form of intrinsic losses, modelled by $\hat{H}_{c,0}$, follow similar lines, and result in the equation of motion [174],

$$\frac{d\hat{a}}{dt} = -\left(i\omega_c + \frac{\kappa}{2}\right)\hat{a} + \sqrt{\kappa_0}\delta\hat{a}_0 + \sqrt{\kappa_{\text{ex}}}\hat{a}_{\text{in}}(t), \quad (2.2.79)$$

where κ_0 is the intrinsic decay rate, $\kappa = \kappa_0 + \kappa_{\text{ex}}$ is the total decay rate, and $\delta\hat{a}_0$ is the zero-mean stochastic process driving the cavity through its intrinsic loss channel. Together with the input-output relation eq. (2.2.78),

$$\hat{a}_{\text{out}}(t) = \hat{a}_{\text{in}}(t) - \sqrt{\kappa_{\text{ex}}}\hat{a}(t), \quad (2.2.80)$$

and the specification of the fluctuations associated with the intrinsic and external (waveguide) decay channel (here $n_{c,j}$ is the average thermal occupation of the channel $j \in \{0, \text{in}\}$),

$$\begin{aligned} \langle \delta\hat{a}_j^\dagger(t)\delta\hat{a}_j(0) \rangle &= n_{c,j}\delta(t) \\ \langle \delta\hat{a}_j(t)\delta\hat{a}_j^\dagger(t) \rangle &= (n_{c,j} + 1)\delta(t), \end{aligned} \quad (2.2.81)$$

this completes the description of the optical cavity.

Typically, the optical cavity is excited using a coherent source at a definite optical frequency ω_ℓ , so that,

$$\hat{a}_{\text{in}}(t) = (|\bar{a}_{\text{in}}| + \delta\hat{a}_{\text{in}}(t))e^{-i\omega_\ell t}. \quad (2.2.82)$$

It proves convenient to adopt a description where the explicit time dependent factor $e^{-i\omega_\ell t}$ is implicit. At the level of the equation of motion eq. (2.2.79) and the input-output relation eq. (2.2.80), this is implemented by the transformation^{2.35}, $\hat{a} \rightarrow \hat{a}e^{-i\omega_\ell t}$. Equations (2.2.79) and (2.2.80) then take the form,

$$\begin{aligned} \frac{d\hat{a}}{dt} &= \left(i\Delta - \frac{\kappa}{2}\right)\hat{a} + \sqrt{\kappa_0}\delta\hat{a}_0 + \sqrt{\kappa_{\text{ex}}}\hat{a}_{\text{in}}(t) \\ \hat{a}_{\text{out}}(t) &= \hat{a} - \sqrt{\kappa_{\text{ex}}}\hat{a}_{\text{in}}(t), \end{aligned} \quad (2.2.83)$$

where Δ is the detuning between the input field in eq. (2.2.82) and the cavity, viz.

$$\Delta := \omega_\ell - \omega_c.$$

Steady-state spectroscopy with a coherent source

In a typical spectroscopy experiment, as shown in fig. 2.7, aiming to identify and characterise the whispering-gallery modes of the cavity, the cavity is pumped using a laser at frequency ω_ℓ (see eq. (2.2.82)), and the transmitted power, $P_{\text{out}} = \hbar\omega_\ell \langle \hat{a}_{\text{out}}^\dagger \hat{a}_{\text{out}} \rangle$, is monitored as the laser frequency ω_ℓ is swept over the cavity resonance ω_c . In the experiment, we ensure that ω_ℓ is swept much slower than the cavity decay rate κ so that P_{out} is the steady-state transmission of the cavity.

In order to arrive at the relevant observable, we start from the equations determining the intracavity field eq. (2.2.83), expressed for the mean field:

$$\frac{d\langle \hat{a} \rangle}{dt} = \left(i\Delta - \frac{\kappa}{2}\right)\langle \hat{a} \rangle + \sqrt{\kappa_{\text{ex}}}\bar{a}_{\text{in}}.$$

The resulting steady-state intracavity field,

$$\bar{a} := \langle \hat{a} \rangle_{\text{ss}} = \frac{-\sqrt{\kappa_{\text{ex}}}}{i\Delta - \kappa/2} \bar{a}_{\text{in}},$$

gives rise to the mean steady-state intracavity photon number,

$$\langle \hat{a}^\dagger \hat{a} \rangle_{\text{ss}} = |\bar{a}|^2 = \frac{\kappa_{\text{ex}} |\bar{a}_{\text{in}}|^2}{\Delta^2 + (\kappa/2)^2} = \frac{4}{\kappa} \left(\frac{\kappa_{\text{ex}}/\kappa}{1 + (4\Delta^2/\kappa^2)} \right) \frac{P_{\text{in}}}{\hbar\omega_\ell},$$

that reflects the response of the cavity as a resonant build-up of the pump power $P_{\text{in}} := \hbar\omega_\ell \langle \hat{a}_{\text{in}}^\dagger \hat{a}_{\text{in}} \rangle$, depending on the relative detuning $\frac{\Delta}{\kappa/2}$ and the cavity-waveguide coupling efficiency,

$$\eta_c := \frac{\kappa_{\text{ex}}}{\kappa} = \frac{\kappa_{\text{ex}}}{\kappa_{\text{ex}} + \kappa_0}.$$

^{2.35} Corresponding to a unitary transformation by the rotation operator, $\hat{R}(\phi) = e^{-i\phi\hat{a}^\dagger\hat{a}}$, of the hamiltonian \hat{H}_c in eq. (2.2.70); i.e. $\hat{H}_c \rightarrow \hat{R}(\omega_\ell t)\hat{H}_c\hat{R}^\dagger(\omega_\ell t)$.

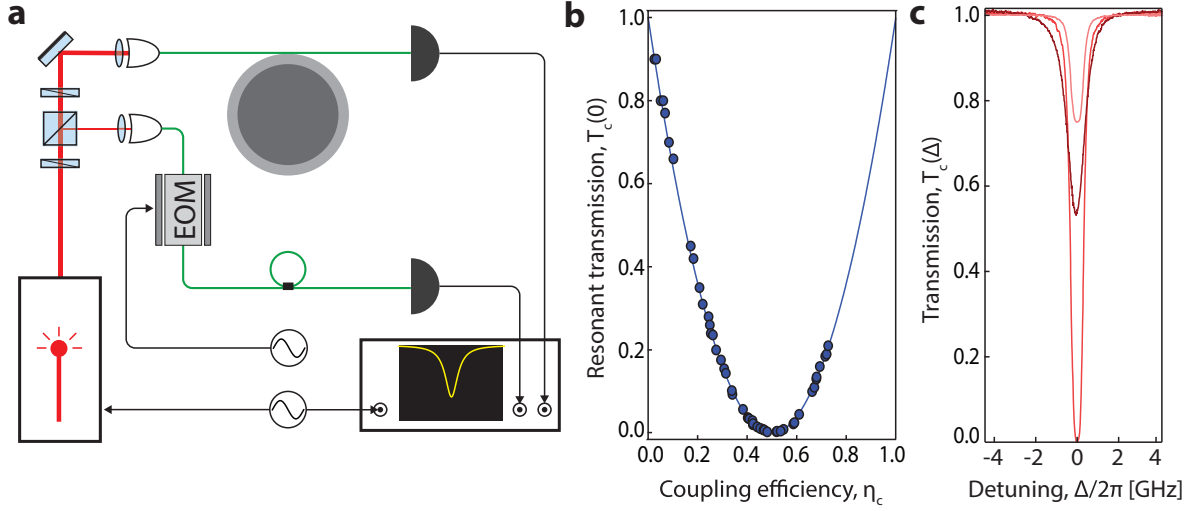


Fig. 2.7 – **Steady-state spectroscopy.** (a) Experimental schematic of the spectroscopy scheme: laser light is coupled into a fiber taper which is then brought in close proximity to the whispering gallery mode cavity. (b) Transition from under-coupled to over-coupled regime, as the coupling efficiency η_c is varied. Relative position of the fiber taper and the cavity controls the waveguide coupling rate κ_{ex} . (c) Examples of cavity transmission when the cavity is under-coupled (light red), critically coupled (red), and over-coupled (dark red). See text for details regarding calibration of the detuning.

Finally, the steady-state transmission, $T_c(\Delta) := P_{\text{out}}/P_{\text{in}}$, for a given pump detuning,

$$T_c(\Delta) = 1 - \frac{4\eta_c(1 - \eta_c)}{1 + (4\Delta^2/\kappa^2)},$$

exhibits a Lorentzian suppression on approaching resonance ($|\Delta| \rightarrow 0$). However, the cavity only absorbs all the power on resonance, i.e. $T_c(0) = 0$, when the coupling is *critical*, i.e. $\eta_c = \frac{1}{2}$, corresponding to the case where the power coupled in by the waveguide exactly compensates for the power lost through the intrinsic decay channel.

These aspects are illustrated in fig. 2.7, by directly measuring the transmission $T_c(\Delta)$. A widely tunable external cavity diode laser (NewFocus Velocity) is coupled into a fiber taper, which is brought within the evanescent field of the whispering-gallery mode cavity. The relative position of the fiber and cavity is controlled using a piezo-positioning stage (Attocube, ANPx101) which allows for sub-nm precision in taper-cavity gap. As the taper is brought closer into the evanescent field, the external coupling rate κ_{ex} increases [172], thereby allowing for control of the coupling efficiency η_c – a unique feature of this coupling technique. Control of input polarisation achieves perfect phase-matching into the resonant modes of the cavity. In order to obtain transmission signals as shown in fig. 2.7c, the laser frequency is swept while the cavity transmission is monitored on a photodetector. In order to calibrate the laser frequency sweep, a part of the laser light is directed onto a fiber-loop cavity of known FSR^{2.36} (≈ 250 MHz). This allows calibration of the relative detuning between the laser and the whispering gallery mode cavity. Figure 2.7b shows the variation in the resonant transmission

^{2.36} The fiber-loop cavity is made by splicing together the ends of a 50:50 fiber beam-splitter using an approximately known length of fiber. In order to calibrate the FSR of this cavity, laser light is phase modulated using an EOM, as shown in fig. 2.7a, imparting sidebands of known frequency separation. Thus the loop cavity FSR is calibrated to a known RF modulation frequency.

as a function of the coupling efficiency η_c , obtained by varying the taper-cavity gap. The intrinsic decay rate of the cavity, κ_0 , is obtained in the limit of heavy under-coupling ($\eta_c \rightarrow 0$). The data in fig. 2.7c suggests that $\kappa_0 \approx 2\pi \cdot 450$ MHz, a typical value observed in measurements of the optical cavity with a nanobeam coupled to it^{2.37}.

This spectroscopic technique, by providing access to the cavity's amplitude response, allows for stabilising the laser-cavity detuning at any point within the cavity bandwidth, except on resonance. Another technical disadvantage is that since the cavity's amplitude response is susceptible to drifts in probe power and cavity coupling, the detuning is affected by these factors.

Modulation spectroscopy

Another spectroscopic technique relies not on using the cavity's response to a mean optical field, but rather to fluctuations in the input optical field. In order to describe it, it is therefore necessary to see how fluctuations in the input optical field manifest an intracavity fluctuations, and how they subsequently appear in the outgoing field.

Separating out the mean steady state intracavity amplitude from its fluctuating part, viz.

$$\hat{a}(t) = |\bar{a}| + \delta\hat{a}(t),$$

where, $|\bar{a}| := \sqrt{\langle \hat{a}^\dagger \hat{a} \rangle_{ss}} = \left(\frac{4\eta_c}{\kappa} \frac{|\bar{a}_{in}|^2}{1 + (4\Delta^2/\kappa^2)} \right)^{1/2}$,

and inserting it into eq. (2.2.83), results in the equation of motion for the fluctuating part,

$$\delta\hat{a}(t) = \left(i\Delta - \frac{\kappa}{2} \right) \delta\hat{a}(t) + \sqrt{(1 - \eta_c)\kappa} \delta\hat{a}_0(t) + \sqrt{\eta_c\kappa} \delta\hat{a}_{in}(t).$$

^{2.37} For this case, where $\kappa_0 \ll \omega_c$, the intrinsic decay rate may be understood as a combination of several effects [175], i.e.,

$$\kappa_0 = \kappa_{rad} + \kappa_{vol} + \kappa_{surf} + \kappa_{mech} = \omega_c \left(Q_{rad}^{-1} + Q_{vol}^{-1} + Q_{surf}^{-1} + Q_{mech}^{-1} \right),$$

here expressed as contributions to the optical Q-factor. The first term Q_{rad}^{-1} models the losses arising from imperfect confinement of light in the whispering-gallery mode; when the cavity is large (the cavity radius, $R_c > 10 \cdot \lambda$, for example) the losses due to radiation is expected to provide a limit [175] $Q_{rad} < 10^{11}$. In contrast, the data shown in fig. 2.7 features $Q \approx 8 \cdot 10^5$. Losses in the cavity volume, leading to the contribution Q_{vol}^{-1} , arise from optical absorption in SiO₂; at the operating wavelength of 780 nm, estimates suggest $Q_{vol} < 10^{10}$ [175, 176]. Effects such as scattering off of surface inhomogeneities [175, 177] and/or contamination from water absorption [176], that depend on the surface area, go into Q_{surf}^{-1} . Water absorption at 1500 nm is known to provide the limit $Q_{surf,H_2O} < 10^9$, which is known to be recoverable after sustained bake-out [176]; at 780 nm, the effect is expected to be smaller, mediated by harmonics of the absorption at 1500 nm. Unlike micro-cavities formed by surface reflow [166], for the disk geometry employed in this thesis (see fig. 2.6c), surface scattering is known to play an important role in limiting the optical-Q [178]. A simple model suggests that [179] $Q_{surf,scat} \propto R_c^{1/2} \langle \ell_{surf}^2 \rangle^{-1} \ell_{surf,corr}^{-2}$, where R_c is the disk radius, $\langle \ell_{surf}^2 \rangle$ is the variance in the surface roughness and $\ell_{surf,corr}$ the correlation length of the roughness pattern. Compared against the value of $Q_{surf,scat} \approx 10^9$ reported in [179], our value of $Q \approx 10^6$ would imply a roughness pattern for which $\langle \ell_{surf}^2 \rangle^{1/2} \ell_{surf,corr} \approx (150 \text{ nm})^2$. Given that this is an unusually large number, we believe that the contribution Q_{mech} due to optical losses in the presence of the beam is responsible for the observed linewidth.

Taking Fourier transforms of either side,

$$\delta\hat{a}[\Omega] = \chi_a[\Omega] \left(\sqrt{(1-\eta_c)\kappa} \delta\hat{a}_0[\Omega] + \sqrt{\eta_c\kappa} \delta\hat{a}_{\text{in}}[\Omega] \right), \quad (2.2.84)$$

$$\text{where, } \chi_a[\Omega] = \left(-i(\Omega + \Delta) + \frac{\kappa}{2} \right)^{-1},$$

is the susceptibility of the intracavity optical field to fluctuations in the input optical field. Note that the susceptibility encodes the cavity response as well as the laser-cavity detuning. The fluctuations in the outgoing field, given by the input-output relation eq. (2.2.80),

$$\delta\hat{a}_{\text{out}}[\Omega] = (1 - \eta_c\kappa \chi_a[\Omega]) \delta\hat{a}_{\text{in}}[\Omega] - \sqrt{\eta_c(1-\eta_c)\kappa} \chi_a[\Omega] \delta\hat{a}_0[\Omega], \quad (2.2.85)$$

carries this information, and may be retrieved by probing the cavity using an input of known spectral content.

One way to perform this, originally developed by Pound, Drever, Hall (PDH) and others, involves frequency modulating the input field. In our experiment, depicted in fig. 2.8a, the input field $\hat{a}_{\text{in}}(t)$ is passed through an electro-optic modulator (EOM), picking up a sinusoidal modulation of its phase, viz.

$$\begin{aligned} \hat{a}_{\text{in}}(t) &= |\bar{a}_{\text{in}}| e^{-i(\omega_\ell t - \xi_{\text{mod}} \sin \Omega_{\text{mod}} t)} \\ &\approx |\bar{a}_{\text{in}}| e^{-i\omega_\ell t} \left(1 + \frac{\xi_{\text{mod}}}{2} e^{i\Omega_{\text{mod}} t} - \frac{\xi_{\text{mod}}}{2} e^{-i\Omega_{\text{mod}} t} \right), \end{aligned} \quad (2.2.86)$$

approximated as sidebands at frequencies $\omega_\ell \pm \Omega_{\text{mod}}$ with depth $\xi_{\text{mod}} \ll 1$. The transmitted field is given by,

$$\hat{a}_{\text{out}}(t) = |\bar{a}_{\text{in}}| e^{-i\omega_\ell t} \left(\chi_a^{\text{out}}[0] + \frac{\xi_{\text{mod}}}{2} \chi_a^{\text{out}}[\Omega_{\text{mod}}] e^{i\Omega_{\text{mod}} t} - \frac{\xi_{\text{mod}}}{2} \chi_a^{\text{out}}[-\Omega_{\text{mod}}] e^{-i\Omega_{\text{mod}} t}, \right)$$

where, $\chi_a^{\text{out}}[\Omega] := 1 - \eta_c\kappa \chi_a[\Omega]$, represents the susceptibility of the output field to the input field (see eq. (2.2.85)). The transmitted sidebands now encode the cavity response, which appears in the detected photocurrent,

$$\begin{aligned} \langle \hat{I}_{\text{out}} \rangle &\propto |\bar{a}_{\text{in}}|^2 |\chi_a^{\text{out}}[0]|^2 + |\bar{a}_{\text{in}}|^2 \frac{\xi_{\text{mod}}^2}{4} \left(|\chi_a^{\text{out}}[\Omega_{\text{mod}}]|^2 + |\chi_a^{\text{out}}[-\Omega_{\text{mod}}]|^2 \right) \\ &\quad + |\bar{a}_{\text{in}}|^2 \xi_{\text{mod}} \text{Re} \left[(\chi_a^{\text{out}}[0] \chi_a^{\text{out}}[\Omega_{\text{mod}}] - \chi_a^{\text{out}}[0]^* \chi_a^{\text{out}}[-\Omega_{\text{mod}}]) e^{-i\Omega_{\text{mod}} t} \right] \\ &\quad + |\bar{a}_{\text{in}}|^2 \frac{\xi_{\text{mod}}}{2} \text{Re} \left[\chi_a^{\text{out}}[\Omega_{\text{mod}}] \chi_a^{\text{out}}[-\Omega_{\text{mod}}]^* e^{2i\Omega_{\text{mod}} t} \right], \end{aligned}$$

as a DC term, a term oscillating at the modulation frequency Ω_{mod} , and one oscillating at twice the modulation frequency. For a cavity with a symmetric response about resonance, the DC term does not carry unambiguous information regarding the laser-cavity detuning. The term oscillating at Ω_{mod} does furnish this information.

As shown in fig. 2.8, the photocurrent is band-pass-filtered to isolate the component at Ω_{mod} , appropriately amplified (Minicircuits ZFL-500LN, or Femto HVA-200M) and mixed-down (Minicircuits ZP-3) with an electronic local oscillator (LO) at Ω_{mod} . Care is taken to

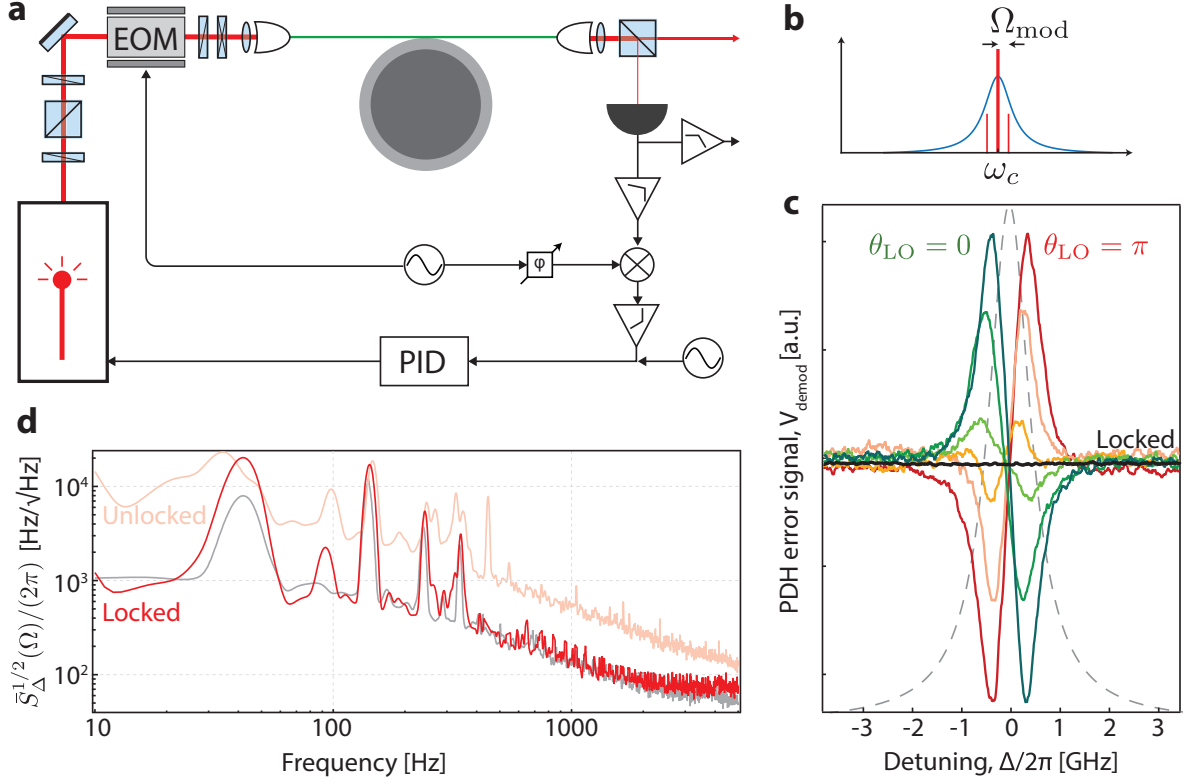


Fig. 2.8 – **Frequency modulation spectroscopy.** (a) Experimental schematic of the spectroscopy scheme: an EOM driven by a RF generator produces frequency modulation sidebands on the detuned probe laser. The cavity transmission is detected using an avalanche photodetector, whose output is demodulated by a phase-tuned RF local oscillator. The mixer output may additionally be used to stabilise the probe on cavity resonance. (b) Schematic of the single-sideband technique: near resonance, the frequency modulation sidebands get transduced by the cavity phase response to amplitude modulation in transmission. Ideally, on resonance, the transmitted sidebands interfere destructively. (c) Demodulated output from the mixer as the laser is swept over cavity resonance. The various traces show the voltage trace as the electronic LO phase is tuned over half a cycle. The gray dashed line is an overlay of the cavity magnitude response plotted from the estimate of the linewidth obtained from the PDH signal. Black trace shows an in-loop signal once the laser is locked to cavity resonance. (d) Residual laser-cavity detuning noise estimated using the input into the laser frequency actuator. Gray is electronic noise in the control loop.

ensure that the double-balanced mixer is operated in its linear regime and that its output passes through appropriate image-rejection filters. The LO is a phase-controlled copy of the signal used to drive the phase modulator, i.e. $V_{\text{LO}} = |V_{\text{LO}}| \sin(\Omega_{\text{mod}}t + \theta_{\text{LO}})$. The demodulated voltage at the output of the mixer,

$$V_{\text{demod}} \propto |\bar{a}_{\text{in}}|^2 \zeta_{\text{mod}} \cdot |V_{\text{LO}}| \cdot M_{\text{PDH}} \sin(\theta_{\text{LO}} + \theta_{\text{PDH}}). \quad (2.2.87)$$

Here, the magnitude (M_{PDH}) and phase (θ_{PDH}) of the PDH error signal is determined by the identity,

$$M_{\text{PDH}} e^{i\theta_{\text{PDH}}} = \chi_a^{\text{out}}[0] \chi_a^{\text{out}}[\Omega_{\text{mod}}] - \chi_a^{\text{out}}[0]^* \chi_a^{\text{out}}[-\Omega_{\text{mod}}] \approx \Omega_{\text{mod}} \left[\frac{d|\chi_a^{\text{out}}[\Omega]|^2}{d\Omega} \right]_{\Omega=0},$$

where the approximation is for the case where the modulation frequency is much smaller than the cavity bandwidth, i.e. $\Omega_{\text{mod}} \ll \frac{\kappa}{2}$, and therefore, $\chi_a^{\text{out}}[\Omega_{\text{mod}}] \approx \chi_a^{\text{out}}[0] + \Omega_{\text{mod}} \frac{d\chi_a^{\text{out}}}{d\Omega}$. In this

unresolved-sideband case, $\theta_{\text{PDH}} \approx 0$, and the demodulated voltage, maximised for the choice $\theta_{\text{LO}} = 0$, provides the derivative of the magnitude response of the cavity transmission.

Figure 2.8c shows examples of the demodulated voltage as θ_{LO} is varied over half a cycle. At the optimal setting of the LO phase, $\theta_{\text{LO}} \approx 0$, the demodulated voltage provides the best error signal for stabilising the laser frequency to cavity resonance, i.e. $\Delta = 0$. This is realised by sending a copy of V_{demod} through a PI controller, appropriate filtering stages, and into the laser frequency controller actuating on the diode current. The black trace shows the actuator input when the laser is locked. Figure 2.8d shows the power spectral density of the actuator input, calibrated in units of laser-cavity detuning, providing an estimate of the residual detuning noise when the laser is nominally locked. Note that the PDH error signal voltage (eq. (2.2.87)), $V_{\text{demod}} \propto \Omega_{\text{mod}}$, enabling calibration of the voltage noise in units of frequency. Low frequency broadband suppression of detuning noise $< 10^3 \text{ Hz}/\sqrt{\text{Hz}}$ at offset frequencies up to 1 kHz is easily achieved in our experiment; this is mainly limited by background electronic noise (grey trace) from the photodetector and control electronics. This level of detuning noise suppression proves crucial for experiment reported in Chapter 4, where this data will be revisited.

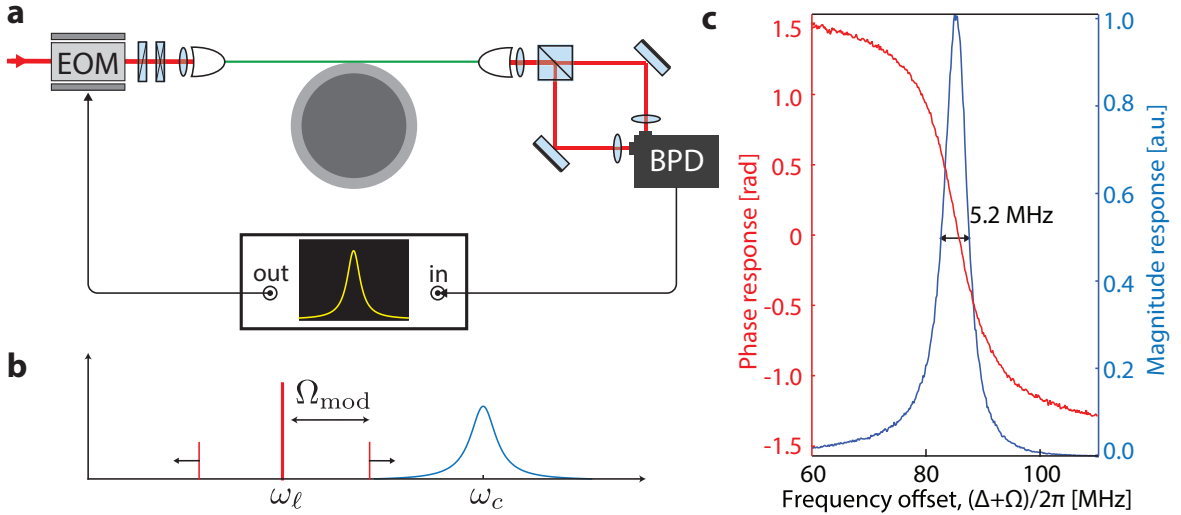


Fig. 2.9 – **Single-sideband modulation spectroscopy.** (a) Experimental schematic of the spectroscopy scheme: an EOM driven by a network analyser imprints sidebands on the detuned probe laser. The cavity transmission is detected using a pair of balanced photodetectors, whose output is demodulated by the network analyser. (b) Schematic of the single-sideband technique: by being far detuned from the cavity resonance ω_c , specifically $|\Delta| \gg \kappa$, as the modulation frequency Ω_{mod} is swept, only one of the sidebands probes the cavity. (c) Example of a response taken on a microtoroid cavity, showing a linewidth of $\kappa = 2\pi \cdot 5.2 \text{ MHz}$.

A variant of frequency-modulation spectroscopy which may be profitably employed when the cavity bandwidth is small compared to the accessible modulation frequency will be briefly described now. The central advantage of this technique, over standard PDH spectroscopy (as above), is that very little optical power actually enters the cavity; for exceptionally high-Q cavities suffering from low threshold for optical nonlinearities [180], this can be a technical boon.

As shown in fig. 2.9b, the probe laser is far detuned from the cavity, i.e. $\Delta \ll -\frac{\kappa}{2}$, so that only one of the phase-modulation sidebands (here, upper sideband) probes the cavity response. In this effectively single-sideband modulation scenario, no extraneous interference occurs with

the lower sideband, giving a demodulated voltage,

$$V_{\text{demod}} \propto |\bar{a}_{\text{in}}|^2 \zeta_{\text{mod}} \cdot |\chi_a^{\text{out}}[\Omega_{\text{mod}}]| \sin(\theta_{\text{LO}} + \arg \chi_a^{\text{out}}[\Omega_{\text{mod}}]),$$

which, unlike the PDH voltage (eq. (2.2.87)), directly provides access to the real ($\theta_{\text{LO}} = \frac{\pi}{2}$) and imaginary ($\theta_{\text{LO}} = 0$) parts of the cavity response.

In the experiment, as shown in fig. 2.9a, both the modulation and demodulation are performed using a RF network analyser (Agilent, E5061B), so that the photodetected signal can be simultaneously demodulated over the two phases. Combining this quadrature-demodulated signal gives the magnitude and phase response of the cavity shown in fig. 2.9c. Being a coherent detection technique, exceptionally low intracavity photon numbers ($|\bar{a}|^2 < 100$) may be reliably used, at the expense of longer averaging time.

In closing, we note that an additional frequency modulation on the sidebands allows for stabilisation of the probe laser at a variable offset detuning from cavity resonance.

2.2.3 Photon-phonon coupling in a cavity

An optical cavity resonant at a discrete set of frequencies ω , defined as a structure supporting harmonic electromagnetic fields

$$\mathbf{E}(\mathbf{r}, t) = \mathbf{E}(\mathbf{r})e^{-i\omega t}, \quad \mathbf{H}(\mathbf{r}, t) = \mathbf{H}(\mathbf{r})e^{-i\omega t}, \quad (2.2.88)$$

is described by the Maxwell equations [170],

$$\nabla \times \mathbf{E}(\mathbf{r}) = i\omega \mu(\mathbf{r}) \mathbf{H}(\mathbf{r}), \quad \nabla \times \mathbf{H}(\mathbf{r}) = -i\omega \epsilon(\mathbf{r}) \mathbf{E}(\mathbf{r}), \quad (2.2.89)$$

where μ is the magnetic permeability (a strictly real number), and ϵ is the electric permittivity (a possibly complex number^{2.38}). Note that the resonance frequency ω is allowed to be complex, so as to describe intrinsic losses of the cavity. The assumption that the resonance frequencies form a discrete set implies that the domain, V , forming the cavity is finite; we assume that this domain is simply-connected so that all the usual manipulations of vector calculus hold.

In this setting, the cavity may be perturbed only via a limited set of changes: (1) perturbation of the dielectric constants, μ, ϵ , through the introduction/removal of material, and/or, (2) changes in the cavity domain V , for example by changes in the boundary ∂V . Both perturbations lead to a change in the cavity frequency ω . When these effects are caused by an underlying elastic deformation field \mathbf{u} (as defined in section 2.2.1), a coupling between the cavity electromagnetic field and the elastodynamic field results, which we compute now.

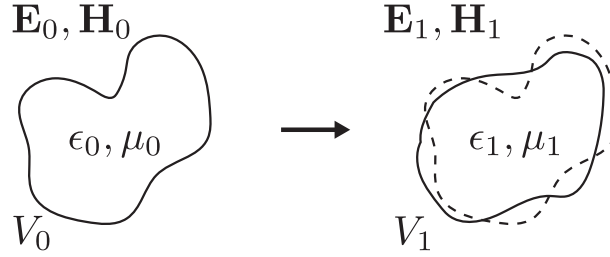


Fig. 2.10 – **Schematic of cavity perturbation.** Left shows region V_0 forming a cavity of material characterised by dielectric constants ϵ_0, μ_0 ; right shows the region deformed to a new domain V_1 , and with possibly different dielectric constants ϵ_1, μ_1 .

Following the work of Bethe and Schwinger [181] (see also [182]), we consider the two configurations shown in fig. 2.10, depicting a cavity perturbed in shape, i.e. $V_0 \rightarrow V_1$, and dielectric constants $(\epsilon_0(\mathbf{r}), \mu_0(\mathbf{r})) \rightarrow (\epsilon_1(\mathbf{r}), \mu_1(\mathbf{r}))$. Each situation is defined by equations analogous to eq. (2.2.89), viz.

$$\begin{aligned} \nabla \times \mathbf{E}_0 &= i\omega_0 \mu_0 \mathbf{H}_0, & \nabla \times \mathbf{H}_0 &= -i\omega_0 \epsilon_0 \mathbf{E}_0, \\ \nabla \times \mathbf{E}_1 &= i\omega_1 \mu_1 \mathbf{H}_1, & \nabla \times \mathbf{H}_1 &= -i\omega_1 \epsilon_1 \mathbf{E}_1. \end{aligned} \quad (2.2.90)$$

^{2.38} The second Maxwell equation follows from $\nabla \times \mathbf{H} = \mathbf{J} + \epsilon \frac{\partial \mathbf{E}}{\partial t}$, where ϵ is the real-valued electric permittivity. Assuming that losses in the cavity are modelled by the presence of a finite conductivity σ , i.e. the current density $\mathbf{J} = \sigma \mathbf{E}$, gives $\nabla \times \mathbf{H} = \left(\sigma + \epsilon \frac{\partial}{\partial t}\right) \mathbf{E}$. Inserting the ansatz eq. (2.2.88) gives, $\nabla \times \mathbf{H} = -i\epsilon\omega \left(1 + i\frac{\sigma}{\omega\epsilon}\right) \mathbf{E}$. The identification, $\epsilon \left(1 + i\frac{\sigma}{\omega\epsilon}\right) \rightarrow \epsilon$, results in a phenomenological permittivity that is complex.

The general strategy is to relate the frequency shifts to mechanical quantities of the electromagnetic field, i.e. its energy and momentum. The change in these mechanical quantities can then be related to the motion of the elastic field.

In order to do this, the first and last equations are re-expressed as,

$$\begin{aligned}\mathbf{H}_1^* \cdot (\nabla \times \mathbf{E}_0) &= i\omega_0\mu_0\mathbf{H}_1^* \cdot \mathbf{H}_0 \\ \mathbf{E}_0 \cdot (\nabla \times \mathbf{H}_1^*) &= i\omega_1\epsilon_1^*\mathbf{E}_1^* \cdot \mathbf{E}_0,\end{aligned}$$

and subtracted to get,

$$\nabla \cdot (\mathbf{H}_1^* \times \mathbf{E}_0) = i(\omega_1\epsilon_1^*\mathbf{E}_1^* \cdot \mathbf{E}_0 - \omega_0\mu_0\mathbf{H}_1^* \cdot \mathbf{H}_0), \quad (2.2.91)$$

where the left-hand side is expressed using the identity $\nabla \cdot (\mathbf{f} \times \mathbf{g}) = \mathbf{g} \cdot \nabla \times \mathbf{f} - \mathbf{f} \cdot \nabla \times \mathbf{g}$. Similar manipulation of the remaining two equations in eq. (2.2.90) gives,

$$\nabla \cdot (\mathbf{H}_0 \times \mathbf{E}_1^*) = -i(\omega_0\epsilon_0^*\mathbf{E}_1^* \cdot \mathbf{E}_0 - \omega_1\mu_1\mathbf{H}_1^* \cdot \mathbf{H}_0). \quad (2.2.92)$$

Adding eq. (2.2.92) and eq. (2.2.91), integrating the resulting equation over the perturbed domain V_1 , and applying Gauss's theorem, results in the Bethe-Schwinger equation [181],

$$\begin{aligned}\oint_{\partial V_1} (\mathbf{H}_1^* \times \mathbf{E}_0 + \mathbf{H}_0 \times \mathbf{E}_1^*) \cdot d\mathbf{A} &= i \int_{V_1} [(\omega_1\epsilon_1^* - \omega_0\epsilon_0^*)\mathbf{E}_1^* \cdot \mathbf{E}_0 \\ &\quad + (\omega_1\mu_1 - \omega_0\mu_0)\mathbf{H}_1^* \cdot \mathbf{H}_0] d^3r,\end{aligned}$$

where \mathbf{A} denotes the normal to the boundary surface ∂V_1 . Expressing the above equation in a shorthand notation,

$$\mathcal{I}^{(V)} = \omega_1 \mathcal{I}_1^{(\epsilon, \mu)} - \omega_0 \mathcal{I}_0^{(\epsilon, \mu)}$$

$$\text{where, } \mathcal{I}^{(V)} := -i \oint_{\partial V_1} (\mathbf{H}_1^* \times \mathbf{E}_0 + \mathbf{H}_0 \times \mathbf{E}_1^*) \cdot d\mathbf{A} \quad (2.2.93)$$

$$\mathcal{I}_{0,1}^{(\epsilon, \mu)} := \int_{V_1} (\epsilon_{0,1}^* \mathbf{E}_1^* \cdot \mathbf{E}_0 + \mu_{0,1} \mathbf{H}_1^* \cdot \mathbf{H}_0) d^3r,$$

the frequency shift of the cavity is given by the formally exact recursion,

$$\omega_1 = \omega_0 + \frac{\mathcal{I}^{(V)}}{\mathcal{I}_0^{(\epsilon, \mu)}} - \omega_1 \left(\frac{\mathcal{I}_1^{(\epsilon, \mu)} - \mathcal{I}_0^{(\epsilon, \mu)}}{\mathcal{I}_0^{(\epsilon, \mu)}} \right). \quad (2.2.94)$$

A series of systematic approximations may now be performed; firstly the recursion eq. (2.2.94) is iterated once to obtain the approximate fractional frequency shift,

$$\frac{\delta\omega}{\omega_0} := \frac{\omega_1 - \omega_0}{\omega_0} \approx \frac{\omega_0^{-1}\mathcal{I}^{(V)}}{\mathcal{I}_0^{(\epsilon, \mu)}} - \frac{\mathcal{I}_1^{(\epsilon, \mu)} - \mathcal{I}_0^{(\epsilon, \mu)}}{\mathcal{I}_0^{(\epsilon, \mu)}}; \quad (2.2.95)$$

and secondly, the integrals \mathcal{I} may be estimated approximately.

2. FOUNDATIONS

The surface integral $\mathcal{I}^{(V)}$ (see eq. (2.2.93)) consists of two terms. However, assuming that the boundaries $\partial V_{0,1}$ are essentially lossless (i.e. both the initial domain, and the perturbed domain have no intrinsic radiation loss), the electric field satisfies the boundary condition $\mathbf{E}_i|_{\partial V_i} = 0$ for each scenario $i = 0, 1$. Under this assumption,

$$\begin{aligned}\mathcal{I}^{(V)} &\approx -i \oint_{\partial V_1} \mathbf{H}_1^* \times \mathbf{E}_0 \cdot d\mathbf{A} \\ &= -i \left(\oint_{\partial V_1 - \partial V_0} + \oint_{\partial V_0} \right) \mathbf{H}_1^* \times \mathbf{E}_0 \cdot d\mathbf{A} \\ &= -i \oint_{\partial V_1 - \partial V_0} \mathbf{H}_1^* \times \mathbf{E}_0 \cdot d\mathbf{A},\end{aligned}\tag{2.2.96}$$

where by $\partial V_1 - \partial V_0$, we mean the surface enclosing the volume $\Delta V := V_1 - V_0$, defined as the set difference of the two domains.

The final approximation consists of assuming that the perturbation does not appreciably alter the mode structure of the cavity, so that,

$$\mathbf{E}_1 \approx \mathbf{E}_0, \quad \mathbf{H}_1 \approx \mathbf{H}_0.\tag{2.2.97}$$

Inserting this in eq. (2.2.96),

$$\mathcal{I}^{(V)} \approx -i \oint_{\partial V_1 - \partial V_0} \mathbf{H}_0^* \times \mathbf{E}_0 \cdot d\mathbf{A} = -\omega_0 \int_{\Delta V} \left(\epsilon_0 |\mathbf{E}_0|^2 - \mu_0 |\mathbf{H}_0|^2 \right) d^3r,\tag{2.2.98}$$

where the second equality is a consequence of Poynting's theorem [170]. Under the approximation eq. (2.2.97), the integrals $\mathcal{I}_{0,1}^{(\epsilon,\mu)}$ take the form,

$$\begin{aligned}\mathcal{I}_0^{(\epsilon,\mu)} &\approx \int_{V_0} \left(\epsilon_0^* |\mathbf{E}_0|^2 + \mu_0 |\mathbf{H}_0|^2 \right) d^3r \\ \mathcal{I}_1^{(\epsilon,\mu)} - \mathcal{I}_0^{(\epsilon,\mu)} &\approx \int_{V_0} \left(\Delta\epsilon^* |\mathbf{E}_0|^2 + \Delta\mu |\mathbf{H}_0|^2 \right) d^3r,\end{aligned}\tag{2.2.99}$$

where $\Delta\epsilon^* := \epsilon_1 - \epsilon_0$, and, $\Delta\mu := \mu_1 - \mu_0$, are the perturbations in the dielectric constants.

Inserting the approximate integrals eqs. (2.2.98) and (2.2.99) into the fractional frequency shift equation (eq. (2.2.95)) shows that, at the crude level of perturbation theory carried out here, the frequency shift arises from two independent contributions, viz.

$$\frac{\delta\omega}{\omega_0} \approx \left(\frac{\delta\omega}{\omega_0} \right)_V + \left(\frac{\delta\omega}{\omega_0} \right)_{\epsilon,\mu}$$

$$\text{where, } \left(\frac{\delta\omega}{\omega_0} \right)_V = - \frac{\int_{\Delta V} \left(\epsilon_0 |\mathbf{E}_0|^2 - \mu_0 |\mathbf{H}_0|^2 \right) d^3r}{\int_{V_0} \left(\epsilon_0^* |\mathbf{E}_0|^2 + \mu_0 |\mathbf{H}_0|^2 \right) d^3r}\tag{2.2.100}$$

$$\text{and, } \left(\frac{\delta\omega}{\omega_0} \right)_{\epsilon,\mu} = - \frac{\int_{V_0} \left(\Delta\epsilon^* |\mathbf{E}_0|^2 + \Delta\mu |\mathbf{H}_0|^2 \right) d^3r}{\int_{V_0} \left(\epsilon_0^* |\mathbf{E}_0|^2 + \mu_0 |\mathbf{H}_0|^2 \right) d^3r}.$$

The first terms arises purely from volume deformation of the cavity domain, while the second arises purely from changes in dielectric constant(s) within the cavity. Note that for a predominantly dielectric cavity, for which the electric field energy is much larger than the magnetic energy, an increase in the cavity dielectric constants and/or an increase in the cavity volume, both lead to a decrease in the resonance frequency. This analogy has been previously used to model moving boundary effects as an effective dielectric perturbation [183]. Finally we note that the conceptual ambiguities associated with identifying the force applied by an electromagnetic field on a moving body [184, 185] appear to be less severe in the approach outlined here, wherein the emphasis is on a well-defined observable – cavity frequency – and not on the details of the microscopic light-matter interaction.

2.2.3.1 Effective description: simplified cavity optomechanics

The equations eq. (2.2.100) describes the effect of volume deformations and dielectric perturbations on an electromagnetic cavity. If both these effects are assumed to be due to an underlying elastic displacement field^{2.39} \mathbf{u} (see section 2.2.1), i.e.

$$\Delta V \approx (\nabla \cdot \mathbf{u})V_0, \quad \Delta \epsilon^* \approx (\nabla \epsilon^*) \cdot \mathbf{u}, \quad \Delta \mu = (\nabla \mu) \cdot \mathbf{u}, \quad (2.2.101)$$

then eq. (2.2.100) provide a description of the cavity electromagnetic field interacting with the elastic field. Note however that other forms of coupling, for example through the elasto-optic effect [186, 187], which renders volume deformation and dielectric perturbation not independent, do not follow the above prescription.

Confining attention to the case of a dielectric cavity undergoing perturbation of its electric permittivity due to an elastic deformation (other cases are treated identically), the cavity frequency shift in eq. (2.2.100) takes the form,

$$\delta\omega(t) \approx \frac{-\omega_0 \int_{V_0} |\mathbf{E}_0|^2 (\mathbf{u} \cdot \nabla \epsilon^*) d^3r}{\int_{V_0} (\epsilon_0 |\mathbf{E}_0|^2 + \mu_0 |\mathbf{H}_0|^2) d^3r} = -\sum_n G_n x_{zp,n} (\hat{b}_n + \hat{b}_n^\dagger). \quad (2.2.102)$$

The second equality is obtained by employing the elastic mode expansion (eq. (2.2.21)),

$$\mathbf{u}(\mathbf{r}, t) = \sum_n \tilde{\mathbf{u}}_n(\mathbf{r}) x_{zp,n} (\hat{b}_n + \hat{b}_n^\dagger),$$

and defining the *cavity frequency pull parameter*,

$$G_n := \omega_0 \frac{\int_{V_0} |\mathbf{E}_0|^2 (\tilde{\mathbf{u}}_n(\mathbf{r}) \cdot \nabla \epsilon^*) d^3r}{\int_{V_0} (\epsilon_0 |\mathbf{E}_0|^2 + \mu_0 |\mathbf{H}_0|^2) d^3r}. \quad (2.2.103)$$

^{2.39} The following relations are derived as follows. The volume change, ΔV , due to an elastic displacement \mathbf{u} is that swept out by the surface element $d\mathbf{A}$ transverse to the displacement, i.e.

$$\Delta V = \int \mathbf{u} \cdot d\mathbf{A} = \int (\nabla \cdot \mathbf{u}) d^3\mathbf{r} \approx \nabla \cdot \mathbf{u} \int d^3\mathbf{r} = (\nabla \cdot \mathbf{u})V_0.$$

For the dielectric constants, say ϵ^* , a Taylor expansion gives,

$$\Delta \epsilon^* \approx \frac{\partial \epsilon^*}{\partial \mathbf{r}} \cdot d\mathbf{r} = (\nabla \epsilon^*) \cdot \mathbf{u}.$$

Finally, the total hamiltonian of the photon-phonon system takes the form (eqs. (2.2.24) and (2.2.70)),

$$\begin{aligned}\hat{H} &= \hbar\omega_c(\mathbf{u})\hat{a}^\dagger\hat{a} + \sum_n \hbar\Omega_n \left(\hat{b}_n^\dagger\hat{b}_n + \frac{1}{2} \right) \\ &= \hbar\omega_c\hat{a}^\dagger\hat{a} - \sum_n \hbar(G_n x_{zp,n})\hat{a}^\dagger\hat{a}(\hat{b}_n + \hat{b}_n^\dagger) + \sum_n \hbar\Omega_n \left(\hat{b}_n^\dagger\hat{b}_n + \frac{1}{2} \right).\end{aligned}\quad (2.2.104)$$

The photon-phonon interaction, mediated by elastic perturbation of the cavity field, takes the form of several low frequency ($\Omega_n \ll \omega_c$) simple harmonic mechanical oscillators coupled to a single cavity mode via a (predominantly) dispersive mechanism. Note that the unambiguously defined product, the *vacuum optomechanical coupling rate*,

$$g_{0,n} := G_n x_{zp,n} = G_n \left(\frac{\hbar}{2m_n\Omega_n} \right)^{1/2},$$

characterises the strength of the coupling between the photon and phonon degrees of freedom.

On the one hand, the optomechanical coupling leads to a cavity frequency shift, $\sum_n G_n \hat{x}_n$, linearly proportional to the mechanical oscillator position. On the other hand, each mechanical mode experiences a radiation pressure force,

$$\hat{F}_{\text{rad},n} = -\hbar G_n \hat{a}^\dagger \hat{a},$$

proportional to the intracavity photon number.

We now focus on a single mechanical mode, described by its position $\hat{x} = x_{zp}(\hat{b} + \hat{b}^\dagger)$, interacting with a cavity field at the rate $g_0 = Gx_{zp}$. The equations of motion for the intracavity optical field \hat{a} and the mechanical oscillator position \hat{x} , that follow from the hamiltonian in eq. (2.2.104), together with the cavity-waveguide coupling and loss terms of either subsystem (see eqs. (2.2.27) and (2.2.79)), are [51],

$$\begin{aligned}\dot{\hat{a}} &= \left(i(\Delta - G\hat{x}) - \frac{\kappa}{2} \right) \hat{a} + \sqrt{(1 - \eta_c)\kappa} \delta\hat{a}_0 + \sqrt{\eta_c\kappa} \hat{a}_{\text{in}} \\ \ddot{\hat{x}} + \Gamma_m \dot{\hat{x}} + \Omega_m^2 \hat{x} &= m^{-1} \left(\delta\hat{F}_{\text{th}} - \hbar G \hat{a}^\dagger \hat{a} \right).\end{aligned}$$

Steady-state shifts

These equations of motion, due to their nonlinearity, sustain several steady-states. Employing the ansatz,

$$\hat{a}(t) = \bar{a} + \delta\hat{a}(t), \quad \hat{x}(t) = \bar{x} + \delta\hat{x}(t),$$

the steady-state amplitudes are determined by the nonlinear algebraic relations,

$$\bar{a} = \frac{-\sqrt{\eta_c\kappa} \bar{a}_{\text{in}}}{i(\Delta - G\bar{x}) - \kappa/2}, \quad \bar{x} = -\frac{\hbar G}{m\Omega_m^2} |\bar{a}|^2. \quad (2.2.105)$$

Schematically, this leads to a static shift in the mean laser-cavity detuning due to the mean position of the mechanical element, \bar{x} , leading to a change in the mean intracavity photon number. The resulting delayed radiation pressure force causes the mean position of the

oscillator to change; ultimately, the steady-state is stable when these changes are self-consistent [188].

In order to investigate the potential instability, eq. (2.2.105) may be expressed as the cubic equation,

$$\frac{\bar{x}}{x_{\text{zfp}}} + \left(\frac{2\Delta}{\kappa} - \frac{2g_0}{\kappa} \frac{\bar{x}}{x_{\text{zfp}}} \right)^2 \frac{\bar{x}}{x_{\text{zfp}}} = -\frac{g_0}{\Omega_{\text{m}}} n_{c,\text{res}},$$

for the normalised steady-state displacement \bar{x}/x_{zfp} . Here $n_{c,\text{res}} = \frac{4\eta_c}{\kappa} |\bar{a}_{\text{in}}|^2$, the mean intracavity photon number on resonance, proxies the injected power in this equation. The necessary condition for bistability is that at least two roots of this equation are real. This happens when [189],

$$\frac{2\Delta}{\kappa} < -\sqrt{3}, \quad \text{and,} \quad n_{c,\text{res}} > n_{c,\text{thresh}} := \left(\frac{1}{3\sqrt{3}} \right) \frac{\kappa\Omega_{\text{m}}}{g_0^2}.$$

However these are not sufficient conditions [190]. For the system employed in this thesis, the static optomechanical bistability threshold, $n_{c,\text{thresh}} \approx 2 \cdot 10^6$, while the maximum mean intracavity photon numbers employed are 100 times smaller.

The detuning instability due to an inconsistent steady-state has been observed in experiments in the 1980's employing very low frequency ($\Omega_{\text{m}} \approx 2\pi \cdot 1 \text{ Hz}$) oscillators [191, 192].

The steady-state, if stable, leads to a static radiation pressure force, $\hbar G |\bar{a}|^2$, that causes a shift in the mechanical oscillator resonance frequency,

$$\Omega_{\text{m,stat}}^2 = m^{-1} \frac{\partial}{\partial \bar{x}} (\hbar G |\bar{a}|^2),$$

which has also been observed in early experiments with low frequency oscillators [193].

Dynamical back-action

Assuming a stable steady-state, fluctuations $\delta\hat{a}, \delta\hat{x}$ are governed by linearised equations of motion [51],

$$\begin{aligned} \delta\dot{\hat{a}} &= \left(i\Delta - \frac{\kappa}{2} \right) \delta\hat{a} + ig_0\sqrt{n_c} \frac{\delta\hat{x}}{x_{\text{zfp}}} + \sqrt{(1-\eta_c)\kappa} \delta\hat{a}_0 + \sqrt{\eta_c\kappa} \delta\hat{a}_{\text{in}} \\ \delta\dot{\hat{x}} + \Gamma_{\text{m}}\delta\dot{\hat{x}} + \Omega_{\text{m}}^2\delta\hat{x} &= m^{-1} \left(\delta\hat{F}_{\text{th}} - \hbar \frac{g_0\sqrt{n_c}}{x_{\text{zfp}}} \left(e^{-i\theta_c} \delta\hat{a} + e^{i\theta_c} \delta\hat{a}^\dagger \right) \right) \end{aligned} \quad (2.2.106)$$

Here we define the magnitude, n_c , and phase, θ_c , of the steady-state intracavity amplitude \bar{a} , given by,

$$n_c := \frac{4\eta_c}{\kappa} \frac{|\bar{a}_{\text{in}}|^2}{1 + (4\Delta^2/\kappa^2)}, \quad \theta_c := \arctan \frac{2\Delta}{\kappa}.$$

The former quantity, n_c , is the mean intracavity photon number. In the case of a single cavity mode, the phase θ_c is redundant, since it may be accommodated for by using an appropriately retarded input field (i.e. $\hat{a}_{\text{in}} \rightarrow \hat{a}_{\text{in}} e^{-i\theta_c}$). Note however that when the cavity is embedded in an interferometer, as for example in our experiments, this corresponds to an equivalent advancement of the LO phase. Keeping this in mind we henceforth set $\theta_c = 0$.

2. FOUNDATIONS

Note finally that the vacuum interaction strength g_0 , is enhanced by the presence of a large ($n_c \gg 1$) intracavity photon number, to the dressed interaction strength,

$$g := g_0 \sqrt{n_c}.$$

It is in fact this dressing of the interaction strength that makes it possible to observe dynamical optomechanical phenomena despite the fact that the cavity frequency shift caused by the per-photon force, $\hbar G$, is small compared to the cavity linewidth κ .

Expressed in terms of the Fourier transform, $\delta\hat{a}[\Omega]$, $\delta\hat{x}[\Omega]$, eq. (2.2.106) takes the form,

$$\begin{aligned} \delta\hat{a}^{(g)}[\Omega] &= \delta\hat{a}^{(0)}[\Omega] + \chi_a^{(0)}[\Omega] \cdot ig \frac{\delta\hat{x}^{(g)}[\Omega]}{x_{zp}} \\ \delta\hat{x}^{(g)}[\Omega] &= \delta\hat{x}^{(0)}[\Omega] - \chi_x^{(0)}[\Omega] \cdot \frac{\hbar g}{x_{zp}} \left(\delta\hat{a}^{(g)}[\Omega] + \delta\hat{a}^{(g)}[-\Omega]^\dagger \right), \end{aligned} \quad (2.2.107)$$

where the intrinsic susceptibilities,

$$\chi_a^{(0)}[\Omega] = \left(-i(\Omega + \Delta) + \frac{\kappa}{2} \right)^{-1}, \quad \chi_x^{(0)}[\Omega] = m^{-1} (\Omega_m^2 - \Omega^2 - i\Omega\Gamma_m)^{-1}, \quad (2.2.108)$$

dictate the response of the cavity and the phonon modes to their respective generalised forces in the absence of optomechanical coupling. In the above equations, we have further defined the intrinsic motion of the cavity field and the mechanical oscillator in the absence of optomechanical coupling:

$$\begin{aligned} \delta\hat{a}^{(0)}[\Omega] &:= \chi_a^{(0)}[\Omega] \left(\sqrt{(1 - \eta_c)\kappa} \delta\hat{a}_0[\Omega] + \sqrt{\eta_c\kappa} \delta\hat{a}_{in}[\Omega] \right) \\ \delta\hat{x}^{(0)}[\Omega] &:= \chi_x^{(0)}[\Omega] \delta\hat{F}_{th}[\Omega], \end{aligned} \quad (2.2.109)$$

while, $\delta\hat{a}^{(g)}$, $\delta\hat{x}^{(g)}$ denote these variables modified by the finite optomechanical interaction.

The generalised forces that drive the optomechanical system in the presence of a finite coupling come in two forms – ones that are due to the dynamics of either mode, and those due to stochastic fluctuations from the environment. The former effectively leads to a re-normalisation of the susceptibilities – an effect called *dynamical back-action* [51, 194, 195]; the latter leads to *stochastic back-action* [51, 64, 65, 67, 96, 196]^{2.40}. When the fluctuations due to the environment are limited to the level allowed by quantum mechanics – for the optical cavity, this means that $\delta\hat{a}_0$, $\delta\hat{a}_{in}$ are in their vacuum state, and for the mechanical oscillator, $\delta\hat{b}_{in}$ is in the vacuum state – *quantum (stochastic) back-action* exclusively drives the motion of the optical cavity and the mechanical oscillator.

Dynamical back-action of the cavity field on the mechanical oscillator becomes prominent when the photon lifetime in the cavity is comparable to the mechanical oscillator period. In

^{2.40} Although widely credited to the investigations of Braginsky's group in Moscow in the 1970's [64, 194], it appears that dynamical back-action was observed and described in the 1930's by a group led by Hartley at Bell Labs [197]. It is however unclear whether the effect was solely due to radiation pressure. It is interesting to note Hartley's recognition of the mechanism being analogous to Raman scattering, an effect that was only described in the previous decade.

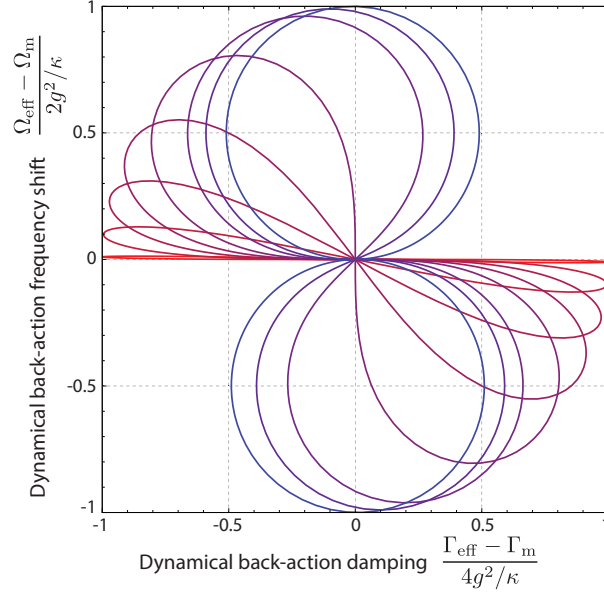


Fig. 2.11 – **Dynamic back-action**. Parametric plot of the normalised optical spring shift vs. the normalised damping, due to dynamic back-action. Each trace is plotted as the normalised detuning, $\frac{2\Delta}{\kappa}$, varies from $-\infty \dots +\infty$. The different traces represent values of the sideband resolution factor, $\frac{2\Omega_m}{\kappa}$ – red represents $\Omega_m = 10^{-2} \cdot \frac{\kappa}{2}$ – deep in the sideband unresolved regime, while blue represents, $\Omega_m = 10^2 \cdot \frac{\kappa}{2}$ – deep in the sideband resolved regime.

this conventional regime ($\kappa \gtrsim \Omega_m \gg \Gamma_m$), the modified dynamics of the mechanical oscillator,

$$\delta\hat{x}^{(g)}[\Omega] = \chi_x^{(g)}[\Omega] (\delta\hat{F}_{\text{th}}[\Omega] + \delta\hat{F}_{\text{BA}}[\Omega]),$$

obtained by solving eq. (2.2.107), features a re-normalised susceptibility,

$$\chi_x^{(g)}[\Omega]^{-1} = \chi_x^{(0)}[\Omega]^{-1} + i\hbar \left(\frac{g}{x_{\text{zfp}}} \right)^2 \left(\chi_a^{(0)}[\Omega] - \chi_a^{(0)}[-\Omega]^* \right) \quad (2.2.110)$$

that modifies the response of the oscillator to the forces that come from its environment – the ambient thermal environment, as well as the stochastic back-action

$$\delta\hat{F}_{\text{BA}}[\Omega] := -\hbar \frac{g}{x_{\text{zfp}}} \left(\delta\hat{a}^{(0)}[\Omega] + \delta\hat{a}^{(0)}[-\Omega]^\dagger \right) = -\hbar \frac{g}{x_{\text{zfp}}} \sqrt{2} \delta\hat{q}^{(0)}[\Omega], \quad (2.2.111)$$

due to the optical environment due to the optomechanical coupling. Note that the stochastic back-action force is due to fluctuations in the amplitude of the intracavity field, which, for a strong field, is equivalent to intracavity photon number fluctuations.

The re-normalised mechanical susceptibility [51],

$$\begin{aligned} \frac{\chi_x^{(g)}[\Omega]^{-1}}{m} &\approx \frac{\chi_x^{(0)}[\Omega]^{-1}}{m} + 2ig^2\Omega_m (\chi_a^{(0)}[\Omega_m] - \chi_a^{(0)}[-\Omega_m]^*) \\ &= (-\Omega^2 + \Omega_m^2 - i\Omega\Gamma_m) + 2ig^2\Omega_m (\chi_a^{(0)}[\Omega_m] - \chi_a^{(0)}[-\Omega_m]^*) \\ &= -\Omega^2 + \left[\Omega_m^2 + 2g^2\Omega_m \text{Re} i(\chi_a^{(0)}[\Omega_m] - \chi_a^{(0)}[-\Omega_m]^*) \right] \\ &\quad - i\Omega \left[\Gamma_m - 2g^2 \frac{\Omega_m}{\Omega} \text{Im} i(\chi_a^{(0)}[\Omega_m] - \chi_a^{(0)}[-\Omega_m]^*) \right] \end{aligned}$$

describes a harmonic oscillator with a shifted frequency,

$$\begin{aligned}\Omega_{\text{eff}} &:= \left[\Omega_m^2 + 2g^2 \Omega_m \operatorname{Re} i(\chi_a^{(0)}[\Omega_m] - \chi_a^{(0)}[-\Omega_m]^*) \right]^{1/2} \\ &\approx \Omega_m + \frac{2g^2}{\kappa} \left(\frac{2(\Delta + \Omega_m)/\kappa}{1 + (2(\Delta + \Omega_m)/\kappa)^2} + \frac{2(\Delta - \Omega_m)/\kappa}{1 + (2(\Delta - \Omega_m)/\kappa)^2} \right),\end{aligned}\quad (2.2.112)$$

and modified linewidth [51],

$$\begin{aligned}\Gamma_{\text{eff}} &:= \Gamma_m - 2g^2 \frac{\Omega_m}{\Omega} \operatorname{Im} i(\chi_a^{(0)}[\Omega_m] - \chi_a^{(0)}[-\Omega_m]^*) \\ &\approx \Gamma_m + \frac{4g^2}{\kappa} \left(\frac{1}{1 + (2(\Delta + \Omega_m)/\kappa)^2} - \frac{1}{1 + (2(\Delta - \Omega_m)/\kappa)^2} \right).\end{aligned}\quad (2.2.113)$$

Figure 2.11 shows the modification of the mechanical frequency, *optical spring*, against the possible values of the linewidth modification, *optical damping*, as the laser-cavity detuning is varied from negative values, into resonance, and large positive values. The various traces show the effect of the sideband resolution, $\frac{2\Omega_m}{\kappa}$, which dictates the efficiency of the autonomous feedback enforced by the cavity that leads to dynamic back-action. Such dynamic back-action on the mechanical oscillator leading to optical spring [198, 199], linewidth narrowing (amplification) [200–202] or damping (cooling) [203–207] have been observed. In the resolved-sideband regime, characterised by $\kappa \ll \Omega_m$, it becomes possible to cool the mechanical oscillator to a level where its energy is comparable to the energy in its ground state [208–211].

Modification of the optical susceptibility,

$$\chi_a^{(g)}[\Omega]^{-1} = \chi_a^{(0)}[\Omega]^{-1} + i\hbar \frac{g^2}{x_{\text{zp}}^2} \chi_x^{(0)}[\Omega]$$

leads to dynamical back-action on the optical field due to the mechanical oscillator. In the conventional regime this manifests as an optomechanically-induced absorption/transparency [212–214]. In an unconventional regime, characterised by $\Gamma_m \gtrsim \kappa$, which was studied by the author [215], modification of the optical susceptibility can lead to phenomena analogous to lasing. Indeed, the symmetry between the re-normalised optical and mechanical susceptibilities imply that mechanically-induced dynamical back-action on the optical mode is possible. Thus, radiation pressure optomechanical coupling provides an opportunity to control mechanical motion by modifying its susceptibility – an example of autonomous control. The fundamental limit to autonomous control of this kind is set by quantum back-action.

However, it is the alternate provision – that of being able to precisely measure mechanical motion – that a major part of this thesis is concerned with. In particular, in the unresolved sideband regime (i.e. $\kappa \gg \Omega_m$), dynamical back-action is a weak effect, and therefore it becomes possible to measure the intrinsic mechanical motion. The fundamental limit of how well the measurement can be performed is again set by quantum back-action.

2.3 Linear measurements II: cavity-enhanced interferometry

The cavity field, the *meter*, by being coupled to the mechanical oscillator, the *system*, can realise the ideal linear measurement model considered in section 2.1. The task of this measurement chain is to allow for the inference of the intrinsic mechanical motion (defined in eq. (2.2.109)),

$$\delta\hat{x}^{(0)} = \chi_x^{(0)}[\Omega] \delta\hat{F}_{\text{th}}[\Omega].$$

However, the linear coupling between the cavity field and the oscillator precludes the possibility of having exclusive access to the intrinsic motion. From eq. (2.2.107), the intracavity field consists of three terms,

$$\begin{aligned} \delta\hat{a}^{(g)}[\Omega] = & \delta\hat{a}^{(0)}[\Omega] + \left(\frac{ig}{x_{\text{zpt}}} \right) \chi_a^{(0)}[\Omega] \chi_x^{(g)}[\Omega] \chi_x^{(0)}[\Omega]^{-1} \delta\hat{x}^{(0)}[\Omega] \\ & + \left(\frac{ig}{x_{\text{zpt}}} \right) \chi_a^{(0)}[\Omega] \chi_x^{(g)}[\Omega] \delta\hat{F}_{\text{BA}}[\Omega]; \end{aligned} \quad (2.3.1)$$

the first due to the unavoidable intrinsic fluctuations of the intracavity field, the second that contains the transduced motion of the oscillator (possibly modified by dynamical back-action), and the third, the motion of the oscillator driven by the fluctuations of the intracavity field (i.e. quantum back-action).

Since we are interested in retrieving the intrinsic motion, it is desirable that the measurement has no dynamical back-action, i.e. $\chi_x^{(g)}[\Omega] = \chi_x^{(0)}[\Omega]$. From the expressions for the optical spring and damping in eqs. (2.2.112) and (2.2.113), it follows that for resonant probing, i.e. $\Delta = 0$, dynamic back-action is nullified, thus realising an ideal position measurement.

In this case, the cavity transmission, given by the input-output relation (eq. (2.2.80)), carries all three components:

$$\begin{aligned} \delta\hat{a}_{\text{out}}[\Omega] = & \left(1 - \frac{2\eta_c}{1 - 2i\Omega/\kappa} \right) \delta\hat{a}_{\text{in}}[\Omega] - \left(\frac{2\sqrt{\eta_c(1 - \eta_c)}}{1 - 2i\Omega/\kappa} \right) \delta\hat{a}_0[\Omega] \\ & - i \left(\frac{\sqrt{\eta_c}}{1 - 2i\Omega/\kappa} \right) \left(\frac{2g}{\sqrt{\kappa}} \right) \frac{\delta\hat{x}^{(0)}[\Omega] + \delta\hat{x}_{\text{BA}}[\Omega]}{x_{\text{zpt}}}; \end{aligned} \quad (2.3.2)$$

the first two terms represent the intrinsic cavity field leaking out in transmission, while the second line shows the position fluctuations transduced by the measurement interaction, contaminated by the back-action driven position fluctuations,

$$\delta\hat{x}_{\text{BA}}[\Omega] := \chi_x^{(0)}[\Omega] \delta\hat{F}_{\text{BA}}[\Omega].$$

From eq. (2.3.2), it is apparent that the role of the cavity is to enhance measurement sensitivity: roughly, the photon flux (per frequency band at frequency Ω from carrier) corresponding to the zero-point motion (in a frequency bandwidth Γ_m about Ω_m) is $(1 + 4\Omega_m^2/\kappa^2)^{-1} \cdot \eta_c \cdot \frac{4g^2}{\kappa}$. The frequency dependent pre-factor $(1 + 4\Omega_m^2/\kappa^2)^{-1}$ may be interpreted as an additional efficiency penalty arising from the finite bandwidth of the cavity acting as a low-pass filter with respect to the mechanical motion, when the intracavity photon number is kept fixed. In

the deep unresolved-sideband regime, $\Omega_m \ll \kappa$, this efficiency factor is unity. Theoretically, therefore, probing on resonance with a sufficiently large bandwidth cavity provides the ideal meter to sense a given oscillator motion. Assuming $\frac{\Omega_m}{\kappa} \approx 0$, fluctuations of the mechanical oscillator position are confined to the phase quadrature of the output field, given by,

$$\begin{aligned} \delta \hat{p}_{\text{out}}[\Omega] = & (1 - 2\eta_c) \delta \hat{p}_{\text{in}}[\Omega] - 2\sqrt{\eta_c(1 - \eta_c)} \delta \hat{p}_0[\Omega] \\ & - \sqrt{2\eta_c} \left(\frac{2g}{\sqrt{\kappa}} \right) \left(\frac{\delta \hat{x}^{(0)}[\Omega] + \delta \hat{x}_{\text{BA}}[\Omega]}{x_{\text{zp}}} \right). \end{aligned}$$

A homodyne detector tuned to the phase quadrature directly detects $\delta \hat{p}_{\text{out}}$. We define the observable $\delta \hat{y}_{\text{hom}}$ that models the position-equivalent record of the homodyne detector,

$$\delta \hat{y}_{\text{hom}}[\Omega] := -\frac{x_{\text{zp}}}{\sqrt{2\eta_c}} \left(\frac{\sqrt{\kappa}}{2g} \right) \delta \hat{p}_{\text{out}}[\Omega] = \delta \hat{x}_{\text{imp,hom}}[\Omega] + \delta \hat{x}^{(0)}[\Omega] + \delta \hat{x}_{\text{BA}}[\Omega].$$

Here, we have defined,

$$\delta \hat{x}_{\text{imp,hom}}[\Omega] := x_{\text{zp}} \left(\frac{\sqrt{\kappa}}{2g} \right) \left(\frac{2\eta_c - 1}{\sqrt{2\eta_c}} \delta \hat{p}_{\text{in}}[\Omega] + \sqrt{2(1 - \eta_c)} \delta \hat{p}_0[\Omega] \right), \quad (2.3.3)$$

the position-equivalent imprecision in the measurement record; for the relevant conditions ($\Delta = 0, \Omega_m \ll \kappa$), the motion induced by the coupling to the meter – *measurement back-action* – is given by,

$$\delta \hat{x}_{\text{BA}}[\Omega] = \left(\frac{2g}{\sqrt{\kappa}} \right) \frac{\hbar \chi_x^{(0)}[\Omega]}{x_{\text{zp}}} \left(\sqrt{2\eta_c} \delta \hat{q}_{\text{in}}[\Omega] + \sqrt{2(1 - \eta_c)} \delta \hat{q}_0[\Omega] \right). \quad (2.3.4)$$

Note that the definition of the back-action motion depends on the system-meter coupling alone, while that of the measurement imprecision depends also on the meter-detector coupling (i.e. the choice of detector used to measure the meter state – here, homodyne detection).

For quantum-noise-limited optical fields, the measurement imprecision and measurement-back action spectral densities take the form (following from eqs. (2.3.3) and (2.3.4)),

$$\begin{aligned} \bar{S}_{xx}^{\text{imp,hom}}[\Omega] &= \frac{x_{\text{zp}}^2}{4\eta_c} \left(\frac{\kappa}{4g^2} \right) \\ \bar{S}_{xx}^{\text{BA}}[\Omega] &= \frac{\hbar^2}{x_{\text{zp}}^2} \left| \chi_x^{(0)}[\Omega] \right|^2 \left(\frac{4g^2}{\kappa} \right) = \left| \chi_x^{(0)}[\Omega] \right|^2 \bar{S}_{FF}^{\text{BA}}[\Omega], \end{aligned} \quad (2.3.5)$$

so that the product between the quantum-limited back-action force, and the quantum-limited imprecision,

$$\bar{S}_{FF}^{\text{BA}}[\Omega] \bar{S}_{xx}^{\text{imp,hom}}[\Omega] \geq \frac{\hbar^2}{4\eta_c}, \quad (2.3.6)$$

which can approach the ideal lower bound of $\frac{\hbar^2}{4}$, when the cavity is heavily over-coupled (i.e. $\eta_c \rightarrow 1$). Therefore, in principle, the cavity optomechanical interaction, together with homodyne detection of the optical field, is capable of achieving the ideal performance of a linear quantum measurement chain.

The total noise power in the homodyne measurement record, described in terms of the spectral density of the observable $\delta\hat{y}_{\text{hom}}$,

$$\begin{aligned}\bar{S}_{yy}^{\text{hom}}[\Omega] &= \bar{S}_{xx}^{(0)}[\Omega] + \bar{S}_{xx}^{\text{imp,hom}}[\Omega] + \bar{S}_{xx}^{\text{BA}}[\Omega] \\ &\geq \bar{S}_{xx}^{(0)}[\Omega] + 2\sqrt{\bar{S}_{xx}^{\text{imp,hom}}[\Omega] \cdot \left|\chi_x^{(0)}[\Omega]\right|^2 \bar{S}_{FF}^{\text{BA}}[\Omega]} \\ &\geq \bar{S}_{xx}^{(0)}[\Omega] + \frac{\hbar}{\sqrt{\eta_c}} \left|\chi_x^{(0)}[\Omega]\right|,\end{aligned}\quad (2.3.7)$$

contains a minimum excess noise at each frequency arising from the quantum fluctuations in the optical field, commensurate with the general considerations of section 2.1. In the case of cavity-enhanced interferometry, as considered here, the excess fluctuations arise from the vacuum fluctuations in the phase of the optical beam that sets the measurement imprecision in a homodyne detector, and vacuum fluctuations in the amplitude quadrature of the same beam, that drives the oscillator.

For the given linear measurement chain – resonant optical cavity embedded in a homodyne interferometer – there exists an absolute minimum apparent motion seen at the detector output, which is the standard quantum limit for the scenario. This is achieved when all classical sources of noise and imprecision are absent, i.e. for $n_{\text{m,th}} = 0$ and $\eta_c = 1$. In this ideal case, the peak spectral density of apparent position fluctuations given by eq. (2.3.7),

$$\bar{S}_{xx}^{\text{SQL}}[\Omega_m] := \min \bar{S}_{yy}^{\text{hom}}[\Omega_m] = 2\bar{S}_{xx}^{\text{zP}}[\Omega_m] = \frac{4x_{\text{zP}}^2}{\Gamma_m}, \quad (2.3.8)$$

is twice the intrinsic zero-point motion of the oscillator (defined in eq. (2.2.29)). This apparent motion provides a fundamental and natural scale to compare the performance of any linear measurement of the position fluctuations of a mechanical oscillator. In fact, the apparent position fluctuations, $\bar{S}_{yy}^{\text{hom}}$, referred to the standard quantum limit,

$$\frac{\bar{S}_{yy}^{\text{hom}}[\Omega]}{\bar{S}_{xx}^{\text{SQL}}[\Omega_m]} = n_{\text{imp,hom}} + \frac{(\Omega_m \Gamma_m)^2}{(\Omega^2 - \Omega_m^2)^2 + (\Omega \Gamma_m)^2} \left(n_{\text{m,th}} + n_{\text{m,BA}} + \frac{1}{2} \right), \quad (2.3.9)$$

may be simply parametrised in terms of equivalent thermal quanta describing the three different contributions to the measurement record. Here, $n_{\text{m,th}} + \frac{1}{2}$, is due to the intrinsic motion (thermal and zero-point) of the oscillator, while the measurement imprecision and back-action contributions are encoded as,

$$\begin{aligned}n_{\text{imp,hom}} &:= \frac{\bar{S}_{xx}^{\text{imp,hom}}[\Omega_m]}{\bar{S}_{xx}^{\text{SQL}}[\Omega_m]} = \frac{1}{16\eta C_0 n_c}, \\ n_{\text{m,BA}} &:= \frac{\bar{S}_{xx}^{\text{BA}}[\Omega_m]}{\bar{S}_{xx}^{\text{SQL}}[\Omega_m]} = C_0 n_c.\end{aligned}\quad (2.3.10)$$

Here we have introduced the dimensionless, *single-photon cooperativity*,

$$C_0 := \frac{4g_0^2}{\kappa\Gamma_m}, \quad (2.3.11)$$

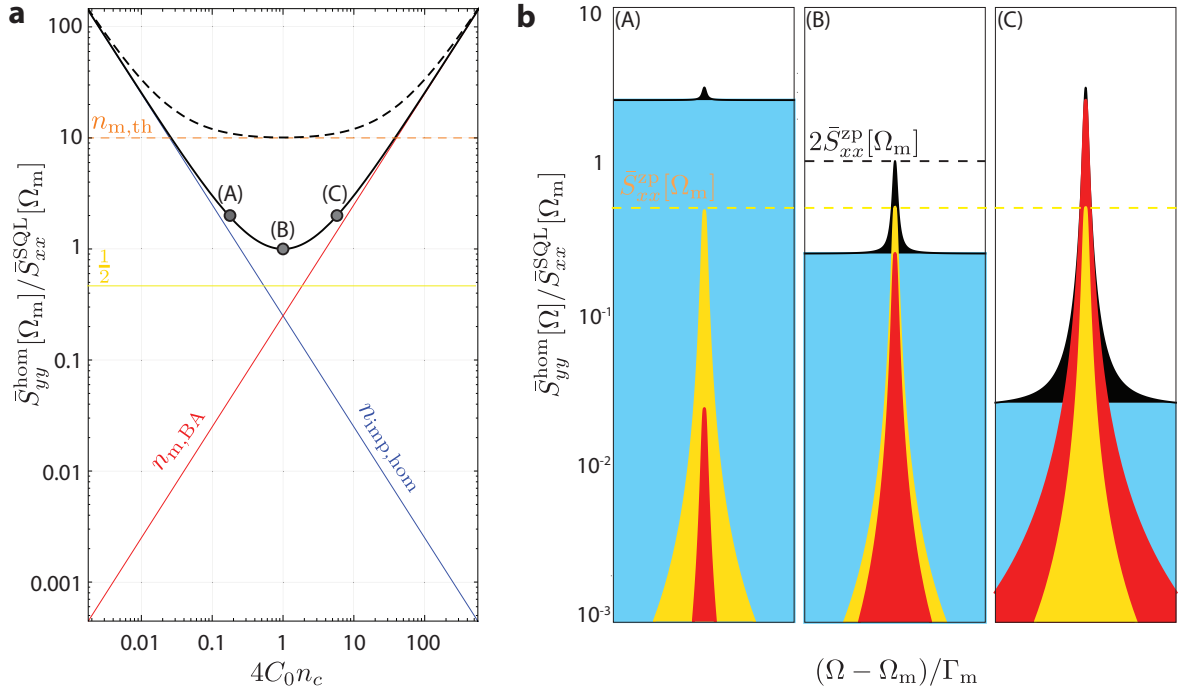


Fig. 2.12 – **Anatomy of the standard quantum limit of position measurement.** (a) Plot shows the phonon-equivalent total signal and its noise budget. Imprecision noise (blue) decreases with measurement strength, while back-action noise increases proportionately so as to maintain the imprecision-back-action product (eq. (2.3.12)). Yellow is the zero-point motion of the oscillator. Black shows the total phonon-equivalent noise at the output of the detector. Orange dashed shows intrinsic thermal motion when the oscillator is in a thermal state; black dashed shows the total noise in this case. (b) Spectra for three different points along the thick black curve in (a). Here, black shows the spectrum of the observable $\delta\hat{y}_{\text{hom}}$ normalised to the SQL. Blue shows the contribution from imprecision, which goes down as the measurement strength is increased; red is the back-action due to the measurement, going up with measurement strength. Yellow is the zero-point motion.

that describes the merits of the linearised optomechanical system as a position sensor; η describes the total efficiency of the measurement chain, including input-output coupling due to the cavity and losses in the homodyne interferometer. The imprecision-back-action product in eq. (2.3.6) takes the form,

$$n_{m,BA} n_{imp,hom} = \frac{1}{4\hbar^2} \bar{S}_{FF}^{\text{BA}}[\Omega_m] \bar{S}_{xx}^{\text{imp,hom}}[\Omega_m] \geq \frac{1}{16\eta_c}, \quad (2.3.12)$$

in terms of the phonon-equivalent quantities.

Figure 2.12 depicts the contribution of ideal homodyne imprecision and measurement back-action to the record of a linear position measurement. Figure 2.12 shows the peak spectral density $\bar{S}_{yy}[\Omega_m]$ normalised to its value at the SQL. As the measurement strength, here proxied by the intracavity photon number n_c , is increased, the imprecision contribution (blue) goes down due to the properties of phase shot-noise of a coherent optical field, while the back-action contribution (red) increases, as the oscillator experiences an increased photon recoil. Together with the zero-point motion (yellow), this gives the ideal characteristic of the total noise power in the detector output (black). The standard quantum limit is the point marked (B), where the

detector output exhibits a minimum, achieved at the intracavity photon number,

$$n_c^{\text{SQL}} := \frac{1}{4C_0}.$$

As shown in fig. 2.12b sub-panel (B), at the SQL, the total output is twice the zero-point motion (seen in eq. (2.3.8)). In fact, from eqs. (2.3.8) to (2.3.10), it follows that at the SQL, the total phonon-equivalent noise at the detector output,

$$n_m^{\text{SQL}} := \left[n_{\text{imp,hom}} + n_{\text{BA}} + \frac{1}{2} \right]_{n_c=n_c^{\text{SQL}}} = \frac{1}{4} + \frac{1}{4} + \frac{1}{2} = 1;$$

i.e. imprecision and back-action contribute equally and exactly half the zero-point motion [69].

In the non-ideal case, where the oscillator has a finite thermal occupation (i.e. $n_{\text{m,th}} > 0$), the excess thermal motion (orange dashed in fig. 2.12a) adds a constant excess to the detector output spectrum $\bar{S}_{yy}^{\text{hom}}$ precluding the possibility of realising an ideal measurement with the above noise budget. However, the imprecision-back-action product in eq. (2.3.6) may be amended by taking into account the thermal force noise from the environment, \bar{S}_{FF}^{th} , to give the inequality,

$$\begin{aligned} \bar{S}_{FF}^{\text{tot}}[\Omega] \bar{S}_{xx}^{\text{imp,hom}}[\Omega] &\geq \frac{\hbar^2}{4\eta_c} \geq \frac{\hbar^2}{4}, \\ \text{equivalently, } (n_{\text{m,th}} + n_{\text{m,BA}}) n_{\text{imp,hom}} &\geq \frac{1}{16\eta_c} \geq \frac{1}{16}, \end{aligned} \quad (2.3.13)$$

where $\bar{S}_{FF}^{\text{tot}}[\Omega] := \bar{S}_{FF}^{\text{th}}[\Omega] + \bar{S}_{FF}^{\text{BA}}[\Omega]$ accounts for the total force noise on the oscillator. The black dashed trace in fig. 2.12 is a plot of the right hand side of this inequality for the case $n_{\text{m,th}} = 10$. Despite the presence of thermal noise that precludes the possibility of achieving the absolute minimum, $\bar{S}_{xx}^{\text{SQL}}$, the total-force-imprecision product in eq. (2.3.13) characterises the ideality of the detector subject to the constraints of quantum mechanics.

As indicated by eq. (2.3.13), achieving such quantum-limited measurement necessitates two requirements to be met:

- (a) a quantum-limited meter, i.e. one that satisfies, $n_{\text{m,BA}} n_{\text{imp,hom}} \rightarrow \frac{1}{16}$
- (b) sufficiently low measurement imprecision, so that $n_{\text{m,th}} n_{\text{imp,hom}}$ is minimised.

Assuming that the first condition, essentially due solely to the optical field, is met, the second condition is tantamount to the fact that the motion of the oscillator is dominated by measurement back-action, i.e. $n_{\text{m,BA}} \gtrsim n_{\text{m,th}}$. In this case, the mechanical oscillator is predominantly coupled to the environment that performs the measurement.

2.4 Experimental platform: cryogenic near-field cavity optomechanics

Quantum phenomena do not occur in a Hilbert space, they occur in a laboratory.

ASHER PERES

Quantum-limited measurements of the position fluctuations of a thermally-driven oscillator, as discussed previously, essentially requires that the motion of the oscillator has a significant component due to measurement back-action. This condition,

$$\frac{n_{m,BA}}{n_{m,th}} = \frac{C_0 n_c}{n_{m,th}} \gtrsim 1,$$

relies on having an optomechanical system with a large single-photon cooperativity C_0 , a low thermal phonon occupation $n_{m,th}$ and the ability to sustain sufficiently large intracavity photon numbers while remaining a linear transducer. The *quantum cooperativity* [51],

$$\frac{C_0}{n_{m,th}} = \frac{4g_0^2}{\kappa(n_{m,th}\Gamma_m)} \approx \frac{(\hbar G)^2}{k_B T} \cdot \frac{1}{\kappa} \cdot \frac{1}{m\Gamma_m},$$

characterises the requirement for fixed intracavity photon number. Clearly, the experimental system must consist of a low-mass low-loss mechanical oscillator integrated with a high-Q optical cavity imparting a large per-photon radiation pressure force operating at sufficiently low temperature.

2.4.1 Stressed nanostring coupled to an optical microcavity

The radiation pressure of light, exerting a very feeble force, requires a specially engineered mechanical object so as to induce appreciable motion. The field of contemporary cavity optomechanics [51] achieves this goal by employing low-mass mechanical objects coupled to intense optical fields in a small mode-volume cavity.

Practical requirements – the need for a highly stable and miniature frequency reference for integrated circuits – led researchers towards high-Q nanomechanical oscillators in the 1960's [216]. By the late 90's, these initial ideas had given birth to a host of electronic devices and sensors based on nanomechanical oscillators [217, 218]. It was hoped that by simultaneously shrinking the size of the oscillator (low m), while maintaining the mechanical quality (low Γ_m), quantum back-action on nanomechanical objects could be witnessed and exploited [219].

Phenomenologically however, the mechanical quality factor,

$$Q_m = 2\pi \frac{\text{energy stored in elastic motion}}{\text{energy lost per cycle}} = \frac{\Omega_m}{\Gamma_m}, \quad (2.4.1)$$

was found to obey the rough scaling with volume [220–222], $Q_m \propto V_m^{1/3}$, suggesting that conventional nanomechanical oscillators may not simultaneously achieve low mass and high Q_m . A welcome break from this trend was observed in nanostring oscillators with intrinsic

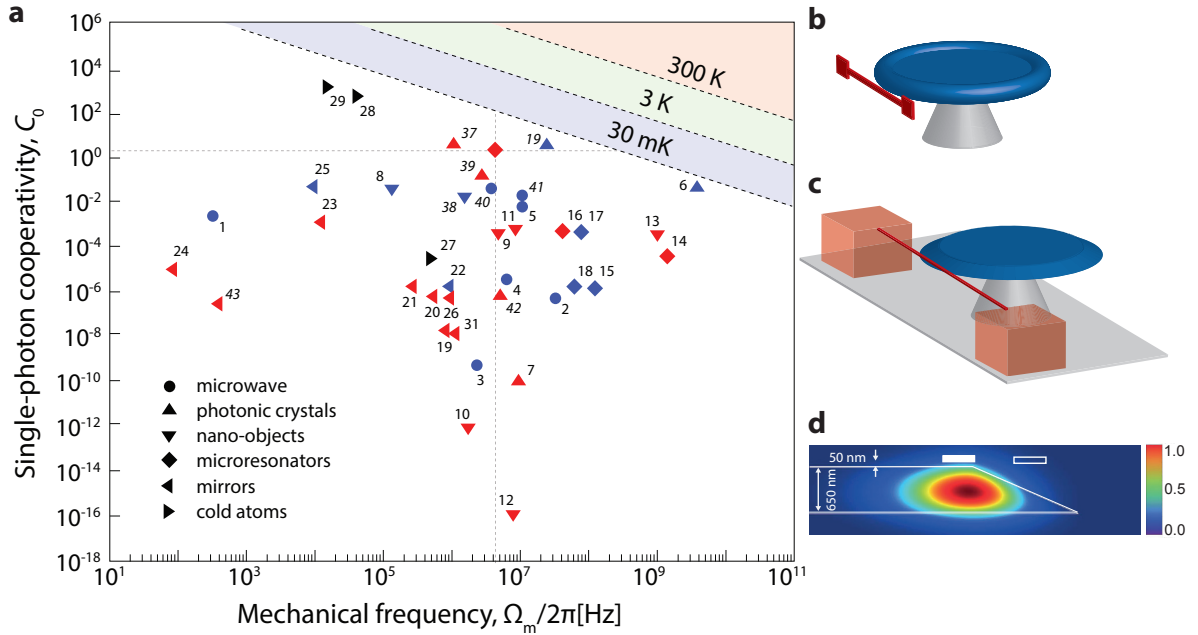


Fig. 2.13 – **Unity single-photon cooperativity with near-field gradient coupling.** (a) Survey of the contemporary landscape of cavity optomechanics in terms of the typically achieved single-photon cooperativity C_0 (adapted from [167]). (b) In the original near-field gradient force optomechanics architecture developed in our group [49, 227], a high-stress Si_3N_4 nanobeam (red) is manually placed in the evanescent field of an SiO_2 optical microcavity. (c) In the approach followed in this thesis, building upon an earlier generation of work [228], the nanobeam and micro-cavity are heterogeneously integrated on a chip for improved technical stability, making it convenient for cryogenic deployment. (d) An example finite-element simulation showing the difference between the current generation device and the previous generation. In the previous generation, the nanobeam (white outline) was placed far outside the maximum of the evanescent field gradient, whereas in the current generation (white solid), the beam is at the optimal position.

tensile stress [223, 224], exhibiting $Q_m \approx 10^6$ at an oscillation frequency of $\Omega_m \approx 2\pi \cdot 1$ MHz at room temperature. The conventional understanding is that the pre-stress of the elastic medium increases the stored elastic energy without affecting intrinsic loss mechanisms [225, 226].

However due to their small transverse dimensions ($\sim 10 - 100$ nm), the nanobeam geometry does not have a large cross-section for electromagnetic scattering, making them not susceptible to scattering type [18] radiation pressure forces. Therefore, their interaction with optical cavity fields is mediated by gradient type forces [49, 227, 229–232].

The approach followed in our group [49, 227, 228] relies on coupling a high-Q nanostring to the evanescent field of a high-finesse whispering gallery optical cavity. The low mass ($m \lesssim 5$ pg) of the oscillator gives a large zero-point motion ($x_{z\text{p}} \gtrsim 100$ pm). In order to realise a large frequency pull parameter G , the first generation of devices [49, 227], shown in fig. 2.13a, were realised by manually positioning the nanobeam in the evanescent field of a whispering-gallery micro-toroid cavity, realising $G \approx 2\pi \cdot 1$ GHz/nm. Operating at room temperature, this system could realise a measurement imprecision at the standard quantum limit [49]. In a second generation [228], shown in fig. 2.13, the nanobeam and microcavity were integrated on-chip, to improve operational stability. However, in the second generation device, the placement of the nanobeam relative to the cavity was not optimal – essentially having to

do with the fabrication procedure employed. The devices used in this thesis, while nominally similar to fig. 2.13b, are based on a vastly improved fabrication procedure [167] capable of placing the nanobeam at the optimal position in the evanescent optical field so as to maximise the gradient force. Future theses from the group will discuss the fabrication process in depth, see [167] for details.

Ultimately, the optomechanical system employed here features single photon cooperativities,

$$C_0 \approx 1 \cdot \left(\frac{g_0/2\pi}{25 \text{ kHz}} \right)^2 \left(\frac{0.5 \text{ GHz}}{\kappa/2\pi} \right) \left(\frac{5 \text{ Hz}}{\Gamma_m/2\pi} \right), \quad (2.4.2)$$

of order unity; Figure 2.13a shows a survey of the contemporary landscape of cavity optomechanics in terms of C_0 . Despite the fact that the quantum cooperativity, $C_0/n_{m,\text{th}} \ll 1$ at any technologically feasible cryogenic temperature, by being able to probe the cavity with a sufficiently large intracavity photon number ($n_c \lesssim 10^5$), and operating at 4 K, we are able to achieve $(C_0/n_{m,\text{th}})n_c \approx 1$.

The remainder of this section details the prevailing understanding of the various parameters that go into the single photon cooperativity, and technical details regarding the cryogenic experiment. Extraneous (classical) sources of imprecision and back-action will be considered in chapter 3.

2.4.1.1 Near-field coupling

The expression for the cavity frequency pull parameter in terms of the perturbation caused by the presence of the dielectric nanobeam is given by eq. (2.2.103),

$$G = \frac{\omega_c}{2} \frac{\int |\mathbf{E}(\mathbf{r})|^2 (\tilde{\mathbf{u}}(\mathbf{r}) \cdot \nabla \epsilon) d^3r}{\int \epsilon |\mathbf{E}(\mathbf{r})|^2 d^3r}, \quad (2.4.3)$$

where we have used the fact that for a high-Q cavity, the energy in the magnetic field equals the energy in the electric field, to express G in terms of the electric field alone. Here the integrals are taken over the entire volume of the cavity optical field including the evanescent field. The integral in the numerator gives the cavity frequency shift due to the presence of the nanobeam within the evanescent field of the cavity mode. Application of straightforward vector identities (and neglecting surface terms) reveal that this perturbation may be expressed as the sum of two contributions,

$$\int \epsilon \tilde{\mathbf{u}} \cdot (\nabla |\mathbf{E}|^2) d^3r + \int \epsilon |\mathbf{E}|^2 (\nabla \cdot \tilde{\mathbf{u}}) d^3r;$$

the first couples the beam displacement to a generalised force due to the gradient in the electric field intensity, while the second arises from volume deformations of the beam due to the incident field intensity, interpreted as a scattering-type force. For nanobeams with dimensions comparable to the optical wavelength, the gradient force dominates.

In order to estimate the coupling, we now make a few simplifying assumptions. Firstly, although the frequency pulling parameter depends on the geometric overlap between the electric field and the beam displacement profile, it is acceptable to neglect this dependence, and later accommodate it in the definition of the single-photon coupling g_0 , via an effective

zero-point motion. Thus we may redefine (equivalent to the identification $\tilde{\mathbf{u}} \cdot \nabla \epsilon = \epsilon_{\text{beam}} - 1$),

$$G = \frac{\omega_c}{2} \frac{\partial}{\partial z} \left(\frac{\int_{\text{beam}} (\epsilon_{\text{beam}}(\mathbf{r}) - 1) |\mathbf{E}(\mathbf{r})|^2 d^3r}{\int_{\text{disk}} \epsilon |\mathbf{E}(\mathbf{r})|^2 d^3r} \right) \approx \frac{\omega_c}{2} \frac{\partial}{\partial z} \left(\frac{\nu_{\text{SiN}}^2 - 1}{\nu_{\text{SiO}_2}^2} \frac{|\mathbf{E}_{\text{max}}^{\text{beam}}|^2}{|\mathbf{E}_{\text{max}}^{\text{disk}}|^2} \frac{V_{\text{beam,opt}}}{V_{\text{disk,opt}}} \right)$$

where the approximation parametrises the coupling rate in terms of an effective optical volume of the disk (beam), $V_{\text{disk(beam),opt}}$, given by the optical energy in the disk (beam) normalised to the maximum electric field intensity in the disk (beam), i.e.,

$$V_{\text{disk(beam),opt}} |\mathbf{E}_{\text{max}}^{\text{disk}}|^2 = \int_{\text{disk(beam)}} |\mathbf{E}|^2 d^3r.$$

Secondly, for a beam whose transverse dimensions are much less than the vertical evanescent decay length [233, 234],

$$\ell_{\text{ev}} \approx \frac{\lambda_c/2\pi}{\sqrt{\nu_{\text{SiO}_2}^2 - 1}} \approx \frac{\lambda_c}{12} \sim 100 \text{ nm},$$

of the cavity mode, its effective optical volume may be simplified into the form, $V_{\text{beam,opt}} = \mathcal{A}_{\text{beam}} \ell_{\text{eff}}$, where $\mathcal{A}_{\text{beam}}$ is the geometric cross-sectional area and ℓ_{eff} is an effective sampling length. Similarly for the disk, its optical volume may be approximated by, $V_{\text{disk,opt}} = 2\pi r_{\text{disk}} \mathcal{A}_{\text{disk}}$, where r_{disk} is the geometric radius, and $\mathcal{A}_{\text{disk}}$ is the effective transverse area of the whispering-gallery mode. Finally, assuming that the vertical evanescence leads to an exponential decay in the maximum field intensity between the disk and the beam, i.e. $|\mathbf{E}_{\text{max}}^{\text{beam}}|^2 = |\mathbf{E}_{\text{max}}^{\text{disk}}|^2 \cdot \alpha \exp(-z/\ell_{\text{ev}})$, the near-field coupling strength may be approximated by [167],

$$G \approx \frac{\omega_c}{2\ell_{\text{ev}}} \frac{\nu_{\text{SiN}}^2 - 1}{\nu_{\text{SiO}_2}^2} \frac{\mathcal{A}_{\text{beam}} \ell_{\text{eff}}}{2\pi r_{\text{disk}} \mathcal{A}_{\text{disk}}} \alpha e^{-z/\ell_{\text{ev}}}. \quad (2.4.4)$$

In practice, the evanescent length ℓ_{ev} , the mode cross-section $\mathcal{A}_{\text{disk}}$, and the geometric pre-factor α need to be determined from a numerical solution of Maxwell's equations [167]. A simple estimate may however be made by replacing these parameters using known approximations for the case of a toroidal cavity [49]: the evanescent length $\ell_{\text{ev}} \approx \lambda_c/12$, while the mode cross-section $\mathcal{A}_{\text{disk}} \approx 0.15 \cdot r_{\text{disk}}^{7/12} t_{\text{disk}}^{1/4} \lambda_c^{7/6}$ and the geometric pre-factor, $\alpha \approx 1.1(\lambda_c/r_{\text{disk}})^{1/3}$. Using the known refractive index, $\nu_{\text{SiN}} = 2$, and the typical geometric parameters of the disk and beam, eq. (2.4.4) suggests a coupling strength of $G \approx 2\pi \cdot 1 \text{ GHz/nm}$ – within 10% of the prediction from a full finite-element simulation.

In order to arrive at the vacuum optomechanical coupling rate, g_0 , the zero-point motion of the effective point mass equivalent of the beam must be known. In principle, this again requires detailed knowledge of the overlaps between the extended elastic mode profile, $\tilde{\mathbf{u}}$, of the beam, and the optical cavity field, \mathbf{E} , of the disk [120]. The simple approximation, valid for the fundamental mode with an anti-node at the optical mode, involves assuming, $x_{\text{zp}}^2 \approx \hbar/(2\rho \mathcal{A}_{\text{disk}} \ell_{\text{eff}} \Omega_m) \approx (33 \text{ fm})^2$, giving, $g_0 = G x_{\text{zp}} \approx 2\pi \cdot 33 \text{ kHz}$ – within 15% of the measured value.

2.4.2 Measurement and calibration of thermomechanical motion

Since the motion of the mechanical oscillator imparts phase fluctuations commensurate with the motion in the intracavity field, a phase discriminator (i.e. a phase-to-amplitude conversion)

is required to infer the mechanical motion. In one approach, the cavity may be used as a phase discriminator, for which detuned operation (i.e. $\Delta \neq 0$) is necessary – so-called *side-of-line* detection. In another approach, the cavity may be embedded in one arm of an interferometer, in which case resonant probing (i.e. $\Delta = 0$) is possible.

The technical ease of side-of-line detection is considerably offset by two deficiencies: (a) the modification of mechanical susceptibility due to dynamic back-action at any finite detuning $\Delta \neq 0$ with sufficient probe power, and, (b) the difficulty of achieving shot-noise-limited detection when the probe is considerably reduced to avoid dynamic back-action. Indeed, from eq. (2.2.54), the transmitted signal power required to be shot-noise limited in direct photodetection for a detector with finite NEP, is

$$P_{\text{shot}} = \frac{\mathcal{R}}{2\eta q_e} \bar{S}_P^{\text{NE}}[\Omega].$$

For typical trans-impedance-amplified silicon ($\eta \approx 0.85$) photodetectors (for example, New-Focus 1801 characterised in fig. 2.2), $P_{\text{shot,PD}} \approx 100 \mu\text{W}$. Avalanche photodetectors (APD) can have much lower $P_{\text{shot,APD}} \approx 0.5 - 1 \mu\text{W}$, however, their high-sensitivity avalanche stage tends to saturate around $2P_{\text{shot,APD}}$.

For these reasons, it has proven useful to employ phase discrimination using an external interferometer, i.e. homodyning or heterodyning the cavity transmission with a strong LO^{2.41}. In this case, the LO sets the shot noise background for detection, so that large powers $P_{\text{LO}} \approx 1 - 5 \text{ mW}$ may be employed, limited only by the damage threshold of the silicon photodiodes of the balanced detector (for unbalanced detectors, saturation of the amplifying electronics sets a lower limit on the usable LO power).

Figure 2.14a shows the standard experimental setup to detect thermal motion of the nanobeam coupled to the optical microdisk cavity. When the cavity is probed on resonance, and the homodyne is locked to the phase quadrature, the voltage spectrum of its trans-impedance-amplified (gain H_{VI}) photocurrent takes the form (see eq. (2.2.62)),

$$\bar{S}_V^{\text{hom}}[\Omega] = |H_{VI}[\Omega]|^2 \left(\mathcal{R}^2 \bar{S}_P^{\text{NE}} + 2\eta q_e \mathcal{R} P_{\text{LO}} + 4\eta^2 \mathcal{R}^2 P_{\text{LO}} P_{\text{sig}} \bar{S}_\phi^{\text{cav}}[\Omega] \right),$$

where $\bar{S}_\phi^{\text{cav}}$ is the total phase noise contribution from the cavity. In the vicinity of mechanical modes, $\bar{S}_\phi^{\text{cav}}[\Omega] = (G/\Omega)^2 \bar{S}_x[\Omega]$, where G is the frequency pull parameter of the relevant mechanical mode. Figure 2.14d shows such a voltage noise spectrum measured using a spectrum analyser at the output of the homodyne interferometer.

In order to calibrate such a spectrum in physically relevant units (example, apparent mechanical motion), it appears to be necessary to have detailed knowledge of the transfer function of each element in the measurement chain. However this is not necessary. For example, if it is known that the mechanical oscillator is in equilibrium at a certain temperature T , then the voltage noise spectrum, expressed in the form (irrespective of the nature of the

^{2.41} A common-path interferometer, for example using the frequency modulation spectroscopy technique described in section 2.2.2.5, technically easier to implement, is not preferred in a cryogenic environment due to the large (mW range) LO powers that might scatter in the cold environment.

2.4. Experimental platform: cryogenic near-field cavity optomechanics

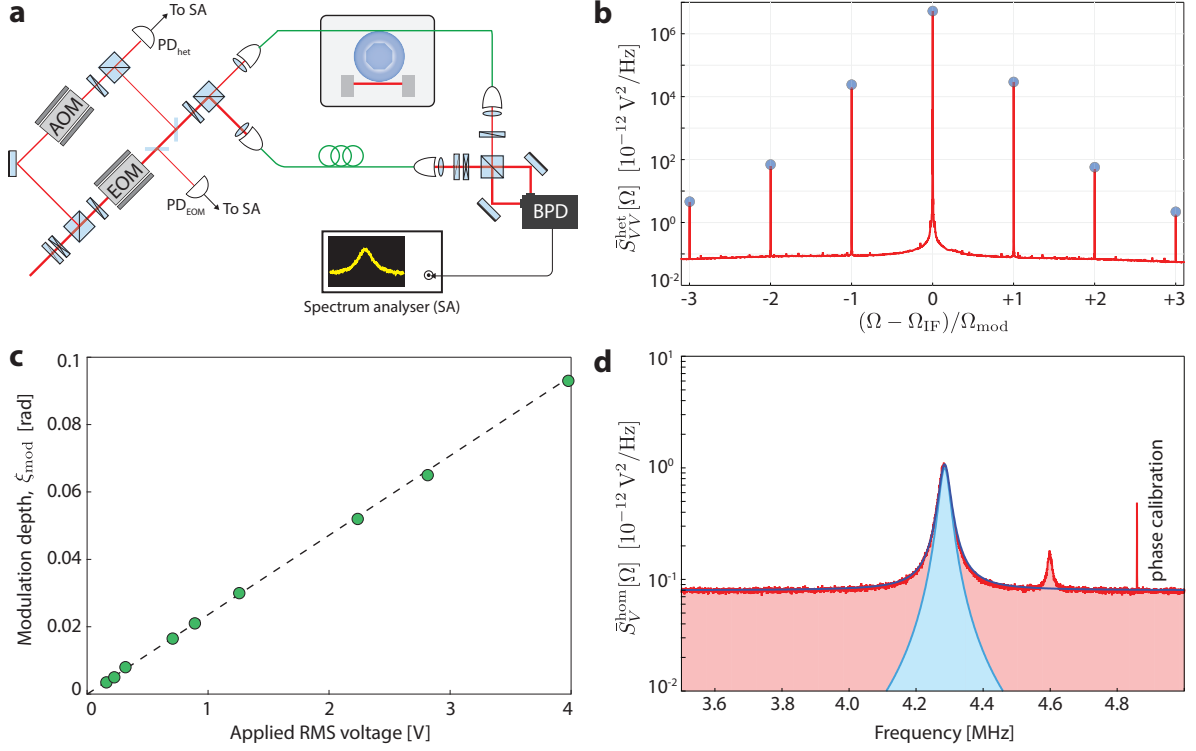


Fig. 2.14 – **Frequency noise calibration.** (a) Schematic of the experimental setup used to perform direct calibration of the frequency noise imparted on the transmitted optical field due to thermomechanical motion. An EOM is used to impart a known phase modulation at a pre-determined field frequency; an AOM is used to derive a heterodyne local oscillator. (b) Output of the heterodyne detector, visualising the phase modulation sidebands imparted by the EOM. Here the modulation frequency, $\Omega_{\text{mod}} \approx 2\pi \cdot 4.85 \text{ MHz}$, while the heterodyne intermediate frequency, $\Omega_{\text{IF}} = 2\pi \cdot 78 \text{ MHz}$. (c) The modulation depth ξ_{mod} is verified to be linear in the voltage applied to the EOM over a decade in both. (d) Voltage noise spectrum at the output of the homodyne detector, showing thermal motion of the fundamental out-of-plane mode at $\Omega_m \approx 2\pi \cdot 4.315 \text{ MHz}$, together with the phase modulation calibration tone. Here the oscillator is in contact with buffer gas so that to a good degree it may be assumed to be in thermal equilibrium; however, the mechanical Q is deteriorated by gas-damping (see section 2.4.3).

linear detection scheme),

$$\bar{S}_V[\Omega] = |H_{Vx}[\Omega]|^2 \left(\bar{S}_x^{\text{imp}}[\Omega] + \bar{S}_x[\Omega] \right) = \bar{S}_V^{\text{imp}}[\Omega] + \underbrace{|H_{Vx}[\Omega]|^2 \bar{S}_x[\Omega]}_{\bar{S}_V^{\text{mech}}}, \quad (2.4.5)$$

may be calibrated by using the equipartition identity (see eq. (2.2.26)),

$$\text{Var}[\hat{x}] = (2n_{m,\text{th}} + 1)x_{\text{zp}}^2 \approx 2x_{\text{zp}}^2 \frac{k_B T}{\hbar \Omega_m}.$$

In practice, implementing this also requires the assumption that $|H_{Vx}[\Omega]|$ is constant in the vicinity of the thermal noise; for high-Q oscillators, this assumption is almost always true. Essentially, calibration involves fixing the number $|H_{Vx}[\Omega_m]|$. The equipartition identity gives,

$$|H_{Vx}[\Omega_m]| \approx \frac{\text{Var}[V_{\text{mech}}]}{2x_{\text{zp}}^2 n_{m,\text{th}}} = \frac{1}{2x_{\text{zp}}^2 n_{m,\text{th}}} \int \left(\bar{S}_V[\Omega] - \bar{S}_V^{\text{imp}}[\Omega] \right) \frac{d\Omega}{2\pi},$$

where the last equality follows from the general relation between the variance of a process and its spectral density given in eq. (2.1.6). If the voltage noise spectrum is further only required to be calibrated in units relative to the zero-point spectral density \bar{S}_x^{zp} , knowledge of x_{zp} is rendered irrelevant.

Ultimately, the equipartition identity may be used to determine the frequency pull parameter G , or the vacuum optomechanical coupling rate g_0 . However, in order to do this, a reference phase/frequency noise is required that is transduced identical to the mechanical motion through the measurement chain. For side-of-line detection and homodyne detection, it is known that laser frequency fluctuation imparted on the probe laser at the cavity input, as shown in fig. 2.14a, is transduced identical to cavity frequency fluctuation [235]. Assuming that the detected voltage noise spectrum is related to cavity frequency fluctuation linearly, i.e.

$$\bar{S}_V[\Omega] = \bar{S}_V^{\text{imp}}[\Omega] + |H_{V\omega}[\Omega]|^2 \bar{S}_\omega[\Omega],$$

the problem is to infer the function $|H_{V\omega}[\Omega]|$. Using an EOM to imprint a known phase modulation of depth ξ_{mod} (see eq. (2.2.86)) at frequency Ω_{mod} , the voltage noise spectrum consists of two terms,

$$\bar{S}_V[\Omega] = \bar{S}_V^{\text{imp}}[\Omega] + |H_{V\omega}[\Omega]|^2 \left(\bar{S}_\omega^{\text{mod}}[\Omega_{\text{mod}}] + \bar{S}_\omega^{\text{cav}}[\Omega] \right), \quad (2.4.6)$$

where the frequency noise spectrum due to the injected modulation is given by,

$$\bar{S}_\omega^{\text{mod}}[\Omega_{\text{mod}}] = \frac{\xi_{\text{mod}}^2}{2} \Omega_{\text{mod}}^2 \delta[\Omega - \Omega_{\text{mod}}].$$

Assuming that the cavity frequency noise arises from the thermal motion of a high-Q oscillator at frequency Ω_m , i.e. $\bar{S}_\omega^{\text{cav}}[\Omega] = G^2 \bar{S}_x[\Omega] = g_0^2 \bar{S}_{x/x_{\text{zp}}}[\Omega]$, eq. (2.4.6) takes the form,

$$\bar{S}_V[\Omega] \approx \bar{S}_V^{\text{imp}}[\Omega] + \underbrace{|H_{V\omega}[\Omega_{\text{mod}}]|^2 \frac{\xi_{\text{mod}}^2 \Omega_{\text{mod}}^2}{2} \delta[\Omega - \Omega_{\text{mod}}]}_{\bar{S}_V^{\text{mod}}} + \underbrace{|H_{V\omega}[\Omega_m]|^2 g_0^2 \bar{S}_{x/x_{\text{zp}}}[\Omega]}_{\bar{S}_V^{\text{mech}}}.$$

Again invoking the equipartition identity, $\text{Var}[\hat{x}/x_{\text{zp}}] = 2n_{\text{m,th}} + 1$, and relating the integral of the voltage noise spectrum to its variance, gives,

$$\frac{\text{Var}[V_{\text{mech}}]}{\text{Var}[V_{\text{cal}}]} \approx \left| \frac{H_{V\omega}[\Omega_m]}{H_{V\omega}[\Omega_{\text{mod}}]} \right|^2 \frac{4g_0^2 n_{\text{m,th}}}{\xi_{\text{mod}}^2 \Omega_{\text{mod}}^2}.$$

If the modulation frequency is sufficiently close to the mechanical frequency that the first factor on the right-hand side can be justified to be unity, then this equation may be used to calibrate the vacuum optomechanical coupling g_0 to the injected frequency modulation. Employing this on the example spectrum shown in fig. 2.14d, gives $g_0 \approx 2\pi \cdot 19$ kHz.

This frequency noise calibration technique crucially relies on the ability to produce a pure known frequency modulation. Residual amplitude modulation (RAM) in the EOM is a well known technical challenge to achieving a pure frequency modulation [236, 237]. The effect of RAM in our experiments is two-fold: excessive RAM leads to large uncertainties in the phase modulation power in the reference tone used for calibration; secondly, since the same EOM is

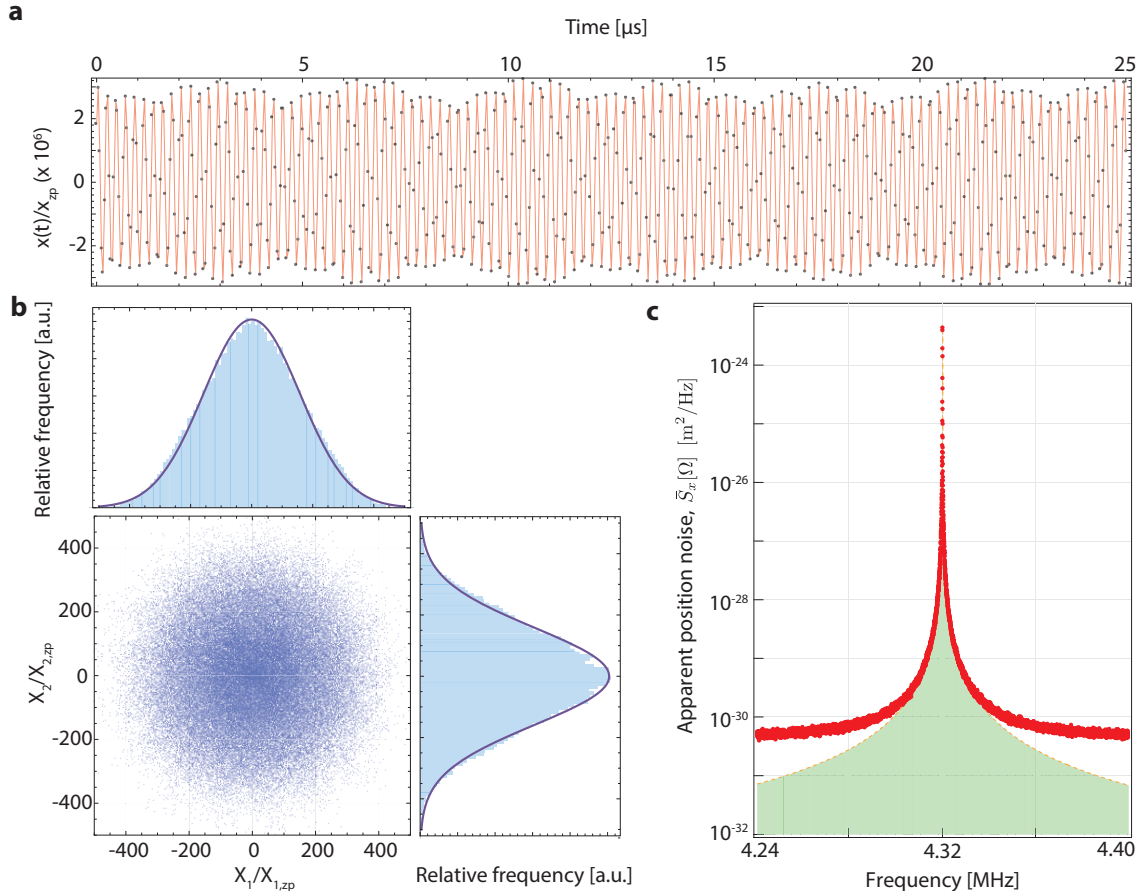


Fig. 2.15 – **Incarnations of thermal motion.** Plots show various representations of thermal fluctuations of the position of the fundamental mode of the nanobeam, inferred from a calibrated homodyne photocurrent record. (a) Time domain trace (bandpass filtered around the mechanical frequency) showing the random amplitude fluctuations caused due to the thermal Langevin force. (b) Quadratures $X_{1,2}(t)$ of the apparent motion $x(t)$, and their marginal distributions (see text for details). (c) Power spectral density computed from the full photocurrent record in (a).

used for producing phase modulation tones for resonantly locking the laser (as described in fig. 2.8), RAM leads to DC offsets in the lock error signal. In the experiment, the presence of RAM is verified and corrected in two ways. A direct photodetector placed immediately in the transmission of the EOM is used to nullify any RAM by adjusting the input polarisation to the EOM; we have achieved relative RAM suppression at the level of 20 dB like this, stable over the course of typical experiments. In addition, heterodyne detection of the EOM transmission, for sufficiently large modulation depth $\zeta_{\text{mod}} \gtrsim 0.01$, resulting in cascaded phase modulation sidebands can be used to diagnose the presence of RAM a posteriori. In the presence of both AM and PM, the first order sidebands exhibit an asymmetry due to the interference of the PM and AM, whereas the higher order sidebands are purely due to PM. Figure 2.14b shows a typical heterodyne voltage noise spectrum showing cascaded sidebands, with the blue points showing the prediction from a pure PM model. It has also proven useful, especially for stable operation exceeding an hour, to actively stabilise the RAM by using the direct photodetection signal after the EOM to feedback on the DC bias of the EOM in a slow feedback loop [237, 238] (see experiment layout in fig. 2.20).

Figure 2.15 shows several forms of thermal motion of the fundamental out-of-plane mode of the nanobeam. The data is taken using a resonant probe optically demodulated in a homodyne interferometer. Panel (a) shows a part of the photocurrent record, bandpass filtered around the mechanical frequency, referred to mechanical position. The amplitude scale is calibrated assuming thermal equilibrium at a temperature of 4 K (details of cryogenic operation follow in section 2.4.3). Panel (c) shows a periodogram power spectral density estimate [239] of the full photocurrent record. Here, the spectrum is calibrated in terms of an absolute position noise through a knowledge of the effective mass of a doubly-clamped beam, $m_{\text{eff}} \approx m_{\text{phys}}/2 \approx 85$ pg. Panel (b) shows the apparent motion $x(t)$ decomposed into its quadratures, $X_{1,2}(t)$ [240]:

$$\begin{aligned} x(t) &= X_1(t) \cos \Omega_m t + X_2(t) \sin \Omega_m t \\ \text{i.e., } X_1[\Omega] &= x[\Omega + \Omega_m] + x[\Omega - \Omega_m] \\ \text{and, } X_2[\Omega] &= -i(x[\Omega + \Omega_m] - x[\Omega - \Omega_m]). \end{aligned}$$

These quadratures are obtained from the calibrated apparent position $x(t)$ by demodulating it at the known mechanical frequency $\Omega_m \approx 2\pi \cdot 4.315$ MHz digitally. Due to the large signal-to-noise of the measurement (seen in panel (c)), the phase-space distribution shown in panel (b) may be assumed to be only negligibly ($\lesssim 1$ ppm) contaminated by the shot-noise of the optical field used for the measurement. The marginal distributions, also shown in panel (b), have variances, $\text{Var}[X_{1,2}] = \frac{1}{2} \text{Var}[x] = (n_{\text{m,th}} + \frac{1}{2})x_{\text{zp}}^2$ consistent with the known thermal occupation.

2.4.3 Cryogenic operation

The relatively low mechanical frequency (fundamental mode, $\Omega_m \approx 2\pi \cdot 4$ MHz) means that the ambient phonon occupation at room temperature is, $n_{\text{m,th}} \approx 10^6$, while the decoherence rate, $n_{\text{m,th}}\Gamma_m \approx 2\pi \cdot 10$ MHz, is larger than a single mechanical period. The necessary condition to observe quantum coherent mechanical oscillations, i.e. $\Omega_m \gtrsim n_{\text{m,th}}\Gamma_m$, is thus not met at room temperature for the systems used in this thesis. It is therefore necessary to employ passive cryogenic cooling to decrease the thermal decoherence rate to a level where this condition is met. For example, by operating at 10 K it would be possible to achieve $\Omega_m \gtrsim 5 \cdot n_{\text{m,th}}\Gamma_m$.

Figure 2.16 shows the schematic of the ^3He buffer gas cryostat (Oxford Instruments, HelioxTL) employed in this thesis, allowing access to temperatures as low as 0.3 K. The cryostat consists of successive concentric layers of thermal isolation: a vacuum chamber whose outer wall is in contact with room temperature pumped down to a pressure of $< 10^{-5}$ mbar; followed by a shield filled with liquid nitrogen, maintained at a temperature of 77 K, further cryo-pumping the outer vacuum chamber to pressures well below 10^{-6} mbar; followed by a shield of liquid ^4He maintained at a temperature of 4 K. These shields isolate an inner cylindrical bore (diameter ≈ 10 cm) where the sample is inserted – the sample volume.

The sample – several (≈ 10) optomechanical devices on a rectangular silicon chip on which they are fabricated – is mounted on the sample head shown in fig. 2.16b. The head is mounted on the end of a retractable probe which can be attached to the top of the sample volume. Samples can be changed by retracting the probe – it slides on two O-rings between a pumped load-lock volume – from the cryostat bore, closing the gate valve to isolate the cryostat volume from the retracted probe, and then detaching the probe from the cryostat. In this manner, samples may be changed while keeping the cryostat cold.

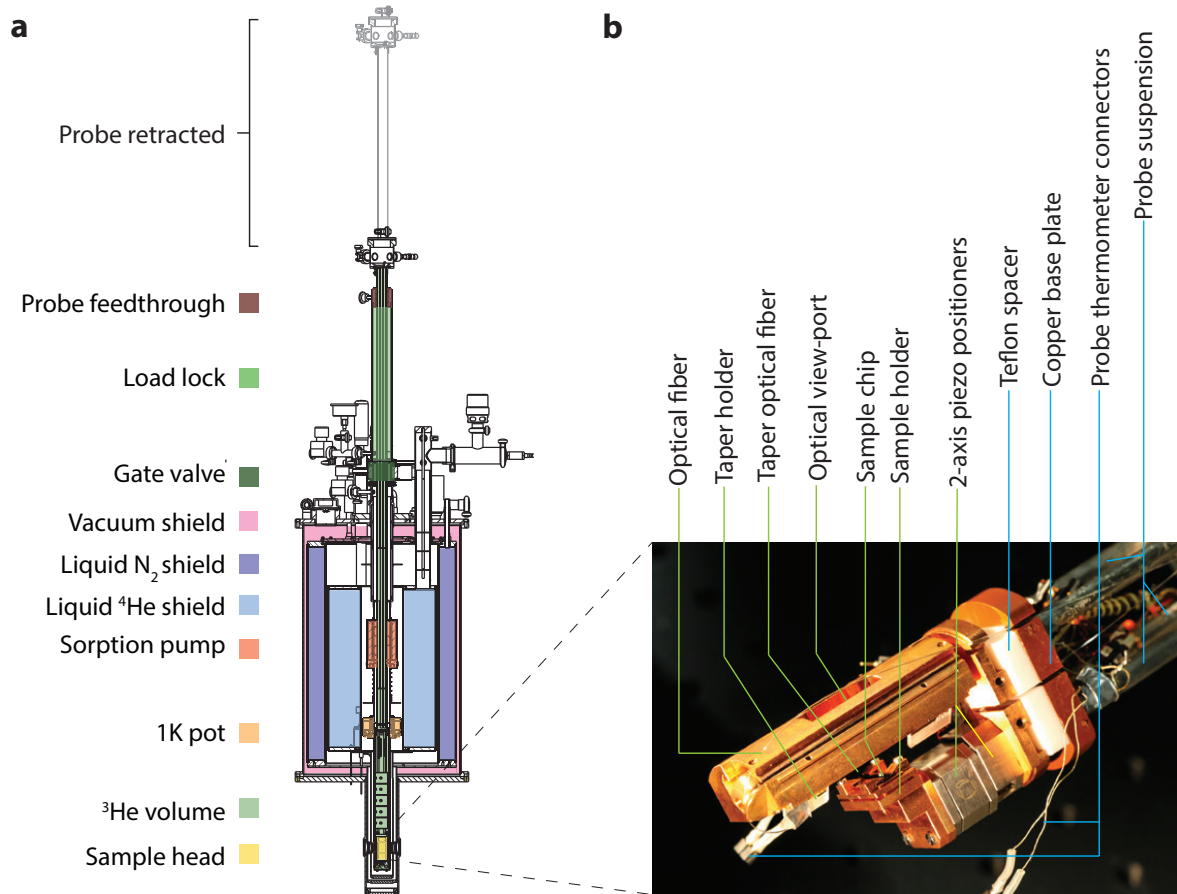


Fig. 2.16 – **Cryogenic apparatus.** (a) Drawing of the ³He buffer gas cryostat used in experiments. The sample chip, containing multiple optomechanical devices is mounted on the sample head (yellow) embedded in the heart of the cryostat. (b) Photograph of the sample head. The chip containing the samples is mounted on a 2-axis piezo-positioner, allowing for coupling into the optical cavity using tapered optical fiber.

The sample head (fig. 2.16b), at the end of the probe, is suspended from hollow steel tubes damped and thermally isolated using Teflon bluffs. The sample chip is mounted on a removable mount and attached onto its face using four clamps. This mount is screwed onto the top of a two-stack piezo-positioner (AttoCube ANPx51/LT). The tapered optical fiber used to optically probe the microcavity is glued onto a custom-made glass holder, which is secured onto the head via a clamp. Care is taken during the assembly of the head to ensure that the desired sample(s) can be coupled using the piezo-positioners – the devices themselves, fabricated on tall ($\approx 100 \mu\text{m}$) mesas on the chip, geometric parallelism between the taper and chip surface is not as stringent. Once the head is assembled, it takes on a copper hood that encloses it on all sides, except for a view-port (see fig. 2.16b).

The sample head, once prepared, is inserted into the cryostat. During insertion, the sample volume is pumped using an internal sorption pump (essentially, large surface-to-volume ratio activated and cleaned charcoal, with a regulated flow of ⁴He behind it to cool); at the same time, it has proven more reliable to hold all the ³He buffer gas in its external reservoir. The probe is then inserted in a continuous motion into the sample volume; finally, it is rotated so that the view-port on the sample head is aligned to the view-port at the bottom of the cryostat.

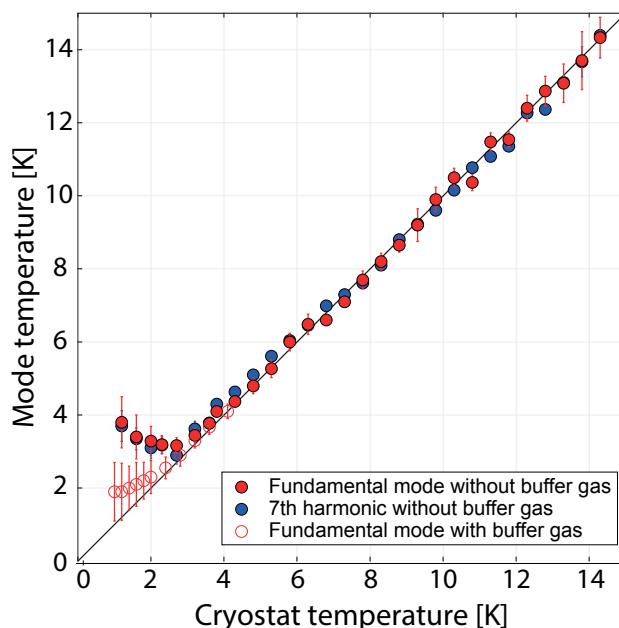


Fig. 2.17 – **Thermalisation with and without buffer gas.** Temperature of the fundamental and 7th harmonic of the nanobeam as a function of the cryostat temperature. Above 4 K, the mechanical modes thermalise to the cryogenic environment despite the absence of buffer gas. In the presence of buffer gas, thermalisation can be achieved down to 2 K. Error bars denote standard errors derived from the statistical dispersion among multiple data points taken at each cryostat temperature.

This view-portal is used to peer into the head using a microscope so as to align the sample and tapered fiber for optical coupling.

In order to cool the sample, ³He is introduced back into the sample volume at a very slow rate – the 15 litres of the buffer gas leaks in over ≈ 2 hours. After an initial phase of radiative cooling from 300 K to about 100 K, the sorption pump is heated up (≈ 25 K) to eject out the buffer gas, which then thermalises the sample holder to the internal walls of the sample volume at 4 K, in contact with the liquid ⁴He shield.

To verify thermalisation of the mechanical modes of the nanobeam, we perform calibrated thermal noise measurements on the modes of the beam. A weak laser ($P_{\text{in}} \lesssim 5$ nW) is far detuned on the red side of the cavity (typically $\Delta < -2\kappa$) so as to prevent any optical modification of the environment seen by the mechanical modes. The laser, passively stable at this detuning, introduces $n_c \approx 2$, intracavity photons on cavity resonance. Figure 2.17 shows the result of this investigation. With all buffer gas evacuated^{2.42}, all modes of the nanobeam thermalise well up to a temperature of 4 K; fig. 2.17 filled red and blue points show the mode temperatures of the fundamental and its 7th harmonic. In the presence of buffer gas however,

^{2.42} By design, this cryostat is not meant for cold operation without buffer gas. In order to achieve low temperatures without having buffer gas in the sample volume, we first condense ³He: this is done by filling the 1 K pot with liquid ⁴He and pumping on it to cool it down to < 2 K; finally the sorption pump is heated to 25 K to eject out all ³He gas and pressurise it. Once condensed, droplets of liquid ³He accumulate at the bottom of the cryostat (the so-called “³He tail”); pumping on the condensed liquid using the sorption pump evaporatively cools the liquid to as low as 0.3 K. Once all the condensed ³He is evaporated, the sample volume is in vacuum and the sample temperature slowly rises.

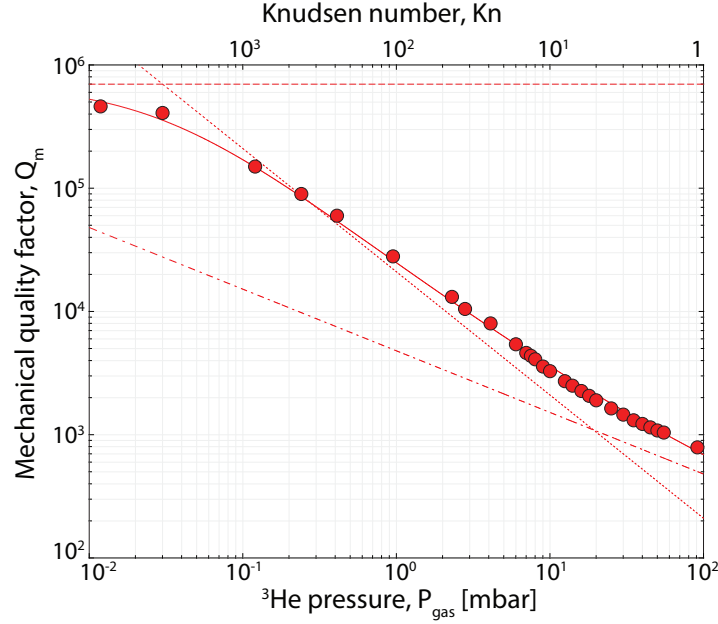


Fig. 2.18 – **Mechanical damping due to buffer gas.** Data points show the mechanical quality factor of the fundamental mode ($\Omega_m = 2\pi \cdot 4.3$ MHz) as a function of the buffer gas pressure in the sample volume. The observed data is understood as arising from two contributions to the quality factor: an internal quality factor, $Q_{m,int} \approx 7 \cdot 10^5$, shown in the broken line; and a gas damping contribution shown in chained and dotted lines (see eq. (2.4.9)). The solid line shows the total model in eq. (2.4.7)). The Knudsen number in the top axis is estimated from eq. (2.4.8), assuming $T_{gas} = 4$ K, $\ell_{gas} \approx 30$ pm (Bohr radius of He), and using $\ell_b = 1 \mu\text{m}$.

modes thermalise well up to about 2 K.

We conjecture that the lack of thermalisation in the absence of buffer gas is due to the lack of thermal conductivity along the beam into the substrate at these very low temperatures. This is consistent with the observation of a universal drop in thermal conductivity of amorphous materials at low temperature [241].

However, for the fundamental mode of the nanobeam, gas damping prevents operating with buffer gas. In fact, the mechanical quality factor observed as a function of pressure, shown in fig. 2.18, may be understood as a sum of two contributions,

$$\begin{aligned} Q_m^{-1}(P_{gas}) &= Q_{m,int}^{-1} + Q_{m,gas}^{-1}(P_{gas}) \\ &= Q_{m,int}^{-1} + Q_{m,gas,visc}^{-1}(P_{gas}) + Q_{m,gas,sque}^{-1}(P_{gas}) \end{aligned} \quad (2.4.7)$$

where $Q_{m,int}$ is the internal quality factor (diluted by stress) when all gas is evacuated, and $Q_{m,gas}(P_{gas})$ is the quality factor due to losses in the presence of buffer gas [216]. Gas damping quality factor is constituted mainly by two physical processes: viscous-type retardation due to the gas [220, 242], and, energy lost by the beam into compressing trapped gas – squeeze-film damping [243]. The nature of viscous damping depends on the nature of the fluid flow; the Knudsen number,

$$\text{Kn} := \frac{\ell_{MF}}{\ell_b} \approx \frac{1}{\sqrt{2\pi}} \cdot \frac{k_B T_{gas}}{\ell_{gas}^3 P_{gas}} \cdot \frac{\ell_{gas}}{\ell_b}, \quad (2.4.8)$$

the ratio between the mean-free path of the gas (ℓ_{MF}) and the characteristic length of the beam (ℓ_b), roughly dictates the damping regime. The second equality estimates the mean-free path based on a statistical model of an ideal gas; here, T_{gas} is the temperature of the gas, while ℓ_{gas} is the semi-classical radius of the gas atom. Note that Kn essentially parametrises the capacity of the surrounding gas to perform work on the beam via thermal forces, or via compressive forces. In the kinetic regime, with $\text{Kn} \gtrsim 10$, damping is essentially due to recoil from independent incoherent scattering events, while at higher pressure, $\text{Kn} \gtrsim 1$, in the hydrodynamic regime, damping is due to the inertia or viscosity of the fluid continuum^{2.43}. For the small beams with relatively small thermal velocities, the fluid flow around the beam is dominated by inertia^{2.44}. Under these conditions, the gas damping contribution is given by [216, 242, 243],

$$Q_{\text{m,gas,visc}}(P_{\text{gas}}) = \begin{cases} \frac{\rho_b}{P_{\text{gas}}} \frac{\ell_t}{4} \frac{\Omega_m}{2\pi} \left(\frac{RT_{\text{gas}}}{M_{\text{gas}}} \right)^{1/2}; & \text{Kn} \gtrsim 10 \\ \frac{\rho_b}{\sqrt{P_{\text{gas}}}} \frac{\ell_{\text{BL}}}{6\pi} \left(\frac{\Omega_m}{2\pi} \right)^{1/2} \left(\frac{2RT_{\text{gas}}}{\mu_{\text{gas}}} \right)^{1/2}; & \text{Kn} \approx 1 \end{cases} \quad (2.4.9)$$

where ρ_b is the mass density of the beam, ℓ_t the thickness of the beam in the direction of motion, ℓ_{BL} is a phenomenological boundary layer thickness, M_{gas} the molar mass of the surrounding gas and μ_{gas} is its dynamic viscosity. Importantly, the scaling with pressure characterises the transition from the kinetic to the hydrodynamic regimes. The models shown in fig. 2.18 (dotted and chained lines) are fits employing this pressure scaling. Squeeze-film damping, in the regime where at least one transverse dimension of the beam (ℓ_t) is comparable to the thickness of the squeezed gas layer ($\ell_{\text{gas,t}}$), leads to a contribution [243, 246],

$$Q_{\text{m,gas,sque}}^{-1} = (\ell_{\text{gas,t}}/\ell_t) Q_{\text{m,gas,visc}}^{-1}$$

which is not seen to be a relevant contribution to the observed data^{2.45}.

Ultimately, the combination of gas damping and inefficient thermalisation forces experiments to be performed at cryogenic temperatures $T \gtrsim 4$ K with all buffer gas evacuated. In principle, this allows us to achieve, $\Omega_m \gtrsim 10 \cdot n_{\text{m,th}} \Gamma_m$, corresponding to $\Gamma_m \approx 2\pi \cdot 6$ Hz. The latter value is independently verified using ring-down measurements.

2.4.3.1 Nature of elastic force: radiation pressure vs. thermoelasticity

Given that the beam does not necessarily thermalise below 4 K, it needs to be investigated whether the thermal gradients established in the beam produce additional mechanical forces – *thermoelastic forces* – and how they compare against the desired radiation pressure force.

^{2.43} It is interesting to note that in the extreme regime, $\text{Kn} \ll 0.1$, the spectrum of gas damping samples the inter-particle collisions of the gas atoms [244, 245] and necessitates a non-Newtonian fluid model – however this regime is not relevant here.

^{2.44} The Reynolds number, $\text{Re} := (\text{beam velocity})(\text{transverse length})/(\text{kinematic viscosity of He})$, determines this. For the beam undergoing thermal motion, its root mean square velocity on resonance is $\sqrt{2n_{\text{m,th}} x_{\text{zp}} \frac{\Omega_m}{2\pi}} \approx 10^{-4}$ m/s. For beam transverse dimension of $0.5 \mu\text{m}$, it follows that, $\text{Re} < 10^{-4}$.

^{2.45} Due to the nature of the problem, it seems reasonable to imagine that for a narrow longitudinal (along the beam) constriction with a transverse opening, squeeze-films get evacuated much more quickly than diffusion would suggest. In fact molecules in a squeeze film execute Lévy walks [247], lending plausibility to their absence after even a short pumping time.

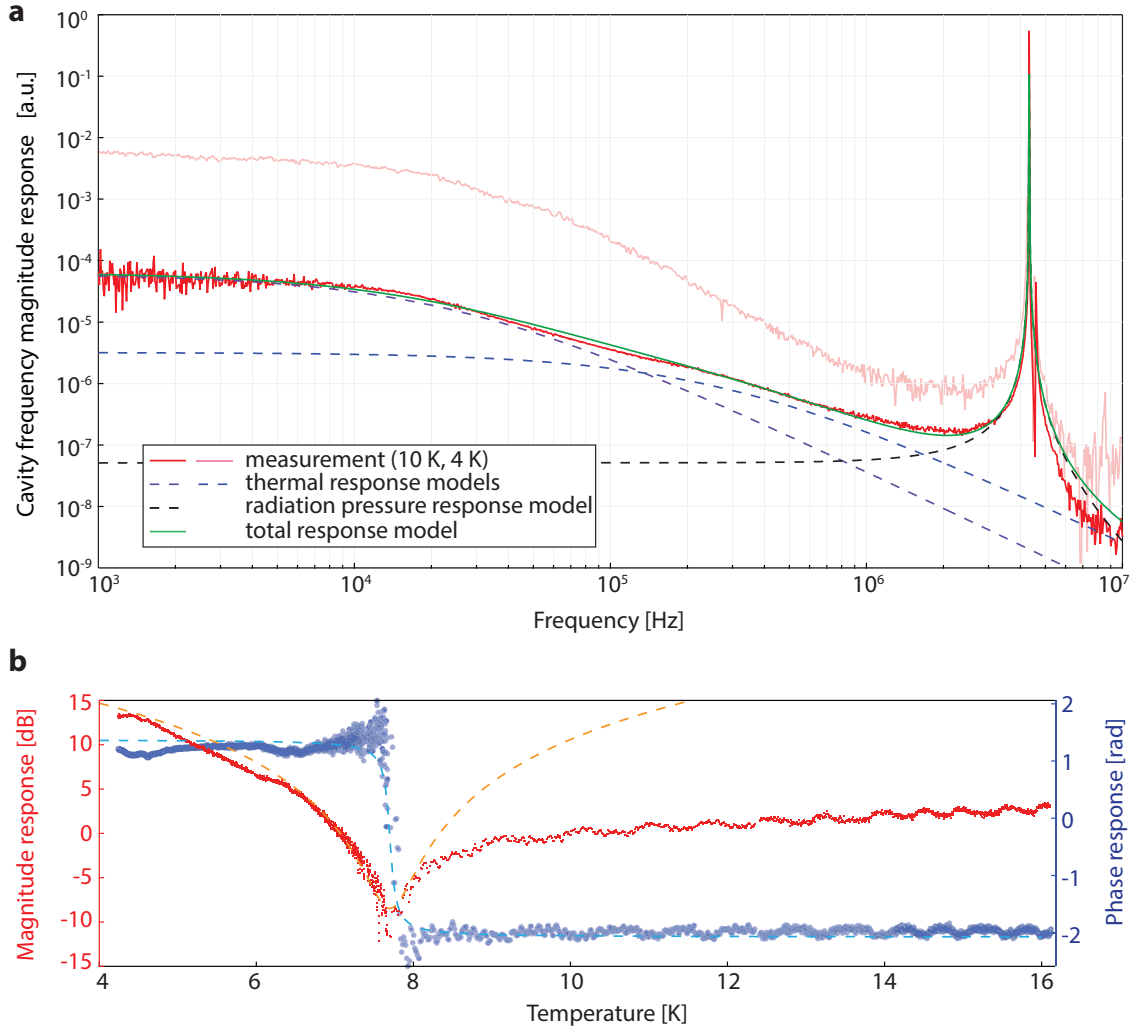


Fig. 2.19 – **Cavity frequency response to intensity modulation.** (a) Frequency response measured by modulating an independent pump beam and demodulating the effect on a resonant probe using a homodyne detector. Red (pink) trace shows data taken at 10 K (4 K). Black dashed is a fit to expected radiation pressure force, which is prompt with respect to the low mechanical frequency $\Omega_m \approx 2\pi \cdot 4.3$ MHz. The blue and purple dashed lines show cavity frequency shifts expected from models of delayed thermal conduction in the disk and/or beam. (b) Low frequency ($\Omega = 2\pi \cdot 2$ kHz) response as a function of cryostat temperature. Red (blue) points show the magnitude (phase) response.

In order to investigate the contribution of these competing forces, we measured the response of the cavity frequency ω_c to modulation of the injected power P_{in} , i.e. $\partial\omega_c/\partial P_{in}$. This is done by using a probe laser locked on the resonance of a cavity mode at 780 nm, while a pump laser is locked on resonance to an independent cavity mode at 850 nm. Care is taken to ensure that there is no optical and/or electronic cross-talk between the two; both lasers are attenuated to (each ≈ 100 nW) ensure no spurious static thermal shifts of cavity resonance. The amplitude of the incident pump is modulated by an intensity modulator driven by a network analyser, while the frequency fluctuations in the probe laser are detected using a homodyne detector whose output voltage is demodulated by the network analyser.

2. FOUNDATIONS

Figure 2.19a shows two examples of such a response measurement, taken at 10 K (red) and 4 K (pink). We understand the measured cavity frequency fluctuation $\delta\omega_c$ as arising from three different sources:

$$\delta\omega_c[\Omega] = \delta\omega_c^{\text{th}}[\Omega] + \delta\omega_c^{\text{mech,the}}[\Omega] + \delta\omega_c^{\text{mech,rad}}[\Omega] \quad (2.4.10)$$

where $\delta\omega_c^{\text{th}}$ is the cavity frequency shift due to material and geometric thermal deformation of the cavity volume, $\delta\omega_c^{\text{mech,the}}$ is due to mechanical motion driven by thermoelastic forces [248, 249] and $\delta\omega_c^{\text{mech,rad}}$ is due to mechanical motion driven by radiation pressure force.

The cavity thermal shift can be understood as arising from change in the cavity length via a finite thermal expansion α_V , or due to material property (refractive index ν) changes, i.e.

$$\delta\omega_c^{\text{th}}[\Omega] = -\omega_c \left(\alpha_V + \frac{1}{\nu} \frac{\partial \nu}{\partial T} \right) \delta T_c[\Omega] = -\omega_c \left(\alpha_V + \frac{1}{\nu} \frac{\partial \nu}{\partial T} \right) \frac{G_c^{\text{th}}}{1 + i\Omega/\Omega_c^{\text{th}}} \delta n_c, \quad (2.4.11)$$

where the cavity temperature change δT_c is assumed to be driven by pump photon number modulation δn_c , and the temperature relaxes via diffusion, modelled as a single-pole response with cut-off Ω_c^{th} and gain G_c^{th} . In fig. 2.19a, the low frequency cut-off at 10 kHz may be identified with Ω_c^{th} , consistent with measurements on toroidal microcavities [250]. Further, the low frequency response G_c^{th} as a function of cryostat temperature, shown in fig. 2.19b, is consistent with the known $\partial \nu / \partial T = 0$ point of silica microcavities at 8 K [251].

The remaining two contributions to $\delta\omega_c$ in eq. (2.4.10) arise from frequency shifts due to mechanical motion, i.e.

$$\begin{aligned} \delta\omega_c^{\text{mech}} &:= \delta\omega_c^{\text{mech,the}} + \delta\omega_c^{\text{mech,rad}} \\ \delta\omega_c^{\text{mech,the}}[\Omega] &= G_{\text{the}} \chi_x[\Omega] \frac{(\kappa_{\text{abs}}/c) \delta n_c}{1 + i\Omega/\Omega_{\text{the}}} \\ \delta\omega_c^{\text{mech,rad}}[\Omega] &= G_{\text{rad}} \chi_x[\Omega] \frac{(\kappa/c) \delta n_c}{1 + i\Omega/\Omega_{\text{rad}}}. \end{aligned} \quad (2.4.12)$$

Here, G_{rad} (G_{the}) is the optomechanical coupling due to radiation pressure (thermoelastic) motion, χ_x is the mechanical oscillator response, $(\kappa/c) \delta n_c$ ($(\kappa_{\text{abs}}/c) \delta n_c$) is the recoil force due to pump photon number modulation, and $\Omega_{\text{rad}} = \kappa/2$ (Ω_{the}) is the characteristic response frequency of the radiation pressure (thermoelastic) force. Note that since $\kappa \gg \Omega_m$, the radiation pressure force is effectively instantaneous, while the thermoelastic force has a finite delay due to the absorption and diffusion of temperature in the nanobeam. It follows that the response measured near the mechanical frequency (where $\delta\omega_c^{\text{th}}$ is negligible),

$$\left| \frac{\delta\omega_c^{\text{mech}}[\Omega]}{\delta n_c[\Omega]} \right| \approx \left| \delta\omega_c^{\text{mech,rad}}[\Omega] \right| \cdot \left| 1 + \frac{G_{\text{the}} \kappa_{\text{abs}}}{G_{\text{rad}} \kappa} \frac{1}{1 + i\Omega/\Omega_{\text{the}}} \right|,$$

provides information regarding the fractional contribution of the thermoelastic force compared to radiation pressure (second factor on the left-hand side). From fig. 2.19a, and other similar measurements, we have determined that radiation pressure dominates at temperatures above 6 K whereas for colder temperatures, thermoelastic back-action is observed.

2.4.4 Experimental schematic

Figure 2.20 shows the schematic of the essential optical and electronic layout of the entire experiment. At the heart of the experiment is a ^3He cryostat (Oxford Instruments, HelioxTL), in which is embedded a chip containing multiple optomechanical devices. A desired device is probed by coupling to its optical cavity using a tapered optical fiber. The tapered optical fiber can be driven by one of three laser sources: a tunable 780 nm external cavity diode laser (NewFocus, Velocity), an 850 nm ECDL, or a Ti:Sa laser (MSquared, Solstis). Typically, the 780 nm laser (ECDL or Ti:Sa) is used for probing the cavity, while the 850 nm laser is used for actuating the cavity and/or the mechanical oscillator.

Both lasers can be locked to cavity resonance; they are frequency modulated using an EOM, and the modulation sideband is demodulated after the cavity transmission is detected on avalanche photodiodes. The cavity is placed in one arm of a balanced Mach-Zehnder interferometer. Indeed, the cavity transmission is directed onto either a balanced homodyne detector, or a balanced heterodyne detector.

In chapter 3, the homodyne configuration, operated using the 780 nm ECDL is used to measure mechanical motion, while the 850 nm ECDL is used to perform feedback control. In chapter 4, the same configuration is employed, with the addition that a part of the 780 nm transmission is directed onto the balanced heterodyne detector. The homodyne detector may also be locked onto the amplitude quadrature, as in chapter 4, to probe for optical squeezing.

During measurements reported in chapter 4, to study quantum correlations in the transmitted optical beam, it was found convenient to synchronise the internal clocks of all RF sources and receivers: this was done by using the 10 MHz signal derived from an atomic clock (not shown in fig. 2.20).

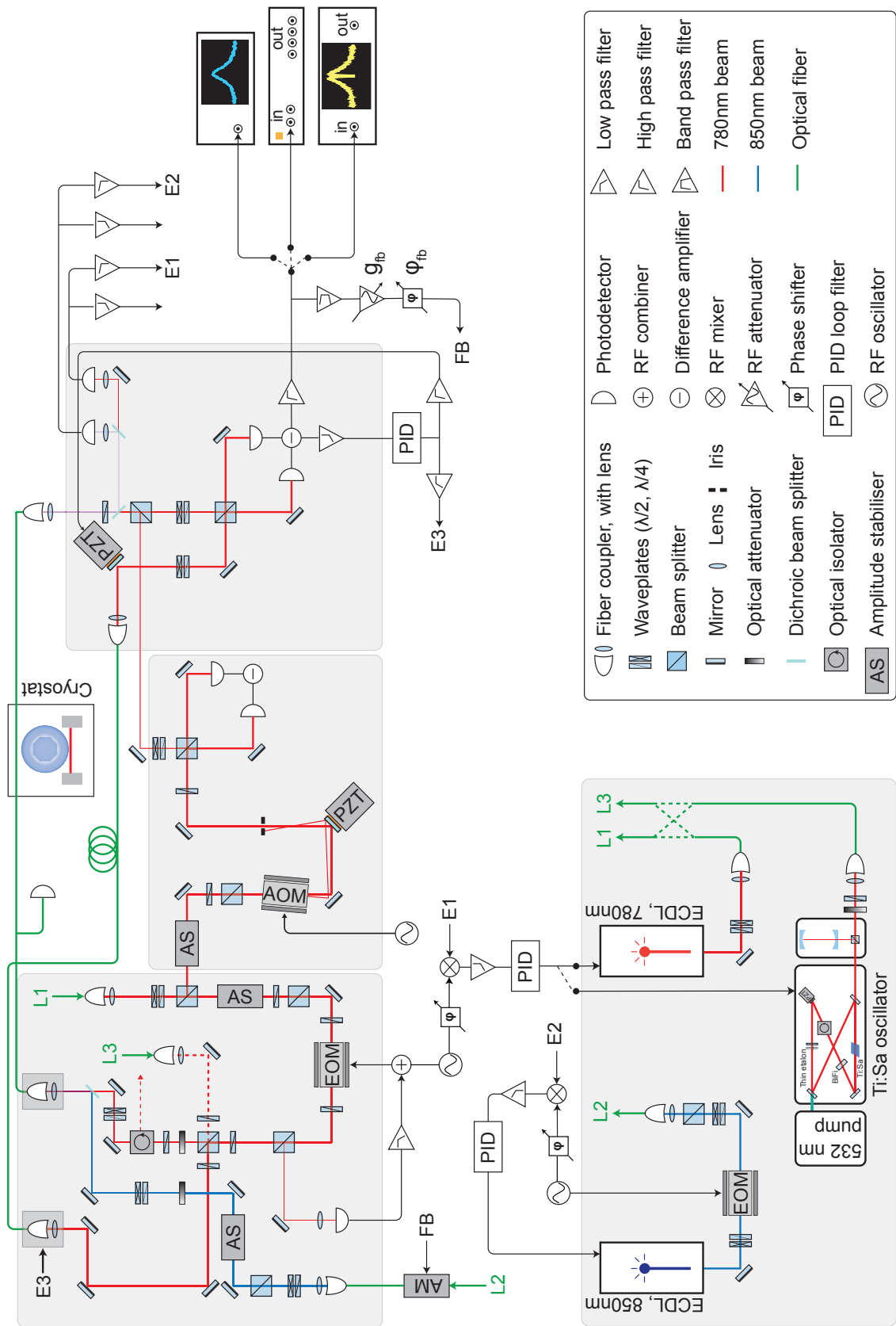


Fig. 2.20 – Layout of the experiment.

3 *Measurement-based control at the thermal decoherence rate*

The ability to exert control over physical systems to a degree where their quantum mechanical behaviour can be probed and manipulated has been the focus of a *second* quantum revolution [252]^{3.1}. The past 40 years have witnessed an exquisite level of control being achieved on atomic systems, mostly fuelled by the availability of the laser as a highly coherent element that synthesises forces that steers atoms towards some desired state. This approach, termed *autonomous control*, essentially relies on engineering a hamiltonian whose open-loop evolution achieves some desired target. In this scenario the essential requirement is to be able to perform control operations within the decoherence time of the desired state.

A different control strategy – *feedback control* – has a much longer and richer historic pedigree. Classical feedback control of a steam governor – a form of oscillatory valve used to regulate a steam engine – developed by Maxwell [253] may be argued to underpin much of the industrial revolution. Precise timekeeping, either using mechanical clockworks [254] or modern atomic standards [255, 256], employ some form of classical control^{3.2}. Indeed, the history of feedback control is intimately intertwined with that of precision measurements: deflection galvanometers were subjected to feedback control [258, 259] to reduce their thermal motion; torsion balances used for precise tests of general relativity were subjected to similar treatment [260]; stochastic cooling of the transverse momentum of anti-proton beams at CERN [261] was instrumental in the observation of the carriers of the weak nuclear force; feedback control of single trapped electrons [262] enable some of the most stringent tests of QED.

In a quantum mechanical description of such “real-time” feedback control [263, 264], the burden of timescale is shifted to the measurement: the measurement must be strong enough to track the quantum fluctuations of the system under control, while simultaneously being weak enough to not impart excess back-action [265]. Spectacular applications of such measurement-based feedback, for example to stabilize microwave Fock states [266, 267] and persistent Rabi oscillations of an artificial atom [268], have been limited to well isolated quantum systems.

For mechanical oscillators, ideal weak position measurements [69] have in fact been available since the advent of the laser, in the context of shot-noise-limited interferometry [196]. Only recently, however, with the confluence of low-loss, cryogenic micromechanics and on-chip,

^{3.1} The first being the consolidation of the theory of quantum mechanics and its experimental verification in well controlled (sub-)atomic systems.

^{3.2} Incidentally, much of the toolbox of autonomous control of atomic systems was developed with a view towards more precise timekeeping [257].

integrated photonics [51], has it been feasible to consider their application to quantum feedback protocols [269, 270]. The main challenge is that for a typical, radio-frequency nanomechanical oscillator, a single quantum of excitation (a phonon) is exchanged with the thermal environment at a rate much faster than it can be measured. In order to control a nanomechanical oscillator using measurement-based quantum feedback, it is necessary that the measurement be ‘weak’ and yet at the same time strong enough to resolve the oscillator’s quantum state in the timescale of its thermal decoherence. This places stringent demands on the measurement precision.

This chapter details the realisation of this possibility, namely, the first demonstration of a continuous measurement capable of resolving the zero-point motion of a solid-state oscillator, and the use of real-time feedback to stabilise its ground state with 16% fidelity [53].

3.1 Theoretical and experimental background

The ensuing sections address the theoretical requirements for being able to perform measurement-based feedback on a mechanical oscillator (in section 3.1.1), and details of its specific implementation in our experiment (in section 3.1.2).

3.1.1 Theory of feedback cooling of a harmonic oscillator

We consider the harmonic oscillator (see section 2.2.1.1) with position fluctuations $\delta\hat{x}$, driven by three stochastic forces: a thermal force ($\delta\hat{F}_{\text{th}}$) associated with the ambient environment (as in section 2.2.1.1), a ‘back-action’ force ($\delta\hat{F}_{\text{BA}}$) associated with the oscillator’s coupling to a measurement device (as in section 2.3), and a feedback force ($\delta\hat{F}_{\text{fb}}$) that controls the oscillator (to be introduced). The dynamics of this system is described by the equation,

$$\begin{aligned} \delta\ddot{\hat{x}} + \Gamma_m \delta\dot{\hat{x}} + \Omega_m^2 \delta\hat{x} &= m^{-1} (\delta\hat{F}_{\text{th}}(t) + \delta\hat{F}_{\text{BA}}(t) + \delta\hat{F}_{\text{fb}}(t)) \\ \text{i.e., } \delta\hat{x}[\Omega] &= \chi_x[\Omega] (\delta\hat{F}_{\text{th}}[\Omega] + \delta\hat{F}_{\text{BA}}[\Omega] + \delta\hat{F}_{\text{fb}}[\Omega]) \end{aligned} \quad (3.1.1)$$

where χ_x is the intrinsic mechanical susceptibility,

$$\chi_x[\Omega]^{-1} = m (-\Omega^2 + \Omega_m^2 - i\Omega\Gamma_m).$$

We adopt the following model for the back-action and feedback forces:

$$\delta\hat{F}_{\text{BA}}[\Omega] = -\chi_{\text{BA}}[\Omega]^{-1} \delta\hat{x}[\Omega] + \delta\hat{F}_{\text{BA,th}}[\Omega] \quad (3.1.2a)$$

$$\delta\hat{F}_{\text{fb}}[\Omega] = -\chi_{\text{fb}}[\Omega]^{-1} \delta\hat{y}[\Omega] + \delta\hat{F}_{\text{fb,th}}[\Omega], \quad (3.1.2b)$$

depicted in the schematic in fig. 3.1. Each force has two components: a ‘dynamic’ component, characterised by a linear susceptibility, that contains correlations with the oscillator’s position, and an effective thermal component. For the back-action force, the dynamic component leads to dynamic back-action, while its thermal component leads to measurement back-action. The dynamic component of the feedback force is linear in the record of the position measurement,

$$\delta\hat{y} := \delta\hat{x} + \delta\hat{x}_{\text{imp}},$$

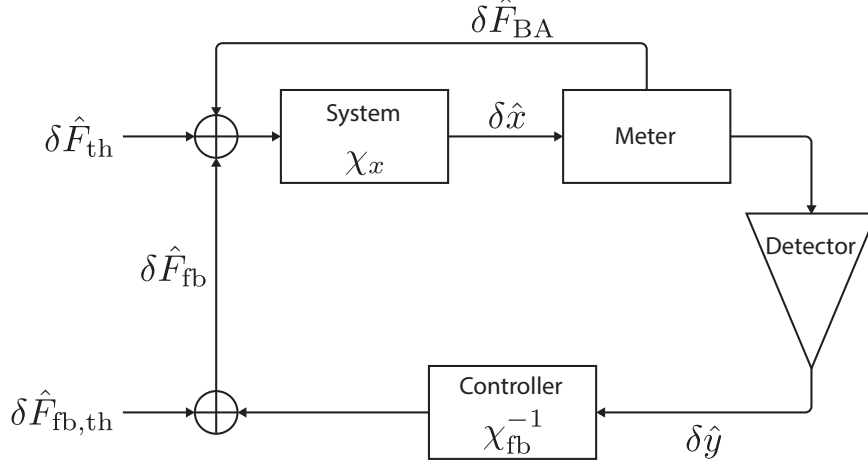


Fig. 3.1 – **Schematic of measurement-based feedback loop.** The oscillator (system) experiences a multitude of forces: the ambient thermal force $\delta\hat{F}_{\text{th}}$, a back-action force $\delta\hat{F}_{\text{BA}}$ arising from its coupling to the optical field (meter), and finally, a feedback force $\delta\hat{F}_{\text{fb}}$ synthesised from the output of a linear detector. Note that contrary to convention [271], the role of an actuator, that converts the controller output to an impressed force, is not made explicit.

where $\delta\hat{x}_{\text{imp}}$ is the measurement imprecision. The thermal component of the feedback force arises from noise picked up in the feedback path – for example, it could model the quantum fluctuations of the actuator that impresses the feedback force $\delta\hat{F}_{\text{fb}}$ on the oscillator. Hereafter, for simplicity, we neglect the dynamic portion of the back-action force (i.e. set $\chi_{\text{BA}}^{-1} = 0$). We revisit this approximation in detail in section section 3.1.2.1.

The equation of motion in eq. (3.1.1) gets modified by the presence of the feedback force in eq. (3.1.2a), to,

$$(\chi_x^{-1} + \chi_{\text{fb}}^{-1}) \delta\hat{x} = \delta\hat{F}_{\text{th}} + \delta\hat{F}_{\text{BA,th}} + \delta\hat{F}_{\text{fb,th}} - \chi_{\text{fb}}^{-1} \delta\hat{x}_{\text{imp}}, \quad (3.1.3)$$

while the in-loop measurement record (the apparent position) satisfies,

$$(\chi_x^{-1} + \chi_{\text{fb}}^{-1}) \delta\hat{y} = \delta\hat{F}_{\text{th}} + \delta\hat{F}_{\text{BA,th}} + \delta\hat{F}_{\text{fb,th}} + \chi_x^{-1} \delta\hat{x}_{\text{imp}}. \quad (3.1.4)$$

Note that in addition to the thermal component, $\delta\hat{F}_{\text{fb,th}}$, feedback introduces an additional thermal force, $\chi_{\text{fb}}^{-1} \delta\hat{x}_{\text{imp}}$, proportional to the measurement noise. In the ideal case, where the measurement imprecision is set by quantum fluctuations in the meter, this force noise constitutes a fundamental limit to the performance of the feedback protocol.

The objective of feedback cooling is to nullify the effect of the ambient thermal force $\delta\hat{F}_{\text{th}}$ on the oscillator. A strategy that realises this goal relies on coupling the oscillator strongly to an alternate less thermal environment. This *cold damping* strategy [269, 270] involves the specific choice,

$$\chi_{\text{fb}}^{-1}[\Omega] = -im\Omega\Gamma_{\text{fb}}[\Omega], \quad (3.1.5)$$

for the feedback filter, ideally with the feedback damping Γ_{fb} given by,

$$\Gamma_{\text{fb}}[\Omega] = g_{\text{fb}}\Gamma_{\text{m}}, \quad (3.1.6)$$

for some dimensionless real *feedback gain* g_{fb} . The effective mechanical susceptibility

$$\begin{aligned}\chi_x^{(g_{\text{fb}})}[\Omega]^{-1} &:= \chi_x[\Omega]^{-1} + \chi_{\text{fb}}[\Omega]^{-1} \\ &= m(-\Omega^2 + \Omega_m^2 - i\Omega\Gamma_m(1 + g_{\text{fb}})),\end{aligned}\quad (3.1.7)$$

featuring an increased damping rate due to feedback, provides for the thermally driven position fluctuations, $\chi_x^{(g_{\text{fb}})}[\Omega_m]\delta\hat{F}_{\text{th}}[\Omega_m] \propto n_{\text{m,th}}/g_{\text{fb}}$, to be suppressed for large values of the feedback gain.

To see how this damping leads to cooling, we reconsider the three components of the thermal environment: (1) an ambient reservoir with which the oscillator equilibrates, (2) a reservoir constituted by stochastic measurement back-action, and (3) a reservoir constituted by stochastic fluctuations of the feedback actuator. For a high-Q oscillator, and in the limit where these noises may be assumed to be Gaussian, each reservoir can be assigned a thermal noise equivalent occupation: $n_{\text{m,th}}$, $n_{\text{m,BA}}$ and $n_{\text{m,fb}}$ respectively. Thus the total effective thermal force may be expressed:

$$\bar{S}_F^{\text{tot}}(\Omega) = (n_{\text{m,th}} + n_{\text{m,BA}} + n_{\text{m,fb}} + \frac{1}{2}) \cdot |\chi_x[\Omega_m]|^{-2} \cdot 2\bar{S}_x^{\text{ZP}}[\Omega_m], \quad (3.1.8)$$

where we have introduced for convenience the (peak) position spectral density in the ground state (eq. (2.2.29)):

$$\bar{S}_x^{\text{ZP}}[\Omega_m] = \frac{4x_{\text{ZP}}^2}{\Gamma_m}.$$

We further introduce the imprecision quanta, n_{imp} , as the apparent thermal occupation associated with noise in the measurement:

$$\bar{S}_x^{\text{imp}}[\Omega] = n_{\text{imp}} \cdot 2\bar{S}_x^{\text{ZP}}[\Omega_m]. \quad (3.1.9)$$

Thus the spectra of physical position and the measurement record, are given by

$$\begin{aligned}\frac{\bar{S}_x[\Omega]}{2\bar{S}_x^{\text{ZP}}[\Omega_m]} &= \frac{(n_{\text{m,th}} + n_{\text{m,BA}} + n_{\text{m,fb}} + \frac{1}{2})\Omega_m^2\Gamma_m^2 + n_{\text{imp}}g_{\text{fb}}^2\Omega^2\Gamma_m^2}{(\Omega_m^2 - \Omega^2)^2 + \Omega^2\Gamma_{\text{eff}}^2} \\ \frac{\bar{S}_y[\Omega]}{2\bar{S}_x^{\text{ZP}}[\Omega_m]} &= \frac{(n_{\text{m,th}} + n_{\text{m,BA}} + n_{\text{m,fb}} + \frac{1}{2})\Omega_m^2\Gamma_m^2 + n_{\text{imp}}((\Omega_m^2 - \Omega^2)^2 + \Omega^2\Gamma_m^2)}{(\Omega_m^2 - \Omega^2)^2 + \Omega^2\Gamma_{\text{eff}}^2}.\end{aligned}\quad (3.1.10)$$

The mean phonon occupancy of the cooled oscillator is then given by

$$\begin{aligned}2n_m + 1 &= \int_0^\infty \frac{\bar{S}_x[\Omega]}{x_{\text{ZP}}^2} \frac{d\Omega}{2\pi} \\ \Rightarrow n_m &= \frac{(n_{\text{m,th}} + n_{\text{m,ba}} + n_{\text{m,fb}} + \frac{1}{2}) + n_{\text{imp}}g_{\text{fb}}^2}{1 + g_{\text{fb}}} - \frac{1}{2}.\end{aligned}\quad (3.1.11)$$

In the relevant limit of $n_{\text{m,th}} \gg \frac{1}{2}$, a minimum of

$$\begin{aligned}n_{\text{m,min}} &\approx 2\sqrt{(n_{\text{m,th}} + n_{\text{m,ba}} + n_{\text{m,fb}})n_{\text{imp}}} - \frac{1}{2} \\ &= \frac{1}{2\hbar} \sqrt{\bar{S}_F^{\text{tot}}[\Omega_m]\bar{S}_x^{\text{imp}}[\Omega_m]} - \frac{1}{2}\end{aligned}\quad (3.1.12)$$

is attained at an optimal gain of

$$g_{\text{fb,opt}} \approx \sqrt{\frac{n_{\text{m,th}} + n_{\text{m,ba}} + n_{\text{m,fb}}}{n_{\text{imp}}}}. \quad (3.1.13)$$

In particular, for the experimentally relevant case of $n_{\text{m,th}} \gg n_{\text{m,fb}}$, the conventional condition for ground state cooling, $n_{\text{m}} < 1$, translates to

$$n_{\text{imp}} < \frac{9}{16}(n_{\text{m,th}} + n_{\text{m,ba}})^{-1}. \quad (3.1.14)$$

3.1.1.1 Limits due to measurement back-action

As discussed in section 2.3, measurement back-action associated with a cavity-optomechanical position measurement is bound by the imprecision-back-action product: $n_{\text{imp}}n_{\text{m,ba}} \geq \frac{1}{16}$. Imposing this limit, eq. (3.1.14) implies that a necessary condition for ground-state cooling is

$$n_{\text{imp}} < (2n_{\text{m,th}})^{-1}, \quad (3.1.15)$$

equivalently, the measurement imprecision has to satisfy,

$$\bar{S}_x^{\text{imp}} < \frac{S_x^{\text{ZP}}}{n_{\text{m,th}}} = \frac{4x_{\text{ZP}}^2}{n_{\text{m,th}}\Gamma_{\text{m}}} = \frac{4x_{\text{ZP}}^2}{\Gamma_{\text{th}}}, \quad (3.1.16)$$

where $\Gamma_{\text{th}} := \Gamma_{\text{m}}n_{\text{m,th}}$ is the thermal decoherence rate. Notably eq. (3.1.16) corresponds to an imprecision $n_{\text{th}}/2$ times below that at the standard quantum limit, or equivalently, a measurement rate [69, 272]

$$\Gamma_{\text{meas}} := \frac{x_{\text{ZP}}^2}{2S_x^{\text{ZP}}} = \frac{\Gamma_{\text{m}}}{16n_{\text{imp}}} > \frac{\Gamma_{\text{th}}}{8}, \quad (3.1.17)$$

comparable to the thermal decoherence rate.

3.1.1.2 Some remarks on thermodynamics

In the regime where feedback cooling is strong ($g_{\text{fb}} \gg 1$) and quantum-limited ($n_{\text{m,fb}} = 0$), intuition can be garnered by noticing that eq. (3.1.11) can be expressed as the detailed balance condition,

$$(n_{\text{m}} + \frac{1}{2})\Gamma_{\text{m}}g_{\text{fb}} \approx (n_{\text{m,th}} + n_{\text{m,BA}})\Gamma_{\text{m}} + n_{\text{imp}} \cdot \Gamma_{\text{m}}g_{\text{fb}}.$$

This suggests that cooling as affected by feedback can be understood as a thermodynamic process which proceeds by the reduction of entropy of the mechanical oscillator to a level ultimately set by the entropy due to the imperfect estimation of the mechanical position.

Note that eq. (3.1.12) approximately conveys that the lowest temperature of the oscillator, $T_{\text{m,min}} \approx 2\sqrt{T_{\text{m,th}}T_{\text{imp}}}$, is the geometric mean of the initial oscillator temperature and that of the measurement reservoir. The first law of thermodynamics, naively applied, would suggest that the lowest temperature be the arithmetic mean, $\frac{1}{2}(T_{\text{m,th}} + T_{\text{imp}})$.

This clash can apparently be reconciled by appealing to the second law of thermodynamics which states that the change in entropy, $dS \geq 0$, always. Assigning an effective heat capacity,

C , to either environment (justified by the fact that both are harmonic oscillators with infinitely many degrees of freedom), the second law insists that,

$$\begin{aligned} dS &= \sum_{i \in \{\text{th,fb}\}} C \int_{T_i}^{T_{\text{final}}} \frac{dT}{T} \geq 0 \\ \Rightarrow \log \frac{T_{\text{final}}^2}{T_{\text{m,th}} T_{\text{imp}}} &\geq 0 \\ \Rightarrow T_{\text{final}} &\geq \sqrt{T_{\text{m,th}} T_{\text{imp}}}. \end{aligned}$$

3.1.2 Measurement and feedback using a cavity

The discussion below traces the precise role of the cavity optomechanical interaction in the continuous measurement of the oscillator position at the thermal decoherence rate. Experimental non-idealities in the system, like internal scattering in the cavity mode warrants a separate discussion here, deviating from the ideal considerations given in section 2.3.

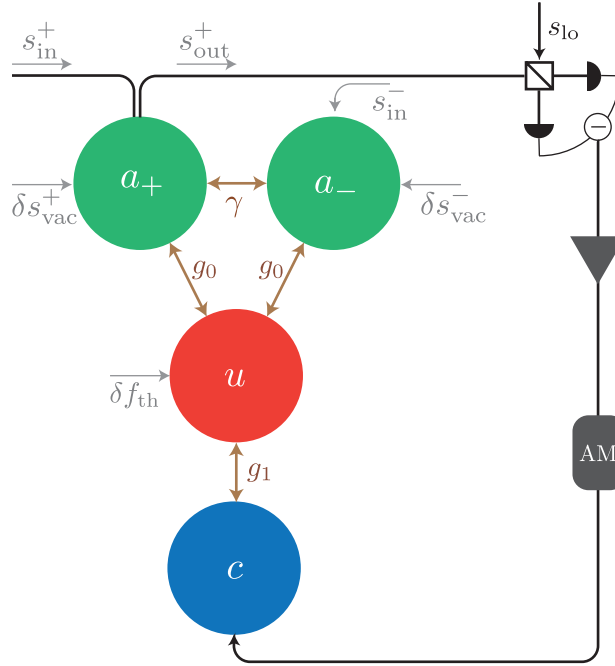


Fig. 3.2 – Schematic of the input, output and couplings between the various subsystems in the experiment.

We adopt the following set of coupled Langevin equations to model the dynamics of the cavity mode (characterised by the slowly varying amplitude of the intracavity field, \hat{a}) and the mechanical mode (characterised by its normalised position, $\hat{z} := \hat{x}/x_{\text{zfp}}$):

$$\begin{aligned} \dot{\hat{a}}_+ &= \left(i\Delta_0 - \frac{\kappa}{2}\right) \hat{a}_+ + \frac{i\gamma}{2} \hat{a}_- + ig_0 \hat{z} \hat{a}_+ + \sqrt{\eta_c \kappa} \hat{a}_{\text{in}}^+ + \sqrt{(1-\eta_c)\kappa} \delta \hat{a}_{\text{vac}}^+ \\ \dot{\hat{a}}_- &= \left(i\Delta_0 - \frac{\kappa}{2}\right) \hat{a}_- + \frac{i\gamma}{2} \hat{a}_+ + ig_0 \hat{z} \hat{a}_- + \sqrt{\eta_c \kappa} \hat{a}_{\text{in}}^- + \sqrt{(1-\eta_c)\kappa} \delta \hat{a}_{\text{vac}}^- \end{aligned} \quad (3.1.18a)$$

$$\ddot{\hat{z}} + \Gamma_m \dot{\hat{z}} + \Omega_m^2 \hat{z} = \delta \hat{f}_{\text{th}} + \hat{f}_{\text{BA}} + \hat{f}_{\text{fb}}. \quad (3.1.18b)$$

Notably, in eq. (3.1.18a) we use a two-mode model to describe the microdisk cavity. Subscripts + and – refer to whispering gallery modes propagating along (‘clockwise’) and against (‘counter-clockwise’) the conventional direction (+) of the injected field, respectively. The two modes are coupled at a rate γ by scattering centres [273], leading to a characteristic splitting of the optical resonance. Motivated by the geometrical nature of the interaction, we assume that both modes share a common vacuum optomechanical coupling rate, g_0 .

Light is physically coupled to the microdisk cavity using an optical fiber as discussed in section 2.2.2.5. In fig. 3.2 and eq. (3.1.18a), we model this coupler as a two port waveguide. Fields entering(exiting) the ‘clockwise’ port, $\hat{a}_{\text{in(out)}}^+$, couple directly to the clockwise cavity mode. Fields entering(exiting) the ‘counter-clockwise’ port, $\hat{a}_{\text{in(out)}}^-$, couple directly to the counter-clockwise mode. The cavity-waveguide coupling rate is $\kappa_{\text{ex}} = \eta_c \kappa$, where $\kappa = \kappa_{\text{ex}} + \kappa_0$ is the total cavity decay rate and κ_0 is the intrinsic cavity decay rate. In addition, each cavity mode is driven through its intrinsic decay channel by a vacuum state with amplitude $\delta \hat{a}_{\text{vac}}^\pm$. Input field amplitudes are here normalised so that $P_{\text{in}}^\pm = \hbar \omega_\ell^\pm |\bar{a}_{\text{in}}^\pm|^2$ is the injected power. $\Delta_0 = \omega_c - \omega_\ell^\pm$ denotes the detuning of the drive field carrier frequency, ω_ℓ^\pm , from the centre frequency of the optical mode doublet, ω_c .

The dynamics of the mechanical oscillator is governed by eq. (3.1.18b). Note that owing to the dimensionless form of \hat{z} , generalised forces $\hat{f}_{\text{th,ba,fb}}$ have dimensions of (time) $^{-2}$; the actual forces (as used in section 3.1.1), in units of Newtons, are given by $\hat{F}_i = m x_{\text{zp}} \hat{f}_i$ ($i \in \{\text{th, opt, fb}\}$). Using this convention, the thermal Langevin force is given by

$$\delta \hat{f}_{\text{th}} = \Omega_m \Gamma_m \sqrt{2(2n_{\text{m,th}} + 1)} \delta \hat{\zeta}_{\text{th}}, \quad (3.1.19)$$

where $\delta \hat{\zeta}_{\text{th}}$ is a unit variance white noise process modelling the thermal fluctuations.

We model the measurement back-action force as the radiation pressure imparted by the excited mode doublet \hat{a}_\pm :

$$\hat{f}_{\text{BA}} = \Omega_m g_0 (\hat{a}_+^\dagger \hat{a}_+ + \hat{a}_-^\dagger \hat{a}_-). \quad (3.1.20)$$

Likewise, the feedback force is modelled as the radiation pressure imparted by an independent, auxiliary cavity mode with amplitude \hat{c} and optomechanical coupling rate g_1 :

$$\hat{f}_{\text{fb}} = \Omega_m g_1 \hat{c}^\dagger \hat{c}. \quad (3.1.21)$$

In the following treatment, both optical modes are driven by optical fields entering the clockwise port of the optical fiber. The field driving mode doublet \hat{a}_\pm is referred to as the ‘sensor’ field. The field driving mode \hat{c} is referred to as the “feedback” field. The counter-clockwise port of the optical fiber is used to monitor the transmitted sensor field, but is otherwise left open.

Steady state. When the cavity is excited by the sensor field, the static component of the ensuing radiation pressure force displaces the oscillator to a new steady-state position, \bar{z} , and leads to a

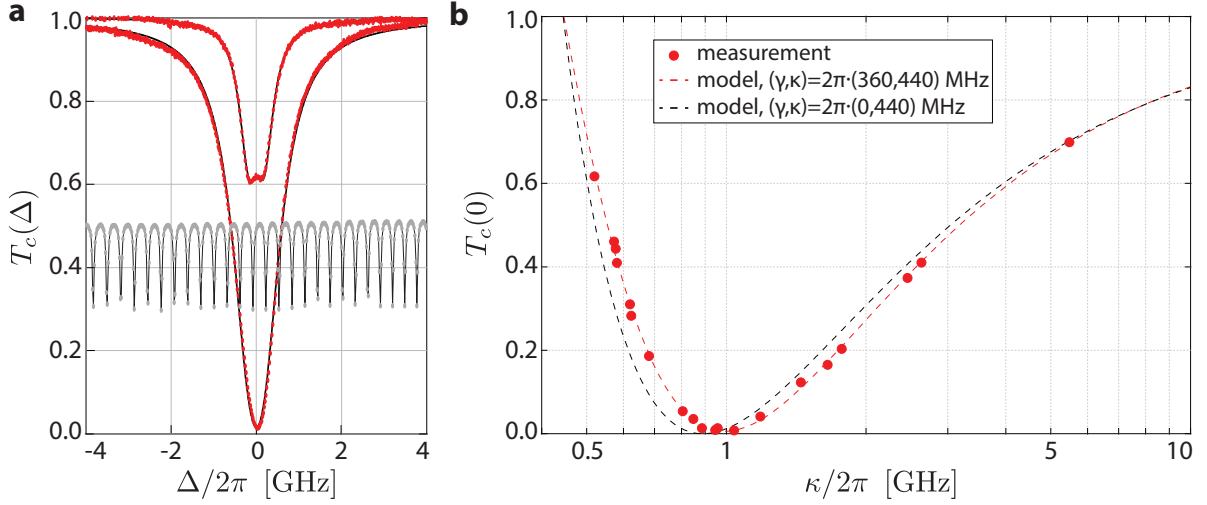


Fig. 3.3 – **Steady state spectroscopy of a cavity mode split by internal scattering.** (a) Red traces show the cavity transmission, $T_c(\Delta)$, recorded as the laser-cavity detuning Δ is changed. The traces show the cavity under-coupled, where the effect of the splitting γ is obvious, and over-coupled where the effect is masked by the loaded linewidth $\kappa = \kappa_0 + \kappa_{\text{ex}}$. The gray trace shows the transmission through a calibrated fiber-loop cavity, recorded simultaneously; its free spectral range provides frequency markers to calibrate the frequency sweep. (b) Transmission on resonance, $T_c(0)$, plotted as a function of the external coupling to the cavity.

renormalisation of the laser-cavity detuning to $\Delta = \Delta_0 + g_0 \bar{z}$. In practice the frequency of the sensor field is stabilised so that $\Delta = 0$. In this case the steady state intracavity field amplitude (\bar{a}) and oscillator position are given by

$$\bar{a}_+ = \sqrt{n_+}, \quad \bar{a}_- = i\sqrt{n_-} \quad \text{and} \quad \bar{z} = \frac{g_0}{\Omega_m}(n_+ + n_-), \quad (3.1.22)$$

where, $n_+ = \frac{4\eta_c}{\kappa} \frac{P_{\text{in}}^+ / \hbar\omega_c}{(1 + \gamma^2/\kappa^2)^2}$ and $n_- = \left(\frac{\gamma}{\kappa}\right)^2 n_+$.

denote the mean intracavity photon number of the clockwise and counter-clockwise modes, respectively. Note that henceforth, we shall denote, $n_c = n_+$, i.e. the intracavity photon number established in the direction of the injected power is that of the clockwise mode.

Splitting of the cavity resonance can be observed spectroscopically in the normalised steady state transmission. Using the input-output relation $\bar{a}_{\text{out}}^+ = \bar{a}_{\text{in}}^+ - \sqrt{\eta_c \kappa} \bar{a}_+$ gives the steady-state cavity transmission,

$$T_c(\Delta) := \frac{P_{\text{out}}^+}{P_{\text{in}}^+} = \left| \frac{\bar{a}_{\text{out}}^+}{\bar{a}_{\text{in}}^+} \right|^2 = 1 - \eta_c \kappa^2 \frac{(\Delta^2 + (\gamma/2)^2 + (\kappa/2)^2) - \eta_c (\Delta^2 + (\kappa/2)^2)}{(\Delta^2 - (\kappa/2)^2 - (\gamma/2)^2)^2}, \quad (3.1.23)$$

consisting of a Lorentzian-like dip, but with the peaks split by γ .

Figure 3.3 shows the steady state transmission of the cavity employed in the experiments reported in this chapter. As described in section 2.2.2.5, the cavity transmission is probed by a diode laser whose frequency is swept over the cavity resonance, while recording the transmission $T_c(\Delta)$. Figure 3.3a traces the steady-state cavity transmission, $T_c(\Delta)$, and shows the effect of cavity mode splitting when under-coupled. Figure 3.3b plots the resonance

transmission, $T_c(0)$, as the cavity coupling efficiency is varied (by varying the physical taper-cavity coupling point). By proper choice of the taper-cavity coupling point, it is possible to achieve over-coupled operation $\eta_c \approx 0.9$.

Fluctuations. Fluctuations of the cavity field, $\delta\hat{a} = \hat{a} - \bar{a}$, and the mechanical position, $\delta\hat{z} = \hat{z} - \bar{z}$, are coupled according to eq. (3.1.18). To first order:

$$\delta\hat{a}_\pm = \left(i\Delta - \frac{\kappa}{2}\right) \delta\hat{a}_\pm + \frac{i\gamma}{2} \delta\hat{a}_\mp + ig_0\bar{a}_\pm \delta\hat{z} + \sqrt{\eta_c\kappa} \delta\hat{a}_{\text{in}}^\pm + \sqrt{(1-\eta_c)\kappa} \delta\hat{a}_{\text{vac}}^\pm \quad (3.1.24a)$$

$$\delta\hat{z} + \Gamma_m\delta\hat{z} + \Omega_m^2\delta\hat{z} = \delta\hat{f}_{\text{th}} + \delta\hat{f}_{\text{fb}} + g_0\Omega_m \sum_{j=\pm} (\bar{a}_j\delta\hat{a}_j^\dagger + \bar{a}_j^*\delta\hat{a}_j). \quad (3.1.24b)$$

The ensuing radiation pressure force fluctuations

$$\delta\hat{f}_{\text{BA}} = g_0\Omega_m \sum_{j=\pm} (\bar{a}_j\delta a_j^\dagger + \bar{a}_j^*\delta a_j) \quad (3.1.25)$$

contain both a dynamic and stochastic component, as detailed in section 3.1.2.1 and section 3.1.2.2, respectively.

Taking the Fourier transforms of eq. (3.1.24) recasts the optomechanical interaction in terms of optical/mechanical susceptibilities, $\chi_{a(z)}$:

$$\begin{aligned} \chi_a^{(\gamma)}[\Omega]^{-1} \delta\hat{a}_\pm[\Omega] &= ig_0 \left(\bar{a}_\pm + \frac{i\gamma}{2} \bar{a}_\mp \chi_a^{(0)}[\Omega] \right) \delta\hat{z}[\Omega] \\ &+ \sqrt{(1-\eta_c)\kappa} \left(\delta\hat{a}_{\text{vac}}^\pm[\Omega] + \frac{i\gamma}{2} \chi_a^{(0)}[\Omega] \delta\hat{a}_{\text{vac}}^\mp[\Omega] \right) \\ &+ \sqrt{\eta_c\kappa} \left(\delta\hat{a}_{\text{in}}^\pm[\Omega] + \frac{i\gamma}{2} \chi_a^{(0)}[\Omega] \delta\hat{a}_{\text{in}}^\mp[\Omega] \right) \end{aligned} \quad (3.1.26a)$$

$$\left(\chi_z[\Omega]^{-1} + \chi_{\text{fb}}[\Omega]^{-1} + \chi_{\text{BA}}[\Omega]^{-1} \right) \delta\hat{z} = \delta\hat{f}_{\text{th}} + \delta\hat{f}_{\text{fb,th}} + \delta\hat{f}_{\text{BA,th}}. \quad (3.1.26b)$$

Here χ_{fb} and χ_{BA} are the modification to the intrinsic mechanical susceptibility due to feedback and dynamic back-action, respectively. Likewise $f_{\text{fb,th}}$ and $f_{\text{BA,th}}$ represent effectively thermal components of the feedback and measurement back-action forces, respectively, adopting the notation from section 3.1.1. Before elaborating, we emphasise the following simplifications in the experimentally relevant ‘bad-cavity’ limit, $\kappa \gg \Omega_m$, assuming a resonantly driven cavity ($\Delta = 0$) and adopting the cold damping strategy:

$$\begin{aligned} \chi_a^{(0)}[\Omega]^{-1} &:= -i(\Omega + \Delta) + \frac{\kappa}{2} \approx \frac{\kappa}{2} \\ \chi_a^{(\gamma)}[\Omega]^{-1} &:= \frac{\chi_a^{(0)}[\Omega]^{-1}}{\chi_a^{(0)}[\Omega]^{-2} + (\gamma/2)^2} \approx \frac{\kappa}{2} \left(1 + \frac{\gamma^2}{\kappa^2} \right) \\ \chi_z[\Omega]^{-1} &:= \Omega_m^2 - \Omega^2 - i\Omega\Gamma_m \\ \chi_{\text{fb}}[\Omega]^{-1} &:= \Omega_{\text{fb}}^2(\Omega) - i\Omega\Gamma_{\text{fb}}(\Omega) \approx -i\Omega\Gamma_m(1 + g_{\text{fb}}) \\ \chi_{\text{BA}}[\Omega]^{-1} &:= \Omega_{\text{BA}}^2(\Omega) - i\Omega\Gamma_{\text{BA}}(\Omega) \approx 0. \end{aligned} \quad (3.1.27)$$

3.1.2.1 Effect of dynamic back-action

When the cavity is driven away from resonance ($\Delta \neq 0$), correlations between the radiation pressure back-action force and the mechanical position give rise to a well known dynamic radiation pressure back-action force [51, 195]. In the high-Q ($\Omega_m \gg \Gamma_m$), bad-cavity ($\kappa \gg \Omega_m$) limit relevant to our experiment, dynamic back-action manifests as a displaced mechanical frequency and passive cold-damping [51]. Accounting for cavity mode splitting, the optically-induced frequency shift ($\Delta\Omega_{\text{BA}}$) and damping rate (Γ_{BA}) are given by:

$$\Delta\Omega_{\text{BA}} := \Omega_{\text{BA}}(\Omega_m) - \Omega_m \approx \frac{2g_0^2}{\kappa} \frac{4\eta_c P_{\text{in}}^+}{\kappa \hbar \omega_c} \sum_{j=\pm} \frac{(\kappa/2)^3 (\Delta + j\gamma/2)}{[(\Delta + j\gamma/2)^2 + (\kappa/2)^2]^2} \quad (3.1.28a)$$

$$\Gamma_{\text{BA}}(\Omega_m) \approx \frac{\Omega_m}{4\kappa} \cdot \frac{2g_0^2}{\kappa} \frac{4\eta_c P_{\text{in}}^+}{\kappa \hbar \omega_c} \sum_{j=\pm} \frac{\kappa^5 (\Delta - j\gamma/2)}{[(\Delta + j\gamma/2)^2 + (\kappa/2)^2]^3}. \quad (3.1.28b)$$

Note that both terms vanish for resonant probing.

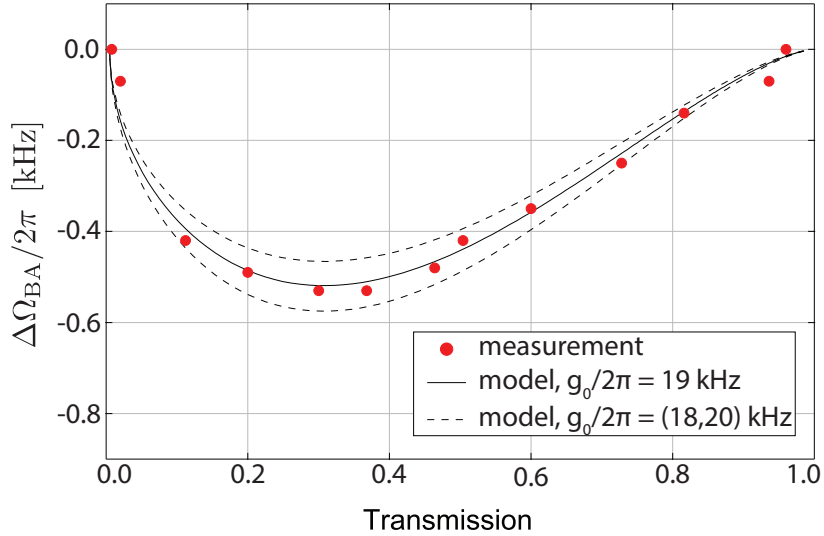


Fig. 3.4 – **Mechanical frequency shift due to dynamic back-action.** Plot shows mechanical frequency shift due to dynamic back-action at various laser-cavity detunings. Model curves are derived from eqs. (3.1.23) and (3.1.28a).

Figure 3.4 depicts the measured mechanical frequency shift with an input power, $P_{\text{in}}^+ \approx 1 \mu\text{W}$, at various detunings; data is plotted against the fraction of the transmitted power, $T_c(\Delta)$ in eq. (3.1.23). In order to make these measurements, the sample is operated with buffer gas evacuated from the cryostat, so as to eliminate deleterious effects from gas damping (see eq. (2.4.9)). The measured dynamic back-action effect provides an independent check of the vacuum optomechanical coupling rate g_0 : fig. 3.4 shows the observed data with model curves derived from eqs. (3.1.23) and (3.1.28a) for the case of a split cavity resonance. The value of the coupling rate obtained thus, $g_0 = 2\pi \cdot 19 \text{ kHz}$, is consistent with a direct calibration (giving $g_0 = 2\pi \cdot 21 \text{ kHz}$). In fact, the $\approx 10\%$ discrepancy provides error estimates for the single-photon cooperativity C_0 , and the ideal measurement imprecision, n_{imp} .

3.1.2.2 Measurement back-action

When the cavity is driven on resonance ($\Delta = 0$), the thermal component of the radiation pressure back-action force takes the form

$$\delta \hat{f}_{\text{BA,th}} = \frac{8g_0\Omega_m}{\sqrt{\kappa}(1+\gamma^2/\kappa^2)} \left\{ \left(\sqrt{n_+} + \frac{\gamma}{\kappa}\sqrt{n_-} \right) \sqrt{\eta_c} \delta \hat{q}_{\text{in}}^+ + \left(\sqrt{n_+} + \frac{\gamma}{\kappa}\sqrt{n_-} \right) \sqrt{1-\eta_c} \delta \hat{q}_{\text{vac}}^+ \right. \\ \left. - \left(\frac{\gamma}{\kappa}\sqrt{n_+} - \sqrt{n_-} \right) \sqrt{\eta_c} \delta \hat{p}_{\text{in}}^- - \left(\frac{\gamma}{\kappa}\sqrt{n_+} - \sqrt{n_-} \right) \sqrt{1-\eta_c} \delta \hat{p}_{\text{vac}}^- \right\}, \quad (3.1.29)$$

where $\hat{q}(\hat{p})$ denote the amplitude(phase) quadrature of each field. In eq. (3.1.29), we have retained the explicit dependence on n_{\pm} in order to emphasise their role in weighting the various noise components. We note that as a consequence of the scattering process, (amplitude)phase fluctuations entering the (clockwise)counter-clockwise mode are converted to intensity fluctuations by two pathways.

Assuming that the drive field is shot-noise limited in its amplitude quadrature ($\bar{S}_{qq}^{\text{in}} = \frac{1}{2}$) and that the cavity is otherwise interacting with a zero temperature bath ($\bar{S}_{qq}^{\text{vac}} = \frac{1}{2} = \bar{S}_{pp}^{\text{vac}}$), we find that the effective thermal occupation due to measurement back-action is given by

$$n_{\text{m,BA}} = C_0 \frac{1}{1+\gamma^2/\kappa^2} (n_+ + n_-) = C_0 n_+, \quad (3.1.30)$$

which is exactly the same as the expression for the case where the cavity modes are unsplit.

3.1.2.3 Modification to measurement imprecision

The cavity transmission, $\delta \hat{a}_{\text{out}}^+ = \delta \hat{a}_{\text{in}}^+ - \sqrt{\eta_c \kappa} \delta \hat{a}_+$, at $\Delta = 0$ is given by,

$$\delta \hat{a}_{\text{out}}^+ = -i\sqrt{\eta_c} \frac{2g_0\sqrt{n_+}}{\sqrt{\kappa}} \left(\frac{1-\gamma^2/\kappa^2}{1+\gamma^2/\kappa^2} \right) \delta \hat{z} \\ + \left(1 - \frac{2\eta_c}{1+\gamma^2/\kappa^2} \right) \delta \hat{a}_{\text{in}}^+ \\ - \frac{\gamma}{\kappa} \left(\frac{2\eta_c}{1+\gamma^2/\kappa^2} \right) \delta \hat{a}_{\text{in}}^- \\ - \frac{2\sqrt{\eta_c(1-\eta_c)}}{1+\gamma^2/\kappa^2} \left(\delta \hat{a}_{\text{vac}}^+ + i\frac{\gamma}{\kappa} \delta \hat{a}_{\text{vac}}^- \right). \quad (3.1.31)$$

As depicted in fig. 3.2, the transmitted field is amplified in a balanced homodyne receiver with a coherent local oscillator (LO) \hat{a}_{LO} . Following the discussion of homodyne detection in section 2.2.2.3 the operator corresponding to the homodyne detector photocurrent is,

$$\delta \hat{I}_{\text{hom}} = 2 |\bar{a}_{\text{LO}}| \left(\delta \hat{p}_{\text{out}}^+ \cos \theta_{\text{LO}} - \delta \hat{q}_{\text{out}}^+ \sin \theta_{\text{LO}} \right),$$

where $|\bar{a}_{\text{LO}}|$ is the amplitude of the large coherent LO field, and θ_{LO} the relative mean phase between the LO and the cavity transmission. The path length of the LO arm is electronically locked to maintain $\theta_{\text{LO}} \approx 0$, so that the homodyne signal picks out the phase quadrature of the cavity transmission containing the position fluctuations $\delta \hat{z}$. For photodetectors with

gain G_d (A/W) and quantum efficiency η_d , the resulting shot-noise-normalised spectrum of photocurrent fluctuations is given by (eq. (2.2.62)),

$$\bar{S}_I^{\text{hom}}[\Omega] = G_d^2 \eta_d \left(1 + \eta_d \eta_c \frac{16g_0^2 n_+}{\kappa} \left(\frac{1 - \gamma^2/\kappa^2}{1 + \gamma^2/\kappa^2} \right)^2 \bar{S}_z[\Omega] \right),$$

giving the imprecision in the estimation of $\delta\hat{z}$ from the homodyne photocurrent,

$$\bar{S}_z^{\text{imp}}[\Omega] = \frac{\kappa}{16\eta g_0^2 n_+} \left(\frac{1 + \gamma^2/\kappa^2}{1 - \gamma^2/\kappa^2} \right)^2,$$

where $\eta = \eta_d \eta_c$ is the total detection efficiency. Expressed as an equivalent phonon occupation,

$$n_{\text{imp}} = \left(\frac{1}{16\eta C_0 n_+} \right) \left(\frac{1 + \gamma^2/\kappa^2}{1 - \gamma^2/\kappa^2} \right)^2. \quad (3.1.32)$$

Note that mode splitting causes the optical susceptibility (eq. (3.1.24)) to flatten near resonance, leading to divergence of n_{imp} when $\gamma = \kappa$.

3.1.2.4 Effect of non-ideal feedback phase

In the experimentally implemented feedback filter eq. (3.1.5), the phase has to satisfy

$$\arg \left[\chi_{\text{fb}}[\Omega]^{-1} \right] = -(2k + 1) \frac{\pi}{2}, \quad k \in \mathbb{N},$$

for all relevant Fourier frequencies, for efficient cold damping. Note that to satisfy the condition for Markovian feedback [263, 264, 269], the total time delay, $\tau_{\text{fb}} := \phi_{\text{fb}}(\Omega_m)/\Omega_m$, has to satisfy, $\tau < 2\pi/\Gamma_{\text{th}}$, thus constraining the largest phase wrap tolerable.

To achieve minimal dispersion, the delay is implemented by a combined optical/electronic delay line. Here we consider the effect of any residual dispersion and/or non-ideal phase, which we model by,

$$\begin{aligned} \chi_{\text{fb}}[\Omega]^{-1} &= \exp \left[-i \left((2k + 1) \frac{\pi}{2} + \delta\phi_{\text{fb}}[\Omega] \right) \right] m\Omega g_{\text{fb}}[\Omega] \Gamma_m \\ &= -im\Omega g_{\text{fb}}[\Omega] \Gamma_m e^{-i\delta\phi_{\text{fb}}[\Omega]}. \end{aligned} \quad (3.1.33)$$

The corresponding effective susceptibility,

$$\chi_{\text{eff}}[\Omega]^{-1} = m \left(\Omega_{\text{eff}}[\Omega]^2 - \Omega_m^2 - i\Omega \Gamma_{\text{eff}}[\Omega] \right), \quad (3.1.34)$$

features feedback-induced damping, and an additional frequency shift,

$$\begin{aligned} \Gamma_{\text{eff}}(\Omega) &= \Gamma_m [1 + g_{\text{fb}}(\Omega) \cos \delta\phi_{\text{fb}}(\Omega)] \\ \Omega_{\text{eff}}(\Omega) &= \Omega_m \left[1 - g_{\text{fb}}(\Omega) \frac{\Omega \Gamma_m}{\Omega_m^2} \sin \delta\phi_{\text{fb}}(\Omega) \right]^{1/2}. \end{aligned} \quad (3.1.35)$$

Thus, deviations from an ideal phase profile can be observed in the feedback-induced frequency shift, while a non-flat gain profile results in a susceptibility that is no longer Lorentzian. Figure 3.5 shows the magnitude response of the oscillator position to external force fluctuations when $\delta\phi_{\text{fb}} = 0$ ($\delta\phi_{\text{fb}} = \pi/2$) over the relevant bandwidth, showing cold damping (frequency shift).

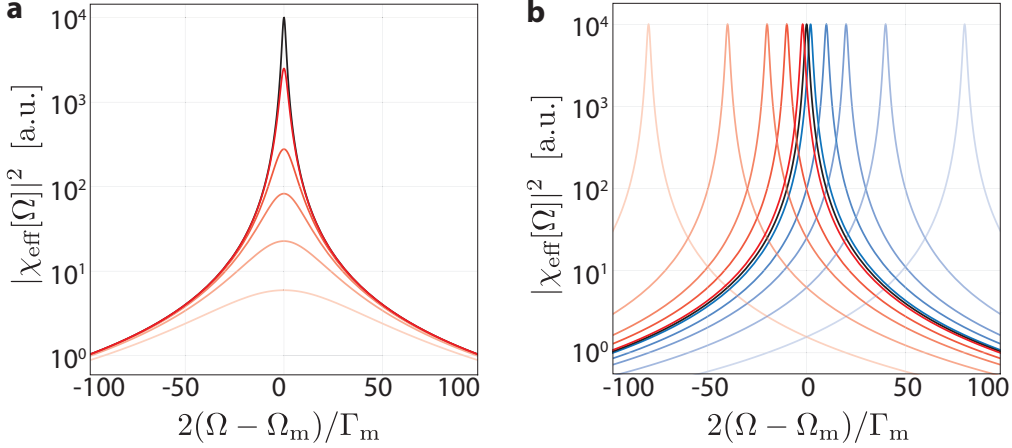


Fig. 3.5 – **Effect of frequency-independent feedback phase.** (a) Effective mechanical susceptibility for the case, $\delta\phi_{\text{fb}} = 0$, across the mechanical bandwidth, leading to cold damping. (b) Effective mechanical susceptibility for the case, $\delta\phi_{\text{fb}} = \pi/2$, leading to a pure frequency shift.

3.1.2.5 Implementation of feedback

Realising the ideal filter appropriate for cold damping not only involves achieving $\delta\phi_{\text{fb}} = 0$ over several tens of linewidths away from mechanical resonance, but also ensuring that extraneous classical noise is not injected in the feedback path, i.e. $n_{\text{fb,th}} \approx 0$, for all values of the electronic gain necessary to achieve $g_{\text{fb}} \approx g_{\text{fb,opt}}$.

Both these requirements are further constrained by the presence of the fundamental in-plane mode of the nanobeam, whose resonance frequency is 500 kHz higher than that of the mode of interest. An initial strategy to mitigate the presence of the in-plane mode, was to implement feedback by band-pass filtering around $\Omega_m = 2\pi \cdot 4.3$ MHz in a bandwidth of $2\pi \cdot 200$ kHz, followed by delaying the signal electronically and feeding into an amplitude modulator driving the feedback laser. The desire to use analog electronics^{3,3} meant that the band-pass filter had to be implemented in super-heterodyne configuration. That is, the photodetector signal was first up-converted to ≈ 70 MHz, where a fixed frequency Butterworth filter was designed to suppress the in-plane mode by more than 20 dB, before the signal was down-converted. However, slight deviations, in the phase $\arg \chi_{\text{fb}}^{-1}$ from the ideal linear phase dependence (at the level of 1%), and in the magnitude $|\chi_{\text{fb}}^{-1}|$ from a constant (at the level of 2%) were observed to lead to a non-Lorentzian susceptibility as observed in the in-loop spectrum. Figure 3.6 shows this effect: the green traces show the measured filter response, while the red traces show the in-loop spectra observed as the magnitude of the feedback gain g_{fb} is increased. The observed spectra, in addition to in-loop “squashing” (see discussion in section 3.2), also exhibits artefacts due to non-ideal phase response. The black traces show predictions from a model for \bar{S}_y (see eq. (3.1.10)) employing the measured feedback filter response (in green).

Ultimately, the sensitivity to small deviations from the ideal feedback filter, combined with the requirement to achieve $g_{\text{fb}} \approx 10^4$, led to the choice of the simplest possible implementation of the feedback electronics. The homodyne signal was split using a directional coupler, low-

^{3,3} It was suspected that the large signal-to-noise ratios, $n_{\text{m,th}}/n_{\text{imp}} \approx 10^8$, required to cool to the ground state, could not be accommodated by a digital controller without causing quantisation artefacts.

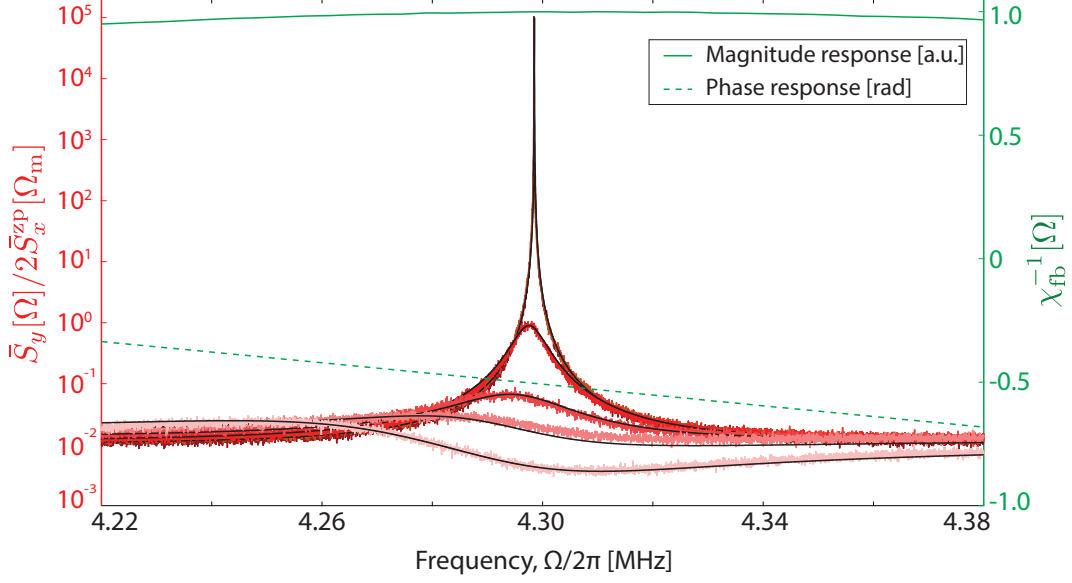


Fig. 3.6 – **Effect of frequency-dependent feedback phase.** In-loop mechanical spectra measured for the case where the feedback filter $\chi_{\text{fb}}^{-1}[\Omega]$ has a frequency dependence that is non-ideal. The red traces show measured in-loop spectra as the feedback gain g_{fb} is increased over three orders of magnitude; the green traces show the measured filter response. The black traces show predictions for the in-loop spectra given in eq. (3.1.10) using the measured filter response as the only free variable.

pass filtered with a single-pole filter^{3.4} at 5 MHz, amplified (Miteq 1525), sent through a tunable passive delay line (Stanford Research Systems DB 64) and attenuated using a voltage-controller attenuator (Minicircuits ZX73), before feeding into the amplitude modulator driving the feedback laser. The feedback filter realised thus, was measured to feature a delay $\tau_{\text{fb}} = 174$ ns implying a linear phase dispersion amounting to $\delta\phi_{\text{fb}}[\Omega_m + \Gamma_{\text{eff}}] - \delta\phi_{\text{fb}}[\Omega_m - \Gamma_{\text{eff}}] \approx 0.3$ rad. The resulting fractional frequency shift $|(\Omega_{\text{eff}} - \Omega_m)/\Omega_m| \approx 10^{-3}$ contributes negligibly. The excess noise added by the electronic chain, characterised by its noise figure, $\mathcal{F} \approx 1.5$ dB, causes an irrelevantly small occupation due to electronic noise, $n_{\text{fb,th}} = \mathcal{F}n_{\text{imp}} \lesssim 10^{-4}$. We henceforth neglect these contributions.

^{3.4} A theorem due to Bode [274] states that, for a causal stable filter, a magnitude response that falls off as some polynomial power, Ω^n , has to experience a minimum phase change over the relevant frequency band of, $n\pi/2$; in this sense, a single-pole transfer function satisfies the ideal requirement for the feedback filter.

3.2 Experimental results

Feedback cooling of an interferometrically measured mechanical oscillator a well-studied [269, 270, 275, 276] control protocol that illustrates both the utility and the challenge of quantum feedback applied to mechanical systems. In feedback cooling protocols, a mechanical oscillator undergoing thermal Brownian motion is steered towards its ground state by minimising a measurement of its displacement, \bar{S}_x (here expressed as a spectral density). The conventional strategy, discussed in section 3.1.1, is to apply a feedback force which is proportional to the oscillator's velocity, thereby damping the motion until it coincides with the measurement imprecision, \bar{S}_x^{imp} . Ground state cooling is possible when the imprecision remains lower than the zero-point fluctuations of the damped oscillator, i.e., if $\bar{S}_x^{\text{imp}} \lesssim \bar{S}_x^{\text{ZP}}/n_{\text{m,th}}$ where \bar{S}_x^{ZP} is the oscillator's undamped zero-point variance and $n_{\text{m,th}}$ is its thermal occupation. Practically, this amounts to resolving the undamped thermal noise, $\bar{S}_x \approx 2n_{\text{m,th}}S_x^{\text{ZP}}$, with a signal-to-noise greater than $2n_{\text{m,th}}^2$. Equivalently, it corresponds to the ability to resolve the zero-point motion of the oscillator at a characteristic measurement rate [69]

$$\Gamma_{\text{meas}} \equiv \frac{x_{\text{zp}}^2}{2S_x^{\text{imp}}} \gtrsim \frac{\Gamma_{\text{th}}}{8}, \quad (3.2.1)$$

where x_{zp} is the oscillator's zero-point amplitude, $\Gamma_{\text{th}} \approx \Gamma_{\text{m}}n_{\text{m,th}}$ is its thermal decoherence rate. Achieving this requirement is a daunting technical challenge, owing to the large thermal occupation and small zero-point amplitude of typical micromechanical oscillators.

3.2.1 Measurement at the thermal decoherence rate

Integration of nanomechanical oscillators with optical and microwave cavities has emerged as a promising pathway to meeting the above requirements. For ideal quantum measurements, characterised by a cavity decay rate $\kappa \gg \Omega_m$ (see section 2.3), a resonant laser field passing through the cavity acquires a phase shift $2G\delta\hat{x}/\kappa$; this can be resolved in a conventional homodyne interferometer with a quantum-noise-limited imprecision of $\bar{S}_x^{\text{imp}} = (8G^2n_c\eta/\kappa)^{-1}$, where n_c is the mean intracavity photon number and $\eta \in [0, 1]$ is the effective photon collection efficiency (see section 3.1.1). The associated quantum-limited measurement rate is given by $\Gamma_{\text{meas}} = 4g_0^2n_c\eta/\kappa = \Gamma_{\text{m}} \cdot C_0n_c\eta$. As described in section 2.4, our system, building on relentless progress in the NEMS/MEMS and photonics communities – dovetailing fabrication techniques which enable substantial miniaturisation of the mechanical resonator and the optical cavity while reinforcing low-loss and strong co-localisation – can in principle achieve $\Gamma_{\text{meas}} \approx \Gamma_{\text{th}}$ at the detector. Previous generations of experiments [50, 277, 278] (see fig. 1.2 for a detailed overview), including those in other research groups, have demonstrated interferometric position measurements with an imprecision below that at the SQL; however, a combination of large thermal occupation, extraneous (classical) sources of imprecision and/or dynamic instabilities prevented achieving sufficiently large measurement rates.

Our system, based on near-field optomechanical coupling [49] (see section 2.2.3), addresses these challenges by the integration of mechanical and optical resonators with widely differing material and geometry. Specifically, the mechanical oscillator possessing an exceptionally high $Q/(\text{mass})$ ratio and low optical absorption [167], while the optical cavity possessing a high $Q/(\text{mode volume})$ ratio and low optical nonlinearity. As discussed in section 2.2.3, coupling is

achieved by carefully localising a portion of the beam within the evanescent volume of one of the microdisk's whispering gallery modes. Both resonators are integrated on a silicon chip, allowing for robust cryogenic operation (see section 2.4).

We here study a system consisting of a $65 \mu\text{m} \times 400 \text{ nm} \times 70 \text{ nm}$ (effective mass $m \approx 2.9 \text{ pg}$) nanobeam placed $\sim 50 \text{ nm}$ from the surface of a $30 \mu\text{m}$ diameter microdisk. The microdisk is optically probed using a low-loss ($\approx 6\%$) fiber-taper and light supplied by a tunable diode laser. Mechanical motion is observed in the phase of the transmitted cavity field using a balanced homodyne interferometer. We interrogate two optical modes: a 'sensor' mode (used for homodyne readout) at $\lambda_c \approx 775 \text{ nm}$ that exhibits an intrinsic photon decay rate of $\kappa_0 \approx 2\pi \cdot 0.44 \text{ GHz}$ and a 'feedback' mode (used for radiation pressure actuation) at $\lambda_c \approx 843 \text{ nm}$ that exhibits a decay rate of $\kappa_0 \sim 2\pi \cdot 1 \text{ GHz}$. For the mechanical oscillator, we use the $\Omega_m \approx 2\pi \cdot 4.3 \text{ MHz}$ fundamental out-of-plane mode of the nanobeam. The optomechanical coupling strength between the oscillator and the sensor mode is $g_0 \approx 2\pi \cdot 20 \text{ kHz}$ (see discussion surrounding fig. 3.4), corresponding to a frequency pulling factor of $G \approx 2\pi \cdot 0.70 \text{ GHz/nm}$ for the estimated zero-point amplitude of $x_{\text{zp}} = \sqrt{\hbar/2m\Omega_m} \approx 29 \text{ fm}$. The experiments were conducted in a ^3He buffer gas cryostat at an operating temperature of $T \approx 4.4 \text{ K}$ ($n_{\text{m,th}} = k_{\text{B}}T/\hbar\Omega_m \approx 2.1 \cdot 10^4$) and at gas pressures below 10^{-3} mbar . Ring-down measurements here reveal a mechanical damping rate of $\Gamma_m \approx 2\pi \cdot 5.7 \text{ Hz}$ ($Q_m \approx 7.6 \cdot 10^5$). Our system is thus able to operate with a near-unity single-photon cooperativity $C_0 = 4g_0^2/\kappa\Gamma_m \approx 0.64$.

In all position sensors, extraneous thermal fluctuations pose a fundamental limit to the achievable imprecision. In cavity-optomechanical sensors, the main sources of extraneous imprecision arise from thermomechanical [279, 280] and thermodynamic fluctuations of the cavity substrate [281–284]. These result in excess cavity frequency noise, $\bar{S}_\omega^{\text{imp,ex}}$, and limit the measurement rate to

$$\Gamma_{\text{meas}} = \frac{g_0^2/2}{\bar{S}_\omega^{\text{imp,shot}}[\Omega_m] + \bar{S}_\omega^{\text{imp,ex}}[\Omega_m]} = \frac{\Gamma_m/16}{n_{\text{imp,shot}} + n_{\text{imp,ex}}}, \quad (3.2.2)$$

where $\bar{S}_\omega^{\text{imp,shot}}$ is the photocurrent shot noise referred to apparent cavity resonance frequency noise. The (ideal) shot-noise imprecision, $n_{\text{imp,shot}} = (16\eta C_0 n_c)^{-1}$ (see eq. (3.1.32)), where now the efficiency η also takes into account the splitting of the cavity mode.

Figure 3.7 shows the extraneous noise floor of our sensor over a broad range of frequencies surrounding the oscillator resonance. We obtained this spectrum by subtracting shot noise from a measurement made with a large intracavity photon number, $n_c > 10^5$. (To mitigate thermo-optic and optomechanical instabilities, the measurement was in this case conducted using $\approx 10 \text{ mbar}$ of gas pressure at an elevated temperature of 15.7 K .) The relevant noise peak, at $\Omega_m \approx 2\pi \cdot 4.3 \text{ MHz}$, due to the thermal motion of the fundamental out-of-plane mode, is measured against an imprecision, $\bar{S}_\omega^{\text{imp,ex}}$, which we understand as arising from three sources:

$$\bar{S}_\omega^{\text{imp,ex}}[\Omega_m] = \bar{S}_\omega^{\text{imp,ex,mech}}[\Omega_m] + \bar{S}_\omega^{\text{imp,ex,cav}}[\Omega_m] + \bar{S}_\omega^{\text{imp,ex,laser}}[\Omega_m]; \quad (3.2.3)$$

noise due to extraneous thermomechanical motion of other modes of the beam and the cavity, extraneous frequency fluctuations due to the cavity substrate, and extraneous frequency noise from the probe laser.

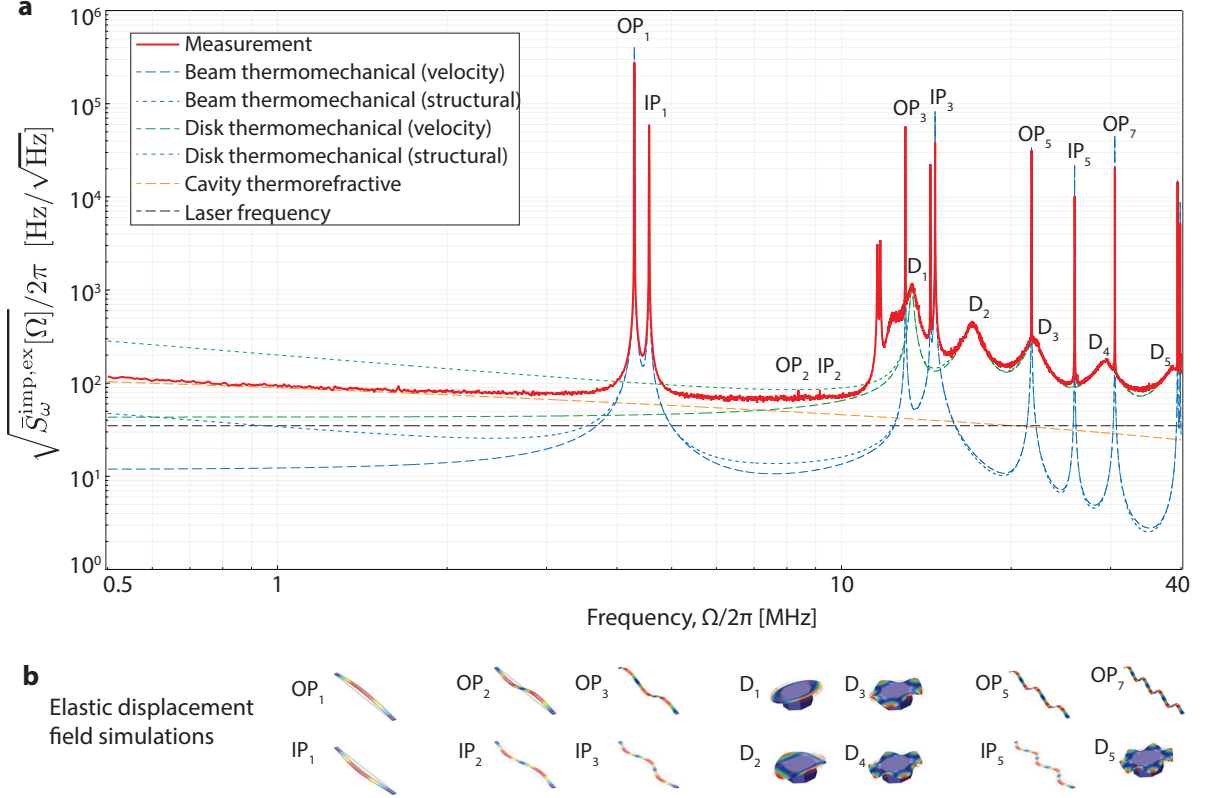


Fig. 3.7 – **Extraneous measurement imprecision.** (a) Red trace shows the shot-noise subtracted homodyne photocurrent calibrated as an apparent frequency noise. The various high-Q peaks are understood to arise from the in-plane (marked IP_n) and out-of-plane (marked OP_n) modes of the nanobeam (blue), while the low-Q peaks are from the mechanical modes of the disk (marked D_n) (green). In the vicinity of the fundamental out-of-plane mode, at $\Omega_m = 2\pi \cdot 4.3$ MHz, measurement imprecision is dominated by a combination of cavity thermorefractive noise (black), and a small contribution from estimated laser frequency noise (orange). (b) Finite-element model simulations of the various mechanical modes seen in the measurement. The simulated displacement field frequencies have excellent agreement with the observed frequencies and dispersion.

High- and low-Q noise peaks correspond to thermal motion of the nanobeam and the microdisk, respectively (see section 3.2.1.1 below). In the vicinity of the fundamental noise peak, we observe an extraneous frequency noise background of $\bar{S}_{\omega}^{\text{imp,ex}} \approx (2\pi \cdot 30\text{Hz}/\sqrt{\text{Hz}})^2$, corresponding to an extraneous position imprecision of $\bar{S}_x^{\text{imp,ex}} \approx (4.3 \cdot 10^{-17}\text{m}/\sqrt{\text{Hz}})^2$. We identify this noise as a combination of microdisk thermorefractive noise [277] (see section 3.2.1.2), diode laser frequency noise [285], and off-resonant thermal motion of the neighbouring beam mode at 4.6 MHz. Owing to the large zero-point motion of the nanobeam, $\bar{S}_{\omega}^{\text{zp}} = 4g_0^2/\Gamma_m = (2\pi \cdot 6.7\text{kHz}/\sqrt{\text{Hz}})^2$ ($\bar{S}_x^{\text{zp}} = (0.95 \cdot 10^{-14}\text{m}/\sqrt{\text{Hz}})^2$), the equivalent bath occupancy of this noise has an exceptionally low value of $n_{\text{imp}}^{\text{ex}} := \bar{S}_{\omega}^{\text{imp,ex}}/2\bar{S}_{\omega}^{\text{zp}} \approx 1.0 \cdot 10^{-5}$, nearly 44 dB below the value at the SQL. Encouragingly, the measurement rate associated with this imprecision, $\Gamma_m/16n_{\text{imp}}^{\text{ex}} \approx 2\pi \cdot 36\text{kHz}$, is equal to the thermal decoherence rate at an experimentally accessible temperature of 1.3 K. The more lenient requirements for feedback cooling to $n_m < 1$ (i.e., $\Gamma_{\text{meas}} < \Gamma_{\text{th}}/8$) should thus be accessible at 10 K.

3.2.1.1 Imprecision due to thermomechanical noise

High- and low-Q noise peaks correspond to the thermal motion of the extraneous modes of the nanobeam and the microdisk (radial breathing, and flexural, modes that have significant optomechanical coupling), respectively. Assuming that all these modes, with position fluctuation \hat{x}_i , are equilibrated at temperature T , and have an optomechanical coupling G_i , their contribution to the frequency noise background under the fundamental mode is,

$$\bar{S}_\omega^{\text{imp,ex,mech}}[\Omega_m] = \sum_i G_i^2 \bar{S}_{x_i}[\Omega_m] = \sum_i G_i^2 |\chi_{x_i}[\Omega_m]|^2 \cdot 4m_i \Gamma_i k_B T. \quad (3.2.4)$$

Here, we have approximated the extraneous modes as independent oscillators, each of effective mass m_i and damping rate Γ_i , driven by a thermal force noise given by the fluctuation-dissipation theorem (see eq. (2.1.16)) in the limit that their mean thermal phonon occupation, $n_{i,\text{th}} := \frac{k_B T}{\hbar \Omega_i} \gg 1$.

Structural resonances like these, typical of bulk resonators, are known to exhibit damping that is not proportional to velocity [286]. The so-called *structural damping* model posits a frequency dependent damping rate such that the different modes have approximately uniform mechanical Q; i.e.,

$$\Gamma_i[\Omega] = \begin{cases} \Gamma_i & \text{velocity damping} \\ \frac{\Gamma_i \Omega_i}{\Omega} & \text{structural damping} \end{cases} \quad (3.2.5)$$

leading to the replacement, $\Gamma_i \rightarrow \Gamma_i[\Omega]$ in the susceptibility and the force noise in eq. (3.2.4). Assuming that the fundamental mode frequency is smaller than the frequencies of the extraneous modes,

$$\bar{S}_\omega^{\text{imp,ex,mech}}[\Omega_m \ll \Omega_i] \approx \sum_i \frac{g_i^2}{\Omega_i} \times \begin{cases} n_{i,\text{th}} \frac{\Gamma_i}{\Omega_i} & \text{velocity damping} \\ \frac{n_{i,\text{th}}}{Q_i} \frac{\Omega_i}{\Omega_m} & \text{structural damping} \end{cases} \quad (3.2.6)$$

implying that if the extraneous modes are structurally damped, a very low frequency for the fundamental mode would be susceptible to larger imprecision due to extraneous thermomechanical noise.

In fig. 3.7, the pair of blue (green) traces show models of thermomechanical noise arising from extraneous modes of the nanobeam (disk). The dashed (dotted) curves assume a velocity (structural) damped model for the motion. Despite the low-Q (≈ 10) of the disk modes, it is seen that the measurement is incompatible with a structural damping mechanism for these modes. For the beam modes, measurements at the frequencies presented in the figure, do not allow discrimination between either model.

3.2.1.2 Imprecision due to cavity substrate noise

Macroscopic optical cavities, like the whispering-gallery cavities we use, equilibrated at some temperature T , experience fundamental thermodynamic fluctuations in its resonance frequency ω_c . Within the electrodynamic description of cavity frequency fluctuations (in section 2.2.3), the two possible causes are fluctuations in volume V and fluctuations in the dielectric constants

of the cavity substrate. For an optical cavity, the latter is the refractive index ν . The cavity frequency, $\omega_c(\nu, V)$, therefore undergoes fluctuations,

$$\delta\omega_c = \frac{\partial\omega_c}{\partial\nu}\delta\nu + \frac{\partial\omega_c}{\partial V}\delta V =: \delta\omega_c^{\text{TRN}} + \delta\omega_c^{\text{TEN}}.$$

When refractive index fluctuations and volume fluctuations are caused by underlying thermodynamic causes, these two contributions lead to thermorefractive (TRN) [283] and thermoelastic (TEN) [282] frequency noise.

Note that the underlying thermodynamic fluctuations are transduced via the coefficients $\frac{\partial\omega_c}{\partial\nu}, \frac{\partial\omega_c}{\partial V}$ measured in *equilibrium*, i.e. at constant temperature T . Although temperature itself does not fluctuate in equilibrium, an apparent temperature fluctuation may be ascribed to the fluctuations in the total energy in equilibrium; the variance of this apparent temperature fluctuation is^{3,5},

$$\text{Var}[T] = \frac{k_B T^2}{C_V} = \frac{k_B T^2}{\rho V c_V}, \quad (3.2.7)$$

where the first equality is expressed in terms of the heat capacity at constant volume C_V , while the second is expressed in terms of the specific heat at constant volume, $c_V = C_V/(\rho V)$, an intensive material property. The implied variance in frequency due to TRN and TEN is therefore,

$$\begin{aligned} \text{Var}[\delta\omega_c^{\text{TRN}}] &= \left(\frac{\partial\omega_c}{\partial\nu} \frac{\partial\nu}{\partial T}\right)^2 \text{Var}[T] = \left(\frac{\omega_c}{\nu} \frac{\partial\nu}{\partial T}\right)^2 \frac{k_B T^2}{\rho V c_V} \\ \text{Var}[\delta\omega_c^{\text{TEN}}] &= \left(\frac{\partial\omega_c}{\partial V} \frac{\partial V}{\partial T}\right)^2 \text{Var}[T] = (\omega_c \alpha_V)^2 \frac{k_B T^2}{\rho V c_V}, \end{aligned} \quad (3.2.8)$$

where $\alpha_V := (1/V)\partial V/\partial T$ is the isobaric thermal expansion coefficient. For macroscopic ultra-stable cavities, TRN has been observed to be a limitation on frequency stability at room temperature [284], and demonstrated to be suppressed at cryogenic temperatures [287]. For small mode-volume microcavities, TRN poses a much larger problem, and has been observed to limit frequency imprecision at the level of $10^3 \text{Hz}^2/\text{Hz}$ at Fourier frequencies of about 1 MHz, at room temperature [277].

For SiO_2 , the material constituting our cavity, the coefficient of transduction for TRN is roughly 100 times larger than the coefficient of transduction for TEN in a wide range of temperatures down to about $T = 1 \text{K}$ [251, 288]; we therefore focus on TRN here. In order to understand the distribution of the variance, $\text{Var}[\omega_c^{\text{TRN}}]$, given in eq. (3.2.8), in frequency, it

^{3,5} This is derived as follows. Assume the body is in thermal equilibrium at temperature T , so that it is described by the canonical thermal state $\hat{\rho} = e^{-\beta\hat{H}}/Z$, with $Z := \text{Tr} e^{-\beta\hat{H}}$, and $\beta := (k_B T)^{-1}$. Then, the average energy is given by, $\langle\hat{H}\rangle := \text{Tr} \hat{H}\hat{\rho} = -\frac{1}{Z}\partial_\beta Z$, while its second moment is, $\langle\hat{H}^2\rangle := \text{Tr} \hat{H}^2\hat{\rho} = \frac{1}{Z}\partial_\beta^2 Z = -\partial_\beta \langle\hat{H}\rangle + \langle\hat{H}\rangle^2$. Subtracting these two expressions give the variance in the energy:

$$\text{Var}[\hat{H}] := \langle\hat{H}^2\rangle - \langle\hat{H}\rangle^2 = -\partial_\beta \langle\hat{H}\rangle = k_B T^2 \partial_T \langle\hat{H}\rangle = k_B T^2 C_V.$$

Here, $C_V := \partial_T \langle\hat{H}\rangle$ is the specific heat at constant volume as defined conventionally. To refer the above variance in energy to an apparent variance in temperature, we again use the definition of the specific heat, $\delta T = \delta E/C_V$, to arrive at, $\text{Var}[T] = \text{Var}[E]/C_V^2 = k_B T^2/C_V$.

is necessary to subscribe to a dynamic model of temperature in the cavity [288]. Assuming diffusive thermal transport, it can be shown that for low-order optical modes, at Fourier frequencies high compared to the inverse thermal diffusion time, $D_T/(2\pi r_{\text{disk}}^2) \approx (10 - 50)$ kHz (here D is the thermal diffusivity of silica, and r_{disk} the radius of the microdisk cavity), the power spectral density of TRN is approximated by [288] ,

$$\bar{S}_{\omega}^{\text{TRN}}[\Omega] \approx \left(\frac{\omega_c}{\nu} \frac{\partial \nu}{\partial T} \right)^2 \cdot \frac{k_B T^2}{\rho V c_V} \cdot \frac{(16\pi)^{1/3} \tau_T}{(\Omega \tau_T)^{1/2} (1 + (\Omega \tau_T)^{3/4})^2}. \quad (3.2.9)$$

Here, $\tau_T^{-1} := D_T/\mathcal{A}_{\text{disk}}$ is the thermal time constant for a mode with transverse cross-section area $\mathcal{A}_{\text{disk}}$.

The thermal diffusivity, $D_T = K_T/\rho c_V$, by being strongly temperature dependent through parameters like the thermal conductivity K_T and specific heat c_V [241], is only known to within 50% uncertainty for silica at cryogenic temperatures, $T \lesssim 10$ K, and depends weakly on the presence of impurities [289]. Using a thermal time constant, $\tau_T^{-1} \approx 5$ MHz, consistent with the known material constants, and estimates of the whispering-gallery mode cross-section, eq. (3.2.9) gives a qualitatively correct scaling of the measured low frequency imprecision noise in fig. 3.7, deviating by about 50% in absolute magnitude.

3.2.1.3 Imprecision due to noise in optical fiber

In addition to the above two sources of frequency noise that arise from the optomechanical system, our experiment is also sensitive to a frequency noise arising from the optical path in the arm of the interferometer containing the optomechanical system. As described in section 2.4.3, this path, passing through the cryostat, predominantly consists of a ≈ 10 m long (single-mode) optical fiber (780HP). Roughly half this length passes through the cryostat (at 4 K), while the other half is at room temperature. Transverse elastic motion of the fiber core, undergoing thermal motion, can inelastically scatter photons off of the longitudinally propagating optical field via the strain-optical effect; this process – *guided acoustic-wave Brillouin scattering* (GAWBS) – is known to cause excess frequency noise in the field exiting the fiber^{3.6} [211, 290].

This source of excess phase noise is measured by inserting a 10 m long optical fiber in the signal arm of our homodyne interferometer. Figure 3.8a blue trace is the result of such a measurement, showing excess frequency noise $\bar{S}_{\omega}^{\text{GAWBS}}[\Omega] = \Omega^2 \bar{S}_{\phi}^{\text{GAWBS}}[\Omega] \approx (2\pi \cdot 1 \text{ Hz}/\sqrt{\text{Hz}})^2$ at Fourier frequencies of $\Omega \approx 2\pi \cdot 20$ MHz, and increasing quadratically with Fourier frequency.

The observed spectrum (blue in fig. 3.8) can be understood using a simple model [290]. The transverse axis-symmetric elastic field of a cylinder of radius r_c – general solution of the Navier equation eq. (2.2.18) in cylindrical coordinates with free boundary conditions – is given by eq. (2.2.21), viz.

$$\mathbf{u}(\mathbf{r}, t) = \sum_n x_n(t) \mathbf{u}_n(\mathbf{r}),$$

^{3.6} Longitudinal elastic modes have a similar effect, but their frequency being larger, the resulting phase noise isn't relevant in our experiment

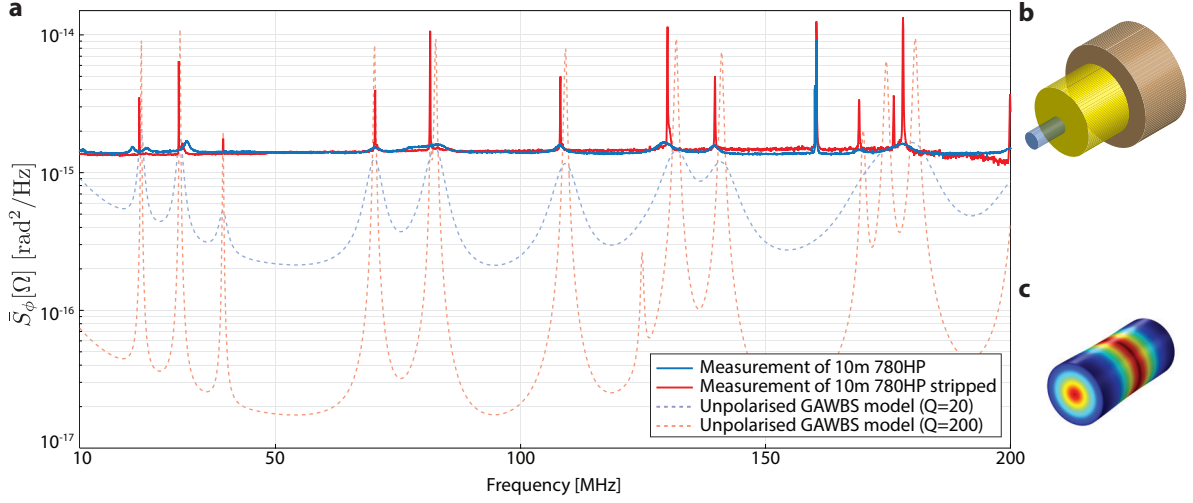


Fig. 3.8 – **Extraneous phase noise from optical fiber.** (a) Blue shows measured phase noise spectrum of a 10m long segment of a standard 780HP optical fiber. The observed low- Q peaks are well described by a theoretical model (blue dashed, $Q = 20$) of unpolarised GAWBS. Red shows the same segment of fiber, but measured after its cladding is etched using buffered hydro-fluoric acid. Removal of the surrounding cladding increases the Q of the modes, leading to localisation of GAWBS-induced phase noise in narrow spectral intervals. Red dashed shows a theoretical model assuming $Q = 200$. (b) Schematic of a typical optical fiber (not to scale), showing the core (blue), which carries the optical field, the cladding surrounding the core (yellow) that provides the refractive index contrast to constrain the propagating optical field transversally, and the coating (brown) that provides for mechanical rigidity. (c) Theoretical elastic displacement field of the core of a $4.5 \mu\text{m}$ radius (typical of 780HP) glass core of the fiber.

where \mathbf{u}_n are the (orthogonal) spatial mode functions of the elastic cylinder, given by (here J_k is the Bessel function of order k and \mathbf{e}_r is the unit radial vector),

$$\mathbf{u}_n(\mathbf{r}) = J_1\left(\alpha_n \frac{r}{r_c}\right) \mathbf{e}_r,$$

and $x_n(t)$ are standard harmonic oscillator amplitudes driven by thermal noise. The frequency of the n^{th} mode, $\Omega_n = \alpha_n(c_T/r_c)$, is determined by the transverse elastic velocity c_T (see appendix B.2), and α_n is determined by the boundary condition via the n^{th} root of the characteristic equation (here c_L is the longitudinal velocity, see appendix B.2),

$$\frac{J_0(\alpha)}{J_2(\alpha)} = \frac{(c_T/c_L)^2}{1 - (c_T/c_L)^2},$$

and describes the dispersion of the elastic modes. The frequencies observed in the measured data in fig. 3.8a, agree well with the frequencies of these transverse elastic modes, shown as the broad resonances with a phenomenological quality factor $Q \approx 20$ in the blue dashed curve.

The phase shift caused by the elastic mode is determined by a combination of two factors: the amplitude of the thermally driven elastic mode x_n , and, the forward scattering cross-section. The amplitude of the thermally driven elastic motion, x_n , is fixed by the equipartition principle

[291]:

$$\begin{aligned} \frac{1}{2}k_B T &= \int_0^L dz \int_0^{2\pi} d\theta \int_0^{r_c} r dr \frac{1}{2}\rho\Omega_n^2 \langle \mathbf{u}_n^*(\mathbf{r}) \cdot \mathbf{u}_n(\mathbf{r}) \rangle \\ \Rightarrow \text{Var}[x_n] &= \frac{k_B T}{m_n \Omega_n^2}, \quad \text{where, } m_n = \rho \cdot \pi r_c^2 L \int_0^{r_c} J_1^2(\alpha_n r / r_c) r dr, \end{aligned} \quad (3.2.10)$$

is the effective mass of the elastic mode. Such thermo-elastic motion of the fiber core leads to refractive index fluctuations, δv , via the strain-optic effect [290, 292], viz.

$$\delta v(\mathbf{r}, t) = \frac{v^3}{2}(p_{11} + p_{12}) \frac{1}{r} \frac{\partial}{\partial r} [r \mathbf{u}(\mathbf{r}, t)] \cdot \mathbf{e}_r,$$

where p_{ij} are the elements of the strain-optic tensor for silica, $p_{11} \approx 0.12$, $p_{12} \approx 0.27$. These fluctuations induce fluctuations in the phase, $\delta\phi$, of the longitudinally propagating electric field; it can be approximated as an average of the transverse field profile, $E(r) \approx (\pi w_c^2)^{-1} e^{-r^2/w_c^2}$, over the refractive index fluctuation profile, viz.,

$$\begin{aligned} \delta\phi_{\text{GAWBS}}(t) &= \frac{2\pi}{\lambda} \int_0^L dz \int_0^{2\pi} d\theta \int_0^\infty r dr \delta v(\mathbf{r}, t) E(r) \\ &= \frac{\pi v^3}{\lambda} (p_{11} + p_{22}) \frac{L}{r_c} \sum_n \alpha_n e^{-\alpha_n^2 w_c^2 / 4r_c^2} x_n(t) \end{aligned} \quad (3.2.11)$$

The spectral density of phase fluctuations due to GAWBS in the optical fiber is thus given by,

$$\bar{S}_\phi^{\text{GAWBS}}[\Omega] = \left(\frac{\pi v^3}{\lambda} (p_{11} + p_{22}) \frac{L}{r_c} \right)^2 \sum_n \alpha_n^2 e^{-\alpha_n^2 w_c^2 / 2r_c^2} \bar{S}_x^n[\Omega], \quad (3.2.12)$$

where \bar{S}_x^n is the thermoelastic motional spectral density consistent with the equipartition principle eq. (3.2.10), viz.,

$$\bar{S}_x^n[\Omega] \approx \frac{\text{Var}[x_n]}{\Gamma_n} \frac{\Gamma_n^2}{(\Omega - \Omega_n)^2 + (\Gamma_n/2)^2}. \quad (3.2.13)$$

Here m_n is the effective mass given in eq. (3.2.10) and $\Omega_n = \alpha_n(c_T/r_c)$ the elastic resonance frequency. The decay rate of the modes, $\Gamma_n \approx \Omega_n/Q$ is dominated by clamping losses due to the fiber cladding. Model curves in fig. 3.8a are plots of eqs. (3.2.12) and (3.2.13).

Frequency noise imprecision, due to GAWBS, around the resonance of the nanobeam mode at $\Omega_m \approx 2\pi \cdot 4.3$ MHz is solely due to the low frequency part of $\bar{S}_\phi^{\text{GAWBS}}$, given by,

$$\bar{S}_\omega^{\text{imp,ex,fiber}}[\Omega] := \Omega_m^2 \bar{S}_\phi^{\text{GAWBS}}[\Omega_m \ll \Omega_n] \approx \left(\frac{\pi v^3}{\lambda} (p_{11} + p_{22}) \frac{L}{r_c} \right)^2 \sum_n \frac{\alpha_n^2}{Q} \frac{k_B T}{m_n \Omega_n}. \quad (3.2.14)$$

Clearly, a large mechanical quality factor for the transverse elastic modes of the optical fiber significantly reduces classical extraneous imprecision due to GAWBS. Figure 3.8a red trace shows engineering of the quality factor of the GAWBS modes, and consequent reduction of frequency noise. The higher Q is achieved by etching the 10m long fiber in buffered HF (40% solution, for an hour), which reduces the cladding diameter from 125 μm to about 90 μm . The resulting increase in Q by a factor of 10, results in $\bar{S}_\omega^{\text{imp,ex,fiber}}[\Omega_m] \lesssim (2\pi \cdot 10^{-3} \text{ Hz}/\sqrt{\text{Hz}})$.

3.2.2 Heisenberg-uncertainty-limited measurement

Despite the realisation of a measurement rate close to the decoherence rate at temperatures below 10 K, an additional, fundamental caveat at once compounds the challenge of feedback cooling and hints at the underlying virtue of quantum feedback: the uncertainty principle for weak continuous measurements (see sections 2.1 and 2.3) predicts a measurement back-action force that disturbs the position of the oscillator by at least the same amount. That is, an imprecision of n_{imp} equivalent quanta results in an increase of the physical occupation by $n_{\text{m,BA}} \geq 1/16n_{\text{imp}}$ (see section 2.3). This penalty would appear to prohibit ground-state cooling, as it entails substantially heating the oscillator to achieve the necessary imprecision. Remarkably, however, feedback counteracts back-action [265, 293], so that a phonon occupancy of $n_{\text{m}} \approx 2\sqrt{n_{\text{imp}}(n_{\text{m,BA}} + n_{\text{m,th}})} - 1/2 < 1$ (eq. (3.1.11)) can still be achieved. The limiting case of $n_{\text{m}} \rightarrow 0$ is approached when the measurement record is dominated by back-action-induced fluctuations. This occurs when the measurement nears unit efficiency [265], i.e., when the measurement rate, $\Gamma_{\text{meas}} = 1/16n_{\text{imp}}$, approaches the effective thermal decoherence rate, $\Gamma_{\text{tot}} = (n_{\text{m,th}} + n_{\text{m,BA}})\Gamma_{\text{m}} \geq \Gamma_{\text{meas}}$. To meet this condition for a typical mechanical oscillator a linear position sensor must achieve an imprecision far ($\sim n_{\text{m,th}}$ times) below the natural scale set by the standard quantum limit (SQL, see section 2.3) ($n_{\text{imp}} = n_{\text{m,BA}} = 1/4$), while maintaining back-action near the uncertainty limit: $4\sqrt{n_{\text{m,BA}}n_{\text{imp}}} \geq 1$.

The performance of our sensor is limited in practice by constraints on the usable optical power, including photon collection efficiency, photothermal and radiation pressure instabilities, and extraneous sources of measurement back-action, such as heating due to optical absorption. We investigate these constraints by recording n_{imp} and n_{m} as a function of intracavity photon number, comparing their product to the uncertainty-limited value, $4\sqrt{n_{\text{imp}}n_{\text{m}}} > 1$ (fig. 3.9). Two considerations are crucial to this investigation. First, in order to efficiently collect photons from the cavity, it is necessary to increase the taper-cavity coupling rate to $\kappa_{\text{ex}} \gtrsim \kappa_0$, thereby increasing the total cavity decay rate to $\kappa = \kappa_0 + \kappa_{\text{ex}}$. We operate at a near-critically coupled ($\kappa_{\text{ex}} \approx \kappa_0$) value of $\kappa \approx 2\pi \cdot 0.91$ GHz, thus reducing the single photon cooperativity to $C_0 \approx 0.31$ in exchange for a higher output coupling efficiency of $\eta_c = (\kappa - \kappa_0)/\kappa \approx 0.52$. Second, in order to minimise \bar{S}_x^{imp} , it is necessary to maximise intracavity photon number while mitigating associated dynamic instabilities. We accomplish this by actively damping the oscillator using radiation pressure feedback. Feedback was performed by modulating the drive intensity, and therefore the intracavity photon number, of the secondary feedback mode using an electronically amplified and delayed (by $\tau \approx 3\pi/2\Omega_{\text{m}}$) copy of the homodyne photocurrent as an error signal. The resulting viscous radiation pressure reduces the phonon occupancy of the mechanical mode to a mean value of $n_{\text{m}} \approx n_{\text{m}}\Gamma_{\text{m}}/(\Gamma_{\text{m}} + \Gamma_{\text{fb}})$, where Γ_{fb} is the optically-induced damping rate. It should be noted that added damping leads to an apparent imprecision $n'_{\text{imp}} = n_{\text{imp}}(\Gamma_{\text{m}} + \Gamma_{\text{fb}})/\Gamma_{\text{m}}$ that differs from the intrinsic value ($\Gamma_{\text{fb}} = 0$). We here restrict our attention to the latter, noting that the associated cooling preserves the apparent imprecision-back-action product: $n_{\text{m}}n'_{\text{imp}} = n_{\text{m}}n_{\text{imp}}$.

Representative measurements of the oscillator's thermal motion are shown in fig. 3.9b. We determine n_{m} and n_{imp} by fitting each noise peak to a Lorentzian with a linewidth of $\Gamma_{\text{eff}} = \Gamma_{\text{m}} + \Gamma_{\text{fb}} + \Gamma_{\text{BA}}$ (including a minor contribution from dynamic back-action, Γ_{BA}), a peak amplitude of $\bar{S}_{\omega}[\Omega_{\text{m}}] \approx 2n_{\text{m}}(\Gamma_{\text{m}}/\Gamma_{\text{eff}})^2\bar{S}_{\omega}^{\text{ZP}}$, and an offset of $\bar{S}_{\omega}^{\text{imp}} = 2n_{\text{imp}}\bar{S}_{\omega}^{\text{ZP}}$. For low intracavity photon number, $n_c \ll n_{\text{m,th}}/C_0$, we observe that the effective bath occupation is dominated by the

3. MEASUREMENT-BASED CONTROL

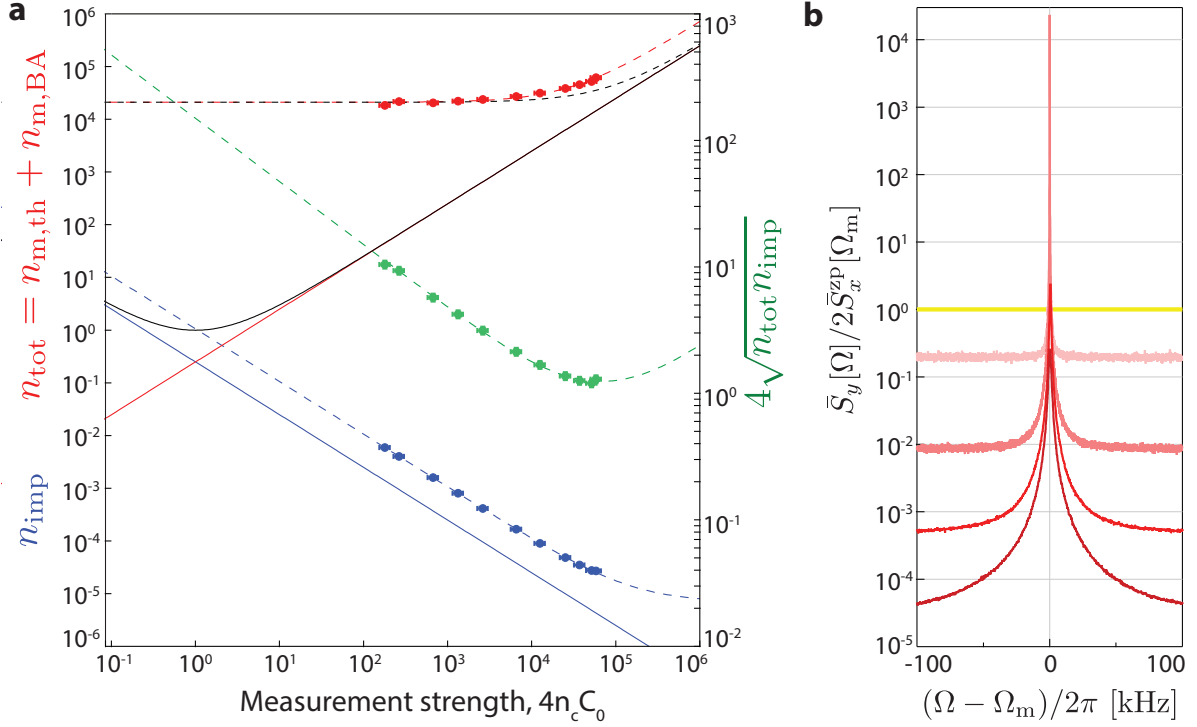


Fig. 3.9 – **Measurement imprecision and back-action versus intracavity photon number.** (a) Red, blue, and green points correspond to measurements of total effective bath occupation, $n_m = n_{\text{m,th}} + n_{\text{m,BA}}$, measurement imprecision referred to an equivalent bath occupation, n_{imp} , and the apparent imprecision-back-action product, $4\sqrt{n_{\text{tot}}n_{\text{imp}}}$, respectively. Solid black line depicts the ideal SQL model, for a zero temperature oscillator, consisting of quantum-limited imprecision (solid blue) $n_{\text{imp}} = (16C_0n_c)^{-1}$, and quantum back-action (solid red) $n_{\text{m,BA}} = C_0n_c$. Dashed black represents the SQL curve for the case of finite thermal occupation of the oscillator, described by $n_m = n_{\text{m,th}} + C_0n_c$. Dashed red and blue lines highlight excursion from their counterparts due to extraneous back-action, $C_0^{\text{ex}} = 0.56$, extraneous imprecision, $n_{\text{imp}}^{\text{ex}} = 0.70 \cdot 10^5$, and imperfect detection efficiency, $\eta = 0.23$, as described in the text. Green line models the apparent force-imprecision product using the eq. (3.2.15). (b) Spectra of the position fluctuations of the oscillator at various measurement strengths. Yellow line marks the peak spectral density at the SQL.

cryostat, $n_m \approx n_{\text{m,th}}$, and that imprecision scales as $n_{\text{imp}} = (16\eta C_0n_c)^{-1}$, where $\eta \approx 0.23$. η represents the ideality of the measurement, and includes both optical losses and reduction in the cavity transfer function due to mode splitting (see section 3.1.2.3). Operating with higher input power — ultimately limited by the onset of parametric instability in higher-order beam modes — the lowest imprecision we have observed is $n_{\text{imp}} \approx 2.7(\pm 0.2) \cdot 10^{-5}$, corresponding to an imprecision 39.7 ± 0.3 dB below that at the SQL. The associated measurement rate, $\Gamma_{\text{meas}} \approx 2\pi \cdot (13 \pm 1)$ kHz, is a factor of 9.2 lower than the rate of decoherence to the ambient 4.4 K bath, $\Gamma_{\text{th}} \approx 120$ kHz. Significantly, this value is within 15% of the requirement for feedback cooling to $n_m < 1$.

For large measurement strengths, quantum measurement back-action [294, 295] should in principle exceed the ambient thermal force. As shown in fig. 3.9, our system deviates from this ideal behaviour due to extraneous back-action, manifesting as an apparent excess cooperativity, C_0^{ex} , and limiting the fractional contribution of quantum back-action to $C_0/(C_0 + C_0^{\text{ex}}) \approx 35\%$. Combining this extraneous back-action with non-ideal measurement transduction/efficiency,

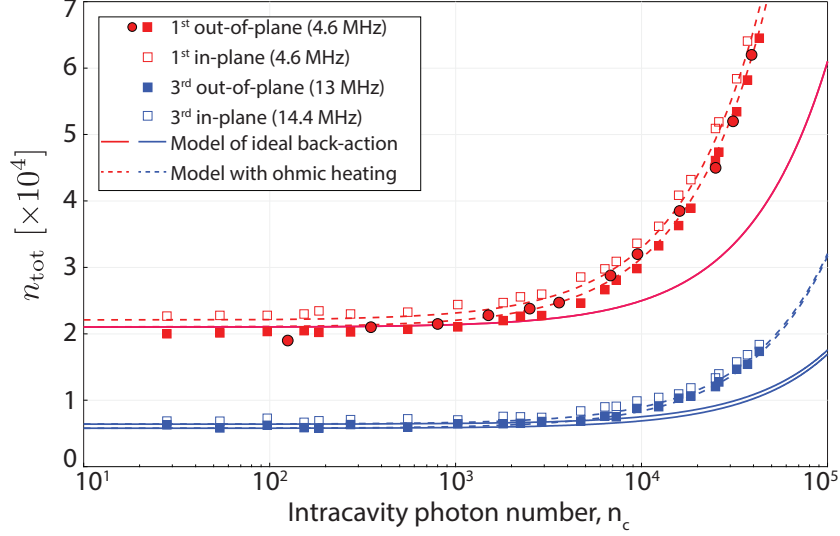


Fig. 3.10 – **Excess back-action due to ohmic heating.** Plot shows a compilation of several measurements of the back-action heating of the four lowest order modes of the nanobeam. Black-circled-red points are data from fig. 3.9a, for the fundamental out-of-plane mode. The square data report the back-action heating of the fundamental out-of-plane (solid red), fundamental in-plane (red), third harmonic out-of-plane (solid blue) and third harmonic in-plane (blue) modes. The solid lines are predictions from a model based on quantum back-action heating alone.

we model the apparent imprecision-back-action product of our measurement (green curve in fig. 3.9a) as

$$4\sqrt{n_{\text{imp}}n_{\text{m}}} = \sqrt{\frac{1}{\eta} \left(1 + \frac{n_{\text{th}}}{C_0 n_c} + \frac{C_0^{\text{ex}}}{C_0} \right) \left(1 + \frac{n_c}{n_c^{\text{ex}}} \right)}, \quad (3.2.15)$$

where $n_c^{\text{ex}} \equiv (16\eta C_0 n_{\text{imp}}^{\text{ex}})^{-1}$ is the photon number at which extraneous and shot-noise imprecision are equal. Operating at $n_c \approx 5 \cdot 10^4 \ll n_c^{\text{ex}}$, we observe a minimum imprecision-back-action product of $4\sqrt{n_{\text{imp}}n_{\text{m}}} \approx 5.0$. Thus we achieve a maximum measurement efficiency of $\Gamma_{\text{meas}}/\Gamma_{\text{tot}} \approx 0.040$.

3.2.2.1 Back-action due to ohmic heating

The origin of the excess back-action cooperativity, C_0^{ex} , remains not fully understood. However, heating due to laser noise can be fully ruled out. Preliminary measurements of the back-action heating of multiple mechanical modes of the nanobeam are shown in fig. 3.10. The fact that the ratio of observed back-action among the different modes do not scale with their known cooperativities strongly suggest that laser noise heating can be ruled out.

The other plausible source, ohmic heating via absorption of laser light in the beam remains a strong candidate. However, attempts to model this scenario using a simple heat transfer model: assuming a point heat source at the centre of the beam taken to be in equilibrium at its clamping points, implies a mode-dependent heating that is lower than what is observed. Given that all modes equilibrate at sufficiently high pressure, where we do not observe any appreciable back-action, we conjecture that the modification of thermal transport (both in terms of a drop in thermal conductivity [241], and maybe even transport mechanism [296]) along the slender beam may be responsible for deviations from simple heat transfer.

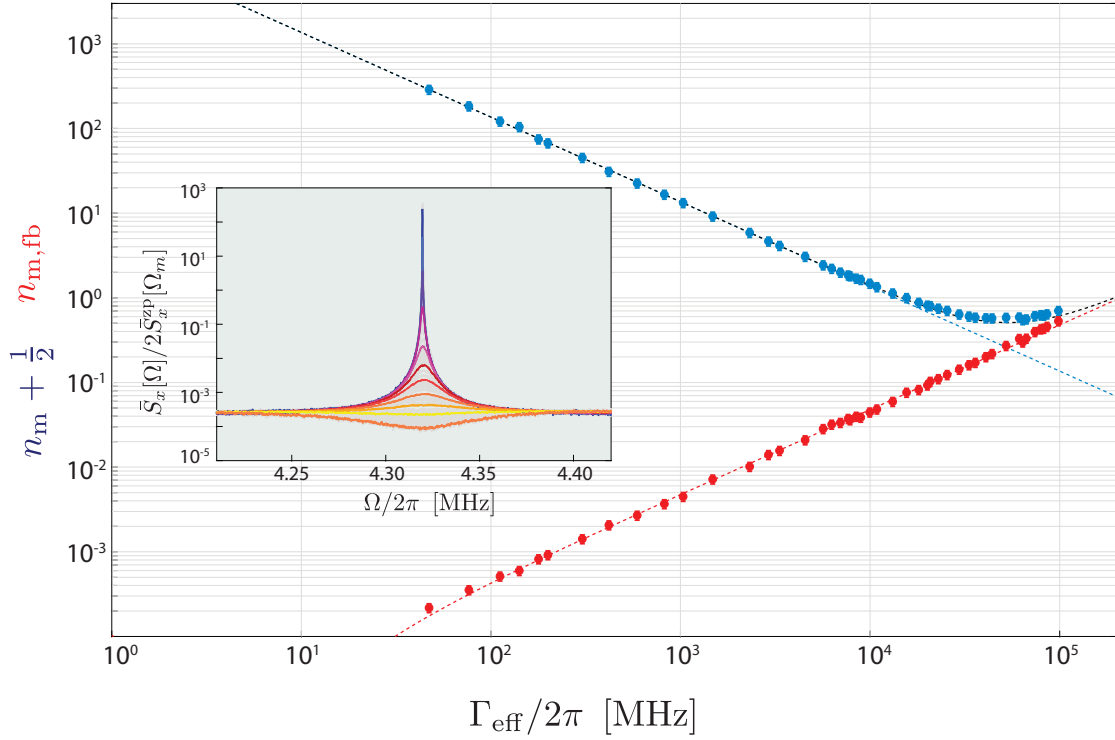


Fig. 3.11 – **Radiation pressure feedback cooling to near the ground state.** Blue and red points correspond to measurements of the phonon occupancy of the mechanical mode, n_m (plus a phonon-equivalent zero-point energy of $1/2$) and its component due to feedback of measurement noise $n_{m,fb} = n_{\text{imp}} g_{\text{fb}}^2 / (1 + g_{\text{fb}})$, respectively, as a function of measured damping rate, $\Gamma_{\text{eff}} = (1 + g_{\text{fb}})\Gamma_m$. Red, blue, and black dashed lines correspond to models of components in eq. (3.2.16): $n_m / (1 + g_{\text{fb}})$, $n_{m,fb}$, and $n_m + 1/2$, respectively, using experimental parameters $\Gamma_m/2\pi = 5.7$ Hz, $n_m = 2.4 \cdot 10^5$, and $n_{\text{imp}} = 2.8 \cdot 10^{-4}$, respectively. Inset: in-loop mechanical noise spectra for various feedback gain settings; fits to these spectra were used to infer blue and red points.

3.2.3 Feedback cooling to near the ground state

As a demonstration of the utility of our measurement efficiency, we consider what temperature can be reached by increasing the strength of the feedback used to damp the oscillator. Ignoring back-action due to the weakly driven ($n_c < 100$) feedback optical mode, the effective phonon occupancy of the cooled mechanical mode depends on the balance between coupling to thermal, measurement, and feedback reservoirs at rates Γ_{th} , $\Gamma_m n_{m,BA}$, and $\Gamma_{\text{fb}} n_{\text{imp}}$, respectively, where g_{fb} is the open loop feedback gain (See S.I.):

$$n_m + \frac{1}{2} = \frac{1}{1 + g_{\text{fb}}} (n_{m,\text{th}} + n_{m,\text{BA}}) + \frac{g_{\text{fb}}^2}{1 + g_{\text{fb}}} n_{\text{imp}} \geq 2\sqrt{n_{\text{imp}}(n_{m,\text{th}} + n_{m,\text{BA}})}. \quad (3.2.16)$$

The minimum value on the RHS of eq. (3.2.16) corresponds to suppressing the apparent position noise to the imprecision noise floor (cf. yellow curve in fig. 3.11, inset). Notably, in the absence of extraneous back-action, $n_m < 1$ requires $n_{\text{imp}} < 1/2n_{m,\text{th}}$.

Figure 3.11 shows the result of feedback cooling using a measurement with an imprecision far below that at the SQL. For this demonstration, imprecision was deliberately limited to $n_{\text{imp}} = 2.9 \cdot 10^{-4}$ in order to reduce contribution from the off-resonant tail of the noise peak at

4.6 MHz (which limits applicability of eq. (3.2.16) to damping rates of $\Gamma_{\text{eff}} \lesssim 2\pi \cdot 200$ kHz). The effective damping rate was controlled by changing the magnitude of the electronic gain, leaving all other parameters (e.g. laser power) unaffected. Fitting the closed loop noise spectrum (see fig. 3.11, inset) to a standard Lorentzian noise squashing model [297], we estimate the phonon occupancy of the mechanical mode from the formula $n_m + 0.5 \approx \Gamma_{\text{eff}} \cdot (\bar{S}_\omega[\Omega_m] + \bar{S}_\omega^{\text{imp}}) / 2\bar{S}_\omega^{\text{zfp}}$, where $\bar{S}_\omega^{\text{imp}}$ denotes the off-resonant background. Accounting for extraneous back-action, we infer a minimum occupation of $n_m \approx 5.3 \pm 0.6$ at an optimal damping rate of $\Gamma_{\text{eff}} \approx 2\pi \cdot 52$ kHz, corresponding to a fractional ground state population of $1/(1 + n_m) \approx 16\%$.

3.3 Conclusion

Collectively, these results establish new benchmarks for linear measurement and control of a mechanical oscillator. The enabling advance is a displacement imprecision 39.7 ± 0.3 dB below that at the SQL, a 100-fold improvement over results reported to date, combined with imprecision-back-action product within a factor of 5.0 of the uncertainty limit, on par with state-of-the-art optomechanical systems. At a moderate cryogenic temperature of 4.4 K, this amounts to the ability to resolve the zero-point motion of our 4.3 MHz oscillator at a measurement rate within an order of magnitude of the intrinsic thermal decoherence rate, $\Gamma_{\text{meas}}/\Gamma_{\text{th}} \approx 0.11$ and with a total measurement efficiency of $\Gamma_{\text{meas}}/\Gamma_{\text{tot}} \approx 0.04$. To illustrate the utility of this advance, we have actively cooled the nanomechanical beam to a mean phonon occupancy of 5.3 ± 0.6 using traditional radiation-pressure cold-damping [270]; this represents a 50-fold improvement over previous active feedback cooling applied to mechanical oscillators [275, 297–301]. Most importantly, since $n_m \ll n_{m,\text{BA}}$, feedback has suppressed $2 \cdot 10^3$ quanta of measurement back-action [293], accessing the regime of *quantum feedback* of a mechanical oscillator.

4 Quantum correlations in measurement-based control

Measurements proceed by establishing correlations between a system and a meter. In a quantum description of this process [264], the effect of measurement persists in the system in the form of measurement back-action. For a class of measurements – continuous linear measurements [62, 69] – where the meter couples linearly and weakly to the system, correlations between the system and meter additionally manifest as back-action-induced quantum correlations between the degrees of freedom of the meter (see section 2.1). A paradigmatic example is the interferometric position readout of a mechanical oscillator (as in section 2.3). The meter in this case is an optical field, which possesses two degrees of freedom (quadratures): amplitude and phase. The position of the oscillator is imprinted onto the phase quadrature. Back-action arises from vacuum fluctuations of the amplitude quadrature, which are imprinted onto the phase via the back-action-driven motion of the oscillator. In a homodyne detector, these quantum correlations manifest as ponderomotive squeezing of an appropriately chosen field quadrature [294, 302, 303]. In a heterodyne detector, they manifest as motional sideband asymmetry [304–307]. Differences between these effects arise from the details of how meter fluctuations are converted to a classical signal by the detection process [145, 305, 308, 309].

In a laboratory setting, quantum correlations in interferometric position measurements (contemporarily studied in cavity optomechanics [51]) are usually obscured by classical noise. An important example is thermal motion of the mechanical element. Two complementary approaches have been used to reduce this noise. Coupling of solid state mechanical oscillators to an optical cavity mode serving as a cold bath – effectively realizing an autonomous feedback loop (i.e. dynamic back-action) – has enabled thermal noise reduction to the level of the zero-point motion [209–211]. In this case, back-action imposes a fundamental limit [310] which may be mitigated by operating in an appropriate parameter regime (the resolved-sideband regime [311, 312]). A second approach, as discussed in chapter 3, relies on feedback of an efficient auxiliary measurement to suppress thermal motion [53, 263, 269, 275, 297–299, 301, 313, 314]. Remarkably, in this active feedback approach, measurement back-action can be suppressed [265, 293]. The penalty is an additional *feedback back-action* associated with the conversion of meter fluctuations into a classical signal, whose strength must be balanced against measurement efficiency.

The experimental results reported in section 4.2 show how feedback of an efficient homodyne measurement can be used to increase the visibility of quantum-correlation-induced motional sideband asymmetry in an out-of-loop heterodyne measurement. We highlight in particular the disappearance of motional sideband asymmetry in the regime of strong feedback

back-action, coinciding with squashing of the in-loop signal. These complementary effects illustrate a conceptual difference between back-action in autonomous and measurement-based feedback. Before embarking on a description of the results, the following sections discuss the origin of sideband asymmetry (section 4.1) and its relation to ponderomotive squeezing (section 4.1.1); how they could in principle be contaminated by laser noise (section 4.1.2.1), and measurements of laser noise used to conduct our experiments that affirm the faithfulness of our measurements (section 4.1.2.2).

4.1 Origin of sideband asymmetry

In the ideal case where an optomechanical system such as ours, in the bad-cavity regime $\kappa \gg \Omega_m$, is probed in the over-coupled regime ($\eta_c = 1$) on resonance with an optical field $\hat{a}_{\text{in}}(t)$, the cavity transmission (see eq. (2.3.2)),

$$\delta \hat{a}_{\text{out}}[\Omega] = -\delta \hat{a}_{\text{in}}[\Omega] - i\sqrt{C\Gamma_m} \left(\frac{\delta \hat{x}^{(0)}[\Omega] + \delta \hat{x}_{\text{BA}}[\Omega]}{x_{\text{zp}}} \right), \quad (4.1.1)$$

carries information regarding the mechanical motion in its phase quadrature. Here, we have introduced the multi-photon cooperativity,

$$C := \frac{4g^2}{\kappa\Gamma_m} = C_0 n_c, \quad (4.1.2)$$

that describes the transduction of mechanical motion onto the phase quadrature.

Equation (4.1.1) might be naively misunderstood to imply that fluctuations in $\delta \hat{a}_{\text{in}}$ sets the measurement imprecision on top of which the total mechanical motion $\delta \hat{x}^{(0)} + \delta \hat{x}_{\text{BA}}$ is resolved. However, the back-action motion $\delta \hat{x}_{\text{BA}}$, given by (see eq. (2.3.4)),

$$\delta \hat{x}_{\text{BA}}[\Omega] = \sqrt{2C\Gamma_m} \frac{\hbar\chi_x^{(0)}[\Omega]}{x_{\text{zp}}} \delta \hat{q}_{\text{in}}[\Omega] \quad (4.1.3)$$

caused by quantum fluctuations in the input amplitude quadrature creates correlations between the transmitted phase and amplitude, so that this naive expectation is false. To see this, note that the transmitted phase quadrature, according to eq. (4.1.1), is given by,

$$\delta \hat{p}_{\text{out}}[\Omega] = -\delta \hat{p}_{\text{in}}[\Omega] - \sqrt{2C\Gamma_m} \left(\frac{\delta \hat{x}^{(0)}[\Omega]}{x_{\text{zp}}} - \sqrt{2C\Gamma_m} \frac{\hbar\chi_x^{(0)}[\Omega]}{x_{\text{zp}}^2} \delta \hat{q}_{\text{out}}[\Omega] \right), \quad (4.1.4)$$

where we have used the expression for $\delta \hat{x}_{\text{BA}}$ in eq. (4.1.3) and the fact that $\delta \hat{q}_{\text{in}} = -\delta \hat{q}_{\text{out}}$. The output phase quadrature, by being related to the output amplitude quadrature (via the finite coherence time of the mechanical oscillator), are correlated with each other within the mechanical oscillator bandwidth; in terms of the (unsymmetrised) cross-correlation spectrum,

$$S_{pq}^{\text{out}}[\Omega] = S_{pq}^{\text{in}}[\Omega] + 2C\Gamma_m \frac{\hbar\chi_x^{(0)}[\Omega]}{x_{\text{zp}}^2} S_{qq}^{\text{out}}[\Omega] = -\frac{i}{2} + \frac{2C\Omega_m\Gamma_m}{\Omega^2 - \Omega_m^2 - i\Omega\Gamma_m}. \quad (4.1.5)$$

Since the intrinsic mechanical motion $\delta \hat{x}^{(0)}$ is uncorrelated with the optical beam, these correlations arise from two sources: correlations between the input amplitude and phase necessitated

by the field commutation relations (see section 2.2.2.1), and those due to interaction of the field with the mechanical oscillator. Cross-correlations observed using linear detectors (linear optomechanical interaction followed by linear detection of the optical field) do not involve any contribution from the vacuum fluctuations of the mechanical oscillator [305, 315].

The two canonical types of linear detection schemes available for optical fields: optical homodyning and heterodyning, reveal phase-amplitude correlations differently. In the following we treat the case of heterodyne detection, while section 4.1.1 deals with homodyne detection.

For a heterodyne detector with a local oscillator field that is frequency-shifted by Ω_{IF} (see discussion of heterodyne detection in section 2.2.2.4), the spectrum of heterodyne photocurrent spectrum centred around Ω_{IF} is (omitting factors due to LO flux and electron charge),

$$\begin{aligned} \bar{S}_I^{\text{het}}[\Omega - \Omega_{\text{IF}}] &\propto \frac{1}{2} \left(\bar{S}_{qq}^{\text{out}}[\Omega] + \bar{S}_{pp}^{\text{out}}[\Omega] \right) + \frac{i}{2} \left(S_{qp}^{\text{out}}[\Omega] - S_{pq}^{\text{out}}[\Omega] \right) \\ &= \frac{1}{2} \left(\bar{S}_{qq}^{\text{in}}[\Omega] + \bar{S}_{pp}^{\text{in}}[\Omega] \right) + \frac{2C\Gamma_m}{x_{\text{zp}}^2} \bar{S}_{xx}[\Omega] + \text{Im} \left(S_{qp}^{\text{out}}[\Omega] - S_{pq}^{\text{out}}[\Omega] \right) \\ &= 1 + \frac{2C\Gamma_m}{x_{\text{zp}}^2} \left(\bar{S}_{xx}[\Omega] + \bar{S}_{xx}^{\text{zp}}[\Omega] - \bar{S}_{xx}^{\text{zp}}[-\Omega] \right). \end{aligned} \quad (4.1.6)$$

Here $\bar{S}_{xx} = \bar{S}_{xx}^{(0)} + \bar{S}_{xx}^{\text{BA}}$ is the total mechanical motion. The additional contribution on either sideband, numerically equal to half of a zero-point motion, arises from the second term in the amplitude-phase correlation in eq. (4.1.5). Ultimately, correlations that arise due to general aspects of linear measurement (similar to the one encountered in the case of the SQL being enforced by fluctuations in the meter in eq. (2.1.21)), conspire to add (subtract) the equivalent of half a phonon of noise power on the upper (lower) sideband in heterodyne detection [54].

4.1.1 Relation to ponderomotive squeezing

In the case where the cavity transmission, $\delta\hat{a}_{\text{out}}$ in eq. (4.1.1), is measured using a homodyne detector, the correlations manifest differently [316]. The observable relevant to homodyne detection is the general quadrature

$$\hat{q}_{\text{out}}^\theta[\Omega] := \delta\hat{q}_{\text{out}}[\Omega] \cos \theta + \delta\hat{p}_{\text{out}}[\Omega] \sin \theta,$$

whose spectrum,

$$\bar{S}_{qq}^{\theta, \text{out}}[\Omega] = \bar{S}_{qq}^{\text{out}}[\Omega] \cos^2 \theta + \bar{S}_{pp}^{\text{out}}[\Omega] \sin^2 \theta + \bar{S}_{pq}^{\text{out}}[\Omega] \sin 2\theta,$$

is directly proportional to the homodyne photocurrent spectrum, $\bar{S}_I^{\theta, \text{hom}}[\Omega]$. For resonant probing, using the expression for $\delta\hat{p}_{\text{out}}$ in eq. (4.1.4) and noting that $\delta\hat{q}_{\text{out}} = -\delta\hat{q}_{\text{in}}$, the homodyne spectrum is (normalised to shot noise),

$$\bar{S}_I^{\theta, \text{hom}}[\Omega] = 1 + \frac{4\eta C\Gamma_m}{x_{\text{zp}}^2} \left(\bar{S}_{xx}[\Omega] \sin^2 \theta + \frac{\hbar}{2} \text{Re} \chi_x^{(0)}[\Omega] \sin 2\theta \right). \quad (4.1.7)$$

The first term, representing the total motion of the oscillator, is positive and symmetric about the mechanical resonance frequency, while the second term is anti-symmetric, and therefore

negative on one side of the mechanical frequency. Indeed, at the (frequency dependent) quadrature defined by (modulo $\pi/2$),

$$\theta_{\text{sq}}[\Omega] := \frac{1}{2} \tan^{-1} \left(-\frac{\hbar \operatorname{Re} \chi_x^{(0)}[\Omega]}{\bar{S}_{xx}[\Omega]} \right), \quad (4.1.8)$$

the homodyne photocurrent spectrum, $\bar{S}_I^{\theta_{\text{sq}}, \text{hom}} \approx 1 - \frac{\hbar^2}{4} (\operatorname{Re} \chi_x^{(0)})^2 / \bar{S}_{xx} < 1$, leading to optical squeezing.

Both sideband asymmetry and optical squeezing arise from the same underlying physics: correlations between the back-action driven motion and the noise source that sets the imprecision at the detector. In the case of heterodyne detection, the imaginary part of the correlation, i.e. $\operatorname{Im} \bar{S}_{pq}^{\text{out}}$, leads to an asymmetry in the recorded sidebands, while for homodyne detection, the real part, $\operatorname{Re} \bar{S}_{pq}^{\text{out}}$ leads to ponderomotive squeezing.

4.1.2 Effect of classical laser noise on sideband asymmetry

The cross-correlation spectrum, S_{pq}^{out} , in eq. (4.1.5) by being directly related to S_{qq}^{out} , can get contaminated by classical contribution to S_{qq}^{out} . These contributions may arise from classical contributions to S_{qq}^{in} (input amplitude noise), or from classical contributions to S_{pp}^{in} (input phase noise) that get transduced by the cavity into S_{qq}^{out} . In the following, a formal treatment of these two contributions is provided.

The effect of laser noise on sideband asymmetry measurements is well-studied for cavity optomechanical systems in the resolved sideband regime [317, 318]. In this case sidebands have been observed separately by scattering them into the cavity with a probe laser red/blue detuned. Here we discuss the effect of laser noise on sideband asymmetry measurements in the bad-cavity regime ($\Omega_m \ll \kappa$), wherein a resonant probe is used to detect the sidebands simultaneously in a heterodyne measurement. A theoretical model relevant for this case is developed in section 4.1.2.1. We also explicitly track the contributions of the mechanical oscillator and optical field commutation relations, to formally establish their relative contribution to heterodyne sideband asymmetry. In section 4.1.2.2, we present measurements confirming the negligible contribution of laser noise to the reported results.

4.1.2.1 Contribution of excess noise for resonant probing

In our experiment, we probe the optomechanical system using a resonant laser at frequency ω_ℓ . The photon flux amplitude operator of the laser, $a_{\text{in}}(t)$, is assumed to have the form (as in eq. (2.2.82)),

$$\hat{a}_{\text{in}}(t) = e^{-i\omega_\ell t} (\bar{a}_{\text{in}} + \delta \hat{a}_{\text{in}}(t)),$$

where $\bar{a}_{\text{in}} = \sqrt{P_{\text{in}} / \hbar \omega_\ell}$ is the mean photon flux and the fluctuations $\delta a_{\text{in}}(t)$ satisfy,

$$[\delta \hat{a}_{\text{in}}(t), \delta \hat{a}_{\text{in}}^\dagger(t')] = \varepsilon_a \delta(t - t').$$

Note that we explicitly “tag” the commutator so as to follow its contribution to the measured quantities [305]; in reality $\varepsilon_a = 1$.

The canonically conjugate quadratures corresponding to the fluctuations are defined as

$$\delta\hat{q}_{\text{in}}(t) := \frac{\delta\hat{a}_{\text{in}}(t) + \delta\hat{a}_{\text{in}}^\dagger(t)}{\sqrt{2}}, \quad \delta\hat{p}_{\text{in}}(t) := \frac{\delta\hat{a}_{\text{in}}(t) - \delta\hat{a}_{\text{in}}^\dagger(t)}{i\sqrt{2}},$$

so that

$$[\delta\hat{q}_{\text{in}}(t), \delta\hat{p}_{\text{in}}(t')] = i\varepsilon_a \delta(t - t'). \quad (4.1.9)$$

Following the ansatz of optical fluctuations adopted in section 2.2.2.1, excess noise in the laser is modelled as Gaussian fluctuations, for which,

$$\begin{pmatrix} \langle \delta\hat{q}_{\text{in}}(t)\delta\hat{q}_{\text{in}}(t') \rangle & \langle \delta\hat{q}_{\text{in}}(t)\delta\hat{p}_{\text{in}}(t') \rangle \\ \langle \delta\hat{p}_{\text{in}}(t)\delta\hat{q}_{\text{in}}(t') \rangle & \langle \delta\hat{p}_{\text{in}}(t)\delta\hat{p}_{\text{in}}(t') \rangle \end{pmatrix} = \frac{1}{2} \begin{pmatrix} \varepsilon_a + 2C_{qq} & i\varepsilon_a + 2C_{qp} \\ -i\varepsilon_a + 2C_{qp} & \varepsilon_a + 2C_{pp} \end{pmatrix} \delta(t - t'). \quad (4.1.10)$$

The terms C_{ij} ($i = q, p$) represent the noise in excess of the fundamental vacuum fluctuations in the field quadratures, distributed uniformly (i.e. “white”) in frequency. We henceforth omit the cross-correlation C_{qp} and attempt to bound its effect via an appropriate inequality^{4.1} (see eq. (2.2.44)). Thus,

$$\begin{pmatrix} \langle \delta\hat{a}_{\text{in}}(t)\delta\hat{a}_{\text{in}}(t') \rangle & \langle \delta\hat{a}_{\text{in}}(t)\delta\hat{a}_{\text{in}}^\dagger(t') \rangle \\ \langle \delta\hat{a}_{\text{in}}^\dagger(t)\delta\hat{a}_{\text{in}}(t') \rangle & \langle \delta\hat{a}_{\text{in}}^\dagger(t)\delta\hat{a}_{\text{in}}^\dagger(t') \rangle \end{pmatrix} = \frac{1}{2} \begin{pmatrix} C_{qq} - C_{pp} & 2\varepsilon_a + C_{qq} + C_{pp} \\ C_{qq} + C_{pp} & C_{qq} - C_{pp} \end{pmatrix}.$$

We now consider an optomechanical system where the optical cavity is driven by a noisy input field satisfying section 4.1.2.1. The mechanical oscillator couples to the cavity field via radiation pressure and is additionally driven by a thermal Langevin force. Fluctuations of the intracavity field amplitude (δa) and the mechanical oscillator amplitude (δb) around their stable steady states satisfy (eq. (2.2.106))

$$\begin{aligned} \dot{\delta a} &= +i\Delta\delta a - \frac{\kappa}{2}\delta a + ig(\delta\hat{b} + \delta\hat{b}^\dagger) + \sqrt{\kappa}\delta\hat{a}_{\text{in}} \\ \dot{\delta b} &= -i\Omega_m\delta b - \frac{\Gamma_m}{2}\delta b + i(g^*\delta a + g\delta a^\dagger) + \sqrt{\Gamma_m}\delta\hat{b}_{\text{in}}. \end{aligned} \quad (4.1.11)$$

Here $\Delta = \omega_\ell - \omega_c$ is the laser detuning, $g = g_0\bar{a}$ is the dressed optomechanical coupling rate, and $\bar{a} = \frac{\sqrt{\kappa}\bar{a}_{\text{in}}}{\frac{\kappa}{2} - i\Delta}$ is the mean intracavity field amplitude. We have also assumed here that the cavity decay rate is dominated by its external coupling, i.e. $\kappa = \kappa_0 + \kappa_{\text{ex}} \approx \kappa_{\text{ex}}$. The mechanical Langevin noise correlators are

$$\begin{aligned} \langle \delta\hat{b}_{\text{in}}(t)\delta\hat{b}_{\text{in}}^\dagger(t') \rangle &= (n_{\text{m,th}} + \varepsilon_b)\delta(t - t') \\ \langle \delta\hat{b}_{\text{in}}^\dagger(t)\delta\hat{b}_{\text{in}}(t') \rangle &= n_{\text{m,th}}\delta(t - t'), \end{aligned}$$

where n_{th} is the ambient mean thermal phonon occupation of the oscillator. Note that we also “tag” the contribution due to the zero-point fluctuation of the thermal bath to determine its role in the observables; in reality $\varepsilon_b = 1$.

^{4.1} In addition, it is known that for semiconductor lasers, phase-amplitude correlations are limited to frequencies close to their relaxation oscillation frequency [319, 320]; the latter is typically at a few GHz from the carrier [285, 321] – irrelevant for our experiment

Equation (4.1.11) can be solved in the Fourier domain,

$$\begin{aligned}\delta\hat{a}[\Omega] &= \chi_a[\Omega] \left[\sqrt{\kappa} \delta\hat{a}_{\text{in}}[\Omega] + ig(\delta\hat{b}[\Omega] + \delta\hat{b}^\dagger[\Omega]) \right] \\ \delta\hat{a}^\dagger[\Omega] &= \delta a[-\Omega]^\dagger = \chi_a^*[-\Omega] \left[\sqrt{\kappa} \delta\hat{a}_{\text{in}}^\dagger[\Omega] - ig^*(\delta\hat{b}[\Omega] + \delta\hat{b}^\dagger[\Omega]) \right]\end{aligned}$$

and

$$\begin{aligned}\begin{pmatrix} \delta\hat{b}[\Omega] \\ \delta\hat{b}^\dagger[\Omega] \end{pmatrix} &= \frac{\sqrt{\Gamma_m}}{\mathcal{N}[\Omega]} \begin{pmatrix} \chi_b^{*-1}[-\Omega] - i\Sigma[\Omega] & -i\Sigma[\Omega] \\ +i\Sigma[\Omega] & \chi_b^{-1}[\Omega] + i\Sigma[\Omega] \end{pmatrix} \begin{pmatrix} \delta\hat{b}_{\text{in}}[\Omega] \\ \delta\hat{b}_{\text{in}}^\dagger[\Omega] \end{pmatrix} \\ &+ \frac{i\sqrt{\kappa}}{\mathcal{N}[\Omega]} \begin{pmatrix} g^*\chi_b^{*-1}[-\Omega]\chi_a[\Omega] & g\chi_b^{*-1}[-\Omega]\chi_a^*[-\Omega] \\ -g^*\chi_b^{-1}[\Omega]\chi_a[\Omega] & -g\chi_b^{-1}[\Omega]\chi_a^*[-\Omega] \end{pmatrix} \begin{pmatrix} \delta\hat{a}_{\text{in}}[\Omega] \\ \delta\hat{a}_{\text{in}}^\dagger[\Omega] \end{pmatrix}.\end{aligned}\quad (4.1.12)$$

Here χ_b and χ_a are the bare mechanical and cavity response functions, respectively, given by,

$$\chi_b[\Omega] := [\Gamma_m/2 - i(\Omega - \Omega_m)]^{-1}, \quad \chi_a[\Omega] := [\kappa/2 - i(\Omega + \Delta)]^{-1}.$$

$\Sigma[\Omega]$ is the mechanical ‘‘self-energy’’,

$$\Sigma[\Omega] = -i|g|^2(\chi_a[\Omega] - \chi_a^*[-\Omega]) = \Sigma^*[-\Omega], \quad (4.1.13)$$

which describes the modification to the mechanical response due to radiation pressure, and

$$\mathcal{N}[\Omega] = \chi_b^{-1}[\Omega]\chi_b^{*-1}[-\Omega] + 2\Omega_m\Sigma[\Omega] = \mathcal{N}^*[-\Omega].$$

The input-output relation [174], $\delta a_{\text{out}} = \delta a_{\text{in}} - \sqrt{\kappa} \delta a$, gives the fluctuations of the output fields in terms of the fluctuations of the input fields:

$$\begin{aligned}\delta\hat{a}_{\text{out}} &= A[\Omega]\delta\hat{a}_{\text{in}} + B[\Omega]\delta\hat{a}_{\text{in}}^\dagger + C[\Omega]\delta\hat{b}_{\text{in}} + D[\Omega]\delta\hat{b}_{\text{in}}^\dagger \\ \delta\hat{a}_{\text{out}}^\dagger &= A^*[-\Omega]\delta\hat{a}_{\text{in}}^\dagger + B^*[-\Omega]\delta\hat{a}_{\text{in}} + C^*[-\Omega]\delta\hat{b}_{\text{in}}^\dagger + D^*[-\Omega]\delta\hat{b}_{\text{in}}\end{aligned}$$

where,

$$\begin{aligned}A[\Omega] &= 1 - \kappa\chi_a[\Omega] - \frac{2i|g|^2\kappa\Omega_m\chi_a[\Omega]^2}{\mathcal{N}[\Omega]} \approx -\left(1 + 4i\frac{\Delta}{\kappa}\right) \left(1 + C_0n_c \frac{2i\Omega_m\Gamma_m}{\mathcal{N}[\Omega]}\right) \\ B[\Omega] &= -\frac{2ig^2\kappa\Omega_m\chi_a[\Omega]\chi_a^*[-\Omega]}{\mathcal{N}[\Omega]} \approx -C_0n_c \frac{2i\Omega_m\Gamma_m}{\mathcal{N}[\Omega]} \\ C[\Omega] &= -\frac{ig\sqrt{\kappa\Gamma_m}}{\mathcal{N}[\Omega]}\chi_a[\Omega]\chi_b^{*-1}[-\Omega] \approx -i\sqrt{C_0n_c} \left(1 + 2i\frac{\Delta}{\kappa}\right) \Gamma_m\chi_b[\Omega] \\ D[\Omega] &= -\frac{ig\sqrt{\kappa\Gamma_m}}{\mathcal{N}[\Omega]}\chi_c[\Omega]\chi_b^{-1}[\Omega] \approx -i\sqrt{C_0n_c} \left(1 + 2i\frac{\Delta}{\kappa}\right) \Gamma_m\chi_b^*[-\Omega].\end{aligned}$$

Here approximate expressions are given for the case of interest, namely, resonant probing ($|\Delta| \ll \kappa$), small sideband resolution ($\Omega_m \ll \kappa$), and weak coupling ($|g| \ll \kappa$). We have also introduced the single-photon cooperativity, $C_0 = 4g_0^2/(\kappa\Gamma_m)$, and the mean intracavity photon number, $n_c = |\bar{a}|^2$.

Balanced heterodyne detection of the cavity output is used to measure motional sideband asymmetry. We assume, as in the experiment, that the local oscillator and signal paths are

balanced in length; together with a balance of power beyond the combining beam-splitter, this ensures suppression of common-mode excess noise [145].

Following standard arguments for heterodyne detection with a LO frequency shifted by Ω_{IF} (see section 2.2.2.4), the photocurrent spectrum normalised to the local oscillator shot noise is given by,

$$\begin{aligned} \bar{S}_{II}^{\text{het}}[\Omega - \Omega_{\text{IF}}] \approx \varepsilon_a + 4C_0 n_c \left[\frac{\Gamma_m^2}{4} |\chi_b[-\Omega]|^2 \left(n_{\text{tot}} + \frac{\varepsilon_b}{2} - \left(\frac{\varepsilon_a}{2} + C_{qq} \right) + \frac{4\Delta\Omega_m}{\kappa^2} C_{pp} \right) \right. \\ \left. + \frac{\Gamma_m^2}{4} |\chi_b[\Omega]|^2 \left(n_{\text{tot}} + \frac{\varepsilon_b}{2} + \left(\frac{\varepsilon_a}{2} + C_{qq} \right) + \frac{4\Delta\Omega_m}{\kappa^2} C_{pp} \right) \right]. \end{aligned} \quad (4.1.14)$$

This represents the heterodyne spectrum measured in the experiment and depicted later in figs. 4.5 and 4.7. Here the total bath occupation, arising from the ambient thermal bath and the measurement back-action due to the meter beam, is given by,

$$n_{\text{tot}} = n_{\text{m,th}} + \underbrace{C_0 n_c \left(\frac{\varepsilon_a}{2} + C_{qq} + \left(\frac{4\Delta\Omega_m}{\kappa^2} \right)^2 C_{pp} \right)}_{n_{\text{BA}}}.$$

The *sideband ratio* extracted from such a spectrum is,

$$\begin{aligned} R &:= \frac{\int_{0^+}^{+\infty} (\bar{S}_{II}^{\text{het}}[\Omega - \Omega_{\text{IF}}] - \bar{S}_{II}^{\text{het}}[\Omega = \Omega_{\text{IF}}^+]) \frac{d\Omega}{2\pi}}{\int_{-\infty}^{0^-} (\bar{S}_{II}^{\text{het}}[\Omega - \Omega_{\text{IF}}] - \bar{S}_{II}^{\text{het}}[\Omega = \Omega_{\text{IF}}^-]) \frac{d\Omega}{2\pi}} \\ &= \frac{n_{\text{tot}} + \frac{\varepsilon_b - \varepsilon_a}{2} - C_{qq} + \frac{4\Delta\Omega_m}{\kappa^2} C_{pp}}{n_{\text{tot}} + \frac{\varepsilon_b + \varepsilon_a}{2} + C_{qq} + \frac{4\Delta\Omega_m}{\kappa^2} C_{pp}} \\ &= \frac{n_{\text{tot}} + \left(\frac{4\Delta\Omega_m}{\kappa^2} C_{pp} - C_{qq} \right)}{n_{\text{tot}} + 1 + \left(\frac{4\Delta\Omega_m}{\kappa^2} C_{pp} + C_{qq} \right)}. \end{aligned} \quad (4.1.15)$$

Firstly, characteristic of linear detection, deviation of R from unity in the ideal case ($C_{qq} = 0 = C_{pp}$) is due to correlations developed between the quantum-back-action driven mechanical motion and the detection process [305, 318]. When C_{qq} and C_{pp} are finite, classical correlations are established that affect R . The response of the cavity (for $\Delta/\kappa \approx 0$) ensures that excess classical correlations due to input amplitude noise lead to an enhanced asymmetry, whereas those arising from input phase noise lead to a common increase in the sideband noise power.

4.1.2.2 Measurement of excess laser noise

Excess amplitude noise

In order to measure the noise in the amplitude quadrature, we employ direct photodetection of the probe laser. The measurement is made at the output of the tapered fiber, with the fiber retracted from the cavity. Analysis of the resulting photocurrent reveals the single-sided spectrum of the incident optical intensity (referred here for convenience to the incident optical power $\hat{P} = \hbar\omega_\ell \hat{n}$, where \hat{n} is the photon flux),

$$\bar{S}_P[\Omega] = (\hbar\omega_\ell)^2 \cdot 2\bar{S}_{nn}[\Omega] = (\hbar\omega_\ell)^2 \cdot 2 \langle \hat{n} \rangle (1 + 2C_{qq}).$$

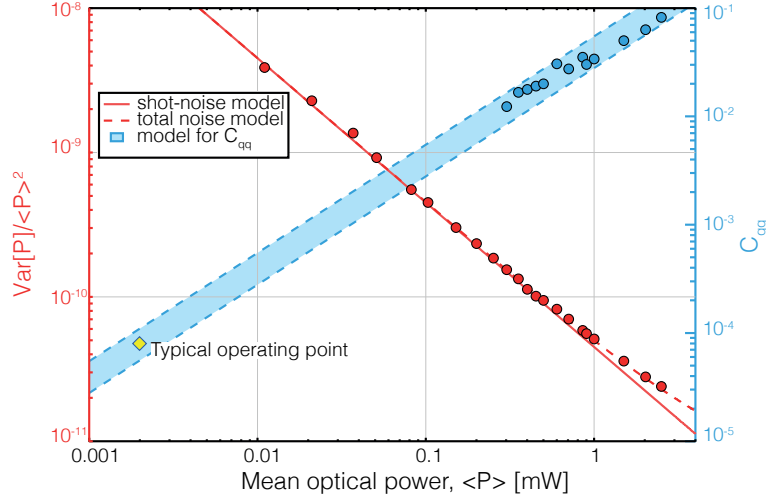


Fig. 4.1 – **Measurement of laser amplitude noise.** Integrated (in a 100 kHz band) relative intensity noise $\frac{\text{Var}[P]}{\langle P \rangle^2} := \int \bar{S}_{\text{RIN}}(\Omega \approx \Omega_m) \frac{d\Omega}{2\pi}$ versus mean optical power. Deviation from shot-noise scaling is evident for $\langle P \rangle \gtrsim 1$ mW, attributed to classical amplitude noise.

A convenient characterisation of the intensity noise is via the relative intensity noise (RIN) spectrum,

$$\bar{S}_{\text{RIN}}[\Omega] := \frac{\bar{S}_P[\Omega]}{\langle \hat{P} \rangle^2},$$

for which, excess amplitude noise manifests as a deviation from the shot-noise scaling $\propto \frac{1}{\langle P \rangle}$; more precisely,

$$C_{qq} = \frac{1}{2} \left(\frac{\langle \hat{n} \rangle}{2} \bar{S}_{\text{RIN}}[\Omega] - 1 \right), \quad (4.1.16)$$

at given incident photon flux. fig. 4.1 shows an inference of C_{qq} using eq. (4.1.16) and a measurement of $\bar{S}_{\text{RIN}}[\Omega]$ versus mean optical power. For typical experimental conditions ($\langle P \rangle = 1 - 5$ mW), $C_{qq} \ll 0.01$, so that its contribution to sideband asymmetry is negligible.

Excess phase noise

Noise in the phase quadrature of the field leaking from the cavity is measured using balanced homodyne detection. This signal reveals phase noise originating from the input laser as well as apparent phase noise from the cavity. Referred to cavity frequency noise, the homodyne photocurrent spectral density is given by,

$$\bar{S}_\omega[\Omega] = \Omega^2 \bar{S}_\phi[\Omega] = \Omega^2 \left(\bar{S}_\phi^{\text{in,shot}}[\Omega] + \bar{S}_\phi^{\text{in,ex}}[\Omega] + \bar{S}_\phi^{\text{cav,ex}}[\Omega] + \bar{S}_\phi^{\text{cav,mech}}[\Omega] \right). \quad (4.1.17)$$

\bar{S}_ω contains contributions from laser phase noise (shot and excess), cavity substrate noise, including thermorefractive [288] and thermomechanical noise [279]. The total excess noise in the phase quadrature is modeled by C_{pp} , which allows us to infer the latter using,

$$\frac{C_{pp}}{\langle \hat{n} \rangle} = \bar{S}_\phi^{\text{in,ex}}[\Omega_m] + \bar{S}_\phi^{\text{cav,ex}}[\Omega_m]. \quad (4.1.18)$$

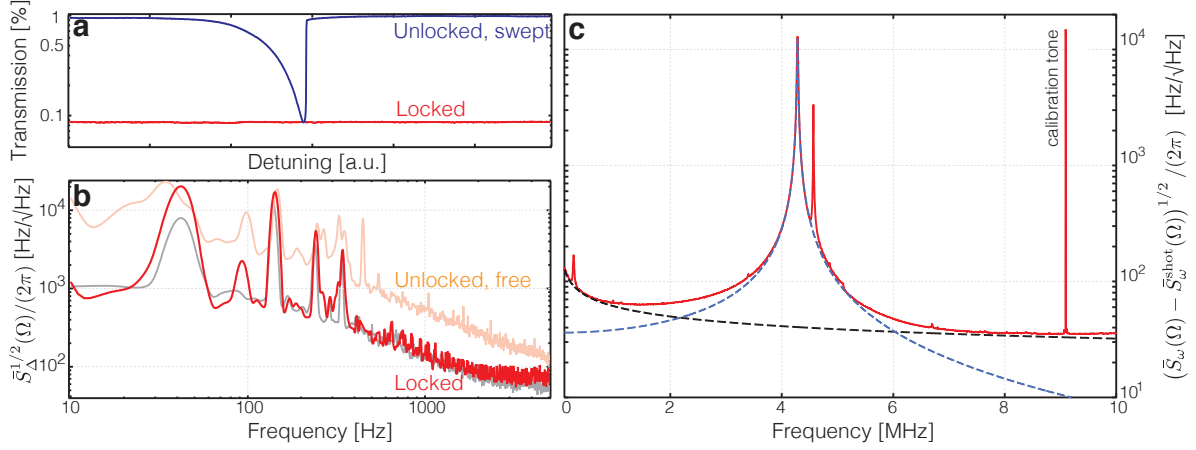


Fig. 4.2 – **Estimate of input-referred phase noise.** (a) Residual detuning offset at DC estimated from transmission signal when the laser is locked to cavity. (b) Spectrum analysis of the lock error signal, generated via frequency-modulation spectroscopy (see section 2.2.2.5), reveals low frequency detuning jitter; when locked (red), apparent detuning noise is limited by electronic noise (gray) in the feedback loop, predominantly from the photodetector. (c) Excess frequency noise around the mechanical frequency inferred from a balanced homodyne measurement of the cavity output on resonance. The shot-noise-subtracted signal (red) is composed of the thermomechanical motion of the mechanical mode (blue dashed) and a contribution from excess frequency noise in the laser and cavity substrate (black dashed).

Figure 4.2c shows a homodyne measurement made with 3 mW of local oscillator power, whose shot-noise has been subtracted. The spectrum is calibrated by referencing it against a known phase modulation tone injected at the input of the homodyne interferometer. The total excess frequency noise (red) is dominated by thermal motion of the in-plane and out-of-plane modes, both of which are gas damped for this measurement. A joint fit to (a) a model of a velocity-damped oscillator (blue, dashed) and, (b) a model combining thermorefractive [288, 322] and white frequency noise (black, dashed), gives an estimate of $\bar{S}_{\omega}^{\text{ex}}(\Omega)$. Near the mechanical frequency, $\bar{S}_{\omega}^{\text{ex}}(\Omega_m) \approx 2\pi \cdot (35 \text{ Hz}/\sqrt{\text{Hz}})^2$, implying (via eq. (4.1.18)), $C_{pp} \approx 30$.

From this estimate of C_{pp} we are able to bound two quantities. First, in conjunction with $C_{qq} \ll 0.01$, the excess noise cross-correlation is bounded as $C_{qp} \ll 1$. Secondly, referring to eq. (4.1.14), we are able to estimate the contribution of phase noise to the heterodyne sideband. This contribution, characterised as an equivalent phonon occupation (since it adds positive noise power to either sideband),

$$n_{\phi} = \frac{\Delta}{\kappa} \frac{4\Omega_m}{\kappa} C_{pp}, \quad (4.1.19)$$

has a mean value determined by the mean offset in the detuning $\bar{\Delta}$. fig. 4.2a allows an estimate, $\bar{\Delta} \approx 0.01 \cdot \kappa$, giving,

$$\bar{n}_{\phi} = \frac{\bar{\Delta}}{\kappa} \frac{4\Omega_m}{\kappa} C_{pp} = 0.0052 \cdot \left(\frac{\bar{\Delta}/\kappa}{0.01}\right)^4 \left(\frac{\Omega_m/2\pi}{4.3 \text{ MHz}}\right) \left(\frac{1 \text{ GHz}}{\kappa/2\pi}\right) \left(\frac{C_{pp}}{30}\right). \quad (4.1.20)$$

Low frequency detuning noise $\delta\Delta$ (fig. 4.2b) causes deviations from this mean, which are significant if their effect is comparable to \bar{n}_{ϕ} . We bound the probability for such “large” statistical excursions using Chebyshev’s inequality [323],

$$\Pr(|n_{\phi} - \bar{n}_{\phi}| > \bar{n}_{\phi}) \leq \frac{\text{Var}[n_{\phi}]}{\bar{n}_{\phi}^2} = \left(\frac{4\Omega_m}{\kappa} \frac{C_{pp}}{\bar{n}_{\phi}}\right)^2 \frac{\text{Var}[\delta\Delta]}{\kappa^2} \approx 10^{-6}. \quad (4.1.21)$$

We thus estimate that mean residual detuning is the leading contribution to phase noise contamination; the contamination, characterised as a phonon-equivalent noise power $\bar{n}_\phi = 0.005$ is however an insignificant contribution to the sideband ratio eq. (4.1.15).

Together with the bounds, $C_{qq} \ll 0.01$ and $C_{qp} \ll 1$, this implies that sources of classical noise may be excluded in the interpretation of the experimental data.

4.2 Experimental results

A pedagogical description of continuous linear measurement is germane to understanding our approach to quantum correlations within the framework of measurement-based control. We denote as $\hat{x}(t)$ the position of a quantum harmonic oscillator and $\hat{y}(t) \propto \hat{x}(t)$ the output of a linear continuous position detector. Since it is a continuous observable, $y(t)$ must commute with itself at different times ($[\hat{y}(t), \hat{y}(t')] = 0$). $\hat{x}(t)$ does not obey this constraint, which requires that the detector output contains an additional noise term $\hat{x}_n(t)$ that enforces the commutator. \hat{x}_n contains two components: an apparent (imprecision) noise, \hat{x}_{imp} , which arises from quantum fluctuations of the meter degree of freedom that is coupled to the detector, and a physical (back-action) noise, \hat{x}_{BA} , which arises from quantum fluctuations of the meter degree of freedom that is coupled to the system. The total detector signal, $\hat{y} = \hat{x} + \hat{x}_{\text{BA}} + \hat{x}_{\text{imp}} \equiv \hat{x}_{\text{tot}} + \hat{x}_{\text{imp}}$, is characterised by a (symmetrised, double-sided ^{4.2}) noise spectrum (see section 2.1),

$$\bar{S}_{yy}(\Omega) = \bar{S}_{xx}^{\text{imp}}(\Omega) + \bar{S}_{xx}^{\text{tot}}(\Omega) + 2\text{Re} \bar{S}_{x_{\text{BA}}x_{\text{imp}}}(\Omega), \quad (4.2.1)$$

which contains terms due to quantum fluctuations of the meter (x_{imp}), total physical motion (x_{tot}), and quantum (imprecision-back-action) correlations, respectively.

In our experiment we monitor the position fluctuations of a cryogenically pre-cooled ($T \approx 6$ K) nanomechanical string coupled dispersively to an optical microcavity [167]. The fundamental mode of the string forms the oscillator (frequency $\Omega_m = 2\pi \cdot 4.3$ MHz, damping rate $\Gamma_m = 2\pi \cdot 7$ Hz). The meter is a laser field passing resonantly through the cavity (wavelength, $\lambda \approx 774$ nm), whose quadratures are monitored simultaneously by a homodyne and a heterodyne detector (fig. 4.3a). The homodyne detector monitors the phase shift of the meter field, which is proportional to $(g_0/\kappa)(x/x_{\text{zp}})$, where $g_0 = 2\pi \cdot 20$ kHz is the cavity frequency shift produced by zero-point displacement $x_{\text{zp}} = \sqrt{\hbar/(2m\Omega_m)}$ of the oscillator (with effective mass $m \approx 2$ pg) and $\kappa = 2\pi \cdot 0.8$ GHz is the cavity decay rate. The heterodyne detector monitors both quadratures of the meter simultaneously (see section 2.2.2.4 for details), giving access to $\bar{S}_{yy}^{\text{het}}(\Omega > 0)$, where $\bar{S}_{yy}^{\text{het}}(\Omega_{\text{IF}} \pm \Omega_m)$ correspond to upper (+) and lower (−) motional sidebands (displaced by the heterodyne intermediate frequency, Ω_{IF}).

Quantum correlations between the phase and amplitude of the meter manifest as optical squeezing at the homodyne detector, or an asymmetry of the heterodyne motional sidebands (see section 4.1). This can be understood from the three terms in eq. (4.2.1), illustrated for example as components of the heterodyne signal in fig. 4.3b (top right panel). Detector imprecision (gray) – arising from the vacuum fluctuations in the phase and amplitude quadrature of the probe – contributes a phonon-equivalent noise of $n_{\text{imp}}^{\text{het}} \equiv \bar{S}_{yy}^{\text{het,imp}}(\Omega_{\text{IF}} \pm \Omega_m) / \bar{S}_{xx}^{\text{ZP}}(\Omega_m)$.

^{4.2}Here, heterodyne spectra are expressed as double-sided symmetrised spectra, for example \bar{S}_{yy} , while homodyne spectra are expressed as the corresponding single-sided symmetrised versions, for example \bar{S}_y

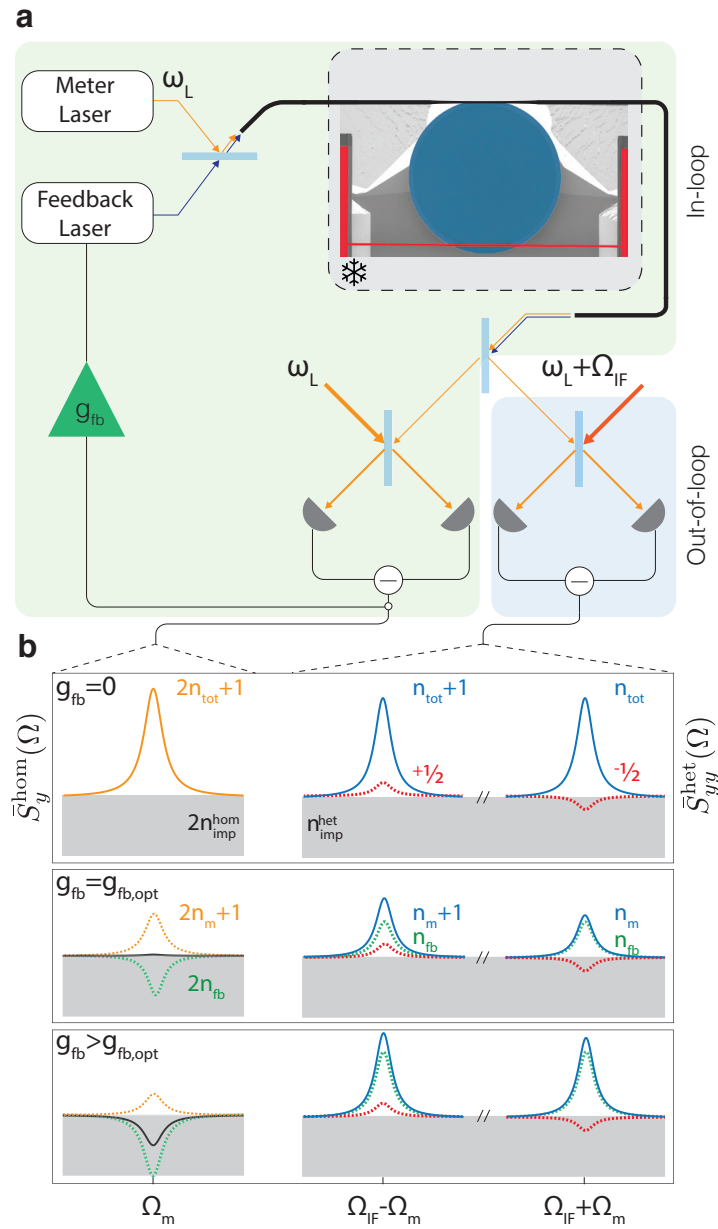


Fig. 4.3 – Using homodyne feedback to increase the visibility of quantum-correlation-induced motional sideband asymmetry. (a) Linear position measurement and feedback control of a nanomechanical string (Si₃N₄, red) is provided by evanescent coupling to an optical microdisk cavity (SiO₂, blue). Whispering gallery modes of the microdisk are driven by a pair of tunable diode lasers using a tapered optical fiber (black). The ‘meter’ field (orange) is directed to a pair of balanced interferometers (homodyne, green; heterodyne, blue). A delayed and an amplified copy of the homodyne signal is imprinted onto the amplitude of the ‘feedback’ field (blue), effecting cold damping of the fundamental beam mode. Taper, nanobeam, and microdisk are integrated into a He cryostat (grey). (b) Schematic of the closed-loop homodyne (left) and heterodyne (right) noise spectrum for various feedback gains. Contributions from measurement imprecision, physical motion, and imprecision-back-action correlations are delineated by colour.

Physical motion – arising from a combination of thermal force and meter back-action – contributes $n_m + \frac{1}{2}$ phonons to each sideband. Imprecision-back-action correlations – arising from

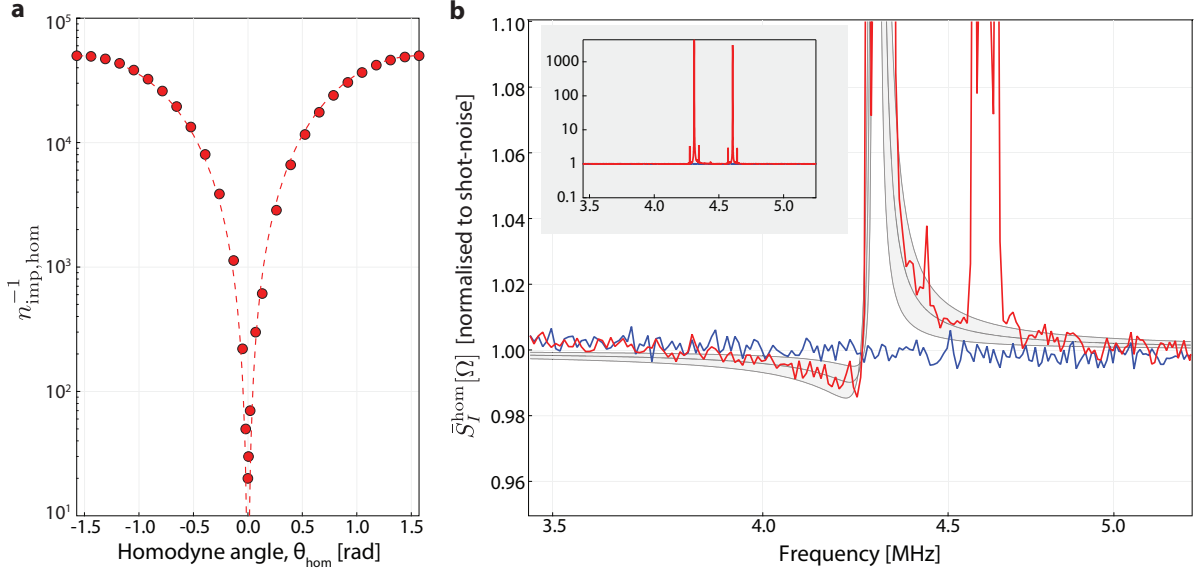


Fig. 4.4 – **Ponderomotive squeezing.** (a) Signal-to-noise ratio of the homodyne detected thermomechanical signal, quoted as an inverse imprecision quanta. Near the phase quadrature ($\theta_{\text{hom}} = \pm\pi/2$), sensitivity to thermal motion is best; near the amplitude quadrature ($\theta_{\text{hom}} \approx 0$), where squeezing is expected, thermal motion is suppressed by about 30 dB. (b) Squeezing spectrum probed using a homodyne detector. Red shows the homodyne photocurrent spectrum of the transmitted meter field, normalised to shot noise (blue trace), recorded at $\theta_{\text{hom}} \approx 0.15$ rad. Gray bands show the model in eq. (4.1.7), incorporating uncertainties in system parameters. Inset shows zoom-out of the frequency landscape around the mechanical mode.

amplitude-phase correlations in the meter – contribute $\pm\frac{1}{2}$ phonons to the lower/upper sideband (red dashed) (see section 4.1), where $\bar{S}_{xx}^{\text{zfp}}[\Omega_m] = \frac{4x_{\text{zfp}}^2}{\Gamma_m}$ is the zero-point position spectral density on resonance. The resulting asymmetry of the sidebands (blue traces),

$$R \equiv \frac{\bar{S}_{yy}^{\text{het}}(\Omega_{\text{het}}^+) - \bar{S}_{yy}^{\text{het,imp}}(\Omega_{\text{het}}^+)}{\bar{S}_{yy}^{\text{het}}(\Omega_{\text{het}}^-) - \bar{S}_{yy}^{\text{het,imp}}(\Omega_{\text{het}}^-)} \approx \frac{n_m}{n_m + 1}, \quad (4.2.2)$$

is commensurate with one phonon and arises purely from quantum correlations in the meter (here $\Omega_{\text{het}}^{\pm} \equiv \Omega_{\text{IF}} \pm \Omega_m$). This asymmetry corresponds directly to the visibility of imprecision-back-action correlations with respect to the total noise power, i.e.,

$$\zeta \equiv \frac{2\text{Re} \bar{S}_{x_{\text{ba}}x_{\text{imp}}}(\Omega_{\text{het}}^+)}{\bar{S}_{xx}^{\text{imp}}(\Omega_{\text{het}}^+) + S_{xx}^{\text{tot}}(\Omega_{\text{het}}^+)} \approx \frac{1 - R}{1 + R} = \frac{1}{2n_m + 1}. \quad (4.2.3)$$

In order to verify the presence of these quantum correlations in the meter field, we first direct the meter to the homodyne detector whose phase is stabilised close to the amplitude quadrature ($\theta_{\text{hom}} \approx 0.15$ rad). Figure 4.4 shows the resulting homodyne photocurrent spectrum, showing optical squeezing at the level of $\approx 1.5\%$, arising from imprecision-back-action correlations in the homodyne detector. Squeezing due to the radiation pressure interaction, recently been observed in other experiments [302, 324, 325], is a canonical indicator of both the intrinsic quantum correlations present in the meter field, and the quantum-limited detection capability of the experiment.

Our objective however, is to increase the sideband asymmetry $1 - R$ in the heterodyne spectrum, and thereby ζ , by actively cold damping the mechanical oscillator using the homodyne measurement as an error signal (as described in chapter 3). Concretely, the homodyne signal is imprinted onto the amplitude quadrature of an independent *feedback* laser resonant with an auxiliary cavity mode ($\lambda \approx 840$ nm). The loop delay is tuned in order to produce a purely viscous radiation pressure feedback force, effectively coupling the oscillator at a rate $\Gamma_{\text{fb}} \approx g_{\text{fb}}\Gamma_{\text{m}}$ to a cold bath with an occupation equal to the phonon-equivalent homodyne imprecision $n_{\text{imp}}^{\text{hom}} = \bar{S}_x^{\text{imp,hom}}(\Omega_{\text{m}})/2\bar{S}_x^{\text{ZP}}[\Omega_{\text{m}}]$ (here g_{fb} is the dimensionless gain of the feedback loop). The occupation of the oscillator is thereby reduced to,

$$n_{\text{m}} + \frac{1}{2} \approx \frac{n_{\text{tot}}}{g_{\text{fb}}} + g_{\text{fb}}n_{\text{imp}}^{\text{hom}} \geq 2\sqrt{n_{\text{tot}}n_{\text{imp}}^{\text{hom}}}, \quad (4.2.4)$$

with the minimum achieved at an optimal gain of $g_{\text{fb}}^{\text{opt}} = \sqrt{n_{\text{tot}}/n_{\text{imp}}^{\text{hom}}}$. (Here, $n_{\text{tot}} = n_{\text{th}} + n_{\text{ba}}$ is the effective bath occupation of the mechanical oscillator, including measurement back-action.) Notably, cold-damping allows access to $n_{\text{m}} \rightarrow 0$ when a highly efficient measurement is used, corresponding to an imprecision-back-action product approaching the uncertainty limit $2\sqrt{n_{\text{tot}}n_{\text{imp}}^{\text{hom}}} \rightarrow \frac{1}{2}$. Two regimes may be identified: (1) an *efficient* feedback regime ($g_{\text{fb}} < g_{\text{fb}}^{\text{opt}}$), in which the motion of the oscillator – resulting from the thermal noise and measurement back action – is efficiently suppressed; (2) an *inefficient* feedback regime, in which thermal force and measurement back-action are overwhelmed by *feedback back-action* $n_{\text{fb}} = g_{\text{fb}}^2 n_{\text{imp}}^{\text{hom}}$ (i.e. feedback of homodyne imprecision noise), resulting in an increase of n_{m} . We explore these regimes in two experiments.

An experimental demonstration of efficient feedback cooling, where feedback back-action is weak ($n_{\text{fb}} < n_{\text{tot}}$), is shown in fig. 4.5. Here $n_{\text{tot}} \approx 7 \cdot 10^4$, corresponding to an effective bath temperature of 13 K (arising partly due to photo-absorption, $n_{\text{ba}} \approx 4 \cdot 10^4$ [53]). From the perspective of the heterodyne measurement, the objective is to ‘distill’ a motional sideband asymmetry of one phonon out of n_{tot} . This is made possible by a low shot-noise-limited homodyne imprecision of $n_{\text{imp}}^{\text{hom}} \approx 1.2 \cdot 10^{-4}$. To trace out the cooling curve in fig. 4.5, the feedback gain is tuned electronically while keeping all other experimental parameters (such as mean optical power and laser-cavity detuning) fixed. Sideband ratio R is extracted from fitting a Lorentzian to each heterodyne sideband and taking the ratio of the fitted areas. The phonon occupation n_{m} is inferred from R as well as the area beneath the lower sideband. In-loop (homodyne) and out-of-loop (heterodyne) noise spectra are shown in fig. 4.5. As a characteristic of the efficient feedback regime, the area under the left sideband decreases linearly with g_{fb} , corresponding to $n_{\text{m}} \propto g_{\text{fb}}^{-1}$ (red circles in fig. 4.5). As the optimal gain is approached, the in-loop spectrum is reduced to the imprecision noise floor (black trace in fig. 4.5). This transition coincides with the ‘appearance’ of a sideband asymmetry of $1 - R \approx 12\%$ ($\zeta \approx 6\%$), corresponding to $n_{\text{m}} \approx 7.3$.

To confirm the faithfulness of these measurements, two major sources of error were investigated:

(1) Drift over the course of measurement can introduce small changes in the relative magnitude of $\bar{S}_{yy}^{\text{het}}[\Omega_{\text{het}}^{\pm}]$. In our experiment, this effect is mitigated by recording both heterodyne sidebands simultaneously. Augmented by operating in the bad cavity regime

4. QUANTUM CORRELATIONS IN MEASUREMENT-BASED CONTROL

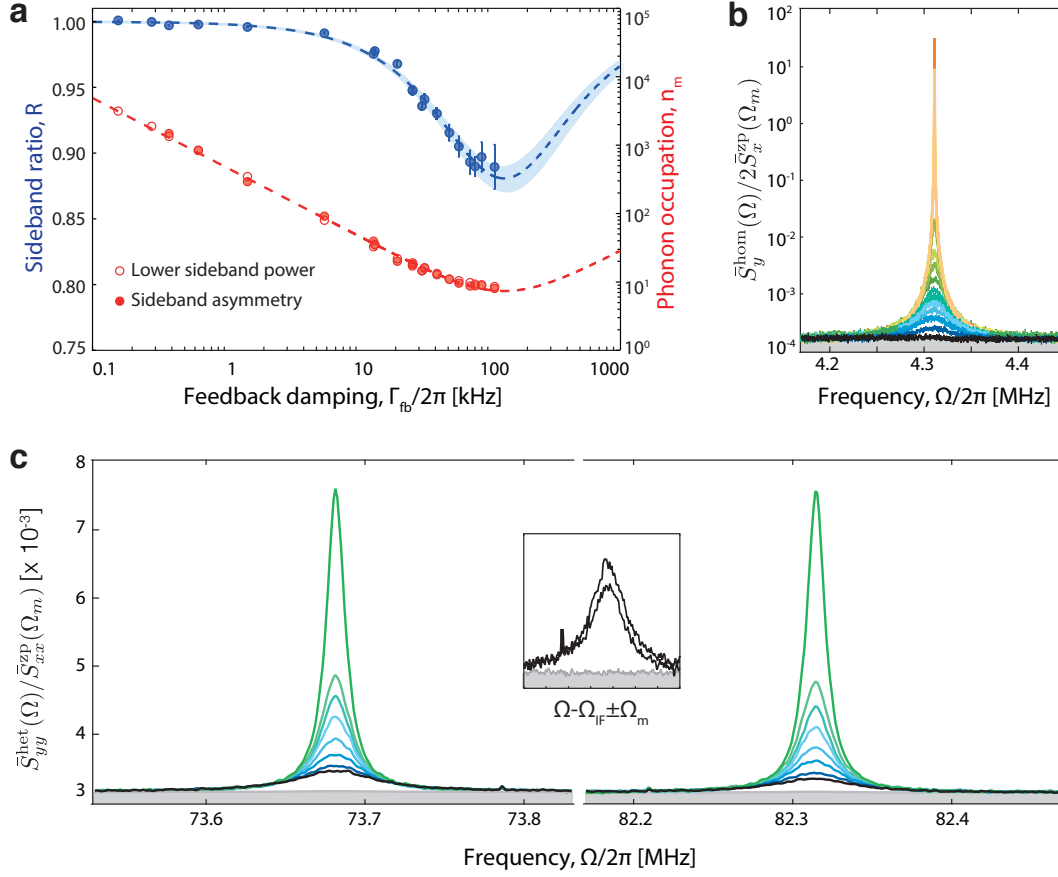


Fig. 4.5 – **Motional sideband asymmetry in the regime of efficient feedback.** (a) Heterodyne sideband asymmetry (R , blue) and inferred mechanical mode occupation (n_m , red) versus closed-loop mechanical damping rate (Γ_{fb}) for various feedback gains. A maximum asymmetry of $1 - R \approx 12\%$ ($n_m \approx 7.3$) appears as the feedback gain approaches its optimal value. Dashed lines correspond to models $R = \frac{n_m}{n_m+1}$ (eq. (4.2.2), blue line) and $n_m + \frac{1}{2} \approx \frac{\Gamma_m}{\Gamma_{fb}} n_{\text{tot}} + \frac{\Gamma_{fb}}{\Gamma_m} n_{\text{imp}}^{\text{hom}}$ (eq. (4.2.4), red line). Solid blue band is a confidence interval based on uncertainties in estimates of n_{tot} , $n_{\text{imp}}^{\text{hom}}$, and Γ_m . Open red circles are independent estimates of n_m based on the area beneath the left heterodyne sideband. (b,c) Homodyne (b) and heterodyne (c) spectra used to obtain (a). Black traces correspond to lowest occupation; asymmetry is highlighted in the inset. Only a subset of heterodyne spectra are shown, for low n_m , with colours matching the corresponding homodyne spectra. An important feature of these spectra are their low imprecision, $n_{\text{imp}}^{\text{hom}} = (16\eta_{\text{hom}} C_0 n_c)^{-1} = 1.2 \cdot 10^{-4}$ and $n_{\text{imp}}^{\text{het}} = (4\eta_{\text{het}} C_0 n_c)^{-1} = 2.9 \cdot 10^{-3}$. This is made possible by the high photon collection efficiency $\eta \sim 0.2$, single photon cooperativity $C_0 = 4g_0^2/\kappa\Gamma_m = 0.3$, and power handling capacity of the microcavity-based sensor (allowing for intracavity photon numbers of $n_c \sim 10^4$).

($\Omega_m/\kappa \sim 10^{-3}$), and the exceptionally low imprecision of the heterodyne measurement, $n_{\text{imp}}^{\text{het}} = (4\eta_{\text{het}} C_0 n_c)^{-1} \approx 3 \cdot 10^{-3}$ (see fig. 4.6a), statistical fluctuations of R over the course of a typical measurement set can be as small as 0.5% (see fig. 4.5c). Error bars for R in fig. 4.5a are derived from the standard deviation of similar data sets (shown in fig. 4.6c), in addition to a small contribution from the fit covariance matrix. At the largest damping rates, the reduced heterodyne signal-to-noise results in insufficient convergence of the periodogram estimate of the spectra (keeping acquisition time and analysis bandwidth fixed), leading to larger error bars, $\delta R = \pm 2\%$.

(2) Excess laser noise affects R by producing additional imprecision-back-action correlations

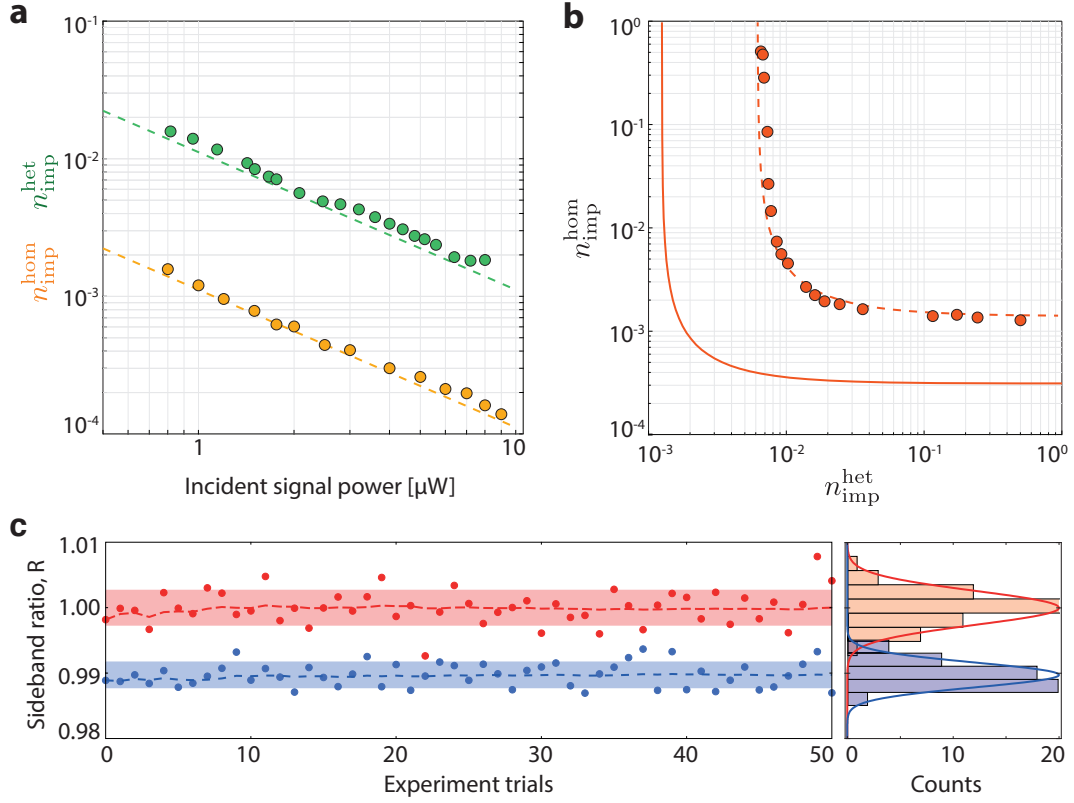


Fig. 4.6 – **Experimental sensitivity and precision.** (a) Deep sub-SQL measurement sensitivity in both the in-loop (homodyne) detector and the out-of-loop (heterodyne) detector. The dashed lines show expected behaviour for quantum-limited detection. (b) Plot shows sensitivity tradeoff between the in-loop and out-of-loop detector; the relative sensitivity is changed by using a waveplate and a polarizing beam-splitter to distribute the signal between the two detectors. The solid line shows expected model for unit detection efficiency; dashed line corresponds to realistic efficiencies of $\eta_{\text{hom}} \approx 20\%$ and $\eta_{\text{het}} \approx 15\%$. (c) Statistical fluctuations of R for low feedback gain, indicating the ability to discriminate a 0.5% asymmetry, corresponding to $n_{\text{m}} \approx 100$.

as discussed in section 4.1.2. Assuming a mean thermal photon occupation of $C_{qq(pp)}$ for the amplitude (phase) quadrature of the injected meter field, the correlator in eq. (4.2.1) becomes (see eq. (4.2.2)),

$$\frac{2\text{Re} \bar{S}_{x_{\text{ba}}x_{\text{imp}}}^{\text{het}}[\Omega_{\text{het}}^{\pm}]}{\bar{S}_{xx}^{\text{ZP}}[\Omega_{\text{m}}]} = \mp \eta_{\text{het}} \left(\frac{1}{2} + C_{qq} \pm \frac{4\bar{\Delta}\Omega_{\text{m}}}{\kappa^2} C_{pp} \right), \quad (4.2.5)$$

where η_{het} is the heterodyne detection efficiency, and $\bar{\Delta}$ is the mean laser-cavity detuning. In our experiment, independent measurements reveal that $C_{qq} < 0.01$ and $C_{pp} < 30$ (owing partly to excess cavity frequency noise) for typical meter powers of $P_{\text{in}} < 5 \mu\text{W}$. Operating on resonance ($\bar{\Delta} \approx 0$) and in the bad-cavity regime substantially reduces sensitivity to C_{pp} . Using a typical value of $\bar{\Delta} = 0.01 \cdot \kappa$, we estimate that $\frac{4\bar{\Delta}\Omega_{\text{m}}}{\kappa^2} C_{pp} < 0.005$ negligibly to eq. (4.2.5).

Having established that our measurements of motional sideband asymmetry are not contaminated by classical artefacts, the results shown in fig. 4.5 may be interpreted as a ‘distillation’ of quantum correlations using efficient feedback. We now explore the complementary regime of inefficient feedback, where feedback back-action is stronger than the thermal force and measurement back-action ($n_{\text{fb}} > n_{\text{tot}}$). We access this regime by changing the homo-

4. QUANTUM CORRELATIONS IN MEASUREMENT-BASED CONTROL

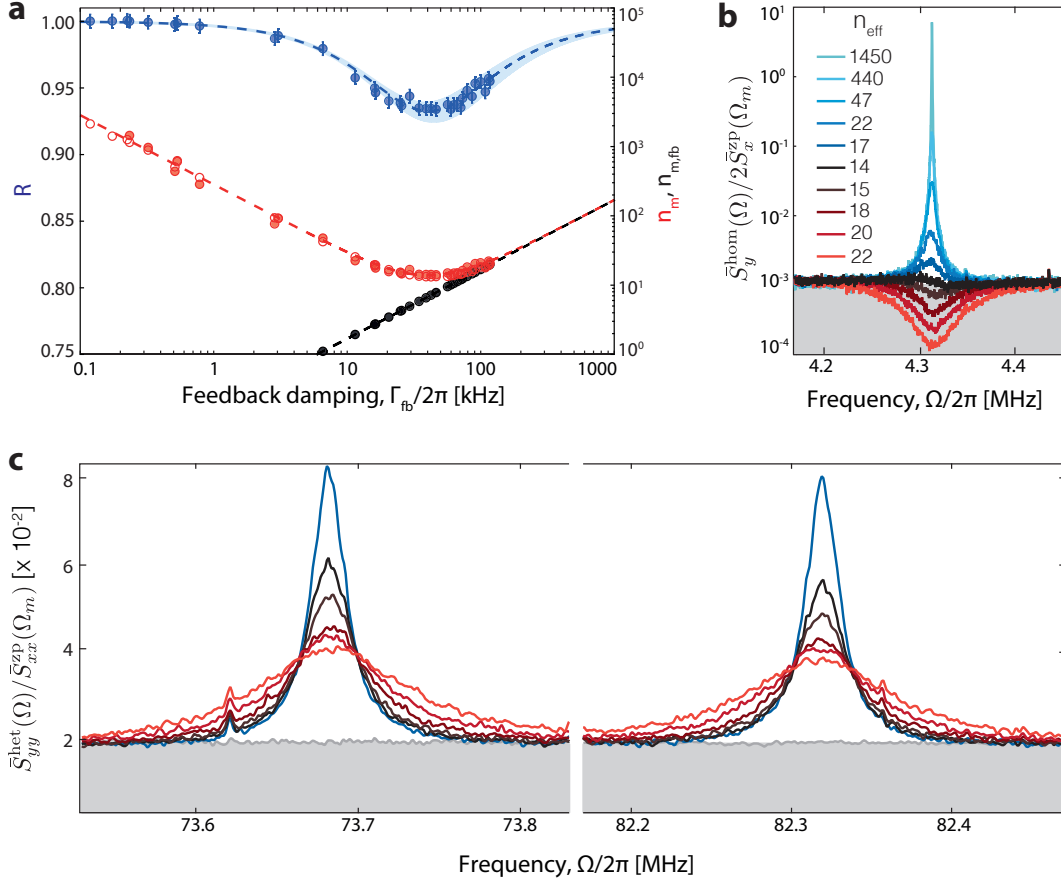


Fig. 4.7 – **Appearance and disappearance of sideband asymmetry.** (a) Repeat of the experiment shown in fig. 4.5 with lower homodyne detection efficiency. Feedback with the same range of gain results in lower asymmetry ($R \approx 6\%$) and access to the ‘strong feedback’ regime in which feedback back-action (n_{fb}) dominates physical motion, resulting in reduced R . Black points are an estimate of the mechanical occupation due to feedback back-action, $n_{m,fb} = \frac{\Gamma_m}{\Gamma_{fb}} n_{fb} = g_{fb} n_{\text{imp}}^{\text{hom}}$, based on the noise floor of the homodyne spectra. (b) In-loop homodyne spectra. In the strong feedback regime, noise is ‘squashed’ (reduced below the open-loop imprecision), corresponding to in-loop squeezing. (c) Out-of-loop heterodyne spectra. Inefficient feedback manifests as an increase in the off-resonant noise power and reduced asymmetry.

dyne/heterodyne splitting ratio, thereby increasing the homodyne imprecision to $n_{\text{imp}}^{\text{hom}} \approx 10^{-3}$. As shown in fig. 4.7, increasing the gain beyond its optimum value (corresponding to $n_m \approx 13.4$ and $1 - R \approx 7\%$), results in a reduction of the homodyne signal below the shot-noise level (fig. 4.7b left panel). Simultaneously, the areas of the heterodyne sidebands increase, while their asymmetry ($1 - R$) decreases. The discrepancy between ‘squashing’ [326, 327] of the in-loop signal and the ‘disappearance’ of sideband asymmetry relates to a basic difference between feedback back-action and meter back-action, namely, feedback back-action is correlated with the in-loop imprecision and not with the out-of-loop imprecision [326].

Squashing of the in-loop signal is caused by correlations between the feedback back-action driven motion x_{fb} and the in-loop measurement imprecision,

$$\frac{2\text{Re}\bar{S}_{x_{fb}x_{\text{imp}}}^{\text{hom}}[\Omega_m]}{2\bar{S}_{xx}^{\text{ZP}}[\Omega_m]} = -n_{\text{imp}}^{\text{hom}} g_{fb}. \quad (4.2.6)$$

represented by the negative-valued green trace in fig. 4.3b (left panel). Interestingly, these classical correlations, in conjunction with the generalised Heisenberg uncertainty principle [62, 69] can be used to predict the transition from efficient to inefficient feedback; viz.

$$\bar{S}_{FF} \cdot \bar{S}_{xx}^{\text{imp,hom}} \geq \frac{\hbar^2}{2} + (2\text{Re} \bar{S}_{Fx_{\text{imp,hom}}})^2, \quad (4.2.7)$$

is saturated for $g_{\text{fb}}^{\text{opt}} = \sqrt{n_{\text{tot}}/n_{\text{imp}}^{\text{hom}}}$ (using $F_{\text{fb}} \propto g_{\text{fb}}x_{\text{imp}}^{\text{hom}}$ and eq. (4.2.6)). The limits of feedback cooling, and the prospects for feedback-based enhancement of quantum correlations, is related to the detection of meter fluctuations and the choice of feedback strategy – optimisation of either seems pertinent (see chapter 5 for some ideas).

4.3 Conclusion

The experiments reported in this chapter probe several distinct and unique features of quantum measurements and feedback. Firstly, quantum correlations between the phase and amplitude of the meter field is shown to manifest in one of two different fashions – optical squeezing, or sideband asymmetry – depending on the nature of the detection process. Both these manifestations are observed using a quantum-noise-limited interferometer operating with an imprecision deeply below the standard quantum limit. Secondly, building on the capability of quantum feedback reported in chapter 3, feedback is used to distil quantum correlations without destroying them. Feedback control of a mechanical oscillator thus joins the exclusive collective of a handful of platforms where manipulation of non-classical resources using feedback has been demonstrated [266, 328–330]. Finally, the fundamental limit of linear feedback control is elucidated: feedback, though capable of suppressing in-loop measurement back-action, is limited by quantum fluctuations amplified by the in-loop detector.

5 Epilogue

*It's a magical world Hobbes ol' buddy...
...let's go exploring!*

BILL WATTERSON, Calvin and Hobbes

The work reported in this thesis broaches a qualitatively new regime of cavity optomechanics, one where the effects of quantum measurement back-action become comparable to the intrinsic motion of the mechanical oscillator^{5.1}. We have accessed this regime by making a measurement of the mechanical oscillator's position fluctuations with an imprecision 40 dB below that at the standard quantum limit, so that the concomitant back-action is in excess of the intrinsic motion [53]. We have demonstrated that being in this regime through an efficient measurement (i.e. saturating the Heisenberg uncertainty principle), offers the possibility of performing measurement-based feedback of the oscillator's state. This may be interpreted as a heuristic principle of information economy – if the state of the oscillator, including random back-action, can be measured with high fidelity, then that measurement record is informationally complete with respect to the state of the oscillator [265]. Once this is true, the record may be used to perform feedback on the oscillator state. We have demonstrated this capability by cooling the oscillator over four orders of magnitude in temperature, resulting in a final average phonon occupation of 5.

A salient feature of being in the measurement back-action dominated regime is that it allows the study of the subtle nature of quantum measurements. In this thesis, we investigate correlations that arise due to the measurement and its relation to measurement-base feedback [54]. In particular, correlations between the amplitude and phase quadratures of the meter beam can be distilled using measurement-based feedback to suppress classical contamination. We also demonstrate the fundamental limitations of this technique, which arise from measurement noise in the detection of the meter state.

5.1 Some future directions

These studies open doors to newer and richer possibilities for the immediate future. On the feedback front, the question of how to optimally treat the measurement record before feeding back, is of prime importance. Section 5.1.1 addresses this problem; the simple filter used in chapters 3 and 4 can in fact be bettered using an optimal filter, at the expense of

^{5.1} This regime has now been accessed in at least one other experiment [295], where a $\Omega_m = 2\pi \cdot 9.3$ MHz mechanical oscillator is measured using a microwave cavity interferometer operated at ≈ 100 mK.

robustness to perturbations in open-loop gain. The other question relates to correlations in linear measurements studied in chapter 4: since the correlations between the amplitude and phase of the meter beam lead to ponderomotive squeezing, one could enquire whether these non-classical effects could be used for enhanced measurement precision. This possibility of quantum-enhanced metrology [331] using quantum correlations developed in-situ during the optomechanical interaction is briefly discussed in section 5.1.2. During the writing of this thesis, quantum-enhanced metrology of this kind has been demonstrated using an optomechanical system at cryogenic temperature [332], and at room temperature (in our group) [333].

5.1.1 Optimal feedback

In the cooling of mechanical oscillator, particularly using measurement-based feedback as in chapter 3, we are interested in minimising the mean phonon occupancy of the oscillator, viz.

$$\min_{\chi_{\text{fb}}} (2n_{\text{m,th}} + 1) = \min_{\chi_{\text{fb}}} \sqrt{\left\langle \frac{\hat{x}^2}{x_{\text{zp}}^2} \right\rangle \left\langle \frac{\hat{p}^2}{p_{\text{zp}}^2} \right\rangle - \left\langle \frac{\hat{x}\hat{p} + \hat{p}\hat{x}}{2x_{\text{zp}}p_{\text{zp}}} \right\rangle},$$

where $x_{\text{zp}}^2 = \frac{\hbar}{2m\Omega_{\text{m}}}$, $x_{\text{zp}}p_{\text{zp}} = \frac{\hbar}{2}$, and, χ_{fb} is a feedback filter. For a thermal state, the constraint reduces to

$$\min_{\chi_{\text{fb}}} \frac{\langle \hat{x}^2 \rangle}{x_{\text{zp}}^2}. \quad (5.1.1)$$

Combined with the linear equation of motion, $\hat{x}[\Omega] = \chi_x[\Omega] \hat{F}_{\text{th}}[\Omega]$, this optimisation problem is an archetype of the *linear quadratic gaussian* (LQG) paradigm of classical control theory [271, 334, 335]. Recently, such problems have been formalised and studied in the quantum mechanical context [336, 337].

In terms of the spectral density, \bar{S}_{xx} , of the physical motion, the constraint in eq. (5.1.1) takes the form,

$$\min_{\chi_{\text{fb}}} \int_{-\infty}^{\infty} \bar{S}_{xx}[\Omega] \frac{d\Omega}{2\pi}, \quad (5.1.2)$$

where, in the presence of feedback (see eq. (3.1.10)),

$$\bar{S}_{xx}[\Omega] = |\chi_{\text{eff}}|^2 \left(\bar{S}_{FF}^{\text{tot}}[\Omega] + |\chi_{\text{fb}}|^{-2} \bar{S}_{xx}^{\text{imp}}[\Omega] \right), \quad (5.1.3)$$

and, $\chi_{\text{eff}}^{-1} = \chi_x^{-1} + \chi_{\text{fb}}^{-1}$ is the effective susceptibility in the presence of feedback. Directly minimising the cost function over the functional form of the feedback filter gives the optimal filter, viz.,

$$\chi_{\text{fb,opt}}[\Omega] = \chi_x^{-1}[\Omega] \frac{\bar{S}_{xx}^{\text{imp}}[\Omega]}{\bar{S}_{FF}^{\text{tot}}[\Omega]}, \quad (5.1.4)$$

for the general case of a stationary imprecision and thermal force. When the imprecision and total force noise are white, as for example when the former is quantum-limited and the latter is due to a Markovian bath, they may be conveniently parametrised in terms of effective occupation quanta n_{imp} and n_{tot} (as defined in eqs. (3.1.8) and (3.1.9)), so that,

$$\chi_{\text{fb,opt}}[\Omega] = \frac{n_{\text{imp}}}{n_{\text{tot}}} \chi_x^*[\Omega]. \quad (5.1.5)$$

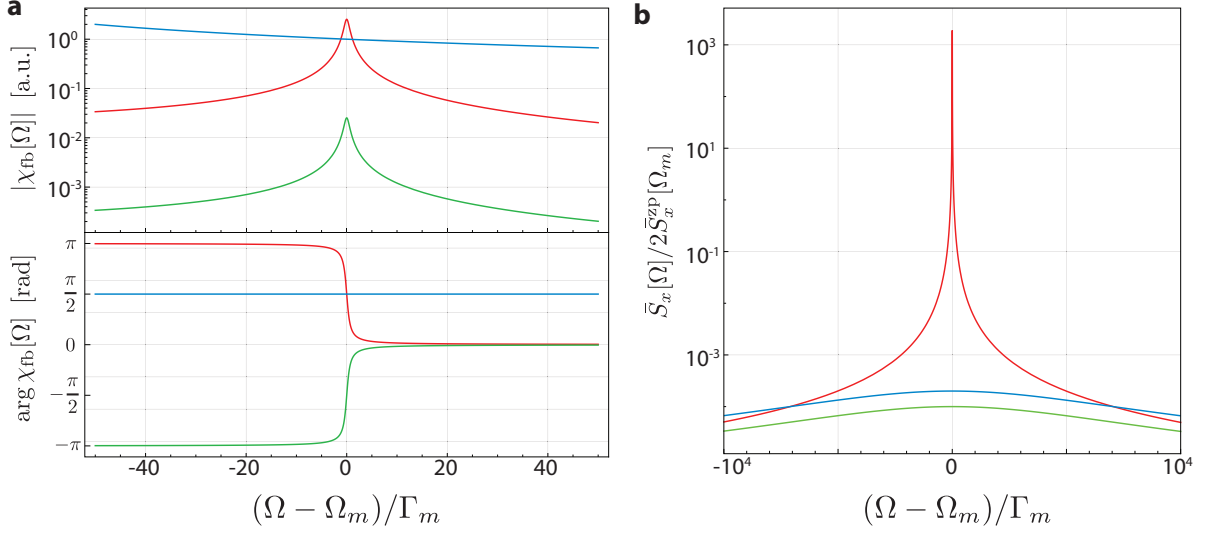


Fig. 5.1 – **Optimal feedback filter.** (a) Top (bottom) shows the magnitude (phase) of the various susceptibilities. Red is the intrinsic mechanical susceptibility χ_x , while blue is the susceptibility of the cold-damping filter $\chi_{fb,cold}^{-1} \propto -ig_{fb}\Omega\Gamma_m$, and green is the susceptibility of the optimal feedback filter $\chi_{fb,opt}$. (b) Spectrum of the physical position of the oscillator for the three cases: red, corresponding to the intrinsic thermal motion, blue corresponding to the coldest case realised by cold-damping, green corresponding to the optimal filter. The optimal filter outperforms the cold-damping filter by a factor of 2.

The optimal feedback filter is therefore the one that exactly replicates the oscillator susceptibility, but with an inverted phase. Figure 5.1a compares this with the conventional cold-damping filter, $\chi_{fb,cold}^{-1} \propto -ig_{fb}\Omega\Gamma_m$, used in the experiments reported in chapter 3.

For given measurement imprecision, n_{imp} , it can be verified that the optimal filter in eq. (5.1.5) realises a physical displacement noise spectral density that is a factor 2 smaller than that realised using the cold-damping strategy. Figure 5.1b depicts this result for a representative set of parameters. However, in the case of the optimal filter, when $\bar{S}_{xx}[\Omega] \ll 2\bar{S}_{xx}^{zp}[\Omega_m]$, the resulting spectrum can no longer be associated with an oscillator in a thermal state, and so care must be enforced when interpreting the result in terms of an average thermal occupation.

In order to understand the improvement offered by the optimal filter, it is useful to treat the role of feedback as being the suppression of the total intrinsic physical motion, $\bar{S}_{xx}^{(0)}$; the superscript indicates the value of the (frequency-independent, complex) feedback gain g_{fb} , which for either strategy is operationally defined as the gain applied to the measurement record before it is processed by the feedback filter, i.e. $\chi_{fb}^{-1} \propto g_{fb}$. Rewriting eq. (5.1.3) using the relation $\bar{S}_{FF}^{tot} = |\chi_x|^{-2} \bar{S}_{xx}^{(0)}$, the physical spectrum for a finite feedback gain is given by,

$$\bar{S}_{xx}^{(g_{fb})}[\Omega] = \left| 1 + \frac{\chi_{fb}^{-1}[\Omega]}{\chi_x^{-1}[\Omega]} \right|^{-2} \bar{S}_{xx}^{(0)}[\Omega] + \left| 1 + \frac{\chi_x^{-1}[\Omega]}{\chi_{fb}^{-1}[\Omega]} \right|^{-2} \bar{S}_{xx}^{imp}[\Omega]. \quad (5.1.6)$$

For both cold-damping and the optimal filter, on resonance, $\chi_{fb}^{-1}[\Omega_m]/\chi_x^{-1}[\Omega_m] = g_{fb}$, where g_{fb} is the feedback gain. However, in the case of cold-damping, added noise due to feedback back-action off resonance precludes the realisation of the gain, $g_{fb} = n_{tot}/n_{imp}$, that is required

by the optimal filter. By shaping the loop response, the optimal strategy succeeds in completely suppressing the intrinsic thermal motion at all frequencies.

5.1.2 Quantum-enhanced metrology

A characteristic feature of linear measurements is that they produce quantum correlations in the meter. As described in chapter 4, for interferometric position measurements, they lead to quantum correlations between the amplitude and phase of the optical field used for the measurement. Homodyne detection of this field produces the (shot-noise normalised) photocurrent spectrum (eq. (4.1.7)),

$$\bar{S}_I^{\theta, \text{hom}}[\Omega] = 1 + \frac{4\eta C \Gamma_m}{x_{zp}^2} \left(\bar{S}_{xx}[\Omega] \sin^2 \theta + \frac{\hbar}{2} \text{Re} \chi_x^{(0)}[\Omega] \sin 2\theta \right), \quad (5.1.7)$$

consisting of the motion of the mechanical oscillator – optimally measured at phase quadrature ($\theta = \pi/2$) – and a contribution due to quantum correlations – absent in the phase quadrature.

The presence of correlations at other quadratures motivates the question of whether they can be employed for a better estimation of the intrinsic motion of the oscillator. The discussion in section 2.3 provides the answer in the specific case of phase quadrature detection – the SQL that arises therein is due to a trade-off between detector imprecision and measurement back-action. In the general setting to be treated here, we will show that quantum correlations can be used to cancel back-action in the measurement, allowing better estimation precision than that dictated by the SQL for phase quadrature detection.

To analyse this idea, we start from the observed photocurrent spectrum in eq. (5.1.7),

$$\bar{S}_I^{\theta, \text{hom}}[\Omega] = 1 + \frac{4\eta C \Gamma_m}{x_{zp}^2} \left(\left(\bar{S}_{xx}^{(0)}[\Omega] + \bar{S}_{xx}^{\text{BA}}[\Omega] \right) \sin^2 \theta + \frac{\hbar}{2} \text{Re} \chi_x^{(0)}[\Omega] \sin 2\theta \right),$$

where the total motion has been split into the intrinsic motion $\bar{S}_{xx}^{(0)}$, which is to be estimated, and the back-action motion (see eq. (2.3.5)),

$$\bar{S}_{xx}^{\text{BA}}[\Omega] = C \frac{\hbar^2 \Gamma_m}{x_{zp}^2} \left| \chi_x^{(0)}[\Omega] \right|^2.$$

Denoting by $\delta \hat{x}_{\text{est}, \theta}$ the unbiased estimator for the position based on the photocurrent record $\delta \hat{I}_\theta$, its spectrum is given by,

$$\bar{S}_{xx}^{\text{est}, \theta}[\Omega] = \frac{\bar{S}_I^{\theta, \text{hom}}[\Omega]}{(4\eta C \Gamma_m / x_{zp}^2) \sin^2 \theta} = \bar{S}_{xx}^{(0)}[\Omega] + \bar{S}_{xx}^{\text{BA}}[\Omega] + \bar{S}_{xx}^{\text{imp}, \theta}[\Omega] + \hbar \cot \theta \text{Re} \chi_x^{(0)}, \quad (5.1.8)$$

where the phase-dependent detection imprecision is given by,

$$\bar{S}_{xx}^{\text{imp}, \theta}[\Omega] = \frac{x_{zp}^2}{4\eta C \Gamma_m \sin^2 \theta} = \frac{\bar{S}_{xx}^{\text{imp}, \pi/2}[\Omega]}{\sin^2 \theta}.$$

In eq. (5.1.8), the objective of the estimation, the intrinsic motion $\bar{S}_{xx}^{(0)}$, is contaminated by three sources: measurement back-action, imprecision, and measurement-induced correlations. Both

back-action and imprecision, by being positive, increase the uncertainty in the estimate of the intrinsic position; however, there are frequency intervals where the correlation term can be negative, and thus can be used to reduce the uncertainty.

The uncertainty in the estimate is given by,

$$\epsilon_x(C, \theta) := \bar{S}_{xx}^{\text{est}, \theta}[\Omega] - \bar{S}_{xx}^{(0)}[\Omega] = \bar{S}_{xx}^{\text{BA}} + \frac{\bar{S}_{xx}^{\text{imp}, \pi/2}}{\sin^2 \theta} + \hbar \cot \theta \operatorname{Re} \chi_x^{(0)}$$

here, we make explicit that the uncertainty depends on the choice of measurement strength (i.e. cooperativity C) and detection angle (θ). For a fixed measurement strength, this uncertainty is minimised for a frequency-dependent detection angle,

$$\theta_{\text{opt}}[\Omega] = 4\eta C \frac{\Omega_m \Gamma_m (\Omega^2 - \Omega_m^2)}{(\Omega^2 - \Omega_m^2)^2 + (\Omega \Gamma_m)^2}$$

which coincides with the optimal angle for the measurement of ponderomotive squeezing given in eq. (4.1.8). At this optimal detection quadrature,

$$\epsilon_x(C, \theta_{\text{opt}}) = \bar{S}_{xx}^{\text{BA}}[\Omega] \left[1 - \eta \left(\operatorname{Re} \chi_x^{(0)} / |\chi_x^{(0)}| \right)^2 \right] + \bar{S}_{xx}^{\text{imp}, \pi/2}[\Omega] < \epsilon_x(C, \frac{\pi}{2}),$$

i.e. at every measurement strength (limited by the detection efficiency, and the technical challenge of realising a stable frequency-dependent detection angle), the ability to estimate the intrinsic motion is enhanced by the cancellation of back-action in the measurement record .

Further optimisation of measurement strength achieves the ultimate bound on the achievable estimation uncertainty. However, broadband enhancement across all Fourier frequencies is not possible [95, 338]; at desired frequency intervals, the minimum uncertainty, $\min_C \epsilon_x(C, \theta_{\text{opt}})$, satisfies,

$$\min_C \epsilon_x(C, \frac{\pi}{2}) \geq \min_C \epsilon_x(C, \theta_{\text{opt}}) = \left[1 - \eta \left(\operatorname{Re} \chi_x^{(0)} / |\chi_x^{(0)}| \right)^2 \right]^{1/2} \cdot \frac{\hbar}{\sqrt{\eta}} |\chi_x^{(0)}|$$

i.e. an uncertainty lower than what is predicted by the SQL for phase quadrature detection.

The ideas described above can be directly transposed to the problem of force estimation. In that context, proper choice of detection angle cancels the back-action force in the measurement record – a technique termed variational measurement [339] (further elucidated in [94, 95]).

Defining an uncertainty for the estimation of the thermal force,

$$\epsilon_F(C, \theta) := \left| \chi_x^{(0)} \right|^{-2} \epsilon_x(C, \theta),$$

it can be shown that [333], an enhancement due to quantum correlations is achieved for (frequency-independent) detection angles away from phase quadrature. Figure 5.2 show the enhancement achieved in a recent experiment where the system described in this thesis was deployed at room-temperature [333]. (That experiment was also the first to demonstrate quantum correlations developed due to a room-temperature mechanical oscillator, despite the large thermal decoherence rate.)

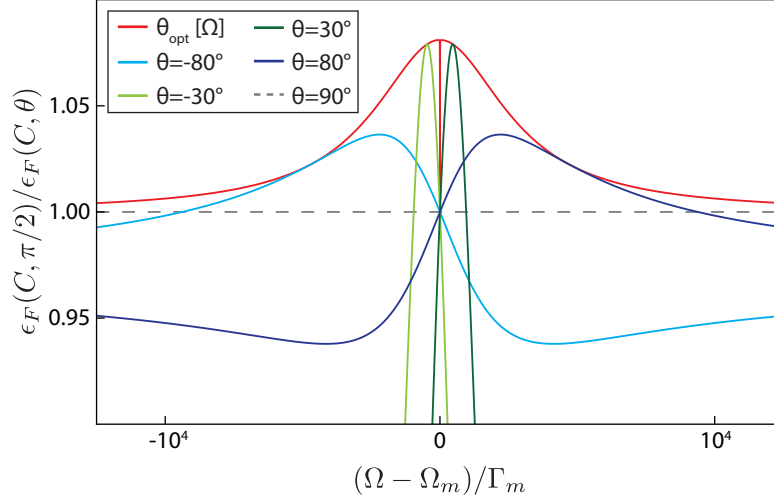


Fig. 5.2 – **Quantum-enhanced force metrology.** Plot shows the reduction in uncertainty in the estimation of thermal force, quoted as the enhancement over conventional phase quadrature detection. An enhancement of 7% was realised, limited by the detection efficiency.

Ultimately, these ideas (and experiments) illustrate a general perspective on quantum metrology. To date, the multitude of experiments that report quantum metrology, do so by following one of two strategies [340]:

- (a) the state of the meter is prepared in some non-classical state [341]; for example, squeezed states of light for interferometric position measurements [342, 343], “NOON” states for super-resolved optical phase measurements [344–346], entangled states of atoms/ions for spectroscopy [347, 348],
- (b) the system-meter coupling is engineered to achieve reduced back-action [92]; for example, by performing a non-demolition measurement [349–351], or measuring only a single quadrature of a mechanical oscillator [352].

A third strategy, that neither requires a priori non-classical states of the meter, or a precisely tuned system-meter interaction, is what has been described above. Such schemes rely on a cunning choice of meter-detector coupling so as to harness non-classical correlations that are developed in-situ during the act of measurement. Indeed, these optimal measurements, in addition to shedding light on the inner workings of quantum measurements, may be envisioned to provide quantum-enhanced record of a state’s trajectory for better feedback control.

A Uncertainty inequalities

For a set of observables $\{\hat{X}_i\}_{i=1,\dots,N}$ of a quantum mechanical system, the fact that their expectation values are determined by an underlying quantum state, determine a set of fundamental bounds to be satisfied by their outcome statistics.

The experiment where an identical quantum state of the system, $\hat{\rho}$, is independently prepared and any of the observables is measured once per preparation, determines a distribution of outcomes for each of the observables. Denoting by $x_i \in \mathbb{R}$ the continuous eigenvalues of the observable \hat{X}_i corresponding to the eigenstate $|x_i\rangle$, the probability distribution of the outcomes of \hat{X}_i is given by [14, 62, 72],

$$\Pr [x_i] = \text{Tr} [|x_i\rangle\langle x_i| \hat{\rho}]. \quad (\text{A.0.1})$$

Broadly, uncertainty relations are general statements that describe the constraints satisfied by the set of these probability distributions.

In the case of a large number of experimental trials, each of these distributions tend to a gaussian distribution, in which case, a convenient measure of measurement uncertainty is the deviation from the mean outcome, represented by the operators,

$$\delta \hat{X}_i := \hat{X}_i - \langle \hat{X}_i \rangle. \quad (\text{A.0.2})$$

The uncertainty in each observable may be characterized as the variance of the distribution,

$$\text{Var} [\hat{X}_i] := \langle \delta \hat{X}_i^2 \rangle, \quad (\text{A.0.3})$$

while the mutual correlations between the observables described by the covariance,

$$\text{Cov} [\hat{X}_i, \hat{X}_j] := \left\langle \frac{1}{2} \{ \delta \hat{X}_i, \delta \hat{X}_j \} \right\rangle, \quad (\text{A.0.4})$$

where the possible non-commutativity of observables necessitates the symmetrization. Note that, $\text{Var} [\hat{X}_i] = \text{Cov} [\hat{X}_i, \hat{X}_i]$. In a general setting, the observables may commute amongst themselves according to,

$$[\hat{X}_j, \hat{X}_k] = i \hat{C}_{jk}, \quad (\text{A.0.5})$$

where \hat{C}_{jk} are some operators encoding the commutation structure. Note that \hat{C}_{jk} are necessarily hermitian, and satisfy, $\hat{C}_{jk} = -\hat{C}_{kj}$.

Theorem 1 (Uncertainty principle). *In the setting described herein, the covariance matrix satisfies the matrix inequality,*

$$\text{Cov} [\hat{X}_j, \hat{X}_k] + \frac{i}{2} \langle \hat{C}_{jk} \rangle \geq 0. \quad (\text{A.0.6})$$

Proof. Note that a general operator, defined by,

$$\hat{M} := \sum_j \alpha_j \delta \hat{X}_j,$$

for some arbitrary complex numbers α_i , satisfies the identity $\hat{M}^\dagger \hat{M} \geq 0$. To see this, note that for any state $|\psi\rangle$,

$$\langle \psi | \hat{M}^\dagger \hat{M} | \psi \rangle = \|\hat{M}|\psi\rangle\|^2 \geq 0,$$

by the general property of norms in (well-defined) Hilbert spaces. In other words $\hat{M}^\dagger \hat{M}$ is a positive operator. By definition, any quantum state, $\hat{\rho}$, is also a positive operator; therefore the product, $\hat{M}^\dagger \hat{M} \hat{\rho}$, must be positive. In particular it follows that, $\text{Tr} [\hat{M}^\dagger \hat{M} \hat{\rho}] \geq 0$. Working out the trace explicitly,

$$\begin{aligned} \text{Tr} [\hat{M}^\dagger \hat{M} \hat{\rho}] &= \sum_{j,k} \alpha_j^* \alpha_k \text{Tr} [\delta \hat{X}_j \delta \hat{X}_k \hat{\rho}] \\ &= \sum_{j,k} \alpha_j^* \alpha_k \text{Tr} \left[\left(\frac{1}{2} \{ \delta \hat{X}_j, \delta \hat{X}_k \} + \frac{1}{2} [\delta \hat{X}_j, \delta \hat{X}_k] \right) \hat{\rho} \right] \\ &= \sum_{j,k} \alpha_j^* \alpha_k \left(\text{Cov} [\hat{X}_i, \hat{X}_j] + \frac{i}{2} \langle \hat{C}_{jk} \rangle \right) \\ &= \boldsymbol{\alpha}^H \mathbf{M} \boldsymbol{\alpha}, \end{aligned}$$

where, $\boldsymbol{\alpha} := [\alpha_1, \dots, \alpha_N]^T$, is the vector of the arbitrary complex numbers α_i , $\boldsymbol{\alpha}^H = (\alpha^*)^T$ is its hermitian conjugate, and \mathbf{M} is a complex matrix whose elements are given by,

$$M_{jk} := \text{Cov} [\hat{X}_i, \hat{X}_j] + \frac{i}{2} \langle \hat{C}_{jk} \rangle.$$

The identity $\text{Tr} [\hat{M}^\dagger \hat{M} \hat{\rho}] \geq 0$ implies that the quadratic form,

$$\boldsymbol{\alpha}^H \mathbf{M} \boldsymbol{\alpha} \geq 0, \quad \text{for any } \alpha_i.$$

This implies that the matrix \mathbf{M} must itself be positive, giving the desired result. \square

Corollary 1 (Robertson-Schrodinger [74, 75]). *For the case of two observables, \hat{X}_1, \hat{X}_2 ,*

$$\text{Var}[\hat{X}_1] \text{Var}[\hat{X}_2] \geq \frac{1}{4} |\langle \{ \delta \hat{X}_1, \delta \hat{X}_2 \} \rangle|^2 + \frac{1}{4} |\langle [\delta \hat{X}_1, \delta \hat{X}_2] \rangle|^2. \quad (\text{A.0.7})$$

Proof. The $N = 2$ case of eq. (A.0.6) gives,

$$\left(\begin{array}{cc} \text{Var} [\hat{X}_1] & \text{Cov} [\hat{X}_1, \hat{X}_2] + \frac{i}{2} \langle [\hat{X}_1, \hat{X}_2] \rangle \\ \text{Cov} [\hat{X}_1, \hat{X}_2] - \frac{i}{2} \langle [\hat{X}_1, \hat{X}_2] \rangle & \text{Var} [\hat{X}_2] \end{array} \right) \geq 0.$$

The sufficient condition for this to be true is that its lowest eigenvalue be positive, i.e.

$$(\text{Var} [\hat{X}_1] + \text{Var} [\hat{X}_2]) - \sqrt{(\text{Var} [\hat{X}_1] - \text{Var} [\hat{X}_2])^2 + 4 \text{Cov} [\hat{X}_1, \hat{X}_2]^2 + \langle [\hat{X}_1, \hat{X}_2] \rangle^2} \geq 0;$$

simplifying this gives the required result. \square

B Miscellaneous on elastodynamics

B.1 Principle of least action: equations of motion, boundary conditions

Following from Section 2.2.1, the action for the elastodynamic field is,

$$\mathcal{S}[[u_i]] = \int dt \int_D d^3r \mathcal{L}(u_i, \dot{u}_i, \partial_j u_i), \quad (\text{B.1.1})$$

for the set of independent displacement fields $u_i(\mathbf{r}, t)$. Note that for the sake of generality, we here retain a possible functional dependence of the Lagrangian on u_i , even though the actual Lagrangian of interest (eq. (2.2.15)),

$$\mathcal{L} = \frac{\rho}{2} \dot{u}_i \dot{u}_i - \frac{1}{2} t_{ij} u_{ij}^{(1)}, \quad (\text{B.1.2})$$

depends only on the derivatives of u_i . Note the constitutive relation for the stress in terms of the strain (eq. (2.2.16))

$$t_{ij} = \alpha_{ijkl} u_{kl}^{(1)}, \quad (\text{B.1.3})$$

with the Hooke tensor given by (eq. (2.2.17)),

$$\alpha_{ijkl} = \mu_1 \delta_{ij} \delta_{kl} + \mu_2 (\delta_{ik} \delta_{jl} + \delta_{il} \delta_{jk}). \quad (\text{B.1.4})$$

The principle of least action dictates that the field configuration $u_i(\mathbf{r}, t)$ that is realized is the one that renders the action minimum. Note that the action eq. (B.1.1) is an example of a *functional*, i.e., a map that associates to a set of functions (here u_i), a real number (here, the value of the definite integral in eq. (B.1.1)). Thus, it is reasonable to compare values of the action for different field configurations and determine one for which the action attains a minimum. In order to determine such a point, we are led to consider a space of test functions, so as to be able to explore the neighbourhood of each element of this functional space in a systematic fashion. Variational calculus [56, 106, 117] provides the machinery to accomplish this task^{B.1}.

We consider the *variation* of the functions u_i ,

$$u_i(\mathbf{r}, t) \rightarrow u_i(\mathbf{r}, t) + \delta u_i(\mathbf{r}, t),$$

^{B.1}incidentally, note that the principle of least action is really a principle of stationary action [117]

where the symbol δ denotes a functional variation, signifying the fact that these changes are simply a device to enable exploration of the functional neighbourhood of u_i . Since the fields u_i are independent, they may be varied independently, and so the corresponding variations δu_i are also independent. The resulting variation in the action is,

$$\delta \mathcal{S} = \int dt d^3r \left[\frac{\partial \mathcal{L}}{\partial u_i} \delta u_i + \frac{\partial \mathcal{L}}{\partial \dot{u}_i} \delta \dot{u}_i + \frac{\partial \mathcal{L}}{\partial (\partial_j u_i)} \delta (\partial_j u_i) \right].$$

The second and third terms of the integrand can be re-expressed as,

$$\begin{aligned} \frac{\partial \mathcal{L}}{\partial \dot{u}_i} \delta \dot{u}_i &= \frac{\partial \mathcal{L}}{\partial \dot{u}_i} \partial_t (\delta u_i) = \partial_t \left(\frac{\partial \mathcal{L}}{\partial \dot{u}_i} \delta u_i \right) - \partial_t \left(\frac{\partial \mathcal{L}}{\partial \dot{u}_i} \right) \delta u_i \\ \frac{\partial \mathcal{L}}{\partial (\partial_j u_i)} \delta (\partial_j u_i) &= \frac{\partial \mathcal{L}}{\partial (\partial_j u_i)} \partial_j (\delta u_i) = \partial_j \left(\frac{\partial \mathcal{L}}{\partial (\partial_j u_i)} \delta u_i \right) - \partial_j \left(\frac{\partial \mathcal{L}}{\partial (\partial_j u_i)} \right) \delta u_i \end{aligned} \quad (\text{B.1.5})$$

and re-inserted back. Thus we arrive at,

$$\begin{aligned} \delta \mathcal{S} &= \int dt \int_D d^3r \left[\frac{\partial \mathcal{L}}{\partial u_i} - \partial_t \left(\frac{\partial \mathcal{L}}{\partial \dot{u}_i} \right) - \partial_j \left(\frac{\partial \mathcal{L}}{\partial (\partial_j u_i)} \right) \right] \delta u_i \\ &\quad + \int_D d^3r \left[\frac{\partial \mathcal{L}}{\partial \dot{u}_i} \delta u_i \right]_{t=0}^{t=\infty} + \int dt \oint_{\partial D} dA_j \frac{\partial \mathcal{L}}{\partial (\partial_j u_i)} \delta u_i. \end{aligned} \quad (\text{B.1.6})$$

Here, the second and third integrals arise from integrating the total derivatives in eq. (B.1.5). In the third integral, this is performed through an application of the divergence theorem, resulting in an integral over the boundary ∂D of the domain D .

For the principle of least action to be implemented in the form,

$$\frac{\delta \mathcal{S}}{\delta u_i} = 0,$$

it is therefore required that each of the integrals in eq. (B.1.6) vanish separately. Since the variations δu_i are arbitrary, this is tantamount to each of the integrands vanishing independently. This results in three conditions:

1. the Euler-Lagrange equations,

$$\frac{\partial \mathcal{L}}{\partial u_i} - \partial_t \left(\frac{\partial \mathcal{L}}{\partial \dot{u}_i} \right) - \partial_j \left(\frac{\partial \mathcal{L}}{\partial (\partial_j u_i)} \right) = 0 \quad (\text{B.1.7})$$

2. fulfilment of initial and/or final conditions,

$$\left[\frac{\partial \mathcal{L}}{\partial \dot{u}_i} \delta u_i \right]_{t=0}^{t=\infty} = 0 \quad (\text{B.1.8})$$

3. fulfilment of boundary conditions,

$$\oint_{\partial D} dA_j \frac{\partial \mathcal{L}}{\partial (\partial_j u_i)} \delta u_i = 0. \quad (\text{B.1.9})$$

Note that the principle of least action not only furnishes the dynamical equation eq. (B.1.7) to be satisfied by the true field configuration, but also provides a consistent set of *natural* boundary conditions eqs. (B.1.8) and (B.1.9).

B.1.1 Equations of motion

To implement the Euler-Lagrange equation eq. (B.1.7), we compute the various terms in it, for the Lagrangian eq. (B.1.2):

$$\begin{aligned}\frac{\partial \mathcal{L}}{\partial u_i} &= 0 \\ \frac{\partial \mathcal{L}}{\partial \dot{u}_i} &= \frac{\partial}{\partial \dot{u}_i} \left(\frac{\rho}{2} \dot{u}_a \dot{u}_a \right) = \frac{\rho}{2} (2 \dot{u}_a \delta_{ia}) = \rho \dot{u}_i \\ \frac{\partial \mathcal{L}}{\partial (\partial_j u_i)} &= \frac{\partial}{\partial (\partial_j u_i)} \left(-\frac{\alpha_{abcd}}{2} (\partial_b u_a) (\partial_d u_c) \right) = -\alpha_{ijcd} (\partial_d u_c).\end{aligned}\tag{B.1.10}$$

Inserting these in eq. (B.1.7) gives,

$$\rho \ddot{u}_i - \alpha_{ijkl} \partial_j \partial_l u_k = 0.\tag{B.1.11}$$

Finally using the explicit form of the Hooke tensor (eq. (B.1.3)) gives the Navier equations,

$$\begin{aligned}\rho \ddot{u}_i &= (\mu_1 + \mu_2) \partial_i \partial_j u_j + \mu_2 \partial_j \partial_j u_i \\ \text{or, } \rho \ddot{\mathbf{u}} &= (\mu_1 + \mu_2) \nabla (\nabla \cdot \mathbf{u}) + \mu_2 \nabla^2 \mathbf{u} \\ &= (\mu_1 + 2\mu_2) \nabla (\nabla \cdot \mathbf{u}) - \mu_2 \nabla \times (\nabla \times \mathbf{u}),\end{aligned}\tag{B.1.12}$$

where the last two forms are expressed using vector operators appropriate for 3D domains. The third form is obtained by using the generally valid vector identity,

$$\nabla \times (\nabla \times \mathbf{u}) = \nabla (\nabla \cdot \mathbf{u}) - \nabla^2 \mathbf{u}.\tag{B.1.13}$$

B.1.2 Boundary conditions

The natural boundary condition eq. (B.1.9), applied to the Lagrangian eq. (B.1.2) results in,

$$\oint_{\partial D} dA_j t_{ij} \delta u_i = 0.$$

Using the fact that (see footnote 2.15), $t_{ij} dA_j = dF_i$, gives the force, the boundary condition reads,

$$\oint_{\partial D} dF_i \delta u_i = 0.$$

Since the variation δu_i are independent of the force on the boundary, this is equivalent to two conditions, viz.

$$\begin{aligned}dF_i|_{\partial D} &= t_{ij} dA_j|_{\partial D} = 0 \\ \delta u_i|_{\partial D} &= 0.\end{aligned}\tag{B.1.14}$$

Physically, the first is appropriate for a free boundary, on which no force impinges, whereas the second is appropriate for a fixed boundary, whose displacement is prescribed.

B.2 Transverse and longitudinal elastic waves

The Navier equations eq. (B.1.12) expressed as a single vector equation,

$$\ddot{\mathbf{u}} = \left(\frac{\mu_1 + 2\mu_2}{\rho} \right) \nabla(\nabla \cdot \mathbf{u}) - \left(\frac{\mu_2}{\rho} \right) \nabla \times (\nabla \times \mathbf{u}), \quad (\text{B.2.1})$$

makes explicit the two kinds of excitations referred to in section 2.2.1. In order to exhibit this claim, we make use of the fact that any vector field, here \mathbf{u} , in a simply connected domain D , maybe expressed uniquely in terms of *potentials*, $\phi(\mathbf{r}, t)$ and $\Phi(\mathbf{r}, t)$:

$$\mathbf{u} = \nabla\phi + \nabla \times \Phi. \quad (\text{B.2.2})$$

Identifying these two terms as \mathbf{u}_L and \mathbf{u}_T respectively, standard vector identities imply $\nabla \cdot \mathbf{u}_T = 0$ and $\nabla \times \mathbf{u}_L = 0$; \mathbf{u}_T (\mathbf{u}_L) is the transverse (longitudinal) component of \mathbf{u} . Substituting this decomposition into eq. (B.2.1), and realizing that the transverse and longitudinal components are independent, results in two wave equations,

$$\begin{aligned} \ddot{\mathbf{u}}_L &= \left(\frac{\mu_1 + 2\mu_2}{\rho} \right) \nabla^2 \mathbf{u}_L \\ \ddot{\mathbf{u}}_T &= \left(\frac{\mu_2}{\rho} \right) \nabla^2 \mathbf{u}_T. \end{aligned} \quad (\text{B.2.3})$$

The phase velocities of the two elastic waves can be immediately identified, viz.,

$$c_L := \sqrt{\frac{\mu_1 + 2\mu_2}{\rho}}, \quad c_T := \sqrt{\frac{\mu_2}{\rho}}. \quad (\text{B.2.4})$$

B.3 Hermiticity of the elastic operator

The elasticity operator $\hat{\mathbf{L}}$, defined in eq. (2.2.20) viz.

$$\hat{L}_{ik} = \frac{\alpha_{ijkl}}{\rho} \partial_j \partial_l, \quad (\text{B.3.1})$$

acts on vector functions \mathbf{u} defined on some finite domain D . Corresponding to some such function \mathbf{v} , we define a linear functional $\langle \mathbf{v}, \cdot \rangle$ that acts as,

$$\langle \mathbf{v}, \mathbf{u} \rangle := \frac{1}{\text{Vol}(D)} \int_D v_i^*(\mathbf{r}) u_i(\mathbf{r}) d^3r. \quad (\text{B.3.2})$$

We now restrict attention to functions \mathbf{u} for which $\langle \mathbf{u}, \mathbf{u} \rangle < \infty$, and satisfies one of the boundary conditions in eq. (B.1.14) viz.

$$\begin{aligned} \text{Type 1: } & dF_i|_{\partial D} = t_{ij} dA_j|_{\partial D} = \alpha_{ijkl} (\partial_j u_i) (\partial_l u_k)|_{\partial D} = 0 \\ \text{Type 2: } & u_i|_{\partial D} = 0, \end{aligned} \quad (\text{B.3.3})$$

where we have assumed (without loss of generality) that in the case of a fixed boundary condition, the boundary displacement is zero.

Each set of such functions – bounded and satisfying boundary condition of Type s ($s = 1, 2$) – forms a Hilbert space^{B.2} \mathcal{H}_s under the inner product $\langle \cdot, \cdot \rangle$. For every $\mathbf{u} \in \mathcal{H}_s$, there is a functional $\langle \mathbf{u}, \cdot \rangle \in \text{Dual}(\mathcal{H}_s)$ in the dual of \mathcal{H}_s [119].

Having identified the two distinct Hilbert spaces at play, the proof of the hermiticity of $\hat{\mathbf{L}}$ is straightforward. Using the definition of $\hat{\mathbf{L}}$ (eq. (B.3.1)),

$$\langle \mathbf{v}, \hat{\mathbf{L}}\mathbf{u} \rangle = \frac{\rho^{-1}}{\text{Vol}(D)} \int_D v_i^*(\mathbf{r}) \alpha_{ijkl} \partial_j \partial_l u_k(\mathbf{r}) \, d^3r. \quad (\text{B.3.4})$$

Manipulating the integral, and freely using the symmetries of the Hooke tensor (eq. (2.2.10)) $\alpha_{ijkl} = \alpha_{jikl} = \alpha_{ijlk} = \alpha_{klji}$,

$$\begin{aligned} \int_D v_i^* \alpha_{ijkl} \partial_j \partial_l u_k \, d^3r &= \int_D v_i^* \alpha_{ijkl} \partial_j \partial_k u_l \, d^3r \\ &= \int_D \partial_j (v_i^* \alpha_{ijkl} \partial_k u_l) \, d^3r - \int_D (\partial_j v_i^*) \alpha_{ijkl} (\partial_k u_l) \, d^3r \\ &= \int_{\partial D} v_i^* \underbrace{\alpha_{ijkl} \partial_k u_l}_{t_{ij}} \, dA_j - \int_D (\partial_j v_i^*) \alpha_{ijkl} (\partial_k u_l) \, d^3r; \end{aligned} \quad (\text{B.3.5})$$

the second equality follows by partial integration, while the third follows from Gauss' theorem. Finally, either type of boundary condition ensures that the first term in the last line is zero. Treating the remaining integral similarly,

$$\begin{aligned} \int_D v_i^* \alpha_{ijkl} \partial_j \partial_l u_k \, d^3r &= - \int_D (\partial_j v_i^*) \alpha_{ijkl} (\partial_k u_l) \, d^3r \\ &= - \int_{\partial D} (\partial_j v_i^*) \alpha_{ijkl} u_l \, dA_k + \int_D (\partial_k \partial_j v_i^*) \alpha_{ijkl} u_l \, d^3r \\ &= - \int_{\partial D} u_i \underbrace{\alpha_{ijkl} \partial_k v_l^*}_{t_{ij}^*} \, dA_k + \int_D (\alpha_{ijkl} \partial_j \partial_l v_k^*) u_i \, d^3r \\ &= \int_D (\alpha_{ijkl} \partial_j \partial_l v_k^*) u_i \, d^3r, \end{aligned} \quad (\text{B.3.6})$$

i.e., the differential operator $\partial_j \partial_l$ can be freely commuted within the integral as long as the functions satisfy one of the boundary conditions (eq. (B.3.3)), and the Hooke tensor is symmetric. In particular, this means that the inner product satisfies,

$$\langle \mathbf{v}, \hat{\mathbf{L}}\mathbf{u} \rangle = \langle \hat{\mathbf{L}}\mathbf{v}, \mathbf{u} \rangle, \quad (\text{B.3.7})$$

i.e. $\hat{\mathbf{L}}$ is hermitian in either Hilbert space $\mathcal{H}_{1,2}$.

^{B.2} Physically the two spaces $\mathcal{H}_{1,2}$ describe the displacement fields for the physically incompatible boundary conditions of each type; mathematically, this incompatibility manifests as the fact that a function satisfying one type of boundary condition does not form a superposition with that satisfying a different boundary condition, such that the superposed function satisfies any well-defined boundary condition. Closure under superposition is necessary for a Hilbert space.

C Response of an imbalanced interferometer

Following the discussion in section 2.2.2.1, assume that the amplitude flux $\hat{a}(t)$ of a coherent source of mean amplitude \bar{a} undergoes classical amplitude and phase fluctuations, so that in the rotating frame (the ansatz in eq. (2.2.45)),

$$a_{\text{in}}(t) = (\bar{a} + \delta\alpha(t))e^{i\delta\phi(t)}, \quad (\text{C.1})$$

where $\delta\alpha(t)$ and $\delta\phi(t)$ are real-valued stochastic processes. Note that since we are interested in classical noise in the amplitude $\delta\alpha(t)$ and in phase $\delta\phi(t)$, all vacuum contributions will be ignored here.

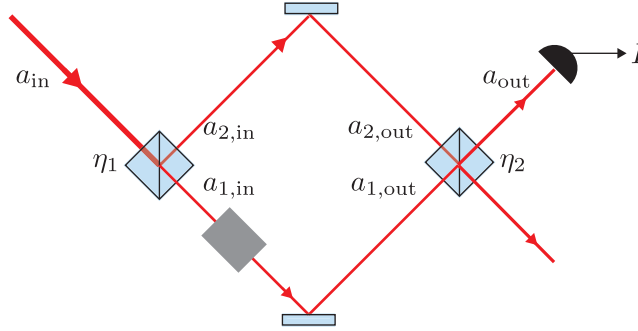


Fig. C.1 – **Schematic of an imbalanced interferometer.** An interferometer in Mach-Zehnder configuration with a noisy input field that is possibly frequency-shifted in one of the arms, and phase delayed in the other.

Figure C.1 shows such a field passing through an interferometer. When the input field is split at a beam splitter of transmissivity η_1 at the input of the interferometer, each arm is fed with the fields $a_{1,\text{in}}(t)$ and $a_{2,\text{in}}(t)$, given by,

$$a_{1,\text{in}}(t) = \sqrt{\eta_1} a_{\text{in}}(t), \quad a_{2,\text{in}}(t) = i\sqrt{1 - \eta_1} a_{\text{in}}(t). \quad (\text{C.2})$$

The first field propagates through a path containing a frequency-shifting element (for example, AOM) implementing a radio frequency shift $\Omega_{\text{IF}} \ll \Omega_{\text{det}} \ll \omega_\ell$ (where Ω_{det} is the final detection span), while the other field propagates through a relative delay (for example using a long path length) of duration τ . The two fields emerging at the end of these paths are,

$$a_{1,\text{out}}(t) = a_{1,\text{in}}(t)e^{-i\Omega_{\text{IF}}t}, \quad a_{2,\text{out}}(t) = a_{2,\text{in}}(t - \tau). \quad (\text{C.3})$$

Finally, the beams are combined at a beam-splitter of transmissivity η_2 and one of the outputs,

$$\begin{aligned} a_{\text{out}}(t) &= \sqrt{\eta_2} a_{1,\text{out}}(t) + i\sqrt{1-\eta_2} a_{2,\text{out}}(t) \\ &= \sqrt{\eta_1\eta_2} a_{\text{in}}(t)e^{-i\Omega_{\text{IF}}t} - \sqrt{(1-\eta_1)(1-\eta_2)} a_{\text{in}}(t-\tau), \end{aligned}$$

is photodetected. The resulting photocurrent $I(t) \propto |a_{\text{out}}(t)|^2$ is given by,

$$\begin{aligned} I(t) &= \eta_1\eta_2 |a_{\text{in}}(t)|^2 + (1-\eta_1)(1-\eta_2) |a_{\text{in}}(t-\tau)|^2 \\ &\quad + 2\sqrt{\eta_1\eta_2(1-\eta_1)(1-\eta_2)} \text{Re} a_{\text{in}}^*(t-\tau)a_{\text{in}}(t)e^{-i\Omega_{\text{IF}}t}. \end{aligned}$$

The last (interference) term, reflected as fluctuations in the photocurrent,

$$\begin{aligned} \delta I(t) &:= \text{Re} a_{\text{in}}^*(t-\tau)a_{\text{in}}(t)e^{-i\Omega_{\text{IF}}t} \\ &= \bar{a}^2 \left(1 + \frac{\delta\alpha(t-\tau)}{\bar{a}}\right) \left(1 + \frac{\delta\alpha(t)}{\bar{a}}\right) \cos[\delta\phi(t) - \delta\phi(t-\tau) - \Omega_{\text{IF}}t], \end{aligned}$$

carry traces of the amplitude and phase fluctuations of the field at the input of the interferometer. Introducing the cumulative relative amplitude fluctuations,

$$\delta A(t) := (\delta\alpha(t) + \delta\alpha(t-\tau)) / \bar{a}, \quad (\text{C.4})$$

and the differential phase fluctuations,

$$\delta\Phi(t) := \delta\phi(t) - \delta\phi(t-\tau), \quad (\text{C.5})$$

the photocurrent fluctuations can be approximated as,

$$\delta I(t) \approx (1 + \delta A(t)) \cos[\delta\Phi(t) - \Omega_{\text{IF}}t]. \quad (\text{C.6})$$

Henceforth, we assume that the amplitude ($\delta\alpha(t)$) and phase ($\delta\phi(t)$) fluctuations are stationary gaussian processes with zero mean; a property that is inherited by $\delta A(t)$, and, $\delta\Phi(t)$. However, due to the nonlinear transformation relating the phase to the photocurrent, the latter is not gaussian.

Despite this fact, useful information about the amplitude and phase fluctuations can be garnered from the lowest order correlation function of the fluctuating photocurrent. Indeed, assuming that the amplitude and phase fluctuations are uncorrelated (see footnote 4.1, on page 143), the two-time correlation of the photocurrent fluctuations take the form,

$$\begin{aligned} \langle \delta I(t)\delta I(0) \rangle &= \bar{a}^2 \left\langle \left(1 + \delta A(t)\right) \left(1 + \delta A(0)\right) \cos[\delta\Phi(t) - \Omega_{\text{IF}}t] \cos[\delta\Phi(0)] \right\rangle \\ &= \bar{a}^2 \left(1 + \langle \delta A(t)\delta A(0) \rangle\right) \left(\langle \cos[\delta\Phi(t)] \cos[\delta\Phi(0)] \rangle \cos \Omega_{\text{IF}}t \right. \\ &\quad \left. + \langle \sin[\delta\Phi(t)] \cos[\delta\Phi(0)] \rangle \sin \Omega_{\text{IF}}t \right). \end{aligned} \quad (\text{C.7})$$

Using standard techniques^{C.1}, the expectation values of the product of the cosine/sine phase terms can be shown to be equal, and given by,

$$\langle \cos[\delta\Phi(t)] \cos[\delta\Phi(0)] \rangle = \langle \sin[\delta\Phi(t)] \cos[\delta\Phi(0)] \rangle = \frac{1}{2} + \frac{1}{2} \exp[-\langle \delta\Phi(t)\delta\Phi(0) \rangle - \langle \delta\Phi(0)^2 \rangle]. \quad (\text{C.8})$$

^{C.1} Re-writing the trigonometric functions as exponentials, multiplying them out, and then using the identity $\langle \exp[i\delta X(t)] \rangle = \exp[-\frac{1}{2} \langle \delta X(t)\delta X(0) \rangle]$, on each exponential term; here δX denotes the relevant random process.

Finally using the Fourier representation of $\delta\Phi$, and then using eq. (C.5),

$$\begin{aligned}
\langle \delta\Phi(t)\delta\Phi(0) \rangle &= \int \frac{d\Omega d\Omega'}{(2\pi)^2} e^{-i\Omega t} \langle \delta\Phi[\Omega]\delta\Phi[\Omega'] \rangle \\
&= \int \frac{d\Omega d\Omega'}{(2\pi)^2} e^{-i\Omega t} \langle \delta\phi[\Omega](1 - e^{i\Omega\tau}) \delta\phi[\Omega'](1 - e^{i\Omega'\tau}) \rangle \\
&= \int \frac{d\Omega d\Omega'}{(2\pi)^2} e^{-i\Omega t} (1 - e^{i\Omega\tau})(1 - e^{i\Omega'\tau}) \cdot 2\pi S_{\phi\phi}[\Omega] \delta[\Omega - \Omega'] \\
&= -4 \int \frac{d\Omega}{2\pi} e^{-i\Omega(t-\tau)} \sin^2\left(\frac{\Omega\tau}{2}\right) S_{\phi\phi}[\Omega],
\end{aligned} \tag{C.9}$$

the two-time correlators in the exponent of eq. (C.8) can be expressed in terms of the spectrum of phase fluctuations. Similarly, the two-time correlator, $\langle \delta A(t)\delta A(0) \rangle$ in eq. (C.7), can be expressed in terms of the spectrum of amplitude fluctuations, viz.

$$\begin{aligned}
\langle \delta A(t)\delta A(0) \rangle &= \int \frac{d\Omega d\Omega'}{(2\pi)^2} e^{-i\Omega t} \langle \delta A[\Omega]\delta A[\Omega'] \rangle \\
&= \int \frac{d\Omega d\Omega'}{(2\pi)^2} e^{-i\Omega t} \langle \delta A[\Omega](1 + e^{i\Omega\tau}) \delta A[\Omega'](1 + e^{i\Omega'\tau}) \rangle \\
&= 4 \int \frac{d\Omega}{2\pi} e^{-i\Omega(t-\tau)} \cos^2\left(\frac{\Omega\tau}{2}\right) S_{\alpha\alpha}[\Omega].
\end{aligned} \tag{C.10}$$

Inserting eq. (C.9) in eq. (C.8) and subsequently in eq. (C.7), and inserting eq. (C.10) in eq. (C.7), taking the limit where $S_{\phi\phi} \ll 1$, and dropping irrelevant constant factors, the photocurrent correlation takes the approximate form,

$$\begin{aligned}
\langle \delta I(t)\delta I(0) \rangle &\propto \sin\left(\Omega_{\text{IF}}t + \frac{\pi}{4}\right) \left[1 + 4 \int \frac{d\Omega}{2\pi} e^{-i\Omega(t-\tau)} \cos^2\left(\frac{\Omega\tau}{2}\right) S_{\alpha\alpha}[\Omega] \right. \\
&\quad \left. + 4 \int \frac{d\Omega}{2\pi} e^{-i\Omega(t-\tau)} \sin^2\left(\frac{\Omega\tau}{2}\right) S_{\phi\phi}[\Omega] \right].
\end{aligned} \tag{C.11}$$

The (symmetrised) spectrum of photocurrent fluctuations recorded by a spectrum analyser is the cosine transform of this quantity. Shifted by the heterodyne beat frequency, the photocurrent spectrum is,

$$\bar{S}_{II}[\Omega - \Omega_{\text{IF}}] \propto \delta[\Omega - \Omega_{\text{IF}}] + 4 \int \frac{d\Omega}{2\pi} \left[\cos^2\left(\frac{\Omega\tau}{2}\right) \bar{S}_{\alpha\alpha}[\Omega] + \sin^2\left(\frac{\Omega\tau}{2}\right) \bar{S}_{\phi\phi}[\Omega] \right]. \tag{C.12}$$

This result is consistent with earlier treatments of phase fluctuations alone [353, 354].

Bibliography

- [1] J. Kepler, “De cometis libelli tres,” (1619).
- [2] I. Newton, *Opera quae exstant omnia*, Vol. III (Londinium, 1782).
- [3] W. Crookes, Phil. Trans. Roy. Soc. **164**, 501 (1874).
- [4] H. Cavendish, Phil. Trans. Roy. Soc. **88**, 469 (1798).
- [5] J. C. Maxwell, *A Treatise on Electricity and Magnetism* (1873).
- [6] E. F. Nichols and G. F. Hull, Phys. Rev. (Series I) **17**, 26 (1903).
- [7] J. H. Poynting, Phil. Trans. Roy. Soc. **175**, 343 (1884).
- [8] J. H. Poynting, *The Mean Density of the Earth* (C. Griffin & Co., 1894).
- [9] P. Lebedew, Ann. der Phys. **311**, 433 (1901).
- [10] H. P. Robertson, Month. Not. Roy. Astr. Soc. **97**, 423 (1937).
- [11] J. A. Burns, P. L. Lamy, and S. Soter, Icarus **40**, 1 (1979).
- [12] P. Musen, J. Geophys. Res. **65**, 1391 (1960).
- [13] M. Jammer, *The Conceptual Development of Quantum Mechanics* (McGraw Hill, 1966).
- [14] P. A. M. Dirac, *The Principles of Quantum Mechanics*, 4th ed. (Clarendon Press, 1982).
- [15] J. L. Hall, Science **202**, 147 (1978).
- [16] T. W. Hänsch and H. Walther, Rev. Mod. Phys. **71**, S242 (1999).
- [17] A. Ashkin, Phys. Rev. Lett. **24**, 156 (1970).
- [18] A. Ashkin, Science **210**, 1081 (1980).
- [19] W. Paul, Rev. Mod. Phys. **62**, 531 (1990).
- [20] H. Dehmelt, Science **247**, 539 (1990).
- [21] D. J. Wineland and H. Dehmelt, Bull. Amer. Phys. Soc. **20**, 637 (1975).
- [22] T. W. Hänsch and A. L. Schawlow, Opt. Commn. **13**, 68 (1975).
- [23] D. J. Wineland, R. E. Drullinger, and F. L. Walls, Phys. Rev. Lett. **40**, 1639 (1978).
- [24] S. Chu, Rev. Mod. Phys. **70**, 685 (1998).
- [25] C. Cohen-Tannoudji, Rev. Mod. Phys. **70**, 707 (1998).
- [26] C. E. Wieman, D. E. Pritchard, and D. J. Wineland, Rev. Mod. Phys. **71**, S253 (1999).
- [27] D. Leibfried, R. Blatt, C. Monroe, and D. J. Wineland, Rev. Mod. Phys. **75**, 281 (2003).
- [28] M. Brune, F. Schmidt-Kaler, A. Maali, J. Dreyer, E. Hagley, J. M. Raimond, and S. Haroche, Phys. Rev. Lett. **76**, 1800 (1996).
- [29] S. Haroche and J.-M. Raimond, *Exploring the Quantum: Atoms, Cavities and Photons* (Oxford University Press, 2006).
- [30] F. Diedrich, J. C. Bergquist, W. M. Itano, and D. J. Wineland, Phys. Rev. Lett. **62**, 403 (1989).
- [31] W. Ketterle, Rev. Mod. Phys. **74**, 1131 (2002).
- [32] E. A. Cornell and C. E. Wieman, Rev. Mod. Phys. **74**, 875 (2002).
- [33] J. Perrin, *Brownian Movement and Molecular Reality* (Taylor & Francis, 1910) translated by F. Soddy of the original in Ann. Chim. Phys. **18**, 5 (1909).
- [34] W. Einthoven, F. W. Einthoven, W. van der Holst, and H. Hirschfeld, Physica **5**, 358 (1925).
- [35] W. J. H. Moll and H. C. Burger, Phil. Mag. **50**, 626 (1925).
- [36] G. Ising, Phil. Mag. **1**, 827 (1926).
- [37] L. S. Ornstein, H. C. Burger, J. Taylor, and W. Clarkson, Proc. Roy. Soc. A **115**, 391 (1927).
- [38] R. V. Jones and C. W. McCombie, Phil. Trans. Roy. Soc. A **244**, 205 (1952).

- [39] J. M. W. Milatz and J. J. Van Zolingen, *Physica* **19**, 181 (1953).
- [40] R. B. Barnes and S. Silverman, *Rev. Mod. Phys.* **6**, 162 (1934).
- [41] C. W. McCombie, *Rep. Prog. Phys.* **16**, 266 (1953).
- [42] J. Clarke, *Proc. IEEE* **77**, 1208 (1989).
- [43] R. G. Knobel and A. N. Cleland, *Nature* **424**, 291 (2003).
- [44] M. D. LaHaye, O. Buu, B. Camarota, and K. C. Schwab, *Science* **304**, 74 (2004).
- [45] A. Naik, O. Buu, M. D. Lahaye, A. D. Armour, A. A. Clerk, M. P. Blencowe, and K. C. Schwab, *Nature* **443**, 193 (2006).
- [46] N. E. Flowers-Jacobs, D. R. Schmidt, and K. W. Lehnert, *Phys. Rev. Lett.* **98**, 096804 (2007).
- [47] M. Poggio, M. P. Jura, C. L. Degen, M. A. Topinka, H. J. Mamin, D. Goldhaber-Gordon, and D. Rugar, *Nature Phys.* **4**, 635 (2008).
- [48] S. Etaki, M. Poot, I. Mahboob, K. Onomitsu, H. Yamaguchi, and H. S. J. van der Zant, *Nature Phys.* **4**, 785 (2008).
- [49] G. Anetsberger, O. Arcizet, Q. P. Unterreithmeier, R. Rivière, A. Schliesser, E. M. Weig, J. P. Kotthaus, and T. J. Kippenberg, *Nature Phys.* **5**, 909 (2009).
- [50] J. D. Teufel, T. Donner, M. A. Castellanos-Beltran, J. W. Harlow, and K. W. Lehnert, *Nature Nanotech.* **4**, 820 (2009).
- [51] M. Aspelmeyer, T. J. Kippenberg, and F. Marquardt, *Rev. Mod. Phys.* **86**, 1391 (2014).
- [52] K. J. Vahala, *Nature* **424**, 839 (2003).
- [53] D. J. Wilson, V. Sudhir, N. Piro, R. Schilling, A. Ghadimi, and T. J. Kippenberg, *Nature* **524**, 325 (2015).
- [54] V. Sudhir, D. J. Wilson, R. Schilling, H. Schütz, A. Ghadimi, A. Nunnenkamp, and T. J. Kippenberg, *arXiv:1602.05942* (2016).
- [55] J. S. Bell, *Phys. World* **3**, 33 (1990).
- [56] W. Heitler, *The Quantum Theory of Radiation*, 3rd ed. (Clarendon Press, 1954).
- [57] W. Bernard and H. Callen, *Rev. Mod. Phys.* **31**, 1017 (1959).
- [58] M. Lax, *Rev. Mod. Phys.* **32**, 25 (1960).
- [59] R. Zwanzig, *Annu. Rev. Phys. Chem.* **16**, 67 (1965).
- [60] W. Weidlich, *Z. Phys.* **248**, 234 (1971).
- [61] G. S. Agarwal, *Phys. Rev. A* **11**, 230 (1975).
- [62] V. B. Braginsky and F. Y. Khalili, *Quantum Measurement* (Cambridge University Press, 1992).
- [63] E. Arthurs and J. Kelly, *Bell. Sys. Tech. J.* **44**, 725 (1965).
- [64] V. B. Braginsky and Y. I. Vorontsov, *Sov. Phys. Usp.* **17**, 644 (1975).
- [65] C. M. Caves, M. Zimmermann, K. S. Thorne, and R. W. Drever, *Rev. Mod. Phys.* **52**, 341 (1980).
- [66] C. M. Caves, *Phys. Rev. D* **26**, 1817 (1982).
- [67] M. Jaekel and S. Reynaud, *Europhys. Lett.* **13**, 301 (1990).
- [68] U. Gavish, B. Yurke, and Y. Imry, *Phys. Rev. Lett.* **93**, 250601 (2004).
- [69] A. A. Clerk, M. H. Devoret, S. M. Girvin, F. Marquardt, and R. J. Schoelkopf, *Rev. Mod. Phys.* **82**, 1155 (2010).
- [70] S. L. Danilishin and F. Y. Khalili, *Living Reviews in Relativity* **15**, 5 (2012).
- [71] R. Landauer, *Nature* **392**, 658 (1998).
- [72] J. von Neumann, *Mathematical Foundations of Quantum Mechanics* (Princeton University Press, 1955).
- [73] A. Fine, *J. Math. Phys.* **23**, 1306 (1982).
- [74] H. P. Robertson, *Phys. Rev.* **46**, 794 (1934).
- [75] E. Schrödinger, *Sitzungsberichte Preus. Akad. Wiss.* **19**, 296 (1930).
- [76] W. Heisenberg, *Z. Phys.* **43**, 172 (1927).
- [77] E. H. Kennard, *Z. Phys.* **44**, 326 (1927).
- [78] H. Weyl, *Theory of groups and quantum mechanics* (1932).
- [79] G. B. Folland and A. Sitaram, *J. Fourier Anal. Appl.* **3**, 207 (1997).
- [80] M. D. Donsker, *Memoirs Am. Math. Soc.* **6**, 12 (1951).
- [81] N. Wiener, *Fourier integrals and certain of its applications* (Cambridge University Press, 1933).
- [82] G. B. Lesovik and R. Loosen, *JETP Lett.* **65** (1997).

-
- [83] U. Gavish, Y. Levinson, and Y. Imry, *Phys. Rev. B* **62**, R10637 (2000).
- [84] R. Kubo, *Rep. Prog. Phys.* **29**, 255 (1966).
- [85] L. P. Kadanoff and P. C. Martin, *Ann. Phys.* **24**, 419 (1963).
- [86] D. Zubarev, *Sov. Phys. Usp.* **3**, 320 (1960).
- [87] T. Dittrich, P. Hanggi, G.-L. Ingold, B. Kramer, G. Schön, and W. Zwerger, *Quantum Transport and Dissipation* (Wiley-VCH, 1998).
- [88] Y. Nazarov, ed., *Quantum Noise in Mesoscopic Physics*, Proceedings of the NATO Advanced Research Workshop (Springer, 2002).
- [89] W. H. Zurek, *Rev. Mod. Phys.* **75**, 715 (2003).
- [90] V. P. Belavkin, *Rep. Math. Phys.* **43**, A405 (1999).
- [91] L. Bouten, R. V. Handel, and M. James, *SIAM J. Control Optimization* **46**, 2199 (2007).
- [92] V. B. Braginsky, Y. I. Vorontsov, and K. S. Thorne, *Science* **209**, 547 (1980).
- [93] R. J. Glauber, *Ann. NY Acad. Sci.* **480**, 336 (1986).
- [94] H. J. Kimble, Y. Levin, A. B. Matsko, K. S. Thorne, and S. P. Vyatchanin, *Phys. Rev. D* **65**, 022002 (2001).
- [95] A. Buonanno and Y. Chen, *Phys. Rev. D* **64**, 042006 (2001).
- [96] A. Pace, M. Collett, and D. Walls, *Phys. Rev. A* **47**, 3173 (1993).
- [97] W. Pauli, *Theory of Relativity* (Dover, 1958).
- [98] R. C. Tolman, *The theory of the relativity of motion* (UC Berkeley Press, 1918).
- [99] B. Carter and H. Quintana, *Proc. Roy. Soc. A* **331**, 57 (1972).
- [100] J. Kijowski and G. Magli, *J. Geom. Phys.* **9**, 207 (1992).
- [101] D. Christodolou, *Ann. Inst. Henri Poincaré* **69**, 335 (1998).
- [102] G. Maugin, *Continuum Mechanics Through the Twentieth Century* (Springer, 2013).
- [103] L. D. Landau and E. M. Lifshitz, *Theory of Elasticity*, 4th ed. (Butterworth-Heinemann, 1975).
- [104] R. Blandford and K. S. Thorne, *Modern Classical Physics* (Princeton University Press, 2016).
- [105] W. Kuhnel, *Differential geometry: curves - surfaces - manifolds* (AMS, 2006).
- [106] C. Lanczos, *The Variational Principles of Mechanics* (Dover, 1970).
- [107] E. P. Wigner, *Proc. Natl. Acad. Sci.* **51**, 956 (1964).
- [108] R. Houtappel, H. van Dam, and E. P. Wigner, *Rev. Mod. Phys.* **37**, 595 (1965).
- [109] J. Polchinski, arXiv:9210046 (1992).
- [110] H. Leutwyler, *Phys. Rev. D* **49**, 3033 (1994).
- [111] L. D. Landau and E. M. Lifshitz, *Mechanics*, 3rd ed. (Butterworth-Heinemann, 1976).
- [112] H. Bacry and J.-M. Levy-Leblond, *J. Math. Phys.* **9**, 1605 (1968).
- [113] M. J. Breuger, *Elementary Crystallography* (John Wiley, 1956).
- [114] I. M. Gelfand, R. Minlos, and Z. Shapiro, *Representations of the rotation and Lorentz Groups and their applications* (Pergamon Press, 1963).
- [115] J. Jerphagnon, D. Chemla, and R. Bonneville, *Adv. Phys.* **27**, 609 (1978).
- [116] P. G. Appleby, B. R. Duffy, and R. W. Ogden, *Glasgow Math. J.* **29**, 185 (1987).
- [117] I. M. Gelfand and S. V. Fomin, *Calculus of Variations* (Prentice-Hall, 1963).
- [118] H. Ezawa, *Ann. Phys.* **67**, 438 (1971).
- [119] K. O. Friedrichs, *Spectral theory of operators in Hilbert space* (Springer-Verlag, 1973).
- [120] M. Pinard, Y. Hadjar, and A. Heidmann, *Eur. Phys. J. D* **7**, 107 (1999).
- [121] G. W. Ford, M. Kac, and P. Mazur, *J. Math. Phys.* **6**, 504 (1965).
- [122] P. Ullersma, *Physica* **32**, 27 (1966).
- [123] P. S. Riseborough, P. Hanggi, and U. Weiss, *Phys. Rev. A* **31**, 471 (1985).
- [124] V. Giovannetti and D. Vitali, *Phys. Rev. A* **63**, 023812 (2001).
- [125] G. Lindblad, *Rep. Math. Phys.* **10**, 393 (1976).
- [126] F. Haake and R. Reibold, *Phys. Rev. A* **32**, 2462 (1985).
- [127] S. Gnutzmann and F. Haake, *Z. Phys. B* **101**, 263 (1996).
- [128] R. F. Streater, *J. Phys. A* **15**, 1477 (1982).
- [129] C. M. Caves and B. L. Schumaker, *Phys. Rev. A* **31**, 3068 (1985).
- [130] J. von Neumann, *Compositio Mathematica* **6**, 1 (1939).
- [131] R. J. Glauber, *Phys. Rev.* **131**, 2766 (1963).

- [132] K. J. Blow, R. Loudon, S. J. D. Phoenix, and T. J. Shepherd, *Phys. Rev. A* **42**, 4102 (1990).
- [133] M. O. Scully and W. E. Lamb, *Phys. Rev.* **159**, 208 (1967).
- [134] S. J. van Enk and C. A. Fuchs, arXiv:quant-ph/0111157 (2001).
- [135] R. Simon, N. Mukunda, and B. Dutta, *Phys. Rev. A* **49**, 1567 (1994).
- [136] J. W. Goodman, *Statistical Optics* (Wiley, 1985).
- [137] S. M. Barnett and D. T. Pegg, *J. Phys. A* **19**, 3849 (1986).
- [138] S. M. Barnett and J. A. Vaccaro, *The Quantum Phase Operator: A Review* (Taylor & Francis, 2007).
- [139] U. Leonhardt, *Rep. Prog. Phys.* **66**, 1207 (2003).
- [140] L. Mandel, E. C. G. Sudarshan, and E. Wolf, *Proc. Phys. Soc.* **84**, 435 (1964).
- [141] R. J. Glauber, *Phys. Rev.* **130**, 2529 (1963).
- [142] M. D. Srinivas and E. B. Davies, *J. Mod. Opt.* **28**, 981 (1981).
- [143] A. W. Hull and N. H. Williams, *Phys. Rev.* **25**, 147 (1925).
- [144] J. G. Graeme, *Photodiode Amplifiers* (McGraw Hill, 1996).
- [145] J. H. Shapiro, *IEEE J. Quant. Elec.* **21**, 237 (1985).
- [146] M. J. Collett, R. Loudon, and C. W. Gardiner, *J. Mod. Opt.* **34**, 881 (1987).
- [147] U. Leonhardt and H. Paul, *Prog. Quant. Elec.* **19**, 89 (1995).
- [148] R. Schnabel, N. Mavalvala, D. E. McClelland, and P. K. Lam, *Nature Comm.* **1**, 121 (2010).
- [149] H. P. Yuen and V. W. Chan, *Opt. Lett.* **8**, 177 (1983).
- [150] S. Steinlechner, B. W. Barr, A. S. Bell, S. L. Danilishin, A. Gläfke, C. Gräf, J.-S. Hennig, E. A. Houston, S. H. Huttner, S. S. Leavey, D. Pascucci, B. Sorazu, A. Spencer, K. A. Strain, J. Wright, and S. Hild, *Phys. Rev. D* **92**, 072009 (2015).
- [151] S. Machida and Y. Yamamoto, *IEEE J. Quant. Elec.* **22**, 617 (1986).
- [152] K. E. Gilliland, H. D. Cook, K. D. Mielenz, and R. B. Stephens, *Metrologia* **2**, 95 (1966).
- [153] A. G. McNish, *Science* **146**, 177 (1964).
- [154] A. M. Yaglom, *Correlation theory of stationary and related random functions*, Vol. 2 (Springer, 1987).
- [155] H. L. Hurd and A. Miamee, *Periodically corelated random sequences* (Wiley, 2007).
- [156] T. Niebauer, R. Schilling, K. Danzmann, A. Rüdiger, and W. Winkler, *Phys. Rev. A* **43**, 5022 (1991).
- [157] F. Quinlan, T. M. Fortier, H. Jiang, and S. A. Diddams, *J. Opt. Soc. Am. B* **30**, 1775 (2013).
- [158] H. Ogura, *IEEE. Trans. Info. Theory* **17**, 143 (1971).
- [159] M. B. Gray, A. J. Stevenson, H.-A. Bachor, and D. E. McClelland, *Opt. Lett.* **18**, 759 (1993).
- [160] M. Rakhmanov, *Appl. Opt.* **40**, 6596 (2001).
- [161] F. Quinlan, T. M. Fortier, H. Jiang, A. Hati, C. Nelson, Y. Fu, J. C. Campbell, and S. A. Diddams, *Nature Phot.* **7**, 290 (2013).
- [162] Z. Y. Ou and H. J. Kimble, *Phys. Rev. A* **52**, 3126 (1995).
- [163] R. D. Richtmeyer, *J. Appl. Phys.* **10**, 391 (1939).
- [164] K. Ujihara, *Output Coupling in Optical Cavities and Lasers* (Wiley-VCH, 2010).
- [165] S. Schiller, *Appl. Opt.* **32**, 2181 (1993).
- [166] D. K. Armani, T. J. Kippenberg, S. M. Spillane, and K. J. Vahala, *Nature* **421**, 925 (2003).
- [167] R. Schilling, H. Schütz, A. Ghadimi, V. Sudhir, D. Wilson, and T. Kippenberg, *Phys. Rev. Applied* **5**, 054019 (2016).
- [168] J. C. Knight, G. Cheung, F. Jacques, and T. A. Birks, *Opt. Lett.* **22**, 1129 (1997).
- [169] M. Cai, O. Painter, and K. J. Vahala, *Phys. Rev. Lett.* **85**, 74 (2000).
- [170] J. A. Stratton, *Electromagnetic Theory* (McGraw Hill, 1941).
- [171] E. Snitzer, *J. Opt. Soc. Am.* **51**, 491 (1961).
- [172] M. L. Gorodetsky and V. S. Ilchenko, *J. Opt. Soc. Am. B* **16**, 147 (1999).
- [173] H. J. Carmichael, *J. Opt. Soc. Am. B* **4**, 1588 (1987).
- [174] C. W. Gardiner, A. S. Parkins, and M. J. Collett, *J. Opt. Soc. Am. B* **4**, 1617 (1987).
- [175] V. B. Braginsky, M. L. Gorodetsky, and V. S. Ilchenko, *Phys. Lett. A* **137**, 393 (1989).
- [176] M. L. Gorodetsky, A. A. Savchenkov, and V. S. Ilchenko, *Opt. Lett.* **21**, 453 (1996).
- [177] M. L. Gorodetsky, A. D. Pryamikov, and V. S. Ilchenko, *J. Opt. Soc. Am. B* **17**, 1051 (2000).
- [178] H. Lee, T. Chen, J. Li, K. Y. Yang, S. Jeon, O. Painter, and K. J. Vahala, *Nature Phot.* **6**, 369 (2012).
- [179] D. W. Vernooy, V. S. Ilchenko, H. Mabuchi, E. W. Streed, and H. J. Kimble, *Opt. Lett.* **23**, 247 (1998).

-
- [180] A. E. Fomin, M. L. Gorodetsky, I. S. Grudin, and V. S. Ilchenko, *J. Opt. Soc. Am. B* **22**, 459 (2005).
- [181] H. A. Bethe and J. Schwinger, *Perturbation theory for cavities*, Tech. Rep. D1-117 (MIT Radiation Laboratory (NRDC), 1943).
- [182] G. D. Wassermann, *Math. Proc. Camb. Phil. Soc.* **44**, 251 (1948).
- [183] S. G. Johnson, M. Ibanescu, M. A. Skorobogatiy, O. Weisberg, J. D. Joannopoulos, and Y. Fink, *Phys. Rev. E* **65**, 066611 (2002).
- [184] P. Penfield and H. A. Haus, *Electrodynamics of moving media* (MIT Press, 1967).
- [185] S. M. Barnett and R. Loudon, *Phil. Trans. Roy. Soc. A* **368**, 927 (2010).
- [186] A. Feldman, *Phys. Rev. B* **11**, 5112 (1975).
- [187] P. T. Rakich, P. Davids, and Z. Wang, *Opt. Exp.* **18**, 14439 (2010).
- [188] L. Bel, J.-L. Boulanger, and N. Deruelle, *Phys. Rev. A* **37**, 1563 (1988).
- [189] S. Mancini and P. Tombesi, *Phys. Rev. A* **49**, 4055 (1994).
- [190] S. Aldana, C. Bruder, and A. Nunnenkamp, *Phys. Rev. A* **88**, 043826 (2013).
- [191] A. Dorsel, J. McCullen, P. Meystre, E. Vignes, and H. Walther, *Phys. Rev. Lett.* **51**, 1550 (1983).
- [192] A. Gozzini, I. Longo, S. Barbarino, F. Maccarrone, and F. Mango, *J. Opt. Soc. Am. B* **2**, 1841 (1985).
- [193] B. S. Sheard, M. B. Gray, C. M. Mow-Lowry, D. E. McClelland, and S. E. Whitcomb, *Phys. Rev. A* **69**, 051801 (2004).
- [194] V. Braginsky and A. Manukin, *Sov. Phys. JETP* **25**, 653 (1967).
- [195] T. J. Kippenberg and K. J. Vahala, *Science* **321**, 1172 (2008).
- [196] C. M. Caves, *Phys. Rev. Lett.* **45**, 75 (1980).
- [197] R. V. L. Hartley, *Bell. Sys. Tech. J.* **15**, 424 (1936).
- [198] T. Corbitt, Y. Chen, E. Innerhofer, H. Müller-Ebhardt, D. Ottaway, H. Rehbein, D. Sigg, S. Whitcomb, C. Wipf, and N. Mavalvala, *Phys. Rev. Lett.* **98**, 11 (2007).
- [199] K. K. Ni, R. Norte, D. J. Wilson, J. D. Hood, D. E. Chang, O. Painter, and H. J. Kimble, *Phys. Rev. Lett.* **108**, 214302 (2012).
- [200] H. Rokhsari, T. J. Kippenberg, T. Carmon, and K. J. Vahala, *Opt. Exp.* **13**, 5293 (2005).
- [201] K. Vahala, M. Herrmann, S. Knunz, V. Batteiger, G. Saathoff, T. W. Haensch, and T. Udem, *Nature Phys.* **5**, 682 (2009).
- [202] M. Evans *et al.*, *Phys. Rev. Lett.* **114**, 161102 (2015).
- [203] S. Gigan, H. R. Böhm, M. Paternostro, F. Blaser, G. Langer, J. B. Hertzberg, K. C. Schwab, D. Bäuerle, M. Aspelmeyer, and A. Zeilinger, *Nature* **444**, 67 (2006).
- [204] O. Arcizet, P.-F. Cohadon, T. Briant, M. Pinard, and A. Heidmann, *Nature* **444**, 71 (2006).
- [205] A. Schliesser, P. Del’Haye, N. Nooshi, K. Vahala, and T. Kippenberg, *Phys. Rev. Lett.* **97**, 243905 (2006).
- [206] T. Corbitt, D. Ottaway, E. Innerhofer, J. Pelc, and N. Mavalvala, *Phys. Rev. A* **74**, 021802(R) (2006).
- [207] J. D. Teufel, J. W. Harlow, C. Regal, and K. W. Lehnert, *Phys. Rev. Lett.* **100**, 197203 (2008).
- [208] T. Rocheleau, T. Ndikum, C. Macklin, J. B. Hertzberg, A. A. Clerk, and K. C. Schwab, *Nature* **463**, 72 (2010).
- [209] J. D. Teufel, T. Donner, D. Li, J. W. Harlow, M. S. Allman, K. Cicak, A. J. Sirois, J. D. Whittaker, K. W. Lehnert, and R. W. Simmonds, *Nature* **475**, 359 (2011).
- [210] J. Chan, T. P. M. Alegre, A. H. Safavi-Naeini, J. T. Hill, A. Krause, S. Gröblacher, M. Aspelmeyer, and O. Painter, *Nature* **478**, 89 (2011).
- [211] E. Verhagen, S. Deleglise, S. Weis, A. Schliesser, and T. J. Kippenberg, *Nature* **482**, 63 (2012).
- [212] S. Weis, R. Rivière, S. Deléglise, E. Gavartin, O. Arcizet, A. Schliesser, and T. J. Kippenberg, *Science* **330**, 1520 (2010).
- [213] A. H. Safavi-Naeini, T. P. Mayer Alegre, J. Chan, M. Eichenfield, M. Winger, Q. Lin, J. T. Hill, D. E. Chang, and O. Painter, *Nature* **472**, 69 (2011).
- [214] X. Zhou, F. Hocke, A. Schliesser, A. Marx, H. Heubl, R. Gross, and T. J. Kippenberg, *Nature Phys.* **9**, 179 (2013).
- [215] A. Nunnenkamp, V. Sudhir, A. Feofanov, A. Roulet, and T. Kippenberg, *Phys. Rev. Lett.* **113**, 023604 (2014).
- [216] W. E. Newell, *Science* **161**, 1320 (1968).
- [217] H. G. Craighead, *Science* **290**, 1532 (2000).

- [218] K. L. Ekinci and M. L. Roukes, *Rev. Sci. Instrum.* **76**, 061101 (2005).
- [219] K. C. Schwab and M. L. Roukes, *Physics Today* **58**, 36 (2005).
- [220] K. Y. Yasumura, T. D. Stowe, E. M. Chow, T. Pfafman, T. W. Kenny, B. C. Stipe, and D. Rugar, *J. Microelectromech. Sys.* **9**, 117 (2000).
- [221] P. Mohanty, D. A. Harrington, K. L. Ekinci, Y. T. Yang, M. J. Murphy, and M. L. Roukes, *Phys. Rev. B* **66**, 085416 (2002).
- [222] M. Imboden and P. Mohanty, *Phys. Rep.* **534**, 89 (2014).
- [223] S. S. Verbridge, J. M. Parpia, R. B. Reichenbach, L. M. Bellan, and H. G. Craighead, *J. Appl. Phys.* **99** (2006).
- [224] S. S. Verbridge, H. G. Craighead, and J. M. Parpia, *Appl. Phys. Lett.* **92**, 013112 (2008).
- [225] Q. P. Unterreithmeier, T. Faust, and J. P. Kotthaus, *Phys. Rev. Lett.* **105**, 027205 (2010).
- [226] S. Schmid, K. D. Jensen, K. H. Nielsen, and A. Boisen, *Phys. Rev. B* **84**, 165307 (2011).
- [227] G. Anetsberger, *Novel Cavity Optomechanical Systems at the Micro- and Nanoscale and Quantum Measurements of Nanomechanical Oscillators*, Ph.D. thesis, LMU Munich (2010).
- [228] E. Gavartin, *Optonanomechanical Systems for Measurement Applications*, Ph.D. thesis, EPFL (2013).
- [229] M. Nieto-Vesperinas, P. C. Chaumet, and A. Rahmani, *Phil. Trans. Roy. Soc. A* **362**, 719 (2004).
- [230] Q. P. Unterreithmeier, E. M. Weig, and J. P. Kotthaus, *Nature* **458**, 1001 (2009).
- [231] M. Eichenfield, R. Camacho, J. Chan, K. J. Vahala, and O. Painter, *Nature* **459**, 550 (2009).
- [232] D. van Thourhout and J. Roels, *Nature Phot.* **4**, 211 (2010).
- [233] B. E. Little and H. A. Haus, *J. Lightwave Tech.* **17**, 704 (1999).
- [234] M. L. Gorodetsky and A. E. Fomin, *IEEE J. Sel. Top. Quant. Elec.* **12**, 33 (2006).
- [235] M. L. Gorodetsky, A. Schliesser, G. Anetsberger, S. Deleglise, and T. J. Kippenberg, *Opt. Exp.* **18**, 23236 (2010).
- [236] E. A. Whittaker, M. Gehrtz, and G. C. Bjorklund, *J. Opt. Soc. Am. B* **2**, 1320 (1985).
- [237] N. C. Wong and J. L. Hall, *J. Opt. Soc. Am. B* **2**, 1527 (1985).
- [238] W. Zhang, M. J. Martin, C. Benko, J. L. Hall, J. Ye, C. Hagemann, T. Legero, U. Sterr, F. Riehle, G. D. Cole, and M. Aspelmeyer, *Opt. Lett.* **39**, 1980 (2014).
- [239] R. B. Blackman and J. W. Tuckey, *The measurement of power spectra* (Dover, 1959).
- [240] T. Briant, P. F. Cohadon, M. Pinard, and A. Heidmann, *Eur. Phys. J. D* **22**, 131 (2003).
- [241] R. O. Pohl, X. Liu, and E. Thompson, *Rev. Mod. Phys.* **74**, 991 (2002).
- [242] F. R. Blom, S. Bouwstra, M. Elwenspoek, and J. H. J. Fluitman, *J. Vac. Sci. Tech. B* **10**, 19 (1992).
- [243] M. Bao and H. Yang, *Sens. Act. A* **136**, 3 (2007).
- [244] V. Yakhot and C. Colosqui, *J. Fluid Mech.* **586**, 249 (2007).
- [245] D. M. Karabacak, V. Yakhot, and K. L. Ekinci, *Phys. Rev. Lett.* **98**, 254505 (2007).
- [246] S. S. Verbridge, R. Ilic, H. G. Craighead, and J. M. Parpia, *Appl. Phys. Lett.* **93**, 013101 (2008).
- [247] S. Schlamminger, C. A. Hagedorn, and J. H. Gundlach, *Phys. Rev. D* **81**, 123008 (2010).
- [248] C. H. Metzger and K. Karrai, *Nature* **432**, 1002 (2004).
- [249] S. De Liberato, N. Lambert, and F. Nori, *Phys. Rev. A* **83**, 033809 (2011).
- [250] A. Schliesser, *Cavity Optomechanics and Optical Frequency Comb Generation with Silica Whispering-Gallery-Mode Microresonators*, Ph.D. thesis, LMU Munich (2010).
- [251] O. Arcizet, R. Rivière, A. Schliesser, G. Anetsberger, and T. Kippenberg, *Phys. Rev. A* **80**, 021803(R) (2009).
- [252] J. P. Dowling and G. J. Milburn, *Phil. Trans. Roy. Soc. A* **361**, 1655 (2003).
- [253] J. C. Maxwell, *Proc. Roy. Soc.* **16**, 270 (1868).
- [254] M. V. Headrick, *IEEE Control Systems* **22**, 41 (2002).
- [255] J. C. Bergquist, S. R. Jefferts, and D. J. Wineland, *Phys. Today* **54**, 37 (2001).
- [256] A. D. Lundlow, M. M. Boyd, J. Ye, E. Peik, and P. O. Schmidt, *Rev. Mod. Phys.* **87**, 637 (2015).
- [257] D. J. Wineland, *Science* **226**, 395 (1984).
- [258] J. M. W. Milatz, J. J. Van Zolingen, and B. B. Van Iperen, *Physica* **19**, 195 (1953).
- [259] J. A. Sirs, *J. Sci. Instrum.* **36**, 223 (1959).
- [260] P. G. Roll, R. Krotkov, and R. H. Dicke, *Ann. Phys.* **26**, 442 (1964).
- [261] D. Möhl, G. Petrucci, L. Thorndahl, and S. van der Meer, *Phys. Rep.* **58**, 73 (1980).
- [262] B. D'Urso, B. Odom, and G. Gabrielse, *Phys. Rev. Lett.* **90**, 043001 (2003).

- [263] H. M. Wiseman, *Phys. Rev. A* **49**, 2133 (1994).
- [264] H. M. Wiseman and G. J. Milburn, *Quantum Measurement and Control* (Cambridge University Press, 2010).
- [265] M. Hatridge, S. Shankar, M. Mirrahimi, F. Schackert, K. Geerlings, T. Brecht, K. Sliwa, B. Abdo, L. Frunzio, S. Girvin, *et al.*, *Science* **339**, 178 (2013).
- [266] C. Sayrin, I. Dotsenko, X. Zhou, B. Peaudecerf, T. Rybarczyk, S. Gleyzes, P. Rouchon, M. Mirrahimi, H. Amini, M. Brune, J.-M. Raimond, and S. Haroche, *Nature* **477**, 73 (2011).
- [267] B. Peaudecerf, C. Sayrin, X. Zhou, T. Rybarczyk, S. Gleyzes, I. Dotsenko, J. Raimond, M. Brune, and S. Haroche, *Phys. Rev. A* **87**, 042320 (2013).
- [268] R. Vijay, C. Macklin, D. H. Slichter, S. J. Weber, K. W. Murch, R. Naik, A. N. Korotkov, and I. Siddiqi, *Nature* **490**, 77 (2012).
- [269] S. Mancini, D. Vitali, and P. Tombesi, *Phys. Rev. Lett.* **80**, 688 (1998).
- [270] J. Courty, A. Heidmann, and M. Pinard, *Eur. Phys. J. D* **17**, 399 (2001).
- [271] T. Kailath, *Linear Systems* (Prentice-Hall, 1980).
- [272] Y. Makhlin, G. Schön, and A. Shnirman, *Rev. Mod. Phys.* **73**, 357 (2001).
- [273] T. J. Kippenberg, S. M. Spillane, and K. J. Vahala, *Opt. Lett.* **27**, 1669 (2002).
- [274] H. Bode, *Network analysis and feedback amplifier design* (Van Nostrand Company, 1945).
- [275] P. Cohadon, A. Heidmann, and M. Pinard, *Phys. Rev. Lett.* **83**, 3174 (1999).
- [276] A. C. Doherty, A. Szorkovszky, G. I. Harris, and W. P. Bowen, *Phil. Trans. Roy. Soc. A* **370**, 5338 (2012).
- [277] G. Anetsberger, E. Gavartin, O. Arcizet, Q. P. Unterreithmeier, E. M. Weig, M. L. Gorodetsky, J. P. Kotthaus, and T. J. Kippenberg, *Phys. Rev. A* **82**, 061804 (2010).
- [278] T. Westphal, D. Friedrich, H. Kaufer, K. Yamamoto, S. Gossler, H. Muller-Ebhardt, S. Danilishin, F. Khalili, K. Danzmann, and R. Schnabel, *Phys. Rev. A* **85**, 063806 (2012).
- [279] A. Gillespie and F. Raab, *Phys. Lett. A* **178**, 357 (1993).
- [280] O. Arcizet, P.-F. Cohadon, T. Briant, M. Pinard, A. Heidmann, J.-M. Mackowski, C. Michel, L. Pinard, O. Français, and L. Rousseau, *Phys. Rev. Lett.* **97**, 133601 (2006).
- [281] W. H. Glenn, *IEEE J. Quant. Elec.* **25**, 1218 (1989).
- [282] V. B. Braginsky, M. L. Gorodetsky, and S. P. Vyatchanin, *Phys. Lett. A* **264**, 1 (1999).
- [283] V. B. Braginsky, M. L. Gorodetsky, and S. P. Vyatchanin, *Phys. Lett. A* **271**, 303 (2000).
- [284] K. Numata, A. Kemery, and J. Camp, *Phys. Rev. Lett.* **93**, 250602 (2004).
- [285] C. E. Wieman and L. Hollberg, *Rev. Sci. Instru.* **62**, 1 (1991).
- [286] P. R. Saulson, *Phys. Rev. D* **42**, 2437 (1990).
- [287] T. Uchiyama, S. Miyoki, S. Telada, K. Yamamoto, M. Ohashi, K. Agatsuma, K. Arai, M.-K. Fujimoto, T. Haruyama, S. Kawamura, O. Miyakawa, N. Ohishi, T. Saito, T. Shintomi, T. Suzuki, R. Takahashi, and D. Tatsumi, *Phys. Rev. Lett.* **108**, 141101 (2012).
- [288] M. L. Gorodetsky and I. S. Grudinin, *J. Opt. Soc. Am. B* **21**, 697 (2004).
- [289] R. Zeller and R. Pohl, *Phys. Rev. B* **4**, 2029 (1971).
- [290] R. Shelby, M. D. Levenson, and P. W. Bayer, *Phys. Rev. B* **31**, 5244 (1985).
- [291] G. van Lear and G. E. Uhlenbeck, *Phys. Rev.* **38**, 1583 (1931).
- [292] A. Yariv, *Quantum Electronics* (John Wiley, 1989).
- [293] H. Wiseman, *Phys. Rev. A* **51**, 2459 (1995).
- [294] T. P. Purdy, R. W. Peterson, and C. Regal, *Science* **339**, 801 (2013).
- [295] J. Teufel, F. Lecocq, and R. Simmonds, *Phys. Rev. Lett.* **116**, 013602 (2016).
- [296] D. G. Cahill, W. K. Ford, K. E. Goodson, G. D. Mahan, A. Majumdar, H. J. Maris, R. Merlin, and S. R. Phillpot, *J. Appl. Phys.* **93**, 793 (2002).
- [297] M. Poggio, C. Degen, H. Mamin, and D. Rugar, *Phys. Rev. Lett.* **99**, 017201 (2007).
- [298] T. Corbitt, C. Wipf, T. Bodiya, D. Ottaway, D. Sigg, N. Smith, S. Whitcomb, and N. Mavalvala, *Phys. Rev. Lett.* **99**, 160801 (2007).
- [299] D. Kleckner and D. Bouwmeester, *Nature* **444**, 75 (2006).
- [300] T. Li, S. Kheifets, and M. G. Raizen, *Nature Phys.* **7**, 527 (2011).
- [301] B. Abbott, R. Abbott, R. Adhikari, P. Ajith, B. Allen, G. Allen, R. Amin, S. Anderson, W. Anderson, M. Arain, *et al.*, *New J. Phys.* **11**, 073032 (2009).

- [302] D. W. C. Brooks, T. Botter, S. Schreppler, T. P. Purdy, N. Brahms, and D. M. Stamper-Kurn, *Nature* **488**, 476 (2012).
- [303] A. H. Safavi-Naeini, S. Gröblacher, J. T. Hill, J. Chan, M. Aspelmeyer, and O. Painter, *Nature* **500**, 185 (2013).
- [304] A. H. Safavi-Naeini, J. Chan, J. T. Hill, T. P. M. Alegre, A. Krause, and O. Painter, *Phys. Rev. Lett.* **108**, 033602 (2012).
- [305] A. Weinstein, C. Lei, E. Wollman, J. Suh, A. Metelmann, A. Clerk, and K. Schwab, *Phys. Rev. X* **4**, 041003 (2014).
- [306] T. P. Purdy, P.-L. Yu, N. S. Kampel, R. W. Peterson, K. Cicak, R. W. Simmonds, and C. A. Regal, *Phys. Rev. A* **92**, 031802 (2015).
- [307] M. Underwood, D. Mason, D. Lee, H. Xu, L. Jiang, A. B. Shkarin, K. Børkje, S. M. Girvin, and J. G. E. Harris, *Phys. Rev. A* **92**, 061801 (2015).
- [308] F. Khalili, H. Miao, H. Yang, A. Safavi-Naeini, O. Painter, and Y. Chen, *Phys. Rev. A* **86**, 033840 (2012).
- [309] L. F. Buchmann, S. Schreppler, J. Kohler, N. Spethmann, and D. M. Stamper-Kurn, *arXiv:1602.02141* (2016).
- [310] R. W. Peterson, T. P. Purdy, N. S. Kampel, R. W. Andrews, L. K. W. Yu, P.-L., and C. A. Regal, *Phys. Rev. Lett.* **116**, 063601 (2016).
- [311] I. Wilson-Rae, N. Nooshi, W. Zwerger, and T. J. Kippenberg, *Phys. Rev. Lett.* **99**, 093901 (2007).
- [312] F. Marquardt, J. Chen, A. A. Clerk, and S. M. Girvin, *Phys. Rev. Lett.* **99**, 093902 (2007).
- [313] P. Bushev, D. Rotter, A. Wilson, F. Dubin, C. Becher, J. Eschner, R. Blatt, V. Steixner, P. Rabl, and P. Zoller, *Phys. Rev. Lett.* **96**, 043003 (2006).
- [314] A. Krause, T. D. Blasius, and O. Painter, *arXiv:1506.01249* (2015).
- [315] V. B. Braginsky, M. L. Gorodetsky, F. Y. Khalili, A. B. Matsko, K. S. Thorne, and S. P. Vyatchanin, *Phys. Rev. D* **67**, 082001 (2003).
- [316] C. Fabre, M. Pinard, S. Bourzeix, A. Heidmann, E. Giacobino, and S. Reynaud, *Phys. Rev. A* **49**, 1337 (1994).
- [317] A. M. Jayich, J. C. Sankey, K. Børkje, D. Lee, C. Yang, M. Underwood, L. Childress, A. Petrenko, S. M. Girvin, and J. G. E. Harris, *New J. Phys.* **14**, 115018 (2012).
- [318] A. H. Safavi-Naeini, J. Chan, J. T. Hill, S. Gröblacher, H. Miao, Y. Chen, M. Aspelmeyer, and O. Painter, *New J. Phys.* **15**, 035007 (2013).
- [319] K. Vahala, C. Harder, and A. Yariv, *Appl. Phys. Lett.* **42**, 211 (1983).
- [320] M. van Exeter, W. Hamel, J. P. Woerdman, and B. Zeijlmans, *IEEE J. Quantum Electronics* **28**, 1470 (1992).
- [321] T. J. Kippenberg, A. Schliesser, and M. L. Gorodetsky, *New J. Phys.* **15**, 015019 (2013).
- [322] V. B. Braginsky, M. L. Gorodetsky, F. Y. Khalili, and K. S. Thorne, *Phys. Rev. D* **61**, 044002 (2000).
- [323] H. Cramer, *Mathematical Methods of Statistics* (Princeton University Press).
- [324] A. H. Safavi-Naeini, S. Gröblacher, J. T. Hill, J. Chan, M. Aspelmeyer, and O. Painter, *Nature* **500**, 185 (2013).
- [325] T. P. Purdy, P. Yu, R. W. Peterson, N. S. Kampel, and C. A. Regal, *Phys. Rev. X* **3**, 031012 (2013).
- [326] M. S. Taubman, H. Wiseman, D. E. McClelland, and H.-A. Bachor, *J. Opt. Soc. Am. B* **12**, 1792 (1995).
- [327] H. M. Wiseman, *J. Opt. B* **1**, 459 (1999).
- [328] D. Ristè, M. Dukalski, C. A. Watson, G. de Lange, M. J. Tiggelman, Y. M. Blanter, K. W. Lehnert, R. N. Schouten, and L. DiCarlo, *Nature* **502**, 350 (2013).
- [329] Y. Liu, S. Shankar, N. Ofek, M. Hatridge, A. Narla, K. Sliwa, L. Frunzio, R. Schoelkopf, and M. Devoret, *Phys. Rev. X* **6**, 011022 (2016).
- [330] K. C. Cox, G. P. Greve, J. M. Weiner, and J. K. Thompson, *Phys. Rev. Lett.* **116**, 093602 (2016).
- [331] V. Giovannetti, S. Lloyd, and L. Maccone, *Science* **306**, 1330 (2004).
- [332] N. S. Kampel, R. W. Peterson, R. Fischer, P.-L. Yu, K. Cicak, R. W. Simmonds, K. W. Lehnert, and C. A. Regal, *arXiv:1607.06831* (2016).
- [333] V. Sudhir, R. Schilling, S. Fedorov, H. Schütz, D. J. Wilson, and T. J. Kippenberg, *arXiv:1608.00699* (2016).

-
- [334] N. Wiener, *Extrapolation, Interpolation and Smoothing of Stationary Time Series* (MIT Technology Press, 1949).
- [335] M. Athans, IEEE. Trans. Auto. Control **16**, 529 (1971).
- [336] M. James, H. Nurdin, and I. Petersen, IEEE Transactions on Automatic Control **53**, 1787 (2008).
- [337] H. I. Nurdin, M. R. James, and I. R. Petersen, Automatica **45**, 1837 (2009).
- [338] H. Miao, H. Yang, R. X. Adhikari, and Y. Chen, Class. Quant. Grav. **31**, 165010 (2014).
- [339] S. P. Vyatchanin and E. A. Zubova, Phys. Lett. A **201**, 269 (1995).
- [340] V. Giovannetti, S. Lloyd, and L. Maccone, Phys. Rev. Lett. **96**, 010401 (2006).
- [341] G. M. D'Ariano, P. Lo Presti, and M. G. A. Paris, Phys. Rev. Lett. **87**, 270404 (2001).
- [342] J. Aasi *et al.*, Nature Phot. **7**, 613 (2013).
- [343] J. B. Clark, F. Lecocq, R. W. Simmonds, J. Aumentado, and J. D. Teufel, Nature Phys. **12**, 683 (2016).
- [344] M. W. Mitchell, J. S. Lundeen, and A. M. Steinberg, Nature **429**, 161 (2004).
- [345] T. Nagata, R. Okamoto, J. L. O'Brien, K. Sasaki, and S. Takeuchi, Science **316**, 726 (2007).
- [346] I. Afek, O. Ambar, and Y. Silberberg, Science **328**, 879 (2010).
- [347] D. Leibfried, M. D. Barrett, T. Schaetz, J. Britton, J. Chiaverini, W. M. Itano, J. D. Jost, C. Langer, and D. J. Wineland, Science **304**, 1476 (2004).
- [348] C. F. Roos, M. Chwalla, K. Kim, M. Riebe, and R. Blatt, Nature **443**, 316 (2006).
- [349] W. Nagourney, J. Sandberg, and H. Dehmelt, Phys. Rev. Lett. **56**, 2797 (1986).
- [350] C. Guerlin, J. Bernu, S. Deléglise, C. Sayrin, S. Gleyzes, S. Kuhr, M. Brune, J.-M. Raimond, and S. Haroche, Nature **448**, 889 (2007).
- [351] B. R. Johnson, M. D. Reed, A. A. Houck, D. I. Schuster, L. S. Bishop, E. Ginossar, J. M. Gambetta, L. DiCarlo, L. Frunzio, S. M. Girvin, and R. J. Schoelkopf, Nature Phys. **6**, 663 (2010).
- [352] J. Suh, A. J. Weinstein, C. U. Lei, E. E. Wollman, S. K. Steinke, P. Meystre, A. A. Clerk, and K. C. Schwab, Science **344**, 1262 (2014).
- [353] J. A. Armstrong, J. Opt. Soc. Am. **56**, 1024 (1966).
- [354] P. Gallion and G. Debarge, IEEE J. Quant. Elec. **20**, 343 (1984).

Curriculum Vitae

Vivishek Sudhir

Permanent address: 'Krishnangie', Puthur Road, Palakkad 678001, India

Email: vivishek.sudhir@gmail.com

Nationality: India, *Date of birth:* 28 June 1988

Professional Education

- | | |
|-------------|--|
| 2011 – 2016 | Ecolé Polytechnique Fédérale de Lausanne, Lausanne, Switzerland
PhD in the group of Prof. Tobias Kippenberg |
| 2010 – 2011 | Imperial College London, London, UK
MRes in Controlled Quantum Dynamics (group of Sir Peter Knight) |
| 2006 – 2010 | Amrita School of Engineering, Ettimadai, India
BTech in Electrical & Electronics Engineering |
| 1994 – 2006 | Central School, Kanjikode, India
All India Senior School Certificate Examination |

Professional Experience

- | | |
|------------------|--|
| May – Aug. 2010 | Indian Institute of Science, Bangalore, India
Research Assistant (group of Prof. V. Natarajan) |
| Jun. – Aug. 2009 | Utrecht University, Utrecht, Netherlands
Summer student at Institute for Theoretical Physics |
| 2007 – 2010 | Indian Institute of Technology Madras, Chennai, India
Institute Fellow (groups of Prof. P. C. Deshmukh and Prof. M. V. Satyanarayana) |